

AD-A184 076

2

MAY 16 1988

USE OF A THERMODYNAMIC ANALOG FOR PNEUMATIC TRANSPORT
IN HORIZONTAL PIPES

Captain Craig A. Myler
HQDA, MILPERCEN (DAPC-OPA-E)
200 Stovall Street
Alexandria, VA 22332

Final Report AUG 87

DTIC
ELECTE
AUG 31 1987
S D D

Army Military Personnel Center

Approved for Public Release; distribution unlimited

PROPERTY OF U.S. AIR FORCE
AEDC TECHNICAL LIBRARY

A thesis submitted to the University of Pittsburgh in partial fulfillment of the requirements for the degree of Doctor of Philosophy in Chemical Engineering

TECHNICAL REPORTS
FILE COPY

87 8 25 170

USE OF A THERMODYNAMIC ANALOGY FOR PNEUMATIC TRANSPORT IN
HORIZONTAL PIPES

by

Craig A. Myler

B.S. in Chemistry, Virginia Military Institute

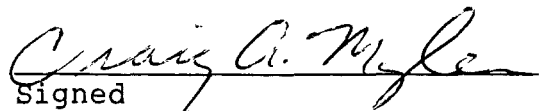
M.S. in Chemical Engineering, University of Pittsburgh

Submitted to the Graduate Faculty
of the School of Engineering
in partial fulfillment of
the requirements for the degree of
Doctor
of
Philosophy

University of Pittsburgh

1987

The author grants permission
to reproduce single copies.


Signed

ACKNOWLEDGMENTS

I will begin by thanking my advisor, Dr. G.E. Klinzing for the advice and encouragement he provided. Dr. Klinzing was my first contact at Pitt and from that early time he showed a genuine interest in my scholastic as well as personal problems and guided me in the right direction.

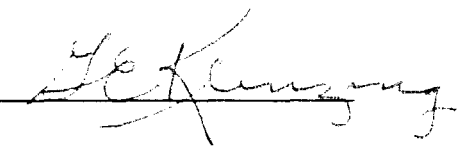
Next, I thank my committee members Dr. A. Brainard, Dr. R.S. Dougall, Dr. M.P. Mathur, and Dr. B. Morsi for their expert advice and opinion. I would like to include here Dr. Hamilton for his solution to a difficult problem.

Next I would acknowledge Mr. Larry Herman and Pye Pyejewski. They trusted me and I them.

I must include acknowledgement of Abdi Zaltash and Shrikant Dhodapkar. We worked hard together and spent many hours discussing subjects we both agreed and disagreed on.

Finally, I would like to recognize my wife Janice. She endured long nights alone and my disagreeable attitudes most of the time we were together with an understanding I am grateful for.

ABSTRACT

Signature 

USE OF A THERMODYNAMIC ANALOGY FOR PNEUMATIC TRANSPORT
IN HORIZONTAL PIPES

Craig A. Myler,
University of Pittsburgh

The use of a thermodynamic analogy for pneumatic transport in horizontal pipes of 0.0266 m and 0.0504 m diameters was investigated. Glass particles of 67, 450, and 900 μm mean diameter and iron oxide particles of 400 μm diameter were transported using air as the carrier gas.

Experimental measurements included particle velocities, pressure drop, and mass flow rate. To determine the phase behavior of the flow required for the thermodynamic analogy, the above measurements were all taken in both the upper and lower halves of the pipe. Particle velocities were obtained by a cross-correlation of signals obtained from two new probes developed for this purpose. Mass flows from the two

halves of the pipe were obtained by splitting the flow with a knife edged separator.

The thermodynamic analogy was found to be capable of describing the phase behavior of the systems studied. This included the dilute phase transport as well as strand type conveying.

Basic modeling resulted in the presentation of a new correlation for particle velocity and an expression for solids friction factor. This correlation is capable of predicting a minimum point in the pressure drop vs. gas velocity relationship which is associated with saltation.

Electrostatic effects are discussed. These include a reverse propagation of surface waves on the walls of the pipe. Destructive electrostatic effects are also included.

DESCRIPTORS

Electrostatics	Horizontal
Particle velocity	Pneumatic transport
Pressure drop	Thermodynamic analogy

TABLE OF CONTENTS

	Page
ACKNOWLEDGEMENTS	ii
ABSTRACT	iii
LIST OF FIGURES	ix
LIST OF TABLES	xix
NOMENCLATURE	xxi
1.0 INTRODUCTION	1
2.0 BACKGROUND	7
2.1 Classical Approaches	7
2.1.1 Force Balance Approach	7
2.1.2 Accounting for Gravity in Horizontal Systems	11
2.1.3 Other Models	12
2.1.3.1 Fundamental Constitutive Equations	12
2.1.3.2 Particle Path Approach	14
2.1.3.3 Dimensional Analysis	15
2.1.3.4 Drift Flux	18
2.1.4 Lift	19
2.2 Thermodynamic Analogy	26
2.2.1 Background in Fluidization	26
2.2.2 The Ideal Gas Analog	29
2.2.3 The van der Waals Analog	33
2.2.3.1 Phase Equilibria in Horizontal Pneumatic Transport	37

	Page
2.2.3.2 Constants in the van der Waals Analog Equation	43
2.2.3.3 The Critical Point Analog . .	46
2.2.3.4 Pressure Drop	47
2.2.4 Discontinuity of the Thermodynamic Analog	51
3.0 EXPERIMENTAL	53
3.1 Bench Scale System	53
3.1.1 Velocity Verification	53
3.1.2 Horizontal System	56
3.1.2.1 Layout and Major Equipment	56
3.1.2.2 Pressure Measurement in the Bench Scale System	60
3.1.2.3 Velocity Measurement	61
3.1.2.4 Flow Splitter in the Bench Scale System	63
3.2 Full Scale System	63
3.2.1 Layout and Major Equipment	65
3.2.1.1 Air Delivery and Conditioning	65
3.2.1.2 Solids Delivery System	67
3.2.1.3 Piping	69
3.2.1.4 Solids Collection	71
3.2.2 Operation	72
3.3 Computer Interface	73
3.3.1 Simultaneous A/D Conversion	73

	Page
3.3.2 Particle Velocity Measurements	74
3.3.3 Pressure Measurements	76
3.4 Solids Particles Used	78
4.0 ANALYSIS OF RESULTS	81
4.1 General Results	81
4.1.1 Flow Visualization	82
4.1.2 Pressure Drop per Unit Length	85
4.1.2.1 The Zenz Type Phase Diagram	87
4.1.2.2 Comparison to Correlations	95
4.1.3 Particle Velocity	101
4.1.4 A Method of Pressure Drop Prediction	109
4.2 Application of the Thermodynamic Analogy	114
4.2.1 The Ideal Gas Analog	114
4.2.2 The van der Waals Analog	116
4.2.2.1 Methodology of Data Analysis	116
4.2.2.2 Regression of the van der Waals Constants	119
4.2.3 The j_p^* vs. Φ Phase Diagram	122
4.2.4 The Flux-Flux Phase Diagram of Tuba ⁽¹⁾	125
4.2.5 An Estimate of the Critical Point Analog	125
4.2.6 Predicting the Pressure Drop Using the van der Waals Analog	128

	Page
4.3 Other Results	132
4.3.1 Pressure Drop Between the Upper and Lower Halves of the Pipe . . .	132
4.3.1.1 Axial Pressure Drop	132
4.3.1.2 Radial Pressure Measurement	133
4.3.1.3 Pressure Drop Fluctuation . .	134
4.3.1.4 Fluctuations in the Upper and Lower Halves of the Pipe	136
4.3.2 Mass Flow Distribution Between the Upper and Lower Halves of the Pipe	140
4.3.3 Electrostatics	143
5.0 CONCLUSIONS	150
5.1 General Conclusions	150
5.2 Application of the Thermodynamic Analog . . .	152
5.3 Other Conclusions	155
APPENDIX A	158
APPENDIX B	209
APPENDIX C	226
APPENDIX D	235
APPENDIX E	253
APPENDIX F	270
APPENDIX G	272
BIBLIOGRAPHY	274

LIST OF FIGURES

Figure No.		Page
2-1	Magnus/Robins Effect on a Rotating Sphere	22
2-2	Domains of Turbulent Influence According to Owens ⁽³⁴⁾	25
2-3	$\frac{U_p}{U_g}$ vs. U_g from the Data of Rizk ⁽⁴⁰⁾	32
2-4	Phase Diagram for Gas-Solid Transport from Canning and Thompson ⁽⁴²⁾	35
2-5	Broad Conditions of Horizontal Dilute Phase Flow	39
2-6	Phase Behavior in Horizontal Dilute Phase Flow	39
2-7	Measurement of Pressure in Thermodynamic Vapor-Liquid Equilibrium Experiment	42
2-8	Critical Point on the Pressure Drop vs. Gas Velocity Phase Diagram - Data of Rizk ⁽⁴⁰⁾	48
3-1	Bench Scale System for Verification of Velocity from Cross-Correlation Using Simultaneous Valves	54
3-2	Results of Particle Velocities Obtained by Voik Fraction Measurement and by Cross-Correlation Techniques in the 0.0266 m Bench Scale System	56
3-3	Bench Scale System (0.0266 m Diameter)	57
3-4	Pressure Tap Placement	62
3-5	Split Electrostatic Ring Probe	62
3-6	Connection and Orientation of Velocity Probes	64

3-7	Detail of Flow Splitter	64
3-8	Air Delivery System in the Full Scale System	66
3-9	Solids Feeder in the Full Scale System	68
3-10	Piping Layout in the Full Scale System	70
3-11	Example Computer Screen Output of Velocity Signals Using the Computer Program PROBE.BAS	77
3-12	Example Computer Output Screen from Cross-Correlation of Velocity Signals Using PROBE.BAS	77
3-13	Pressure Transducer Calibration System	79
4-1	Observed Flow Patterns	84
4-2	Flow Pattern Observed When Flowing PVC in 0.0504 m Diameter System Caused by Electrostatics	86
4-3	Zenz Type Phase Diagram with Two Behaviors Reported to Exist	88
4-4	Pressure Drop vs. Gas Velocity for the 0.0266 m Diameter Bench Scale System Using 450 μ m Glass Beads	90
4-5	Pressure Drop vs. Gas Velocity for the 0.0504 m Diameter Full Scale System Using 450 μ m Glass Beads	91
4-6	Layer of Deposited Solids Formed at the Feed Point	93
4-7	Pressure Drop vs. Gas Velocity in the Acceleration Zone from Dhodapkar ⁽⁵⁹⁾	94

4-8	Comparison of Pressure Drop Calculated Using the Correlation of Konno, Saito, and Maeda ⁽⁶⁰⁾ and the Experimental Pressure Drop . . .	96
4-9	Comparison of Pressure Drop Calculated Using the Correlation of Yang ^(61,62) and the Experimental Pressure Drop	98
4-10	Comparison of Pressure Drop Calculated vs. the Correlation of Weber ⁽⁶³⁾ and the Experimental Pressure Drop	100
4-11	U_p vs. U_g for the 450 μm Glass Beads in the 0.0266 m Diameter Bench Scale System	102
4-12	U_p/U_g vs. U_g for the 450 μm Glass Beads in the 0.0266 m Diameter Bench Scale System	103
4-13	U_p/U_g vs. U_g for the 450 μm Glass Beads in the 0.0504 m Diameter Full Scale System	105
4-14	$U_g - U_t$ vs. Experimental Particle Velocity	107
4-15	Particle Velocity Calculated Using Equation 4-8 vs. Experimental Particle Velocity	108
4-16	Particle Velocity Calculated Using the Correlation of Yang ^(61,62) vs. Experimental Particle Velocity	110
4-17	Comparison of Pressure Drop Calculated Using Equations 4-8 and 4-11 vs. Experimental Pressure Drop	112
4-18	Calculated Pressure Drop vs. Gas Velocity Diagram Using Equations 4-9 and 4-12 for 450 μm Glass Beads Showing the Saltation Correlation of Rizk ⁽⁴⁰⁾	115

4-19	Geometry of Separated Flow Condition . . .	118
4-20	j_p^* vs. Φ^{-1} for the 450 μm Glass Beads in the 0.0266 m Diameter System	123
4-21	j_p^* vs. Φ^{-1} for the 450 μm Glass Beads in the 0.0266 m Diameter System with Lines of Constant j_g^* from the van der Waals Analog Equation Superimposed	124
4-22	j_p^* vs. j_g^* Phase Diagram of Tuba ⁽¹⁾ . . .	126
4-23	j_p^* vs. j_g^* Phase Diagram for the μm Glass Beads in the 0.0266 m Diameter System	127
4-24	Estimation of Critical Point for the 450 μm Glass Beads in the 0.0266 m Diameter System from the Method of Zaltash, et.al. ⁽⁴⁶⁾	129
4-25	Comparison of van der Waals Constants Obtained by Data Regression to Those from Estimation from Pressure Drop Data (450 μm Glass Beads in 0.0266 m Diameter System) . .	130
4-26	$\frac{\Delta P}{L}$ vs. j_p^* for the 450 μm Glass Beads in the 0.0266 m Diameter System	131
4-27	Pressure Drop Fluctuation vs. Gas Velocity for the 900 μm Glass Beads in the 0.0266 m Diameter System	135
4-28	Pressure Drop Fluctuation vs. Gas Velocity for the 67 μm Glass Beads in the 0.0266 m Diameter System	137

4-29	Ratio of Pressure Fluctuation in the Upper Half of the Pipe to that in the Lower Half vs. Gas Velocity for the 450 μm Glass Beads in the 0.0266 m Diameter System	138
4-30	Ratio of Pressure Fluctuation in the Upper Half of the Pipe to that in the Lower Half vs. Gas Velocity for the 450 μm Glass Beads in the 0.0504 m Diameter System	139
4-31	Ratio of Pressure Fluctuation in the Upper Half of the Pipe to that in the Lower Half vs. Gas Velocity for the 67 μm Glass Beads in the 0.0504 m Diameter System	141
4-32	$\frac{W_{su}}{W_{sl}}$ vs. U_g for the 450 μm Glass Beads in the 0.0266 m Diameter System	142
4-33	$\frac{W_{su}}{W_{sl}}$ vs. U_g for the 450 μm Glass Beads in the 0.0504 m Diameter System	144
4-34	Isolation Circuit Designed to Protect from Electrostatic Discharges	147
A-1	Pressure Drop vs. Gas Velocity for the 0.0266 m Diameter System Using 67 μm Glass Beads	159
A-2	Pressure Drop vs. Gas Velocity for the 0.0266 m Diameter System Using 900 μm Glass Beads	160
A-3	Pressure Drop vs. Gas Velocity for the 0.0266 m Diameter System Using 400 μm Iron Oxide	161
A-4	Pressure Drop vs. Gas Velocity for the 0.0504 m Diameter System Using 67 μm Glass Beads	162

A-5	Pressure Drop vs. Gas Velocity for the 0.0504 m Diameter System Using 900 μm Glass Beads	163
A-6	Pressure Drop vs. Gas Velocity for the 0.0504 m Diameter System Using 400 μm Iron Oxide	164
A-7	U_p vs. U_g for the 67 μm Glass Beads in the 0.0266 m Diameter Bench Scale System	165
A-8	U_p vs. U_g for the 900 μm Glass Beads in the 0.0266 m Diameter Bench Scale System	166
A-9	U_p vs. U_g for the 400 μm Iron Oxide in the 0.0266 m Diameter Bench Scale System	167
A-10	U_p vs. U_g for the 67 μm Glass Beads in the 0.0504 m Diameter Full Scale System	168
A-11	U_p vs. U_g for the 450 μm Glass Beads in the 0.0504 m Diameter Full Scale System	169
A-12	U_p vs. U_g for the 900 μm Glass Beads in the 0.0504 m Diameter Full Scale System	170
A-13	U_p vs. U_g for the 400 μm Iron Oxide in the 0.0504 m Diameter Full Scale System	171
A-14	U_p/U_g vs. U_g for the 67 μm Glass Beads in the 0.0266 m Diameter Bench Scale System	172
A-15	U_p/U_g vs. U_g for the 900 μm Glass Beads in the 0.0266 m Diameter Bench Scale System	173
A-16	U_p/U_g vs. U_g for the 400 μm Iron Oxide in the 0.0266 m Diameter Bench Scale System	174

A-17	U_p/U_g vs. U_g for the 67 μm Glass Beads in the 0.0504 m Diameter Full Scale System	175
A-18	U_p/U_g vs. U_g for the 900 μm Glass Beads in the 0.0504 m Diameter Full Scale System	176
A-19	U_p/U_g vs. U_g for the 400 μm Iron Oxide in the 0.0266 m Diameter Bench Scale System	177
A-20	j_p^* vs. Φ^{-1} for the 67 μm Glass Beads in the 0.0266 m Diameter Bench Scale System with Lines of Constant j_g^* from the van der Waals Analog Equation Superimposed . .	178
A-21	j_p^* vs. Φ^{-1} for the 900 μm Glass Beads in the 0.0266 m Diameter Bench Scale System with Lines of Constant j_g^* from the van der Waals Analog Equation Superimposed . .	179
A-22	j_p^* vs. Φ^{-1} for the 400 μm Iron Oxide in the 0.0266 m Diameter Bench Scale System with Lines of Constant j_g^* from the van der Waals Analog Equation Superimposed . .	180
A-23	j_p^* vs. Φ^{-1} for the 67 μm Glass Beads in the 0.0504 m Diameter Full Scale System with Lines of Constant j_g^* from the van der Waals Analog Equation Superimposed . .	181
A-24	j_p^* vs. Φ^{-1} for the 450 μm Glass Beads in the 0.0504 m Diameter Full Scale System with Lines of Constant j_g^* from the van der Waals Analog Equation Superimposed . .	182
A-25	j_p^* vs. Φ^{-1} for the 900 μm Glass Beads in the 0.0504 m Diameter Full Scale System with Lines of Constant j_g^* from the van der Waals Analog Equation Superimposed . .	183

A-26	j_p^* vs. $\Phi-1$ for the 400 μm Iron Oxide in the 0.0266 m Diameter Bench Scale System with Lines of Constant j_g^* from the van der Waals Analog Equation Superimposed . . .	184
A-27	j_p^* vs. j_g^* for the 67 μm Glass Beads in the 0.0266 m Diameter Bench Scale System with Lines of Constant Φ	185
A-28	j_p^* vs. j_g^* for the 900 μm Glass Beads in the 0.0266 m Diameter Bench Scale System with Lines of Constant Φ	186
A-29	j_p^* vs. j_g^* for the 400 μm Iron Oxide in the 0.0266 m Diameter Bench Scale System with Lines of Constant Φ	187
A-30	j_p^* vs. j_g^* for the 67 μm Glass Beads in the 0.0504 m Diameter Full Scale System with Lines of Constant Φ	188
A-31	j_p^* vs. j_g^* for the 450 μm Glass Beads in the 0.0504 m Diameter Full Scale System with Lines of Constant Φ	189
A-32	j_p^* vs. j_g^* for the 900 μm Glass Beads in the 0.0504 m Diameter Full Scale System with Lines of Constant Φ	190
A-33	j_p^* vs. j_g^* for the 400 μm Iron Oxide in the 0.0504 m Diameter Bench Scale System with Lines of Constant Φ	191
A-34	Pressure Drop Fluctuation vs. Gas Velocity for the 450 μm Glass Beads in the 0.0266 m Diameter Bench Scale System	192
A-35	Pressure Drop Fluctuation vs. Gas Velocity for the 400 μm Iron Oxide in the 0.0266 m Diameter Bench Scale System	193

A-36	Pressure Drop Fluctuation vs. Gas Velocity for the 67 μm Glass Beads in the 0.0504 m Diameter Full Scale System	194
A-37	Pressure Drop Fluctuation vs. Gas Velocity for the 450 μm Glass Beads in the 0.0504 m Diameter Full Scale System	195
A-38	Pressure Drop Fluctuation vs. Gas Velocity for the 900 μm Glass Beads in the 0.0504 m Diameter Full Scale System	196
A-39	Pressure Drop Fluctuation vs. Gas Velocity for the 400 μm Iron Oxide in the 0.0504 m Diameter Full Scale System	197
A-40	Ratio of Pressure Fluctuation in the Upper Half of the Pipe to that in the Lower Half vs. Gas Velocity for the 67 μm Glass Beads in the 0.0266 m Diameter Bench Scale System	198
A-41	Ratio of Pressure Fluctuation in the Upper Half of the Pipe to that in the Lower Half vs. Gas Velocity for the 900 μm Glass Beads in the 0.0266 m Diameter Bench Scale System	199
A-42	Ratio of Pressure Fluctuation in the Upper Half of the Pipe to that in the Lower Half vs. Gas Velocity for the 400 μm Iron Oxide in the 0.0266 m Diameter Bench Scale System	200
A-43	Ratio of Pressure Fluctuation in the Upper Half of the Pipe to that in the Lower Half vs. Gas Velocity for the 900 μm Glass Beads in the 0.0504 m Diameter Full Scale System	201

A-44	Ratio of Pressure Fluctuation in the Upper Half of the Pipe to that in the Lower Half vs. Gas Velocity for the 400 μm Iron Oxide in the 0.0504 m Diameter Full Scale System	202
A-45	W_{su}/W_{sl} vs. U_g for the 67 μm Glass Beads in the 0.0266 m Diameter Bench Scale System	203
A-46	W_{su}/W_{sl} vs. U_g for the 900 μm Glass Beads in the 0.0266 m Diameter Bench Scale System	204
A-47	W_{su}/W_{sl} vs. U_g for the 400 μm Iron Oxide in the 0.0266 m Diameter Bench Scale System	205
A-48	W_{su}/W_{sl} vs. U_g for the 67 μm Glass Beads in the 0.0504 m Diameter Full Scale System	206
A-49	W_{su}/W_{sl} vs. U_g for the 900 μm Glass Beads in the 0.0504 m Diameter Full Scale System	207
A-50	W_{su}/W_{sl} vs. U_g for the 400 μm Iron Oxide in the 0.0504 m Diameter Full Scale System	208
C-1	Circuit Used for the Motor Drive of the Solids Feeder in the Full Scale System	229
C-2	Teflon Retaining Ring Assembly for the Solids Feeder in the Full Scale System	231
C-3	Calibration Curve for the Platform Scale Used in the Full Scale System	232

LIST OF TABLES

Table No.		Page
2-1	Dimensionless Groups Obtained from the Formulation of Masoudi ⁽¹⁴⁾	17
2-2	Dimensionless Groups Obtained from Nieh, et.al. ⁽¹⁶⁾	18
2-3	Domains of Turbulent Influence According to Owens ⁽³⁴⁾	25
2-4	Comparison of Tuba's ⁽¹⁾ Ideal Transport Constant With That Predicted by the Ideal Transport Analog Equation	45
3-1	Characteristics of Solids Particles Used	80
4-1	Standard Relative Deviation for Pressure Drop Calculated from Three Methods	101
4-2	Standard Relative Deviation for Pressure Drop Calculated from Equation 4-7	113
4-3	Ideal Transport Constant (R^*) from Experimental Data	116
4-4	a^* and b^* From Regression of Experimental Data	120
4-5	Critical Point Fluxes and Solids Fraction from van der Waals Analog Constants	121
B-1	BMDP Results for the 67 μm Glass Beads in the 0.0266 m Diameter System	210
B-2	BMDP Results for the 450 μm Glass Beads in the 0.0266 m Diameter System	212
B-3	BMDP Results for the 900 μm Glass Beads in the 0.0266 m Diameter System	214

B-4	BMDP Results for the 400 μm Iron Oxide in the 0.0266 m Diameter System	216
B-5	BMDP Results for the 67 μm Glass Beads in the 0.0504 m Diameter System	218
B-6	BMDP Results for the 450 μm Glass Beads in the 0.0504 m Diameter System	220
B-7	BMDP Results for the 900 μm Glass Beads in the 0.0504 m Diameter System	222
B-8	BMDP Results for the 400 μm Iron Oxide in the 0.0504 m Diameter System	224

NOMENCLATURE

a	Constant in the van der Waals equation of state (Pa m ⁶ /kgmol ²)
a*	Constant in the van der Waals analog to pneumatic transport (-)
A=A _t	Cross-sectional area of pipe (m ²)
b	constant in the van der Waals equation (m ³ /kgmol)
b*	constant in the van der Waals analog equation (-)
C _{ds}	Drag coefficient (-)
D _p	Particle diameter (m)
D _t	Pipe diameter (m)
f _s	Solids friction factor (-)
f _g	Gas friction factor (-)
F.A.	Fraction cross-sectional area of strand (-)
F	Average inverse relaxation time for momentum transfer (1/s)
g	Gravitational acceleration (m/s)
j _g	Gas flux (m/s)
j _p	Solids flux (m/s)
j _{pc} *	Dimensionless solids flux at critical point (-)
j _{gc} *	Dimensionless gas flux at critical point (-)
j _p *	Dimensionless solids flux (-)
j _g *	Dimensionless gas flux (-)
M _p	Particle mass (kg)
Δm _g	Mass of gas in differential element δx (kg)
Δm _p	Mass of solids in differential element δx (kg)
P	Pressure (Pa)

P_c	Critical pressure (Pa)
$\frac{\Delta P}{L}$	Pressure drop per unit length (Pa/m)
$\frac{\Delta P_{su}}{L}$	Pressure drop in upper half of pipe with solids flowing (Pa/m)
$\frac{\Delta P_{sl}}{L}$	Pressure drop in lower half of pipe with solids flowing (Pa/m)
$\frac{\Delta P_{au}}{L}$	Pressure drop in upper half of pipe with air only flowing (Pa/m)
$\frac{\Delta P_{al}}{L}$	Pressure drop in lower half of pipe with air only flowing (Pa/m)
$\frac{\Delta P_a}{L}$	Pressure drop with air only flowing (Pa/m)
$\frac{\Delta P_s}{L}$	Pressure drop with solids flowing (Pa/m)
Q_g	Volumetric gas flow rate (m^3/s)
Q_p	Volumetric solids flow rate (m^3/s)
r	Pipe radius (m)
R	Ideal gas constant ($Pa\ m^3/kgmolK$)
R^*	Ideal transport constant (-)
Re_p	Particle Reynolds number ($\rho D_p U_s / \mu_f$)
T_c	Critical Temperature (K)
T	Temperature (K)
U_g	Superficial gas velocity (m/s)
U_f	Actual gas velocity (m/s)

U_{gc}	Gas velocity at critical point (m/s)
U_p	Particle velocity (m/s)
U_{pc}	Particle velocity at critical point (m/s)
U_{pu}	Particle velocity in upper half of pipe (m/s)
U_{pl}	Particle velocity in lower half of pipe (m/s)
U_t	Particle terminal velocity (m/s)
U_s	Slip velocity ($U_f - U_p$) (m/s)
U_a	Tangential velocity (radians/s)
U_τ	Friction velocity at wall (m/s)
V	Molar volume ($m^3/kgmol$)
V_c	Critical molar volume ($m^3/kgmol$)
$W_s = W_{st}$	Solids mass flow rate (kg/s)
W'_{s1}	Mass flow rate of solids in strand (kg/s)
W_{su}	Mass flow rate of solids in upper half of pipe (kg/s)
W_{sl}	Mass flow rate of solids in lower half of pipe (kg/s)

Greek Letters

ε	Void fraction (-)
ε_c	Voidage at critical point (-)
ε_0	Permittivity of free space (farad/m)
η	Kinematic viscosity of gas (m^2/s)
θ	Pipe inclination angle (radians)
λ	Solids friction factor (German) (-)
μ_f	Gas viscosity (Kg/ms^2)
μ	Solids Loading (-)

ρ_g	Gas density (kg/m ³)
ρ_p	Solids density (kg/m ³)
σ	Standard deviation in pressure drop for air only flowing (Pa/m)
σ_s	Standard deviation in pressure drop with solids flowing (Pa/m)
ϕ	Volumetric solids fraction (-)
ϕ_u	Volumetric solids fraction in upper half of pipe (-)
ϕ_l	Volumetric solids fraction in lower half of pipe (-)
ϕ_c	Volumetric solids fraction at critical point (-)
\dagger	Number of Phases (-)

1.0 INTRODUCTION

Pneumatic conveying of solid particles has been practiced for over 100 years. A considerable amount of research has been performed to ascertain fundamental properties of gas-solids systems as well as to provide usable models from which system design can be performed. There exist a variety of correlations for existing data as well as different views of the primary mechanisms in this type of transport. This can partially be attributed to methodology of data collection and reporting as well as insufficient data to support or deny theoretical models.

A specific area of research which requires more fundamental knowledge is horizontal pneumatic conveying. A wide range of phenomenon have been reported for horizontal pneumatic conveying, the most of which can be directly related to the affects of gravity. As the gas velocity in a horizontal pneumatic system is decreased, solids concentration in the bottom of the pipe increases. Further decrease in gas velocity causes saltation of the solids in varying degrees and configurations until, at a sufficiently low gas velocity, solids transport ceases. The above conditions are extremely difficult to describe experimentally. Due to the unsteady nature of the flow system under these conditions, primary variables are difficult to measure. Averaging techniques can lead to

inaccuracies which in turn lead to conflicting reports. An additional problem arises due to the variations possible with the solid particles themselves. Variations in particle size, density, shape, and other properties provide sources for experimental findings which differ from experimenter to experimenter.

An apparent method for overcoming these difficulties in describing horizontal pneumatic transport is through the use of a flow map or phase diagram which would describe the flow behavior over a wide range of parameters for a given gas-solid system. One such approach is through the use of an analog to a thermodynamic system. Phase diagrams for thermodynamic systems provide system properties at various conditions. In the case of a pure component phase diagram, various models have been used to predict system properties with great success.

The ideal gas law is probably the best known of this type model. With this law, pressures, temperatures, and molar volumes of gases can be reasonably predicted over a surprisingly broad range for the simplicity of this model. The basic tenant of the ideal gas model is that molecules do not interact among themselves. An analogy to this is dilute phase pneumatic conveying systems where solids concentrations are very small. The failure of the ideal gas model occurs when there is molecular interaction. Especially when the density of the system approaches that of

} other than
low
collision

a liquid. It is this point which van der Waals addressed in his classic equation of state:

$$(P + a/V^2) \cdot (V - b) = RT \quad (1-1)$$

This model of a thermodynamic system takes into account the interactions between molecules and can predict the existence of a liquid phase. It is this model which will form the basis of the analog to pneumatic transport discussed in this study.

In 1983, Tuba^{(1)*} described the striking similarity of phase diagrams produced by Matsen^(2,3) for gas-solids systems to those of thermodynamic systems. From this similarity, an analog to the van der Waals equation of state for thermodynamic systems was proposed for pneumatic transport systems. The analog model proposed by Tuba took the following form:

$$(J_p^* + a^*\phi) \cdot (1/\phi - b^*) = R^*J_g \quad (1-2)$$

where -

J_p^* = the dimensionless solids flux

J_g^* = the dimensionless gas flux

ϕ = the dimensionless solids concentration

* Parenthetical references placed superior to the line of text refer to the bibliography.

The model was tested on data for the pneumatic conveying of coal in a vertical system and a high correlation of the data was achieved. The degree of correlation obtained and the similarity to the Matsen type phase diagram suggested the need for further study.

The phase diagram model of Tuba was directed toward vertical systems with the intention of being able to map dilute and dense phase regions of flow as well as provide a prediction of choking. But what about horizontal systems? As mentioned above, horizontal systems exhibit a striking difference from vertical systems in the effect of gravity. The separation of the horizontal flow system into separate 'phases' appears to provide a prime reason for investigation of the applicability of a thermodynamic analog to horizontal pneumatic systems. With a phase diagram such as one obtained through the use of van der Waals equation, the coexistence of separate phases can be predicted. This is the aim of the application of the van der Waals analog to horizontal pneumatic conveying.

To test the analog model in horizontal systems required experimental data which provided the three parameters in the analog equation (Equation 1-2) for the two distinct phases proposed to exist. This required the measurement of particle velocity as well as solids mass flow rate in both phases. Additionally, the data set had to provide a

variation in the type of particle transported as well as a variation in pipe diameters.

To acquire the necessary data, two new probes were developed which were capable of measuring particle velocities at two points across the radius of the pipe. The first of these was a modification of the electrostatic ring probe,^(4,5,6) which uses cross-correlation techniques to determine particle velocities between two points along the axis of the pipe. The second was a magnetic coil probe, which also uses the cross-correlation technique.⁽⁷⁾ To obtain the solids mass flow rate of each phase, the pipe was split into two sections using a knife edge, and the mass flow rate of solids in the upper and lower halves of the pipe were obtained. With this information, an estimate of the concentration gradient across the pipe was obtained.

Axial pressure drop and pressure drop fluctuations were measured in both the upper and lower halves of the pipe. It was hoped that these measurements would allow some assessment of the lift occurring in horizontal systems. The lift aspects of the flow were not determined; however, pressure measurements between the upper and lower halves displayed different characteristics which may shed some light on the flow structure.

Classical modeling was performed with the result of a new correlation being proposed which has the capacity to

predict a minimum pressure drop point in horizontal flows. This model includes particle velocity and pressure drop correlation. This model may eliminate the need for separate correlations for saltation and pressure drop.

A discussion of electrostatic effects is included. For a portion of the experimental work these effects were of dramatic importance.

2.0 BACKGROUND

The complexity of completely describing a pneumatic transport system is perhaps best described by Klinzing⁽⁸⁾ as ". . . one of the most challenging problems in fluid mechanics." This complexity is compounded by such things as differences in particle shape and size, particle size distribution, agglomeration of particles and the generation of electrostatic potentials. Much work has been performed in the area of horizontal pneumatic transport, yet there remains wide discrepancies in the correlations of different investigators. In addition to the correlations for pressure drop and conveying velocity, there are numerous correlations available to predict saltation. This situation leads to a number of difficulties in design and operation of pneumatic systems.

2.1 Classical Approaches

2.1.1 Force Balance Approach

An application of Newton's second law to the particles and the gas in horizontal gas-solid system provides the following equations:

$$\Delta m_p \frac{dU_p}{dt} = dF_D - dF_{fp} - \frac{\Delta m_p}{\rho_p} \frac{\partial P}{\partial X} \pm F_{add} \quad (2-1)$$

$$\Delta m_g \frac{dU_f}{dt} = -dF_D - dF_{fg} - \frac{\Delta m_g}{\rho_f} \frac{\partial P}{\partial X} \quad (2-2)$$

where: F_D = drag force
 F_{fp} = frictional force for particles
 F_{fg} = frictional force for gas
 F_{add} = additional forces

With selected representations for these forces, neglecting the additional forces, Equations 2-1 and 2-2 can be written as:

$$\Delta m_p \frac{dU_p}{dt} = \frac{3\Delta m_p \varepsilon^{-4.7} C_{DS} \rho_f (U_f - U_p)^2}{4 (\rho_p - \rho_f) D_p} - \frac{2\Delta m_p f_s U_p^2}{D_t} - \frac{\Delta m_p}{\rho_p} \frac{\partial P}{\partial X} \quad (2-3)$$

$$\Delta m_g \frac{dU_f}{dt} = \frac{-3\Delta m_p \varepsilon^{-4.7} C_{DS} \rho_f (U_f - U_p)^2}{4 (\rho_p - \rho_f) D_p} - \frac{2\Delta m_g f_g U_f^2}{D_t} - \frac{\Delta m_g}{\rho_f} \frac{\partial P}{\partial X} \quad (2-4)$$

At steady state, the acceleration terms are zero. Addition of Equations 2-3 and 2-4 at steady state yields:

$$\frac{2\Delta m_p f_s U_p^2}{D_t} + \frac{2\Delta m_g f_g U_f^2}{D_t} + \left[\frac{\Delta m_p}{\rho_p} + \frac{\Delta m_g}{\rho_f} \right] \frac{\partial P}{\partial X} = 0 \quad (2-5)$$

Expressing Δm_p and Δm_g in terms of void fraction, Equation 2-5 can be written as:

$$\frac{2(1 - \varepsilon) \rho_p f_s U_p^2}{D_t} + \frac{2\varepsilon \rho_f f_g U_f^2}{D_t} + \frac{\partial P}{\partial X} = 0 \quad (2-6)$$

If all the parameters are constant along the axis of the pipe, the pressure drop per unit length can be obtained as:

$$\frac{\Delta P}{L} = \frac{2f_s(1 - \epsilon)\rho_p U_p^2}{D_t} + \frac{2f_g \epsilon \rho_f U_f^2}{D_t} \quad (2-7)$$

If the gas friction factor is obtained from single phase correlations, there are three terms in Equation 2-7 which must be determined to calculate a pressure drop for the system. The three terms are f_s , ϵ and U_p . For a given mass flow rate of solids, U_p and ϵ are related by:

$$\epsilon = 1 - \frac{W_s}{A_t \rho_p U_p} \quad (2-8)$$

Empirical correlations for use in the force balance, Equation 2-7, normally give expressions for f_s and U_p . The particle velocity expressions are normally based on the terminal velocity of the particles and the friction factor is normally dependent on the particle velocity.

A few points should be made concerning the discrepancies between correlations for use in the force balance. First, there is the obvious exclusion of the influence of gravity in the force balance development. This is because the balance is done for the axial flow only and the particles are assumed to have only axial velocity components. A second point is that the drag coefficient is

not easily determined for particle clouds or for particles of irregular shape. Finally, factors such as pipe material, wall roughness, particle size distribution, and gas humidity may have a significant effect on experimental data.

The exclusion of the additional forces in Equation 2-1 is not so much an oversight as it is a realization of the complexities such forces impart to correlation of experimental data. An example of an additional force present in pneumatic systems which greatly complicate accurate correlation are the forces of electrostatics. Yet these forces can play a major role in the force balance. A striking example of this is the data obtained by Zaltash⁽⁶⁾ in a study of electrostatics in vertical pneumatic transport. In Zaltash's experiments, variation of the relative humidity of the transport gas caused, in some cases, a variation in pressure drop of 30% with all other variables held constant. This example points out the importance that additional forces not normally encountered in single phase flows can have in gas-solid systems.

Finally, the force balance as presented here does not directly address the affects of gravity on the horizontal flow. Separate correlations for saltation velocities are normally used in conjunction with the friction factor and particle velocity expressions. Appendix F contains various

correlations used for friction factors, particle velocities, and saltation.

2.1.2 Accounting for Gravity in Horizontal Systems

An attempt to account for the force of gravity in horizontal systems was developed by Barth⁽⁹⁾ and is prevalent in German literature. Barth's development centers on the idea that the particles in a gas-solid flow attempt to fall at their terminal velocity. To maintain suspension of the particles, the gas must impart some energy to the particles aside from that required to maintain their axial velocity. To account for the energy necessary to maintain the particle suspension, Barth uses the ratio of the terminal velocity of the particles divided by the velocity of the gas as a multiplication factor when calculating the additional pressure drop due to solids in horizontal transport.

Weber⁽¹⁰⁾ develops a force balance which incorporates this ratio of terminal velocity to gas velocity. His resulting expression for steady horizontal conveying is:

$$\frac{\Delta P}{L} = \frac{\epsilon f_g \rho_f U_g^2}{2D_t} + (1 - \epsilon)(\rho_p - \rho_f)g \frac{U_t}{U_g} + \frac{(1 - \epsilon) f_s \rho_p U_p^2}{2D_t} \quad (2-9)$$

This expression is without gas or solid acceleration. Additionally, the solids friction factor is not the same as those which would be obtained by the correlations given in

Appendix F, but, in the case of Weber's analysis, would be of the type obtained from correlations such as those given by Bohnet⁽¹¹⁾ or Siegel⁽¹²⁾. Additionally, the lift term has not been shown to be representative of the actual lift occurring in the system; it only qualitatively includes the force of gravity in a horizontal system.

2.1.3 Other Models.

Other models have been or are being used to describe pneumatic transport systems. Some of these are variations on the basic force balance approach, while others are either more fundamentally based or more empirically based. A few will be described as representative of the variations taken in approaching the problem of pneumatic transport.

2.1.3.1 Fundamental Constitutive Equations. This approach is perhaps the most rigorously correct method for modeling gas-solid systems. It is also the most difficult, and to date, even the simplest cases have not been solved. One obstacle is developing the correct equation(s) to describe the flow. By this is meant that the equations used should be generally valid, with simplifications for certain conditions made from the general equation. The violation of this concept is noted for example in the constitutive equations used by Ettehadieh and Gidaspow⁽¹³⁾ for modeling

fluidized beds. Their expression for the gas momentum includes friction terms obtained from the Ergun equation, which, as ϵ goes to 1, does not reduce the equation to the single phase momentum equation. This is not wrong in the context of the equation, which in their study was to model fluidized beds where void fractions much less than one are encountered.

A recent study performed by Massoudi⁽¹⁴⁾ apparently overcomes this difficulty. Massoudi's expressions for continuity and momentum are based on mixture theory and continuum mechanics. By defining the gas solid mixture as a continuum and defining the mixture by means of a combination of the individual components (components being the gas and the solid in a monodisperse gas solid system) contributions to the system as well as their interactions with each other. The momentum balance for a two phase mixture is given as:

$$\rho_p \frac{dU_p}{dt} = \text{div}^p \mathbf{T} - \mathbf{I} + \rho_p \mathbf{h} \quad (2-10)$$

$$\rho_f \frac{dU_f}{dt} = \text{div}^g \mathbf{T} - \mathbf{I} + \rho_f \mathbf{h} \quad (2-11)$$

Where: \mathbf{T}^p and \mathbf{T}^g are partial stress tensors for the particle and gas phases, respectively

\mathbf{I} is an interaction parameter

\mathbf{h} represents external body forces

This development has not yet been validated by experiment, but the approach is unique as a complete description for gas-solid flows. Solutions to the equations will require developments for the interaction term in the equations. Perhaps not so obvious is how to determine the significance of individual terms in the equations. The application of dimensional analysis by Massoudi to his equations will be discussed later.

2.1.3.2 Particle Path Approach. Another approach to modeling pneumatic systems is the particle path approach introduced by Molerus⁽¹⁵⁾. This approach is a modification of the basic force balance approach where the force of friction is broken down into component parts depending on the type of friction encountered. The type of friction is determined by the path a particle takes in moving along the pipe. Five different flight phases are considered by Molerus. They are:

- o Flight under gravitational influence
- o Particle-Particle collision
- o Particle-Wall collision
- o Sliding along the pipe wall
- o Pressure gradient effects

The combination of these five phases results in the following equation for horizontal transport:

(2-12)

$$\frac{\Delta P}{\rho_p} + \frac{3\rho_f C_{DS}(Re_p) U_f^2 L}{4D_p \rho_p} = \left[1 - \frac{\rho_f}{\rho_p} \right] gL(\sin\theta + \xi_f \cos\theta) + \xi_p \frac{[\rho_f \mu]^{1/3}}{[\rho_p]} \frac{LU_f^2}{D_p} + \frac{\xi_w LU_f^2}{D_t}$$

where: ξ_f = friction coefficient

ξ_p = particle-particle collision coefficient

ξ_w = Wall collision coefficient

This type of approach, although addressing some of the weaknesses of the force balance of Equation 2-7, suffers from the availability of experimental data capable of providing the different friction factors proposed. If limiting cases are considered, for example dilute flow where particle-particle collisions are unimportant, Equation 2-12 reduces to a form very similar to Equation 2-7. Providing the proper form for the friction factors of Equation 2-12 will result in Equation 2-7 exactly. As was mentioned earlier, experimental determination of f_g has been difficult, determination of three separate friction factors will be even more so.

2.1.3.3 Dimensional Analysis. An approach to pneumatic transport which has been used to varying degrees is that of dimensional analysis. The biggest drawback to this approach is the number of dimensionless groups which can be formed. Two separate examples will be described to provide some insight to the complexity of this approach.

The first example is the dimensionless analysis performed by Massoudi⁽¹⁴⁾ using a form of Equations 2-10 and 2-11. Massoudi used the particle diameter and the gas velocity to non-dimensionalize his equations. He obtained 14 dimensionless groups which can be reduced to the nine shown in Table 2-1. These are the possible groups obtained without the inclusion of body forces other than gravity, for example electrostatics. Although, for certain situations, the number of groups could be reduced, a general formulation of these groups would be difficult.

The second example is from a study by Nieh, et. al.⁽¹⁶⁾ where the dimensionless groups were obtained by the Buckingham method. Four groups were determined from a core of six groups to be representative of the flow conditions. For their study, the system was considered to be dilute phase at high gas Reynolds numbers. The four primary groups used are shown in Table 2-2. The authors point out that the last two groups, N_{DF} and N_m , contain terms which require values of particle velocity. With certain assumptions they substitute two other dimensionless groups (see Table 2-2).

Using the four groups, N_{ED} , Fr , Y , and Re_p^* , a comparison between a model and prototype pneumatic system was made. Their results appear very good; however, dynamic similarity between the two systems was based solely on particle mass flux distribution measured by iso-kinetic sampling. Although the mass flux distribution may be

Table 2-1

Dimensionless Groups Obtained from
the Formulation of Massoudi (14)

<u>Group</u>	<u>Physical Interpretation</u>
$2\beta_1$	friction
$\frac{\rho_f U_g^2 D_p^2}{\rho_f U_g^2 D_p^2}$	inertia
2α	volume distribution
$\frac{\rho_f U_g^2 D_p^2}{\rho_f U_g^2 D_p^2}$	inertia
$\frac{\lambda_s + \mu_s}{\rho_f D_p U_g}$	Solids Reynolds Number
$\frac{a_1 \rho_p}{\rho_f U_g^2}$	buoyancy
$\frac{a_2 \rho_p}{\rho_f U_g^2}$	buoyancy
$\frac{a_3 D_p}{\rho_f U_g}$	diffusion
$\frac{a_4}{\rho_f}$	diffusion
$\frac{D_{pg} \rho_p}{\rho_f U_g^2}$	gravity (Froude Number)
$\frac{\lambda_f + \mu_f}{\rho_f U_g D_p}$	Fluid Reynolds Number

Table 2-2

Dimensionless Groups Obtained by Nieh, et. al. (16)

<u>Group</u>	<u>Physical Interpretation</u>
$N_{ED} = \left[\frac{\rho_p}{4\epsilon_0} \right]^{1/2} \left[\frac{9}{M_p} \right] \left[\frac{R^2}{D_p} \right]$	Electrostatic repulsion
$Fr = \left[\frac{U_g^2}{D_{tg}} \right]^{1/2}$	Diffusion
	Inertia
	Gravity
$N_{DF} = \left[\frac{4D_p}{D_{tF}^2} \right]^{1/2}$	Relaxation time
	Diffusion time
$N_m = \frac{U_g^2}{RF}$	Relaxation time
	Convection

$$(N_{DF}) \rightarrow \frac{1}{2} = \frac{D_p^2 U_g \rho_p}{18 \eta \rho_f 2R}$$

Inertia parameter

$$(N_m) \rightarrow Re_p^* = \frac{D_p \rho_f U_g}{\mu_f}$$

Reynolds Number

representative of dynamic similarity for a given flow condition, it does not guarantee dynamic similarity through a given range of conditions. The reason for this is that the mass flux itself is dependent on two independent system parameters as given in Equation 2-8.

2.1.3.4 Drift Flux. The Drift Flux model is a multi-phase model which considers the motion of each phase on the basis

of the average motion of the combined flow. Wallis⁽¹⁷⁾ develops the model for two phase flow as follows:

$$j_{21} = U_{21} (1-\epsilon) \quad (2-13)$$

or

$$j_{21} = (1 - \epsilon)j_2 - \epsilon j_1 \quad (2-14)$$

and

$$j_{12} = (1-\epsilon)(U_1 - j) \quad (2-15)$$

where: j_{21} is the drift flux of component 2

j_{12} is the drift flux of component 1

Wallis points out that the the drift flux model is most easily applied when the drift flux is independent of the flow rates of either phase present. This condition is not a general condition in pneumatic systems. Concepts used in the drift flux model are incorporated into the thermodynamic analog to pneumatic transport.

2.1.4 Lift

To conclude the section on classical approaches, a discussion of lift in pneumatic systems is in order. As emphasized earlier, the particles in horizontal pneumatic transport must experience some force in opposition to that of gravity to preclude complete sedimentary flow. Outside of the modification of the force balance attributed to Barth which was described earlier, various individual forces have

been proposed to account for lift. The three most predominant are the Magnus force, particle bouncing, and the force of turbulent dissipation.

The Magnus force occurs due to particle rotation. Particle rotation can occur from collision with the pipe wall, collision between particles, and from fluid shear. If particle collisions are not the primary source for particle rotation, the Magnus force will be greatest in the vicinity of the wall where collisions with the wall occur and the velocity gradient of the fluid is greatest. Some controversy appears to exist concerning the magnitude of the Magnus force as well as the range of flow conditions for which it exists. Prandtl^(18,19) describes the "Magnus Effect" as a boundary layer phenomenon on a rotating cylinder. The application to a sphere is often referred to as the "Magnus Effect"; however, as Barkla and Auchterlonie⁽²⁰⁾ point out, Magnus' experiments were only conducted on cylinders. These authors point out original work done by Robins in 1742 where experiments on spinning spheres gave evidence of a transverse force and the effect of lift on spinning spheres should rightfully be known as the "Robbins effect".

The majority of discussion of the Magnus/Robins effect are for Reynolds numbers ($\rho_f D_p U_s / \mu_f$) either below 1 or greater than 1000. For smaller Reynolds number, Rubinow and Keller⁽²¹⁾ provide a solution of the Navier-Stokes equations

using a combination of the Stokes and Oseen expansions. Their resulting expression for the force on a rotating sphere includes a lift term given by:

$$F_1 = \frac{\pi D_p}{8\rho_f} \times U_g [1 + O(Re_p/2)] \quad (2-16)$$

Use of this equation for spheres rotating parallel to the pipe axis without external body forces would congregate at the center of the pipe.

For higher Reynolds numbers, the boundary layer concepts of the Magnus/Robins effect are appropriate. As mentioned previously, Prandl(18,19) describes the effect for a cylinder as the separation of the boundary layer where the spin of the cylinder opposes the fluid velocity and the retardation or elimination of separation where the spin is in the direction of the fluid (see Figure 2-1). The resulting pressure increase at the base of the sphere and pressure decrease at the top of the sphere results in a lift force. For a cylinder, Prandtl gives a maximum force obtainable corresponding to an angular velocity which is four times the slip velocity. He also mentions that the lift is reduced due to fluid effects from the end of the cylinder. These effects would almost necessarily exist for flow around a sphere. Again, for pipe flow of spherical particles, the Magnus/Robbins effect would cause a tendency

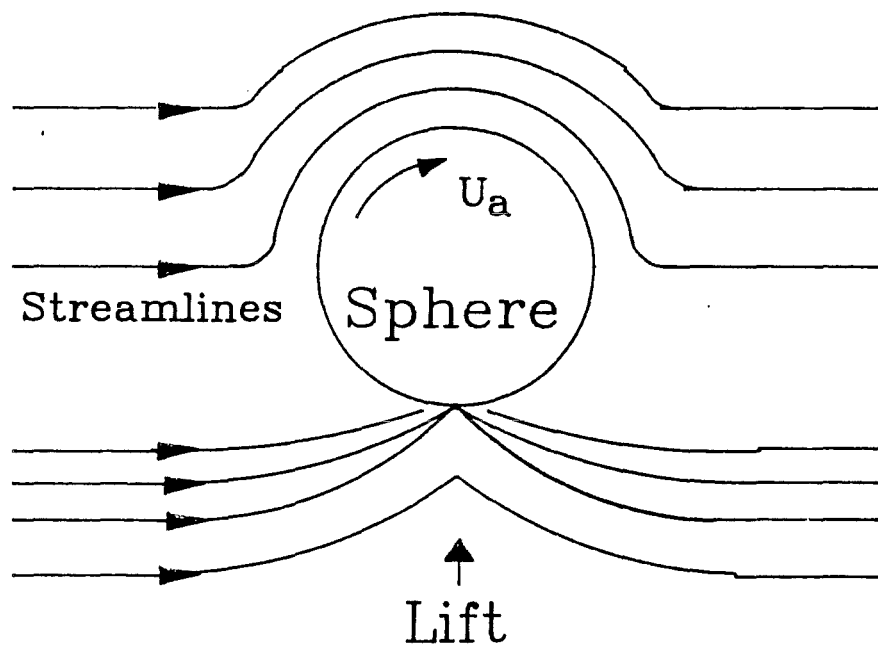


Figure 2-1: Magnus/Robins Effect on a Rotating Sphere

for particles to concentrate at the center of the pipe. A recent empirical relationship for the lift force in the range of $550 < Re_p < 1600$ developed by Tsuji, et. al.(22) from data of a single sphere being bounced off of an inclined plate is given as:

$$F_1 = \frac{C_1 \rho_f U_g^2 \pi D_p^2}{8} \quad (2-17)$$

where: $C_1 = (0.4 \pm 0.1)\lambda$

$$\lambda = D_p U_a / (2U_p)$$

and: $\lambda < 0.7$

A second force accounting for lift of particles from the base of the pipe is through bouncing. Although not a true lift force in the hydrodynamic sense, particle bouncing was reported by Gasterstadt(23) in 1924 as a mechanism by which particles were distributed across the radius of the pipe. The inclusion of this effect in calculations of pneumatic systems appears only recently in computer simulations.(24,25,26,27).

The third mechanism thought to be responsible for particle lift is through interaction of the gas phase turbulence with the particles. Much work has been done concerning the effect of the addition of particles on the turbulence structure of a flowing gas.(28,29,30,31,32,33) These studies have been primarily focused on the stability

of a flow system of flowing particles in a turbulent field or the effect of the mixtures turbulence on particle drag. The systems considered in these studies were usually highly idealized; however, the overwhelming consensus is that the presence of particles has a large impact on the turbulence structure.

Owens⁽³⁴⁾ provided an order of magnitude assessment on the effect of the turbulence in a flowing gas on the particles present in that flow. He argues that for most dilute gas-solids systems the interaction of the particles with the turbulent eddies in the flow is the primary mechanism by which radial flow or lift occurs (except for very small particles undergoing Brownian motion near the walls). The interaction with turbulent eddies is based on the time scale of the eddies and the relaxation time of the particles. Five domains for particle flow (excluding the Brownian motion domain) are given by Owens. These domains are described in Table 2-3 and represented in the fashion of Owens in Figure 2-2 for an 0.0266 m diameter pipe through which particles having a density of 2500 kg/m^3 are transported. As Owens does not discuss the effect the particles have on the turbulence of the gas, the friction velocity is assumed to be that of a pure gas.

Table 2-3

Domains of Turbulent Influence According to Owens (34)

<u>Domain</u>	<u>Characterization</u>	<u>Order of Magnitude Assessment</u>
B	Particle relaxation time above energetic Eddy time scale	$\frac{5 \rho_p U_\tau D_p^2}{9 \rho \eta 1/2 D_t} \sim 1$
C	Particle relaxation time above large Eddy time scale	$\frac{1 \rho_p U_\tau D_p^2}{18 \rho \eta 1/2 D_t} \sim 1$
D	Gravity Significant	$U_t \approx U_\tau$
E	Saltation	$0(1) > \frac{\rho_f U_\tau^2}{\rho_p g D_p} > 0(.01)$
F	Copius Saltation	$\frac{\rho_f U_\tau^2}{\rho_p g D_p} < 0(0.01)$

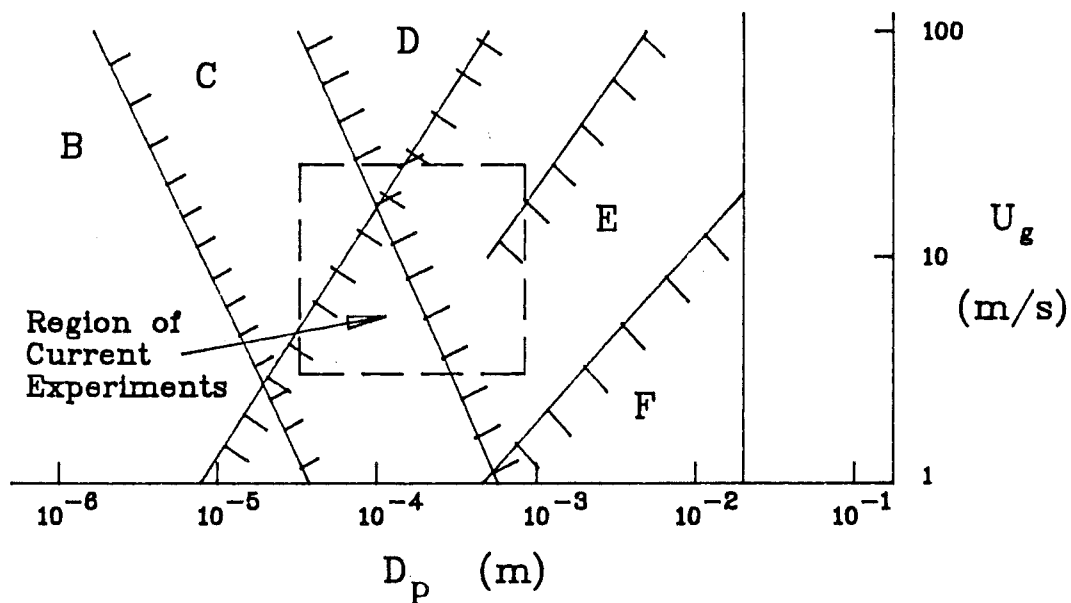


Figure 2-2: Domains of Turbulent Influence According to Owens (34)

2.2 Thermodynamic Analogy

A completely different approach to pneumatic transport is through analogy to a thermodynamic system. The preceding sections pointed out the difficulties associated with classical approaches. Many of the drawbacks of the classical approaches can be eliminated using the thermodynamic analogy. This does not occur without cost, however. The thermodynamic analogy which will be discussed is, at this stage, completely dependent on empirical data and based predominantly on experimental observation. This is not altogether a drawback to its use; however, as classical methods may suffer the same requirement.

It should also be mentioned that analogs to thermodynamics are not new. Other physical systems, such as superconductors and ferromagnetics, can be described using principles of phase transition and critical phenomena.⁽³⁵⁾

2.2.1 Background in Fluidization

A thermodynamic analogy to gas-solid systems is not new. The term fluidized bed was used to describe what was observed in beds of solids having a fluid passed through them at a sufficiently high rate. The mixture (fluid-solid) acted like a fluid. The mixture filled the container

holding it, it flowed with gravity, and waves could be produced on its surface. It was liquid-like. Gelperin and Einstein⁽³⁶⁾ reviewed the analogy between fluidized beds and liquids and pointed many similarities not limited to physical observation. These similarities included physical properties; such as, viscosity, density, and surface tension. They also discussed phase transitions and equilibrium in fluidized systems.

Perhaps, the most detailed single analysis of the analogy between fluidized systems and thermodynamics was reported by Furukawa and Ohmae⁽³⁷⁾. In their article they used a direct thermodynamic analogy to analyze fluidized systems with respect to expansion, viscosity, surface tension, and miscibility. To use the analogy to thermodynamics, they had to define the temperature analog in the fluidized system. To obtain the temperature analog they first defined a potential energy of volume vibration function for the fluidized bed. From this function they then deduced that the kinetic energy of the bed could be expressed as:

$$\text{Kinetic Energy} = \text{Constant} \times \mu_f U_g \quad (2-18)$$

As the kinetic energy in a thermodynamic system can be similarly expressed as a function of temperature, they concluded that the parameter analogous to temperature in a

fluidized bed is the viscosity of the fluid times the gas velocity. They further pointed out that the viscosity of the fluid in a given system remains almost constant leaving the gas velocity alone as the analog to temperature. This development of the analog to temperature is key to the further development of the thermodynamic analogies. Another development determined by Furukawa and Ohmae, but developed by Gelperin and Einstein⁽³⁶⁾ is the analog to the ideal gas constant. This concept came about in connection to the viscosity analog. The Andrade⁽³⁸⁾ equation was found to be able to represent the viscosity data obtained. From the expression the ideal gas constant analog was assumed to depend on particle size and density. A final important point made by Furukawa and Ohmae is that the use of a thermodynamic analogy to fluidization is quite complex owing to the variety of fluids and solids which might be used.

The fluidized bed represents only one phase, that of a liquid, in the thermodynamic analogy. Kondukov and Sosna⁽³⁹⁾ extended the concepts of the analog in their development of a phase rule for a gas-solid system. In their development three different phases are defined; the stationary bed (analogous to the solid phase), the fluidized bed (analogous to the liquid phase), and the entrained bed (analogous to the vapor phase). The only parameter characterizing the system is the fluidizing fluid velocity. For a system of C components existing in Y phases the number

of parameters at equilibrium is $C\Upsilon+1$. On a component basis, $\Upsilon-1$ equations can be written for each component as the sum over all phases for each component is unity. Therefore, the number of dependent variables is established as:

$$\Upsilon + C(\Upsilon - 1) \quad (2-19)$$

and the number of independent variables is:

$$\begin{aligned} F &= (C\Upsilon+1) - \Upsilon - C(\Upsilon - 1) \quad (2-20) \\ &= C - \Upsilon + 1 \end{aligned}$$

This is Kondukov and Sosna's phase rule for a bed of solid particles consisting of C different particles existing in Υ different phases. It is important to note that this phase rule was developed for a bed of particles without the addition of particles to the bed. Additionally, the authors only touch on the concept of equilibrium of the bed in relation to the phase rule and do not discuss the equilibrium of entrained solids once they leave the bed in the analogous vapor state. This will be important in the analogy to thermodynamics in pneumatic transport.

2.2.2 The Ideal Gas Analog

To introduce the analogy to thermodynamics in pneumatic transport it is best to start from the simplest case, that being the analog to a gas. This analogy, as proposed by

Kondukov and Sosna⁽³⁹⁾, is the entrained bed or transport of solid particles. To further simplify matters the transport will be assumed to occur in the dilute phase (dilute phase referring to large void fractions). It is under these conditions that the flow of solids are considered analogous to the ideal gas and will be termed ideal transport.

As was previously discussed, the gas velocity in a gas-solid system is analogous to temperature. It is apparent that the analog to volume is related to the amount of solids present in the system or the solids fraction. This leaves only the choice of an analog to pressure to complete the assignment of parameters in the thermodynamic analogy to pneumatic transport. Tuba⁽¹⁾ chose the solids flux as the parameter analogous to pressure in a thermodynamic system based on representations of phase behavior in gas-solid systems described by both Matsen⁽²⁾ and Wallis⁽¹⁷⁾. This gives three parameters which can be used to specify a given gas-solid system. Tuba placed these parameters in dimensionless form as follows:

$$j_{g^*} = j_g \sqrt{\frac{\rho_f}{gD_t(\rho_p - \rho_f)}} \quad \text{--- (Temperature Analog)} \quad (2-21)$$

$$j_p^* = j_p \sqrt{\frac{\rho_p}{gD_t(\rho_p - \rho_f)}} \quad \text{--- (Pressure Analog)} \quad (2-22)$$

$$\frac{1}{\phi} = \frac{1}{(1 - \epsilon)} \quad \text{--- (Volume Analog)} \quad (2-23)$$

$$\begin{aligned} \text{Where: } j_g &= \frac{Q_g}{A_t} = U_g \\ j_p &= \frac{Q_p}{A_t} = \frac{W_s}{A^p_p} \\ \phi &= (1 - \epsilon) \end{aligned}$$

This form will be used throughout the rest of this treatment of the thermodynamic analogy for pneumatic transport.

With this assignment of variables, the ideal gas analog follows directly as:

$$\frac{j_p^*}{\phi} = R^* j_g^* \quad (2-24)$$

As written here, the ideal gas analog simply relates the fluxes of the gas and the solids and the solids fraction. If the expression is solved for particle velocity and gas velocity (parameters normally reported in the literature), the ideal gas analog takes on the following form:

$$\frac{U_p}{U_g} = R^* \frac{\rho_f}{\rho_p} \quad (2-25)$$

It is this form which is more readily compared to experimental findings. Consider the data of Rizk⁽⁴⁰⁾ shown in Figure 2-3. Rizk's data clearly shows that for high gas

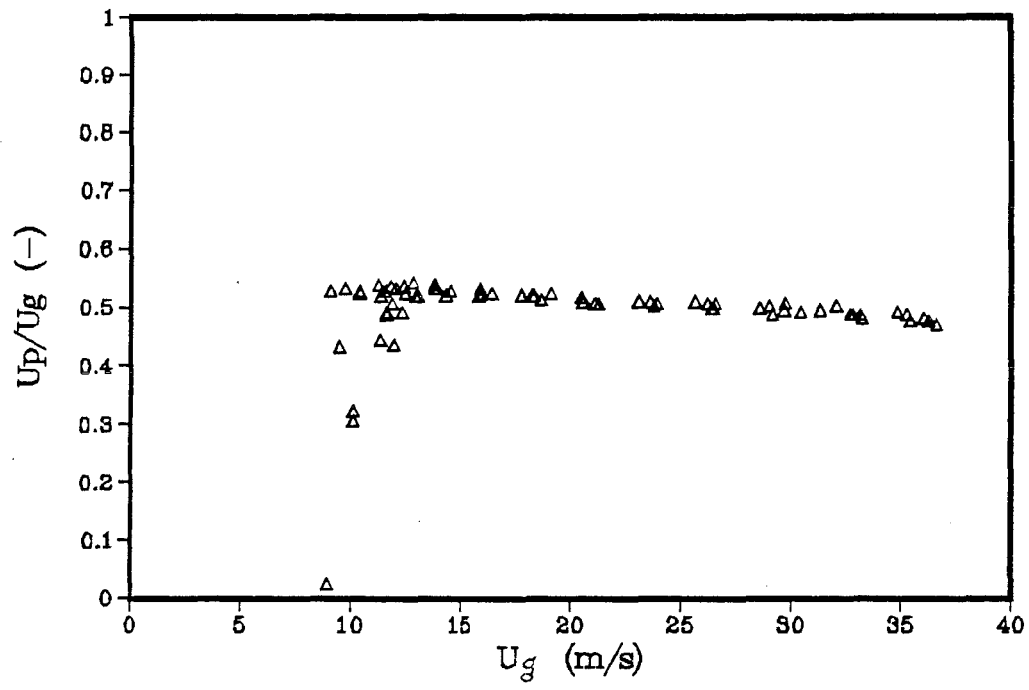


Figure 2-3: $\frac{U_p}{U_g}$ vs. U_g from the Data of Rizk (40)

velocities (corresponding to dilute conditions), the ratio of particle velocity to gas velocity indeed becomes a constant which is what is predicted by the ideal gas analog.

The ideal gas analog is not by itself very convincing as an analog to thermodynamics. This is obvious from the reduced form which it takes in Equation 2-25. The really important aspect of the ideal gas analog is the ability to predict the ideal transport constant R^* and the further demonstration that this constant allows experimental data in the ideal transport condition to be fairly well represented. This point will be further discussed in relation to the further development of the thermodynamic analogy in following sections.

2.2.3 The van der Waals Analog

To this point two widely varying types of gas-solids systems have been described, the fluidized bed and dilute phase pneumatic transport. The middle ground of these two conditions becomes the area of concern when discussing pneumatic transport. It is this middle ground where the minimum energy expenditure for transport exists as well as the instabilities associated with near choking flows or saltation. Ideally, one would be able to describe the gas-solid system using a single model capable of predicting the flow behavior across the entire range of conditions. There have been some attempts in this area; however, the modeling

aspect has been sparse. The first diagrammatic representation of the full spectrum of gas-solid flows was given by Zenz.⁽⁴¹⁾ This approach is the classical pressure drop versus gas velocity phase diagram which exhibits a minimum point at which most authors delineate the change from dilute to dense phase flow. Zenz's approach to design of pneumatic transport systems centers around minimum velocities obtained from this type of diagram. This is also the method of design practiced when using the correlations of Appendix F and the force balance approach given in Section 2.1.1. The problems associated with this approach are the same as those stated in Section 2.1; that is, there are many correlations to choose from, each giving fair results for the system studied, but no one correlation capable of describing all systems nor all conditions. In addition to this, there is very limited data available which covers the range of conditions described. As an example, consider the phase diagram of Canning and Thompson⁽⁴²⁾ shown in Figure 2-4. Although the description is thorough, the data is not directly represented, nor are specific variables such as particle velocity and void fraction available.

An attempt to correct the situation concerning phase diagrams was made by Matsen^(2,3) whereby fluxes were employed in the development of a phase diagram. Matsen's analysis was centered on fluidized beds and vertical

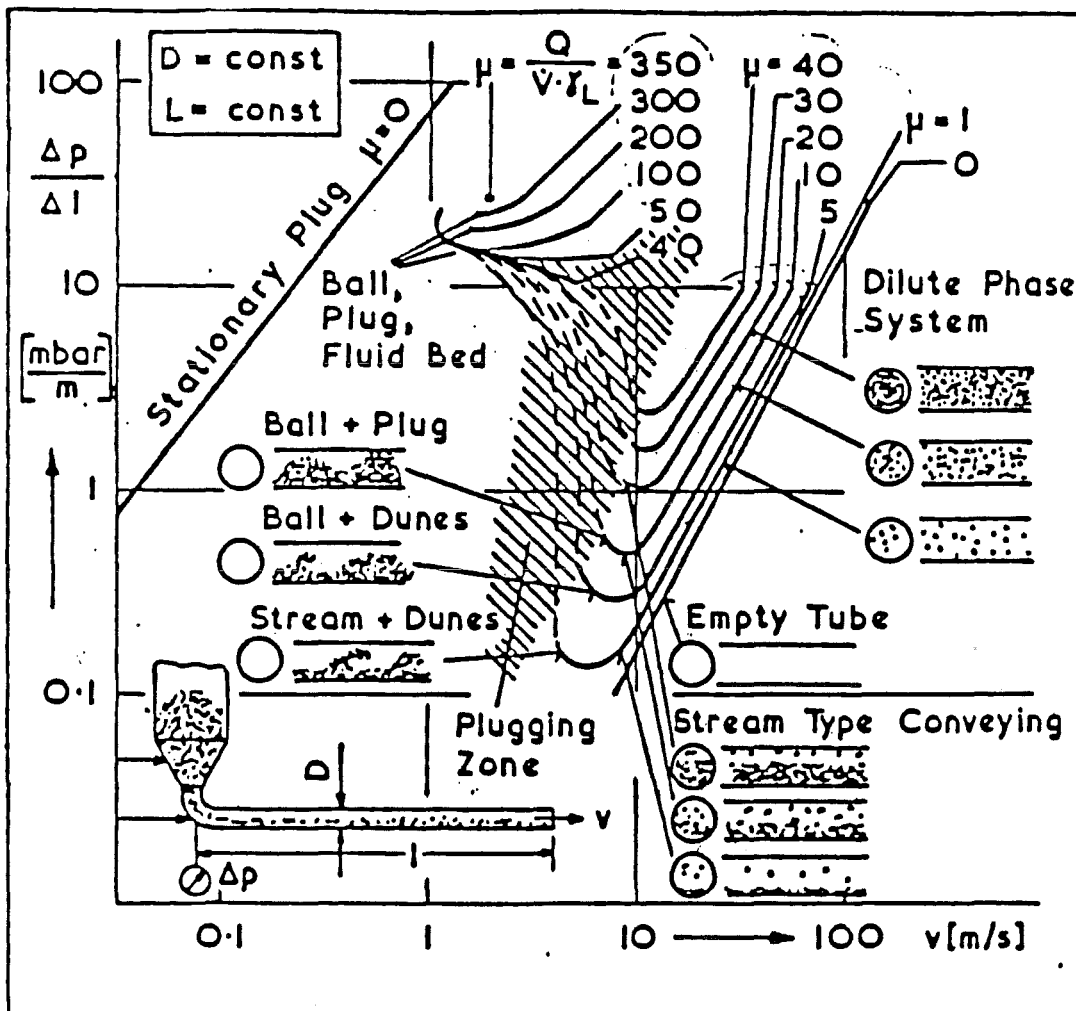


Figure 2-4: Phase Diagram for Gas-Solid Transport from Canning and Thompson⁽⁴²⁾

transport. For conditions of pneumatic transport, Matsen proposed a limiting factor on the particle flux based on the terminal velocity of the particle. This restriction was later reviewed by Matsen⁽²⁾, and he concluded that further quantitative study was required. One of the most important aspects of Matsen's work was the capability of predicting co-existing phases.

It was from Matsen's work that Tuba⁽¹⁾ formulated his description of a phase diagram for pneumatic transport. His initial analysis was based on a slip velocity relationship dependent on the void fraction and constants associated with the system. The particular form chosen for this slip velocity representation followed the flux-flux representation of Matsen. Tuba described an ideal transport equations equivalent to that given at Equation 2-24 but did not develop the ideal transport constant R^* from this relationship. This is primarily due to the choice of particle velocity correlation chosen by Tuba. He chose to use the particle velocity correlation of Hinkle⁽⁴³⁾ to describe the particle velocity relationship. Tuba explained that a relationship such as Hinkle's was incapable of predicting the phenomena of choking in vertical pneumatic systems and therefore did not fully incorporate the concept of ideal transport into his analysis.

Tuba proceeded to choose the non-dimensionalized form of the gas and solid fluxes given in Equations 2-21 and 2-22 following concepts of the drift flux presented by Wallis⁽¹⁷⁾. Using these non-dimensionalized fluxes, Tuba formulated his j-factor equation of state in the form of linear isovoids capable of describing the choking locus described by Matsen⁽²⁾. This j-factor equation of state was termed the "VDW-analog equation" based on its similarity to the thermodynamic van der Waals equation. The equation is given as follows:

$$\left[j_p^* + a^* \phi^2 \right] \left[\frac{1}{\phi} - b^* \right] = R^* j_g^* \quad (2-26)$$

This equation was successfully employed by Tuba in representing vertical pneumatic transport. Tuba also saw the possibility of obtaining the constants a^* , b^* , and R^* from an analog to the critical point in thermodynamics. This analog will be discussed later.

2.2.3.1 Phase Equilibria in Horizontal Pneumatic Transport.

Tuba's thesis was based on vertical pneumatic transport. The concepts employed however are equally valid to horizontal pneumatic transport with the proper definitions of phase equilibria in such systems.

Many authors have described, qualitatively, the phases of horizontal pneumatic transport. A typical description was described earlier as given by Canning and Thompson and

shown in Figure 2-4. Their representation covered the range of a stationary plug to dilute phase flow. If the analog to thermodynamics is considered, and only the liquid and vapor phases are included, two broad conditions of horizontal transport can be considered. These two are shown in Figure 2-5 and represent the entirely "vapor" analog flow which means that the system is dilute and homogeneous, and the two phase flow regime where there is a denser layer of solids flowing under a dilute phase on top. The dilute phase flow condition is what is normally considered in horizontal pneumatic transport well above saltation and can be reasonably represented by the ideal gas analog. The second condition considered, that of a two phase flow has been avoided in design of pneumatic systems due to the risk of saltation. This is not a proper representation of the conditions of the flow. Figure 2-5 only shows two possible states, when in reality there exists an equilibrium of two phase states which progress over a range of conditions. This is better described in Figure 2-6. This figure describes the formation of a denser layer which exists in various equilibrium conditions. At sufficiently low gas velocity, solids will become stationary on the bottom of the pipe with flow of solids continuing above this stationary layer. At this point the phase rule of Kondukov and Sosna⁽³⁹⁾ described earlier can be modified to include the

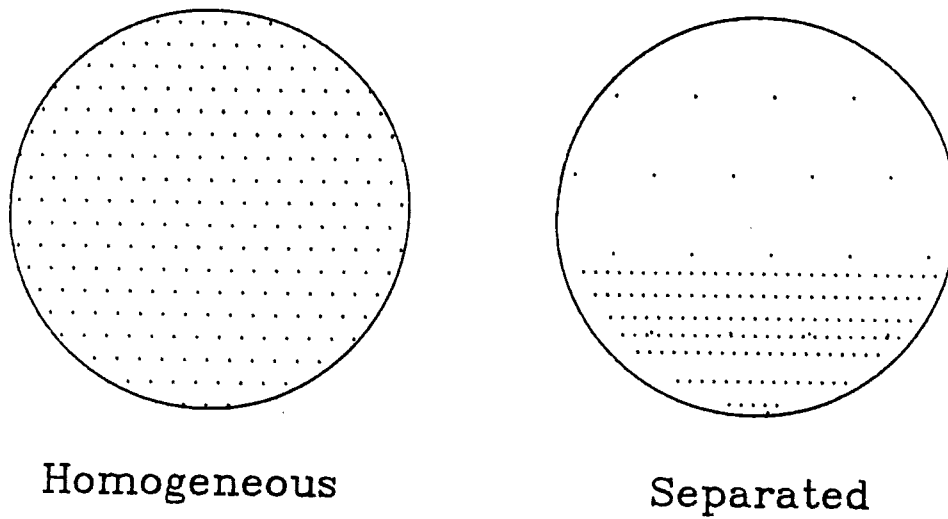


Figure 2-5: Broad Conditions of Horizontal Dilute Phase Flow

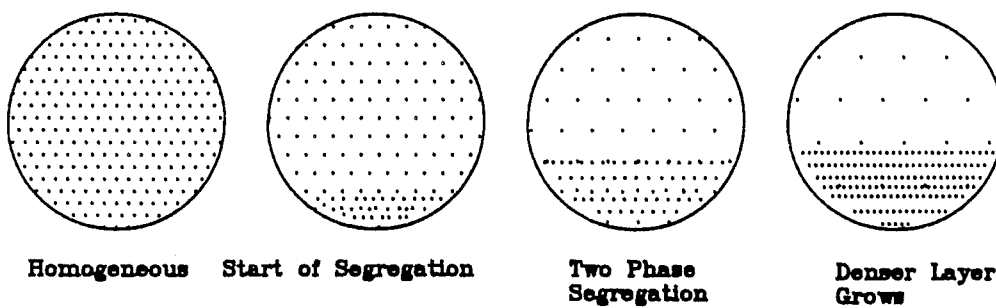


Figure 2-6: Phase Behavior in Horizontal Dilute Phase Flow

separate independent parameter of solids flux. The phase rule for pneumatic transport becomes:

$$F = C - \uparrow + 2 \quad (2-27)$$

This phase rule for gas-solid systems is identical to the simple phase rule in thermodynamics. An interesting point concerning this expression is the prediction of a triple point. Although this condition has not been reported experimentally, its possibility of existence is best described for a horizontal gas solid system. This condition would exist when a sedimentary layer formed on the bottom of the pipe. This layer, analogous to a solid phase, would have particles in constant contact with each other; i.e., not fluidized. A second layer would be formed on the top of this layer, where particles were in close proximity to each other yet had freedom of movement. The third phase would exist as a dilute phase above the other two. If this point does exist in a pneumatic system, it would, by virtue of the phase rule, be susceptible to changes in gas and solid fluxes and therefore be difficult to both obtain and maintain.

For the case of two phases coexisting in horizontal flow it is necessary to know the flux of both the gas and solid in each phase to apply the thermodynamic analogy. This assumes that the distribution of each phase is completely

homogeneous. Unfortunately, real gas solid systems do not exhibit the uniformity one might expect in a thermodynamic system. Fluctuations in the gas and solids fluxes as well as wall disturbances and other factors cause fluctuations in both phases. Additionally, it might be argued that a distribution of the particles across the pipe exists under almost all operating conditions. This also appears in thermodynamic systems although the resultant distribution is often negligibly small. Consider however the thermodynamic experiment shown in Figure 2-7. In this apparatus, measuring the pressure of the system at point 1 would lead to erroneous results if the static head of the liquid were not taken into account. This is also true for point 2 concerning the gas although the static head of the gas would likely be negligible. For the thermodynamic measurement, the pressure should be obtained at point 3, the interface of the gas and the liquid. This would be true for the pneumatic system also. As mentioned before, this interface is not always easily defined and may fluctuate. An additional problem is the gas flux. This parameter is difficult to measure in-situ due to the presence of the solid particles. Recent advances in laser-Doppler anemometry⁽⁴⁴⁾ may provide solutions to the measurement of both fluxes. An approximate method is to assume the gas flux to be the same in each phase and to use the solids flux of the dilute phase as the equilibrium flux to apply in the

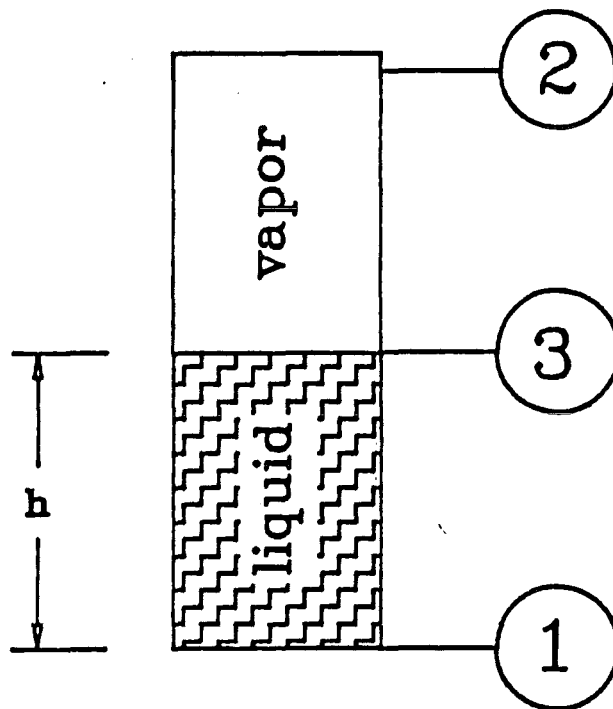


Figure 2-7: Measurement of Pressure in Thermodynamic Vapor-Liquid Equilibrium Experiment

thermodynamic analogy. Experimental verification of the van der Waals analog to horizontal systems and its capacity to represent the phase behavior of these flows will be presented in section 4.

2.2.3.2 Constants in the van der Waals Analog Equation.

Paramount to the use of the van der Waals analog is the ability to obtain the constants R^* , a^* , and b^* . Following thermodynamics there are two methods by which to obtain the constants, regression of experimental data and solution for the inflection at the critical point. Of these two, the critical point method is by far the easiest; however, without a firm knowledge of the critical point, this method is subject to large error. The fundamental ease of this approach however merits further investigation. The critical point analog will be discussed in the following section.

The second method for obtaining the van der Waals constants is through regression of experimental data. This method will provide the best fit of the experimental data but is subject to the inaccuracies of the data itself. In addition to this there is a problem concerning the ideal transport constant. This problem manifests itself in the prediction of the ideal transport constant at the critical point. At the critical point in a thermodynamic system the gas constant predicted by the van der Waals equation is:

$$R = \frac{8P_c V_c}{3T_c} \quad (2-28)$$

Wallas⁽⁴⁵⁾ points out that this expression provides a different gas constant for each gas. He further states that it is normal practice to use the accepted gas constant as a constraint in fitting experimental data and only regress a and b. The fit to experimental data may be improved by allowing the gas constant to take on a fitted value and Wallas mentions that this is sometimes done producing an additional regression constant that Wallas calls R_{vdW} . The situation in the analog to pneumatic transport is not so clear cut. As mentioned in Section 2.2.2, the ideal transport constant is by nature of its definition different for different particles and fluids. Solution for R^* using the van der Waals analog equation yields:

$$R^* = \frac{8 \left[\frac{p_p}{p_f} \right]^{.5} U_{pc}}{3 U_{gc} \epsilon_c} \quad (2-29)$$

This cannot be compared to the R^* obtained from the ideal transport analog without a knowledge of conditions at the critical point. Without this knowledge it is questionable whether to fit the data to three parameters and include R^* as a regressed variable or to use the ideal transport analog, fix R^* , and fit only two parameters. This question was addressed by Zaltash, et. al.⁽⁴⁶⁾ as a problem of

dependence of the equations for the critical point. A comparison of the ideal transport constants obtained by Tuba⁽¹⁾ through regression and the ideal transport constants obtained through the ideal transport analog equation are shown in Table 2-4. The ratio of the particle velocity to gas velocity used to obtain the ideal transport constants were obtained using the conditions reported by Tuba at the five highest gas velocities reported.

Table 2-4

Comparison of Tuba's⁽¹⁾ Ideal Transport Constant With That Predicted by the Ideal Transport Analog Equation.

Series	R_T^* (from Tuba)	R_I^* (from Analog)	% Difference
A	10.5894	10.1442	4.4 %
B	4.04615	3.3166	22.0 %
C	14.5933	12.4800	16.93

Although the difference is relatively small (especially for the Series A), there is an amount of smoothing from the regression technique. A difficulty in further analysis of the data of Tuba arises from the fact that phase equilibrium in the system was not observed or reported. This makes analysis of the two phase region predicted through the use of the van der Waals analog subject to a choking analysis (Tuba's data was for a vertical system) which is uncertain

in itself. Measurements of two phase (dilute/dense) pneumatic transport which include fluxes in each phase have not previously been made.

2.2.3.3 The Critical Point Analog. As previously mentioned, the critical point in a gas-solid flow has yet to be determined experimentally. Two suggestions for the identity of the critical point have been made. The first is in an analog to the fluidized bed and the second is through direct analog and the use of pressure drop diagrams.

Gelperin and Einstein⁽³⁶⁾ suggest an analog to the critical point as well as a melting point analog from the standpoint of the fluidized bed. Their critical point is defined as the gas velocity at the onset of entrainment coupled with the voidage at this point. The problem with this definition is that for an equilibrium condition a solids flux must be constant; otherwise, the bed would diminish and the conditions would be changing. The gas velocity suggested is the terminal velocity of a single particle. This velocity is not in keeping with data presented by Matsen⁽²⁾ in his phase diagrams. Matsen gives a typical value for the critical point (Matsen calls it the End of Choking Envelope) as 5.7 times the terminal velocity of a single particle. Relationships to predict this point to include solids flux and void fraction are not available but studies in fast fluidization may provide data to investigate this point as the critical point analog.

A direct analog approach was suggested by Klinzing, et. al.(47) defining the critical point as the point at which dilute and dense phase transport cease to be distinguishable. As this point would be difficult to determine visually (as is often done with vapor/liquid systems) a method of determining the point of coincidence of the phases is necessary. Zaltash, et.al.(46) suggested the use of the pressure drop versus gas flux diagram as a means of determining the critical point on this basis. Typically, the pressure drop versus gas flux diagram shows a minimum point at which dense and dilute phase flows are distinguished. With an increase in solids flux, this minimum point occurs at larger pressure drop. Conceivably there would be a point of solids flux where the minimum either disappeared or became coincident with the pressure drop corresponding to a bed of solids. This concept is displayed in Figure 2-8 using data from Rizk(40). As previously mentioned, experimental evidence of the critical point for a pneumatic system has not yet been found; however, estimates of this point may be possible from the above two methods.

2.2.3.4 Pressure Drop. Pressure drop in a pneumatic system is a state function of the gas and solids flux. It would be advantageous to be able to predict this parameter from the analog equations. This requires a definition of the

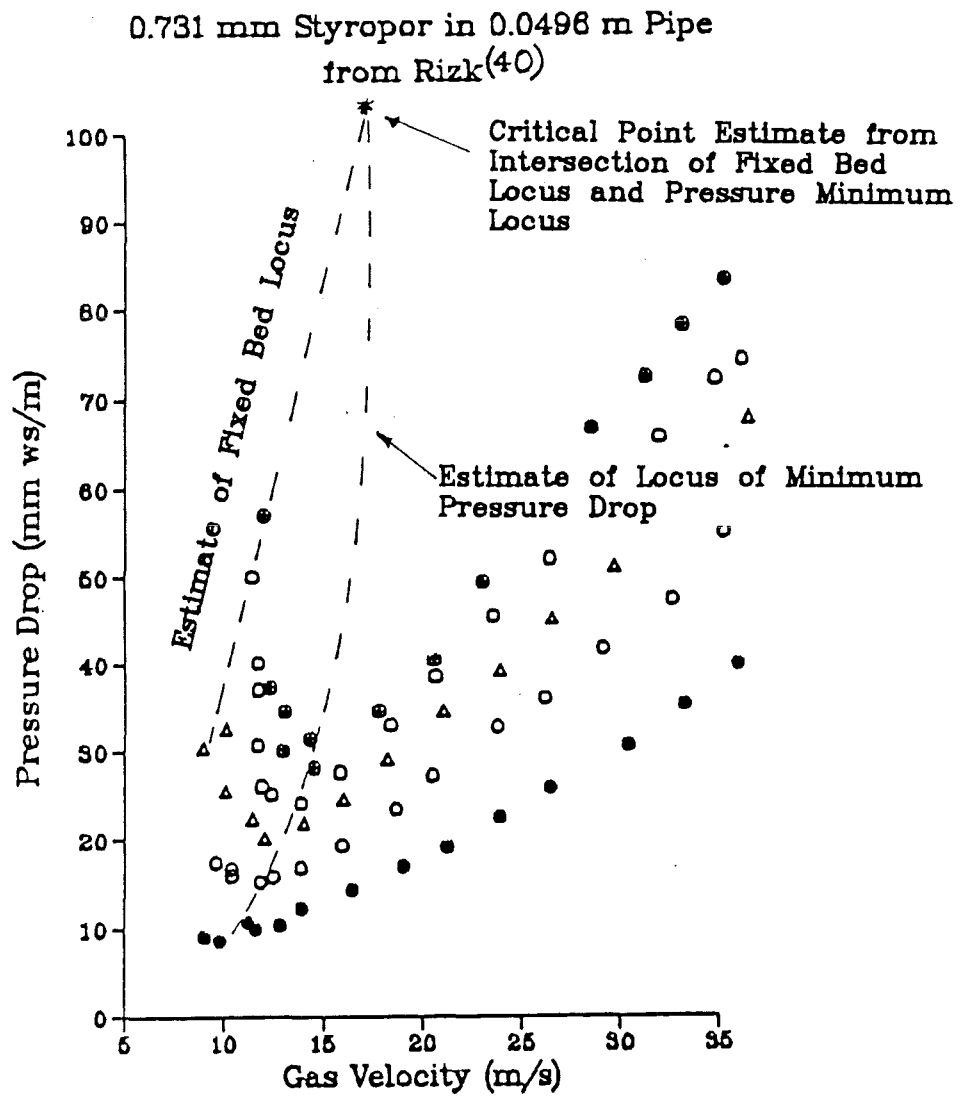


Figure 2-8: Critical Point on the Pressure Drop vs. Gas Velocity Phase Diagram - Data of Rizk⁽⁴⁰⁾

functionality of the pressure drop in terms of the equation of state. Various attempts have been made to define this functionality. Mathur, et.al.⁽⁴⁸⁾ proposed a model based on the minimization of energy as follows:

$$\left[\frac{\partial \Delta P_{\text{friction}}^*}{\partial \phi} \right]_{j_g^*, j_p^*} = 0 \quad (2-30)$$

where: $\Delta P_{\text{friction}}^*$ is a dimensionless pressure drop due to solids friction

This equation was solved by integration of the van der Waals analog equation and the gas frictional term was added to obtain the following expression:

$$\Delta P_{\text{friction}}^* = \left[f_g j_g^{*2} - \phi \right] + \frac{1}{2} \left[\frac{R^* j_g^*}{j_p^*} + b \right] \phi^2 - \frac{a^*}{3 j_p^*} \phi^3 + \frac{a^* b^* \phi^4}{4 j_p^*} \quad (2-31)$$

If a constant of integration is included in the dimensionless pressure drop, this equation can be compared to experimental data to test its validity as well as determine the means by which to non-dimensionalize the pressure drop.

Another approach to the pressure drop using the thermodynamic analogy was proposed by Klinzing, et.al.⁽⁴⁷⁾ where an assumption for the form of the pressure drop functionality is made. In this method a functionality is chosen in terms of two parameters. An example was given as:

$$\text{Assuming: } \frac{\partial (\Delta P^*)}{\partial j_p^*} = C_1 \phi \quad \text{then} \quad (2-32)$$

$$\frac{d j_p^*}{d \phi} = \frac{R j_g^*}{(1-b\phi)^2} - 2 a \phi \quad (2-33)$$

$$\frac{d j_p^*}{d \phi} = - C_1 \phi \left[\frac{R j_g^*}{(1-b\phi)^2} - 2 a \phi \right] \quad (2-34)$$

$$\Delta P^* = \int - C_1 \phi \left[\frac{R j_g^*}{(1-b\phi)^2} - 2 a \phi \right] d\phi \quad (2-35)$$

Now substitute j_g^* from the equation of state to obtain:

$$\Delta P^* = - C_1 \int \phi \left[\frac{R (j_p^* + a\phi^2) (1-b\phi)}{R \phi (1-b\phi)^2} - 2 a \phi \right] d\phi \quad (2-36)$$

(2-37)

$$\Delta P^* = - C_1 \left[\frac{a}{2b} \phi^2 + \frac{a}{b^2} \phi - (j_p^* + \frac{a}{b^2} \ln (1-b\phi)) + \frac{2}{3} a \phi^3 \right] + C_2$$

This method clearly requires the proper choice of functionality for the pressure drop. It also contains constants which would apparently come from experimental data making the usefulness of the method subject to extensive testing, a situation which the analog is supposed to alleviate.

A third method for specifying the pressure drop in a pneumatic system using the analog to thermodynamics is to

treat the pressure drop as an energy function such as the Helmholtz free energy. This would allow calculation of the pressure drop by methods already familiar to engineers. A drawback to this method is that definitions of other thermodynamic analog parameters such as entropy or heat capacity becomes a necessity. If proper definitions can be made, this approach would allow calculation of system parameters for pneumatic transport across a wide range of conditions from a single model.

2.2.4 Discontinuity of the Thermodynamic Analog

There are a few points which must be made concerning discrepancies between thermodynamics and the analog to pneumatic transport. The first of these is the physical differences between horizontal gas-solid systems and vertical systems. How the differences encountered in the flow behavior between these systems can be treated within the framework of the analog to thermodynamics is unclear. There is a difference in the two systems and at present a specification of the system must be made prior to the use of the thermodynamic analog.

A second point is the choice of parameters. Although the gas velocity has been shown to be analogous to temperature, the choice of variables for pressure and volume is not absolute. In addition, the non-dimensionalization of

the parameters was chosen by convention. Of importance is the choice of gas density in the non-dimensionalization of the fluxes. The gas density in a pneumatic system may change appreciably through the system causing the fluxes to change due to internal changes of the system.

A final note is made concerning limits. In a thermodynamic system zero values of pressure and temperature are hypothetical states. In the pneumatic transport analog these states are not only obtainable but can be passed. This discrepancy would be most important in approaching the fluidized bed state from a packed bed.

Even with the above conditions, the thermodynamic analogy to pneumatic transport retains the feature of being able to represent experimental data in a way previously not possible from a single model. It is this feature that gives it a high benefit potential.

3.0 EXPERIMENTAL

The objective of the experimental work was to obtain data from horizontal pneumatic systems from which basic modeling and the Van der Waals analog could be applied to predict the separate phases possible in the system. This required measurement of particle velocity as well as solids flow rate in both the upper and lower portions of the pipe. To accomplish this objective, two separate pneumatic systems were constructed. The first was a bench scale system consisting of a 0.0266 m (1 inch) inside diameter pipe supplied with house air. The second system used a 0.0504 m (2 inch) inside diameter pipe supplied with air from a positive displacement rotary lobe blower.

3.1 Bench Scale System

3.1.1 Velocity Verification

The bench scale system was set up to obtain data in the 0.0254 m pipe as well as to test electronic equipment. The first configuration of this system, as shown in Figure 3-1, was used to obtain data using two independent velocity measurement techniques with the aim of verifying the use of the cross-correlation technique for measuring particle velocity. Two Jamesbury pneumatically actuated full port ball valves were inserted into the system with a known

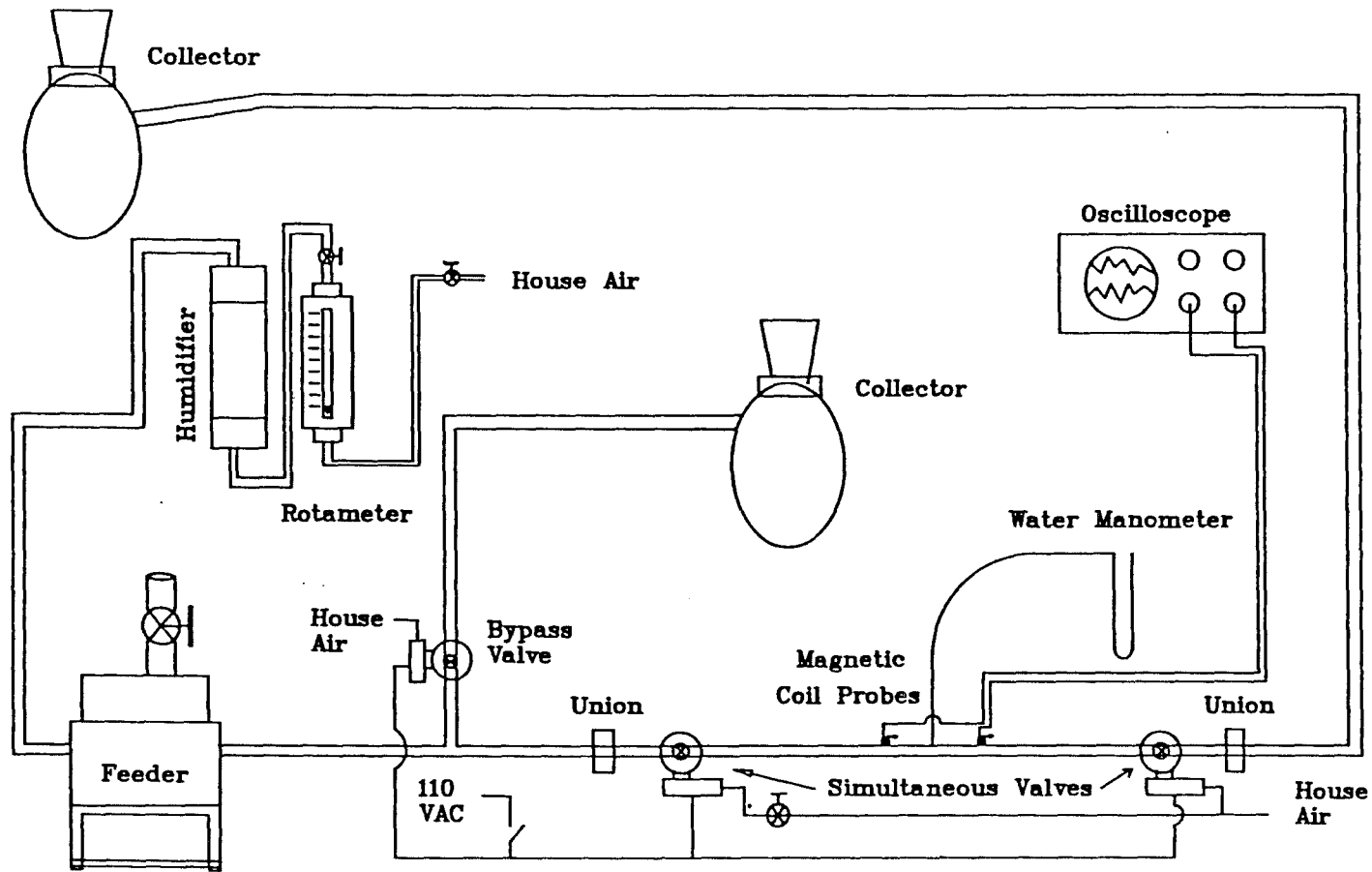


Figure 3-1: Bench Scale System for Verification of Velocity from Cross-Correlation Using Simultaneous Valves

volume of pipe between them. The two valves could be actuated together to achieve an almost instantaneous closure of the flow between the valves. The verification of simultaneous closure was determined by measuring the pressure between the two valves and regulating the availability of air to one of the valves until no pressure fluctuation was obtained upon closure of the two valves. To avoid excessive pressures upstream of the two valves, a third valve was also included in the system which was actuated simultaneously with the other two. This valve was set to open when the other two were closed, and the two phase flow stream was vented to a collection system through the third valve. Data was collected by the cross-correlation of signals from two probes placed on the section of pipe between the two simultaneous valves to obtain particle velocity by this method. Upon collection of the required signals from the probes, the two valves were closed and the solids trapped between the valves collected. The mass of the trapped solids was obtained. Knowing the volume between the valves, the density of the solids, and the mass of the solids trapped between the valves allowed the calculation of the particle velocity. The volume of pipe between the two valves was $1.628 \times 10^{-3} \text{ m}^3$ and the probe separation was 0.61 m. The results of the velocities obtained using both methods are shown in Figure 3-2.

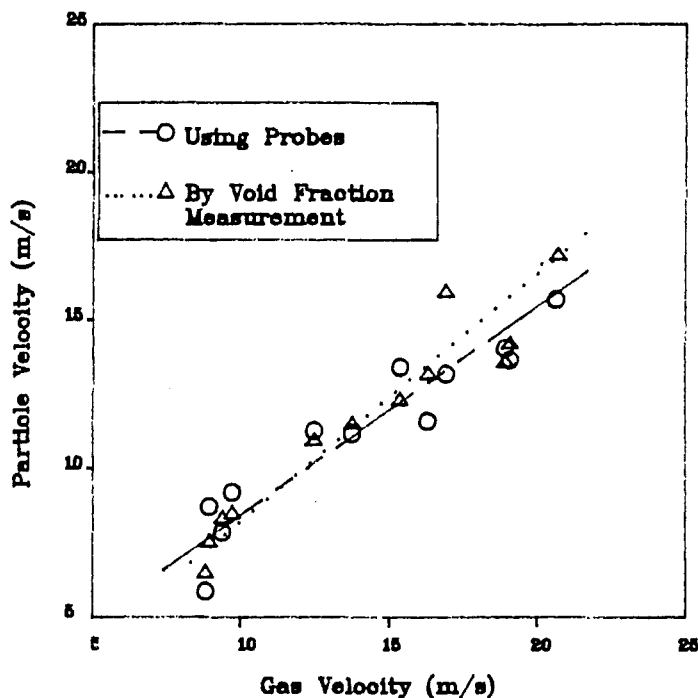


Figure 3-2: Results of Particle Velocities Obtained By Void Fraction Measurement and By Cross-Correlation Techniques in the 0.0266 m Bench Scale System

3.1.2 Horizontal System

3.1.2.1 Layout and Major Equipment. The layout of the 0.0266 m (1.049 inch) bench scale system used to obtain primary data is shown in Figure 3-3. The chosen layout insured all two phase flow sections were horizontal thereby reducing possible effects for orientations other than the horizontal.⁽⁵⁾ The numbering of equipment items in the following paragraphs refer to the numbering sequence of Figure 3-3.

House air was metered into the system through a Brooks Instruments model 110-10K3AlA rotameter (#2) by positioning

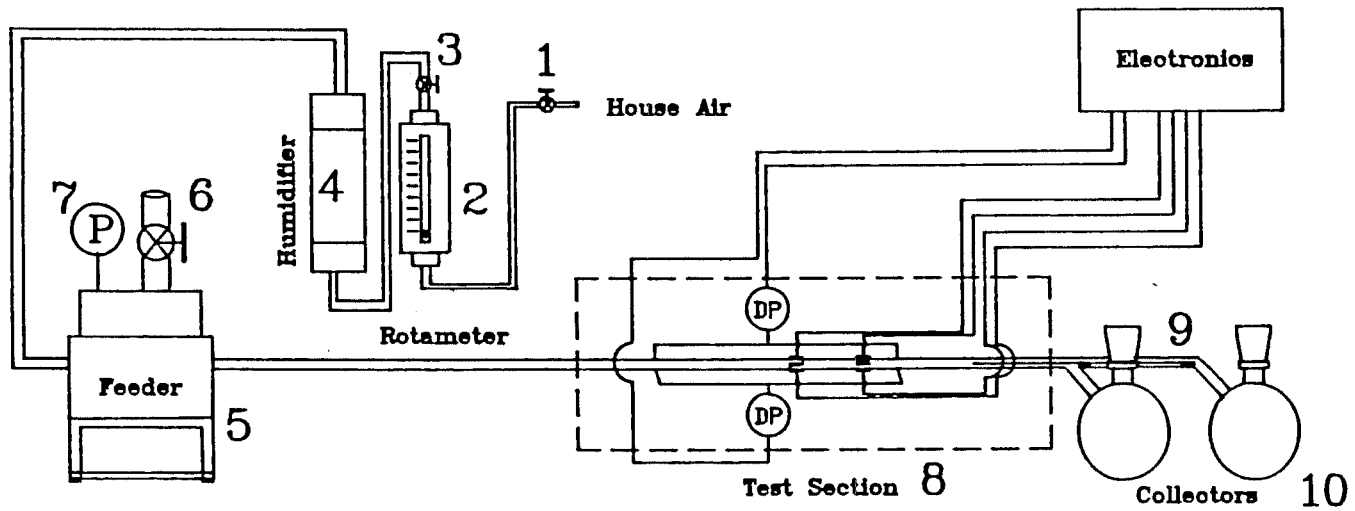


Figure 3-3: Bench Scale System (0.0266 m Diameter)

of valves (#1 and #3). Due to limitations of the house air supply the maximum flow rate obtainable was approximately 50 m³/hr. Following the rotameter was an 0.1016 m diameter by 1.2 m long Plexiglas column (#4) used for conditioning the air. This column was packed with 1.27 cm Intalox saddles topped with sponges. Water was admitted to the base of the column for humidification of the air stream. Air entered the base of the column and forced the water up onto the Intalox saddles where contact humidification could occur. The sponges at the top of the column were used as demisters to preclude water droplets from entering the two-phase section of the system. Relative humidities greater than 75 % were obtained using this column. Humidified air passed through an 0.0127 m diameter tube to the solids feed section of the system. Solids were fed to the system using a Vibra-Screw, Inc. live bin vibrating screw feeder (#5). This feeder allowed solids flow rates to be volumetrically controlled by a dial setting. The screw mechanism on the feeder was modified to allow the use of a continuous auger. An additional modification was made to the feed mechanism to reduce failures due to excessive back pressure on the auger. This modification was a stainless steel chuck which held the auger on teflon tipped set screws. This allowed the motor drive to turn freely if back pressure on the auger became

too great. An aluminum cover was bolted on the top of the feeder bin and sealed by using a rubber gasket. An 0.0508 m ball valve (#6) allowed access through the cover. This cover allowed the screw feeder to be pressurized in order to obtain higher solids flow rates than would be available with the auger alone. A pressure gauge (#7) indicated the pressure in the bin. Solids entered the transport system through a modified tee fitting. The tee fitting was modified to allow the solids a free entry into the system. The modification was made using an 0.0508 m pipe which was tapered to 0.0254 m by 0.0762 m. This pipe was molded to an 0.0254 m section of pipe to form a tee fitting. Air entered one of the 0.0254 m ends of the tee fitting through a 0.0127 to 0.0254 m reducer bushing. Solids were fed downward through the 0.0508 m section. The resulting mixture composed the two phase flow through the rest of the system. The two phase mixture passed through a 1.8 m horizontal section of Schedule 40 PVC pipe (0.0254 m ID) to a 90 degree standard elbow. The elbow was made of copper. After the elbow was a 2.4 m long section of copper pipe. This section was intended to reduce accumulation of static charge in the system and was grounded. After the copper section there was a short length of PVC pipe 0.6 m long. This section was intended to allow static charge to be built up prior to the

test section. The next section of pipe in the system was the test section (#8). This section consisted of a 2.1 m long glass pipe with an actual inside diameter of 0.0266 m. Pressure drop and velocity measurements were made along this section of the pipe and will be discussed separately. Following the test section was a 0.9 m long section of pipe which was designed to split the flow into an upper and lower fraction (#9). Details of this flow splitter are given in Section 3.1.2.4. The two streams entered separate 28.5 liter collection vessels (#10). Air from the two phase mixture passed through filter bags located at the top of each collection vessel leaving the solids from the upper half of the pipe in one vessel and the solids from the bottom half of the pipe in the other vessel. By measuring the time of flow and weighing each vessel the mass flow rate in the upper and lower halves of the pipe were determined.

3.1.2.2 Pressure Measurement in the Bench Scale System.

Measurements of the pressure drop across the test section were made using two Omega model PX164 differential pressure transducers. Pressure taps were made through the wall of the coupling adapters located at each end of the glass test section by drilling an 0.79375 mm (1/32 inch) hole through to the inside of the test section. A larger hole was made into the coupling adapter to accept a 3.175 mm (1/8 inch) steel tube which was glued onto the coupling adapter with an

epoxy resin. One set of taps was made at the top of the test section while the other set of taps was made 15 degrees off center from the bottom of the pipe (see Figure 3-4). The selection of these measuring points was made in order to assess the magnitude of the pressure difference across the radius of the pipe. The lower set of taps was offset from the bottom of the pipe to reduce the frequency of tap blockages due to particle saltation into the taps. Both the upper and lower set of taps were purged periodically to remove trapped solids. The two pressure transducers were connected to the corresponding pressure taps using equal lengths of 6.35 mm (1/4 inch) polyethylene tubing. The required 8 volt excitation voltage for the pressure transducers was supplied with an Acopian model B8G100 power supply. The output from the transducers was fed into the computer acquisition system which will be described in Section 3.3. Specifications for the pressure transducers can be found in Appendix C.

3.1.2.3 Velocity Measurement. Particle velocities were measured across the radius of the pipe in two locations, the upper half of the pipe and the lower half of the pipe. This was accomplished by using a modification of the electrostatic ring probes of Smith and Klinzing⁽⁴⁾. The modification of the probes consisted in a split into two sections separated by an insulator (see Figure 3-5).

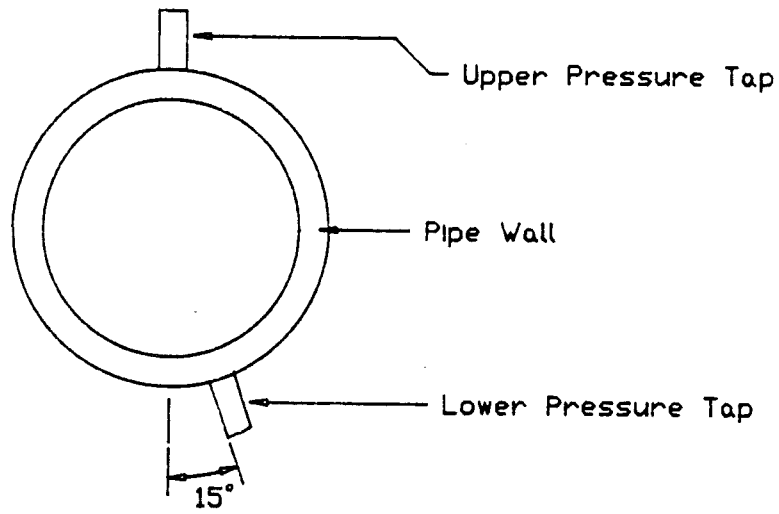


Figure 3-4: Pressure Tap Placement

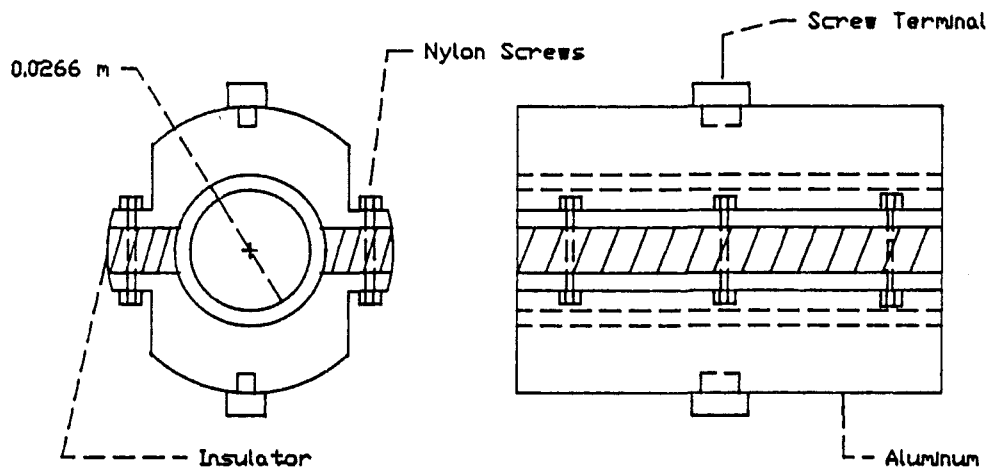


Figure 3-5: Split Electrostatic Ring Probe

Signals caused by contact of the particles and the separate sections of the probes were fed to the computer interface through four Keithly model 610C Electrometers using coaxial cable. The connection and orientation of the probes is shown in Figure 3-6. The probe material was free spinning aluminum with a fiber insulator separating the two halves. Details of the computer acquisition and calculations using the signals obtained from the probes are described in Section 3.3.

3.1.2.4 Flow Splitter in the Bench Scale System. To obtain the mean solids flow rate in both the top half and the bottom half of the pipe a flow splitter was constructed. This splitter is shown in Figure 3-7. It was assumed that the length of pipe between the two outlets from the splitter section did not interfere with the flow pattern at the knife edge of the splitter.

3.2 Full Scale System

A full scale pneumatic transport system was constructed to observe the effect of tube diameter on the flow conditions. This system used 0.0504 m (2 inch) inside diameter copper pipe and was approximately 30 m in length.

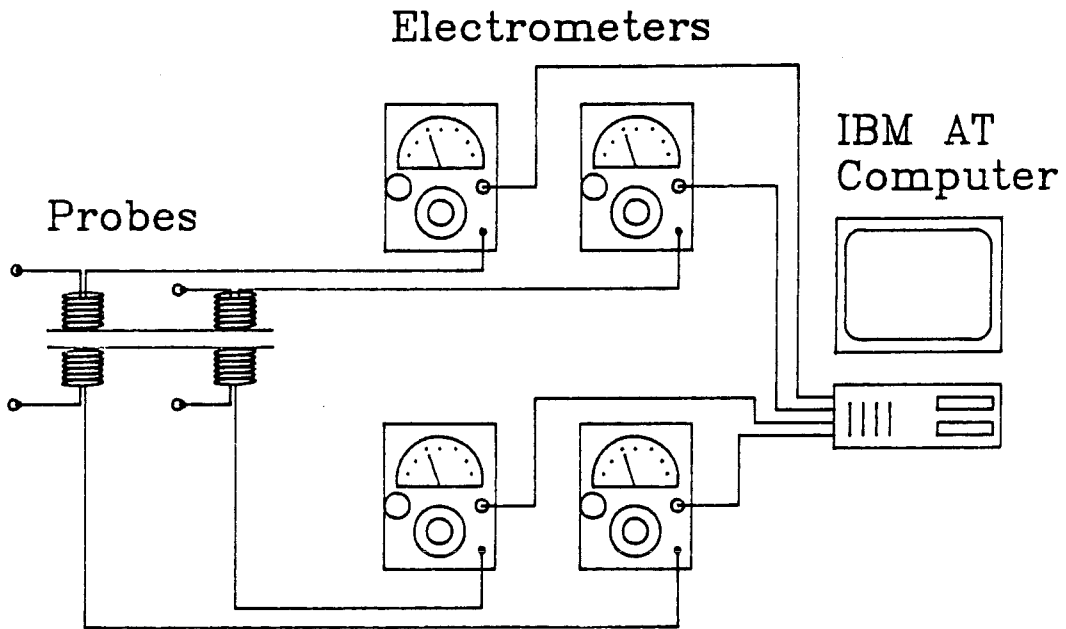


Figure 3-6: Connection and Orientation of Velocity Probes

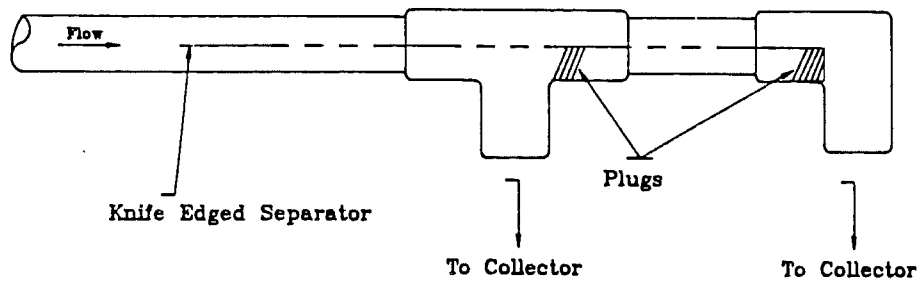


Figure 3-7: Detail of Flow Splitter

3.2.1 Layout and Major Equipment

The system was designed to be used in different configurations with a minimum of reconstruction by use of modular end items. These end items consisted of an air delivery unit, a solids feed system, and solids collection systems. Piping for different configurations was changed according to the desired orientation. Although only one orientation, horizontal, was used for this study, the end items described above will be discussed separately as their construction was based on the modular concept.

3.2.1.1 Air Delivery and Conditioning. Air was supplied to the system through an air delivery/conditioning system mounted on a Unistrut frame. Figure 3-8 shows the layout of the air delivery system. All piping in the air delivery system was 0.0762 m (3 inch nominal) PVC. Parenthetical numbering in the following text refers to the numbering of the equipment items in Figure 3-7. The air source was a Roots-Connersville model 2506J rotary lobe blower (#1). The capacity of the blower was $0.12 \text{ m}^3/\text{s}$ at 41 kPa. The blower was powered by a 7.5 hp, 220 V electric motor (#2). Air from the blower passed through two columns which were used to control the humidity of the air. Water was introduced at the top of the first column (#3) and passed countercurrently to the air stream which was admitted at the bottom. The

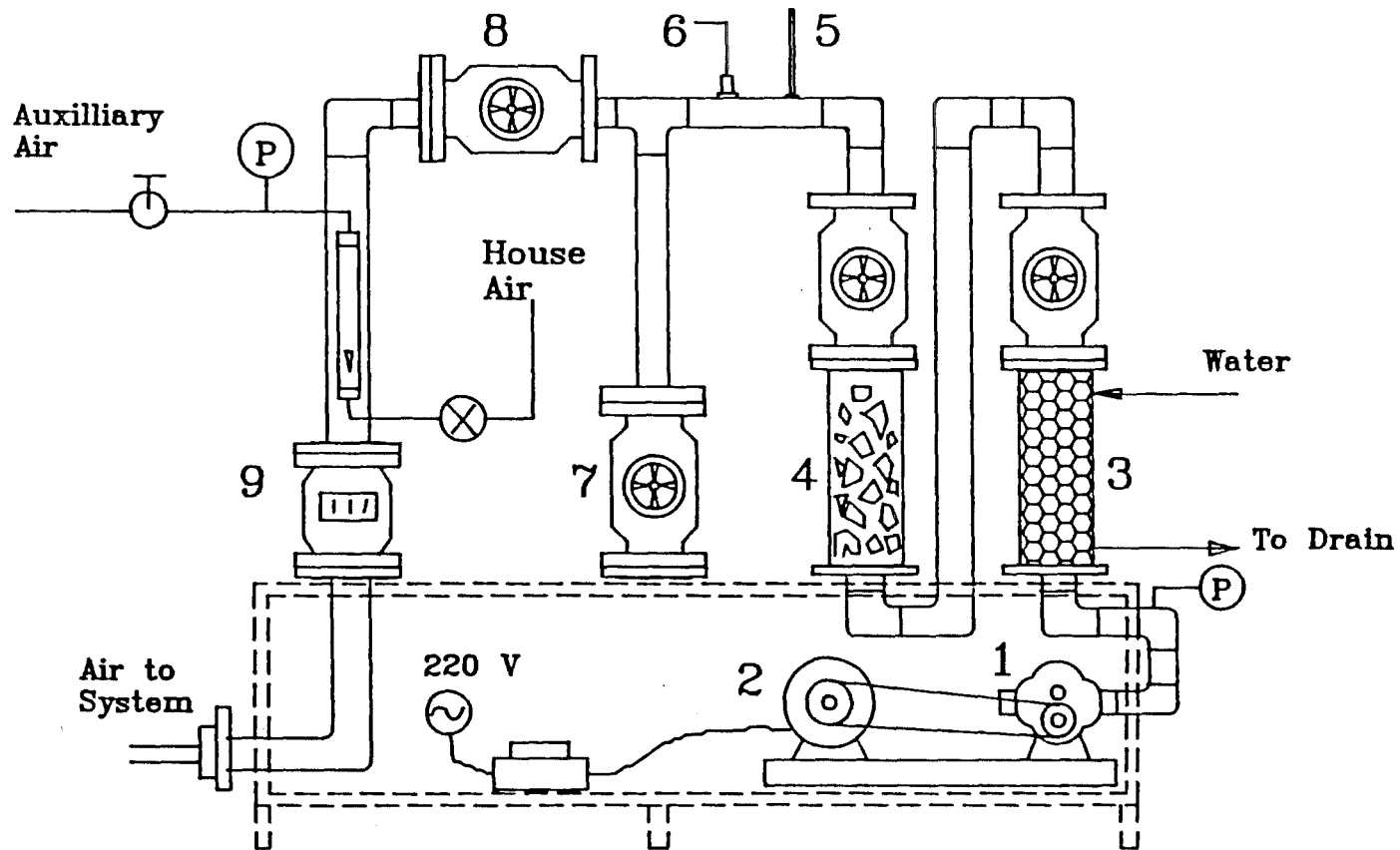


Figure 3-8: Air Delivery System in the Full Scale System

column was packed with 1.27 cm Intalox saddles. The air was then passed through a second column (#4) packed with sponges. The second column served as a mist eliminator. The temperature was measured with a thermometer mounted in the pipe following the second column (#5). Additionally, the humidity was measured using a Hydrodynamics model 15-3050 hygrometer with a probe (#6) mounted through the pipe wall. The air stream was then split into two streams, one stream being discharged to the atmosphere through a 3 inch nominal gate valve (#7), the other stream continuing into the system piping. Another 3 inch nominal gate valve (#8) was used in conjunction with valve (#7) to control the amount of air introduced into the system. An Elster model Q160 turbinometer (#9) was used to measure the amount of air introduced into the system.

3.2.1.2 Solids Delivery System. Solids were introduced into the system using a screw type feeder. The feeder is shown in Figure 3-9. The feeder was based on the feed hopper and motor drive assembly taken from an MSA model Bantam 400 rockdust distributor. A hopper bin was constructed from a 55 gallon steel drum with an aluminum cone cemented to the inside. The drum was attached to the top of the feed hopper. The combination feed hopper, drum and motor assembly were mounted on a unistrut frame.

The original motor design called for a constant motor speed of 1750 rpm at a voltage of 128 VDC and a current of

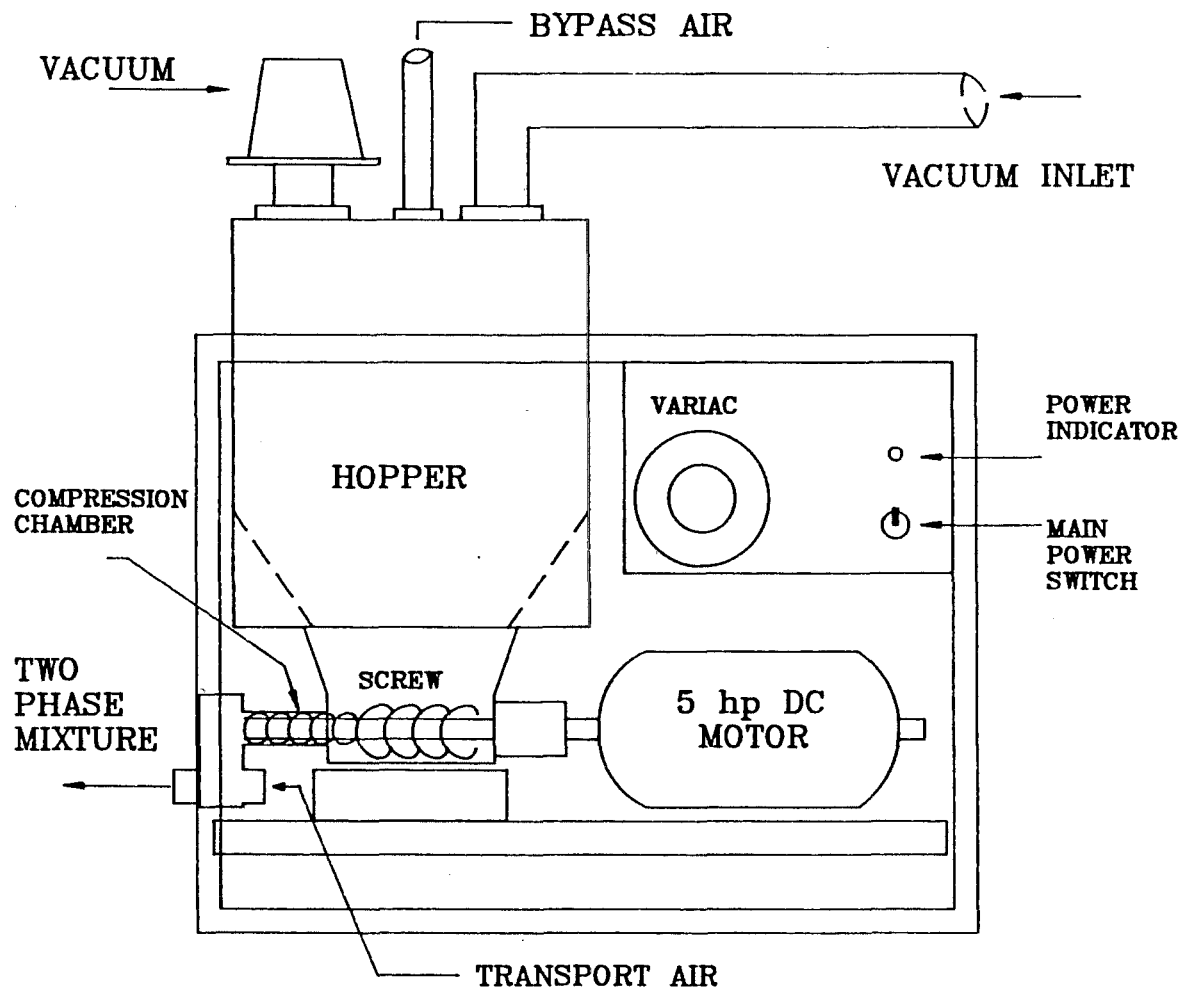


Figure 3-9: Solids Feeder in the Full Scale System

39 A. In order to operate the feeder at different feed rates, a variable speed drive had to be constructed. This drive consisted of a 115 V rectifier circuit to operate the motor field and a variable rectifier circuit to operate the armature circuit. Details of the motor drive are contained in Appendix C.

3.2.1.3 Piping. Piping for the two phase section of the full scale system was primarily of copper tubing with an inside diameter of 0.0504 m. The piping layout is shown in Figure 3-10. Selection of copper tubing was made to eliminate problems of electrostatic discharges which were found to be generated using PVC piping. Two glass viewing sections were inserted in the system. The first of these was a 0.9 m long section immediately following the solids feeder. This section was inserted to observe the two phase flow at the beginning of the acceleration region of the system. The second glass section of pipe was a 2.4 m section inserted prior to the collection system. This section was used to observe the fully developed flow as well as to provide a non-conducting pipe section for use of magnetic coil probes for particle velocity measurement. The final piping element in the system was a flow splitter similar to that used in the bench scale system. This flow splitter was 1.2 m in length and constructed of copper pipe with a stainless steel separator.

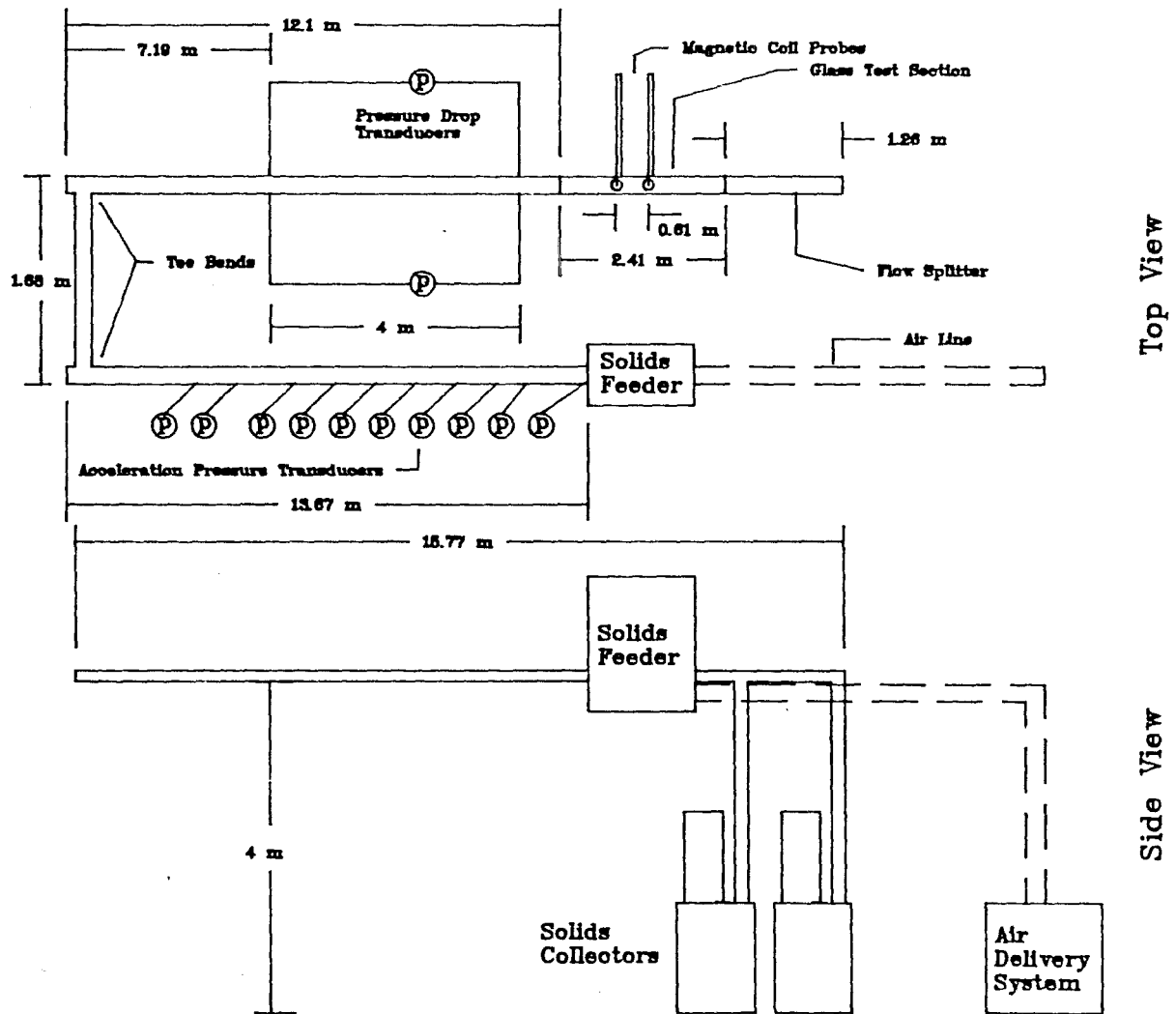


Figure 3-10: Piping Layout in the Full Scale System

Piping from the air delivery unit to the solids feed point was entirely of schedule 40 PVC pipe with an inside diameter of 0.0508 m.

3.2.1.4 Solids Collection. Solids from the two phase mixture were collected in two collection tanks, one for the solids from the lower half of the pipe and one for the solids from the upper half of the pipe. The tanks were standard 55 gal drums with pipe unions attached through their lids for easy connection/removal from the system. Also attached to the lids of each drum was a 1.2 m long section of 1.8 m ID PVC pipe. This pipe was used to reduce the velocity of the air and allow for the settling of the solids in the drums. Paper filter bags were attached to the tops of these pipes to prevent the discharge of fines. Cloth filter bags were placed over the paper bags to prevent gross solids discharge in the case of a rupture in the paper filter bags. By weighing the drums before and after each experimental run, the mass flow of solids in both the upper and lower halves of the pipe was determined. A Circuits and Systems model SX-501 platform scale was used to weigh the drums. A deviation in the actual scale reading was found to exist and the scale was calibrated using known weights. The calibration is given in Appendix C.

3.2.2 Operation

Operation of the full scale system required three operators, one for operation of the computer data acquisition, one for monitoring the air flow rates and humidity, and one for operation of the solids feed system. To start an experimental run, the blower was turned on and the air flow rate adjusted to the desired level. As the actual air flow rate was obtained through timed measurement of the turbine meter, a short BASIC computer program was written to approximate the air flow rate by pressure drop measurement. Once the desired air flow rate was set, the relative humidity of the air was adjusted to above 70 percent except in the case of the iron oxide particles, in which case it was kept as low as possible, typically less than 40 percent. Once the humidity was adjusted, collection of data for the air only condition was started. This included the air flow rate from the turbine meter and pressure drop measurement from the transducers. Once the required data was obtained, the solids flow to the system was started and the time for the solids flow rate was begun. Solids were run for 30 seconds prior to the start of pressure drop and velocity data collection. Pressure drop and then particle velocity data were then obtained using the computer. The air flow rate was again taken while solids were being introduced to the system. Once the required data

was obtained, the solids feed was turned off and time for solids flow stopped. The air to the system was then turned off. The two solids collection drums were then weighed and the solids flow rates for the upper and lower halves of the pipe calculated. The cross-correlation of the signals from the two sets of probes was performed using the computer. The solids were then returned to the feed hopper using the vacuum system and the system was prepared for the next experimental run.

3.3 Computer Interface

Primary data acquisition was accomplished using an IBM-AT personal computer. Programming was done using the Microsoft Quickbasic Compiler. Pressure and velocity data was acquired through analog to digital conversion of signals from transducers and probes. Other data such as air flow rate, solids flow rate, relative humidity, and constant parameters were input through the computer keyboard. The BASIC programs used are included in Appendix D.

3.3.1 Simultaneous A/D Conversion

The A/D converter used for data acquisition was a Data Translations Model DT2818 Simultaneous Sample and Hold converter. This converter was chosen due to its capacity to obtain four analog signals simultaneously. Although the four signals are multiplexed through a single A/D converter,

each signal is first captured and held in a hold amplifier prior to being multiplexed. The importance of this feature is in the measurement of velocity where a cross-correlation between signals is performed in time. As the signals are acquired simultaneously, (at least within the 9 nanosecond acquisition time error), the cross-correlation is void of channel to channel acquisition time errors. The DT2818 was mounted inside the IBM-AT computer in a single expansion slot. A Data Translations Model DT707 Screw Terminal Panel was used to make connections of the analog signals. This screw terminal panel was connected to two series of four BNC connectors which could be independently switched to allow four analog inputs from either series of connectors. Technical details of the DT2818 and DT707 are included in Appendix C.

3.3.2 Particle Velocity Measurements

As mentioned previously, particle velocity measurements were accomplished using a cross-correlation technique. This technique has been used in various configurations with different types of probes.^(4,5,6,7,49,50) Two different probes were used in this study. The first type is a modification of the electrostatic ring probe described by Smith and Klinzing⁽⁴⁾ where a ring of conductive material is placed in contact with the flowing suspension and the

fluctuation in charge produced by particle/conductor contact is measured and cross-correlated to obtain the particle velocity. The modification to the single ring probe was to split the ring into two separate sections separated by an electrical insulating material. The probes used were made of free-spinning aluminum and the conductor was a composite fiber. The two aluminum halves were connected together using nylon screws. A screw terminal was made on each half of the probe. The split ring probe was shown in Figure 3-5. Two of these probes were used in the 0.0266 m diameter bench scale system to obtain particle velocities in the upper and lower halves of the pipe.

The second type of probe used was a magnetic coil probe.⁽⁵¹⁾ This probe was constructed from the magnetic coil element from a solenoid valve. Four probes were attached to the pipe in a two up/two down configuration using plastic tape. This probe was used in the 0.0508 m diameter full scale system and for verification of the cross-correlation technique discussed in Section 3.1.1.

Both types of probes produced signals which were measured and amplified using four Keithly Model 610C Electrometers. The output from the electrometers was a voltage signal ranging from -3 to +3 volts. The

electrometer outputs were connected to the four channels of the DT2818 A/D converter.

The signals from the four probes were processed using the BASIC computer program named PROBE. This program is included in Appendix D. PROBE was written to accept system constants, accept keyboard input variables, collect two or four signals from the velocity probes, cross-correlate the velocity signals, and continuously append an output data file. PROBE produced screen graphics for the signals obtained as well as screen graphics of the cross-correlations of one or two sets of signals. The signal graphics displayed a window of 2400 msec. An example of this screen is shown in Figure 3-11. The cross-correlation was performed on a user defined window. An example of the cross-correlation graphics screen is shown in Figure 3-12.

3.3.3 Pressure Measurements

The primary pressure measurements on both the bench scale and full scale systems were made to assess pressure drop along the pipe axis. Voltage output signals from two Omega model PX164 strain gauge type pressure transducers were input to the computer through the DT2818 interface. The range of these transducers was 0 - 2480 Pa differential with an output signal of 1 to 6 volts.

To convert the voltage output of the transducers into a pressure reading, a computer program called PRESSURE.BAS was

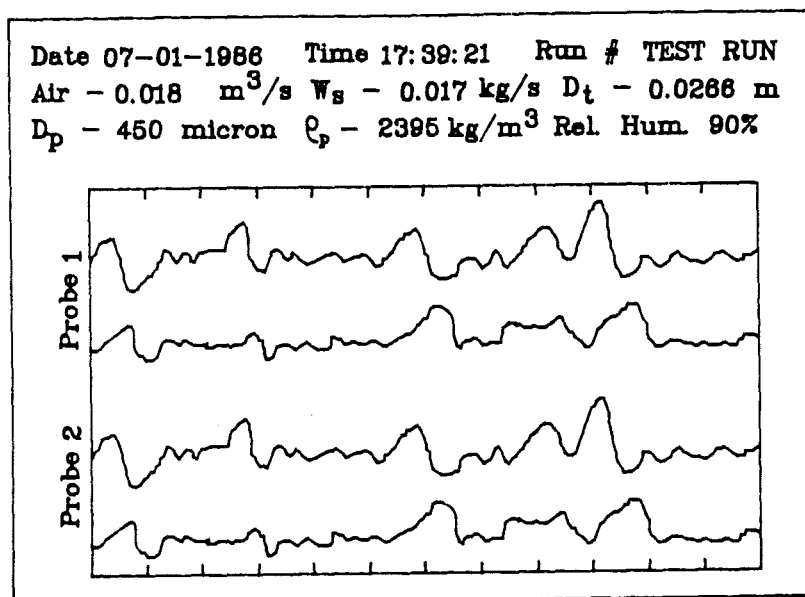


Figure 3-11: Example Computer Screen Output of Velocity Signals Using the Computer Program PROBE.BAS

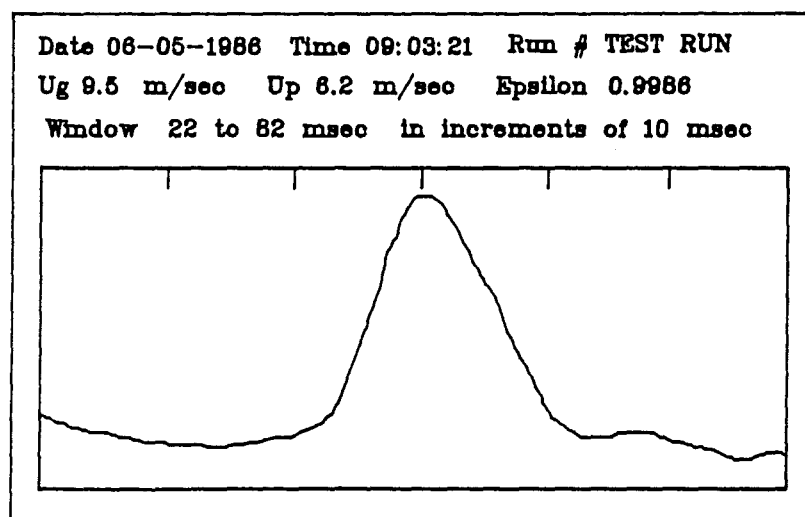


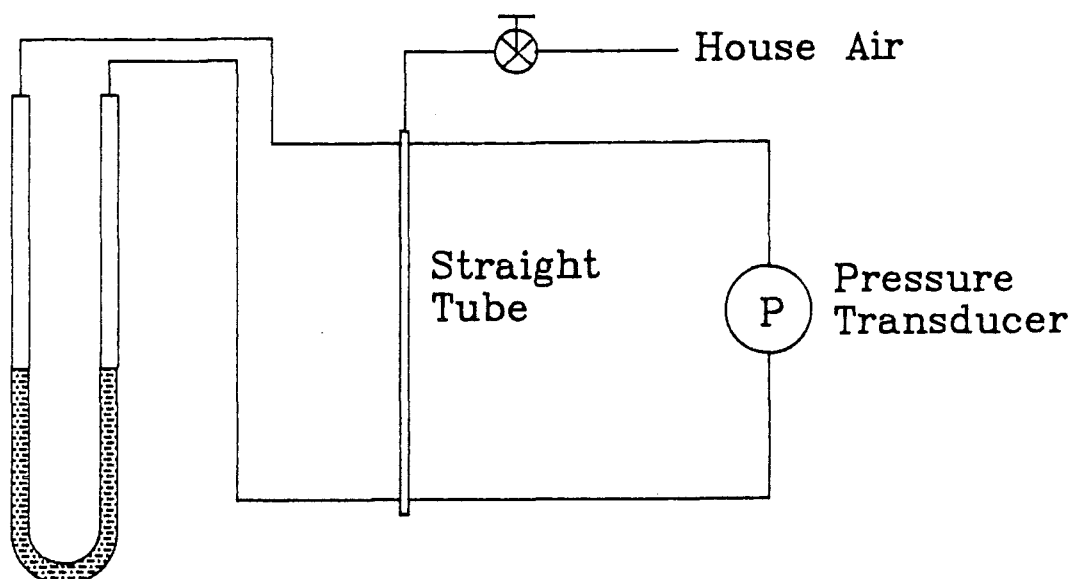
Figure 3-12: Example Computer Output Screen from Cross Correlation of Velocity Signals Using PROBE.BAS

written. This program is included in Appendix D. The program was written to allow calibration of the transducers as well as record pressure readings. Calibration of the transducers was accomplished using a water manometer calibration system shown in Figure 3-13.

Due to the nature of the air delivery system in the 0.0504 m full scale system, the pressure measurement for air alone for a given experimental run was not obtained at the same volumetric air flow rate as when solids were added to the system. This was caused by both the blower characteristics and the use of a bypass valve to control the air flowrate. Experimental pressure drop data for the flow of air without solids was obtained, and a correlation of this data with U_g was determined. The correlation is included in Appendix C.

3.4 Solids Particles Used

Six different solids particles were originally chosen to be used in the experiments. Three of these were glass particles of different sizes with approximately the same densities, two were lower density plastics, PVC and methyl methacrylate, and the last was iron oxide, with a relatively high density. The use of the plastic particles was



Water Manometer

Figure 3-13: Pressure Transducer Calibration System

discontinued due to electrostatic charging which occurred with these particles. This will be discussed in more detail in section 4.

The size of the particles was determined using an Omicron Image Analyzer and the analysis method of Chi⁽⁵²⁾. Terminal velocities were calculated using the computer software package NUMODES⁽⁵³⁾. Densities were measured by adding a known mass of water to a sample of solids and measuring the volume and mass of the mixture. The mass and volume of the water were then subtracted and the density of

the solids obtained. The characteristics of the solids are given in Table 3-1.

Table 3-1
Characteristics of Solids Particles Used

Material	ρ_p (kg/m ³)	D_p (μ m)	Shape	U_t m/s
Glass	2470	67	Sphere	0.46
Glass	2395	450	Sphere	3.97
Glass	2464	900	Crushed	7.45
Iron Oxide	5004	400	Flake	5.87
PVC	1178	137	Roughly Spherical	0.61
Methyl Methacrylate	1251	127	Roughly Spherical	0.59

4.0 ANALYSIS OF RESULTS

The results of the experimental work will be divided into three categories:

1. General Results
2. Application of the Thermodynamic Analogy
3. Other Results

A representative sample of figures will be presented in the text, while the remainder of the figures are included in Appendix A. Tabulated data is included in Appendix E.

4.1 General Results

Certain general results are common to most studies in pneumatic transport and these will be discussed first. These general results fall into the following three categories:

1. Flow Visualization
2. Pressure Drop per Unit Length
3. Particle Velocity

As mentioned earlier, experimental results from various studies can vary considerably. This is most likely due to the various complexities which are associated with gas-solids flows; such as, particle distributions in both size and shape, electrostatic forces, difficulties in measurements, and the general layout and operation of equipment. All of these complexities were experienced to

some degree in the experiments conducted for this study and their significance was of singular importance in some cases.

4.1.1 Flow Visualization

Test sections in both the 0.0266 m and 0.0504 m diameter systems were made of glass, allowing observation of the flow for each experimental run. Flow patterns in each system in the range of gas velocities and solids flow rates studied fell into three basic regimes:

- (1) Apparent Homogeneous Flow
- (2) Non-Homogeneous Suspended Flow
- (3) Separated or Strand Flow

Degrees of saltation were also observed; however, saltation in the test section generally indicated an unsteady flow condition and results for these conditions are not considered here.

An excellent description of visually observed flow patterns was given by Richardson and McLeman⁽⁵⁴⁾ and these patterns have been used by many investigators in their analysis. Their observations in steady flow are incomplete however. They describe a "uniform suspended flow pattern with particles evenly distributed over the cross-section of the pipe." Measurements of the mass flow distribution between the top and bottom halves of the pipe indicate that a truly homogeneous flow is a very singular condition based

on gas velocity, particle characteristics, and pipe size. This is the reason for the description of apparent homogeneous flow given above. Cases where mass flow ratios between the upper and lower halves of the pipe were as low as 0.4 visually appeared to be entirely homogeneous.

Richardson and McLeman indicated a second flow pattern observed prior to flow patterns generated by deposition of particles as a "Non-Uniform Suspended" flow where "particles tend to concentrate in the lower half of the pipe." This flow condition should be separated into two distinct classes, the first of which is non-homogeneous suspended flow. In this condition, the upper half of the pipe is visually less dense than the bottom of the pipe, yet there is no discontinuity between the top and the bottom of the pipe. As will be discussed later, particle velocities between the upper and the lower halves of the pipe do not differ significantly. The second class of flow is the separated or strand flow. This type of flow has been investigated by Molerus⁽⁵⁵⁾ and can be described by a discontinuity between an upper and lower flow, the upper flow being dilute with the lower flow being dense. A fairly clear interface exists between the two phases. This flow should not be confused with flow over a bed of particles as the lower phase is continuously moving, giving the appearance of a strand of particles flowing along the bottom of the pipe. Under some conditions, packets of solids,

loosely termed slugs, were incorporated in the strand. These packets were not always continuous and were associated with discontinuities near the feed. The three flow patterns described above are shown in Figure 4-1.

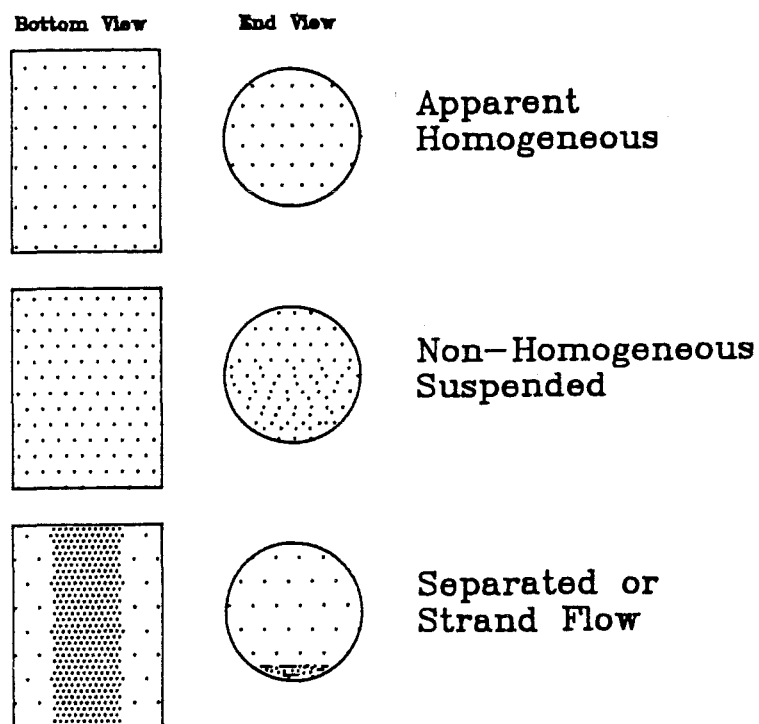


Figure 4-1: Observed Flow Patterns

A separate flow pattern was observed when PVC particles were transported in the 0.0504 m system. This flow pattern is shown in Figure 4-2. This pattern was a direct result of electrostatic forces generated in the system. The waves seen in the photograph traveled in the opposite direction of the gas flow. Whether this movement was actual or simply apparent due to a standing wave being set up is unknown. A central core of solids was transported in the direction of the gas flow. It is believed that the formation of this pattern as well as the traveling nature of the surface waves was caused by an electric potential being formed across the glass test section. A study of electrostatics conducted by Allyn⁽⁵⁶⁾ indicated a removal of electrostatic charge at relative humidities above about 70 percent. Allyn's study was conducted with glass beads on Plexiglas pipe. The flow pattern shown in Figure 4-2 was obtained at a relative humidity between 65 and 70 percent. An increase of relative humidity to over 70 percent caused the complete elimination of the surface wave pattern and the apparent removal of electrostatic charge.

4.1.2 Pressure Drop per Unit Length

The pressure drop across a pneumatic system is the ultimate goal in design of these systems as it determines the energy requirements. As the gas velocity is decreased

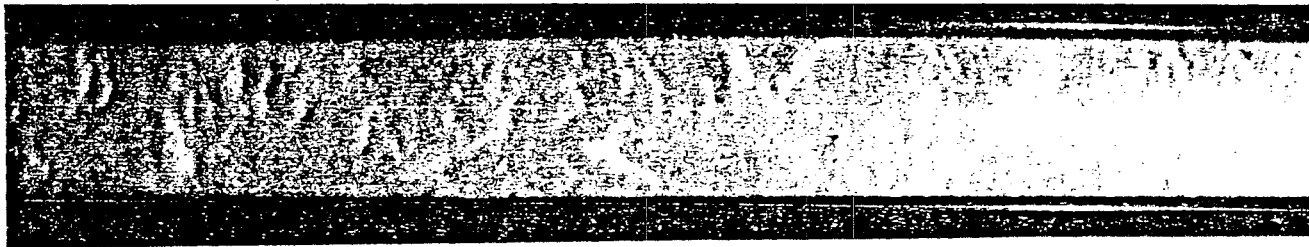
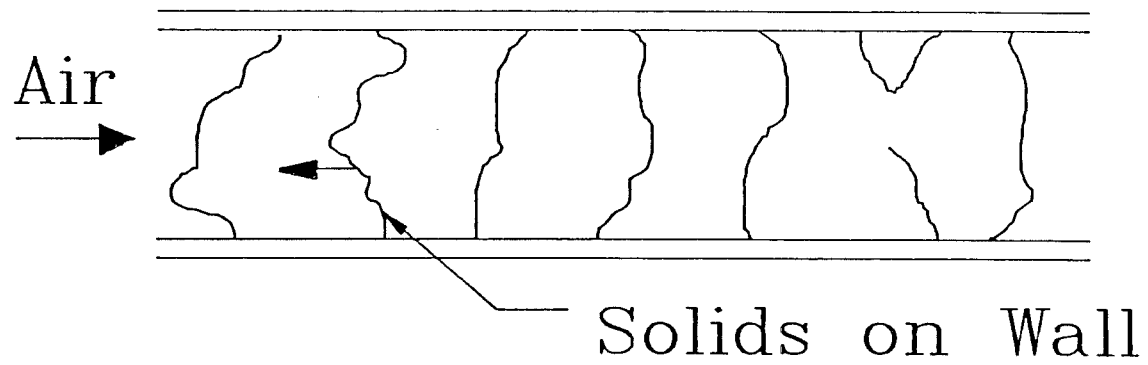


Figure 4-2: Flow Pattern Observed When Flowing PVC in 0.0504 m Diameter System Caused by Electrostatics

in a horizontal pneumatic flow, the additional pressure drop due to the solids presence decreases steadily until a point is reached where the continued decrease in gas velocity causes saltation of the particles. A plot of the pressure drop per unit length vs. gas velocity at constant solids flow rate is the most common representation of the behavior of a pneumatic system.

4.1.2.1 The Zenz Type Phase Diagram. The pressure drop vs. gas velocity at constant solids flow rate diagram is commonly referred to as the Zenz⁽⁵⁷⁾ type phase diagram in pneumatic conveying. Its utility in design is such that it provides the energy requirements as well as the volumetric flow rate of gas for various solids flow rates. For horizontal pneumatic conveying, Zenz⁽⁴¹⁾ reported a sharp discontinuity at the point of saltation, whereby an increase in pressure drop across the system was solely due to the formation of a layer of stationary particles formed on the base of the pipe causing a new steady state at a reduced cross-sectional area for flow. Others^(11,12,40) have described a not so abrupt increase in the pressure drop in varying degrees of saltation. Zenz attributed the not so abrupt increase to a failure to achieve steady state conveying. The two descriptions are shown in Figure 4-3. Both of these descriptions were observed in this study and a possible explanation lies in the lengths and diameters of

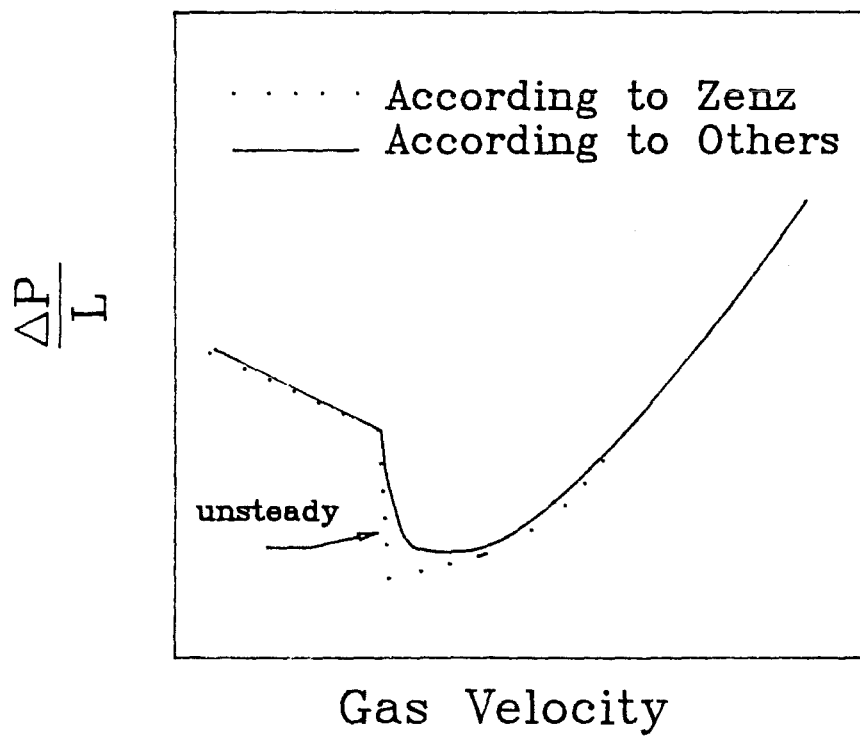


Figure 4-3: Zenz Type Phase Diagram with Two Behaviors Reported to Exist

the systems studied. Figure 4-4 is a plot of pressure drop vs. gas velocity for the 0.0266 m diameter system using 450 micron glass beads. The increase in pressure drop at the lower gas velocities did not correspond to a sedimentary layer forming across the test section. Pulsations in the form of sliding dunes and a sliding layer corresponding to strand flow are the reasons for the increase in mean pressure drop. The corresponding data for the 0.0504 m diameter system (Figure 4-5) shows no increase in pressure drop for the system at low gas velocities. This can be attributed to the blower characteristic curve and the use of a throttle valve for controlling the gas flow rate. Matsumoto, et. al.⁽⁵⁸⁾ have given a description of the stability of this type of system, which can be simply put that an increase in pressure in the system causes a decrease in the volumetric flow of the gas. At the lower end of the pressure vs. gas velocity curve, any increase in pressure causes a decrease in gas velocity and subsequently a further increase in pressure. This ultimately results in the system completely plugging. Observations at the feed point in the 0.0504 m diameter system showed that the acceleration region in a horizontal system is of key importance to the operation of the rest of the system. Deposition of particles at the feed point was observed in the 0.0504 m diameter system similar to what Zenz described, except that the deposition

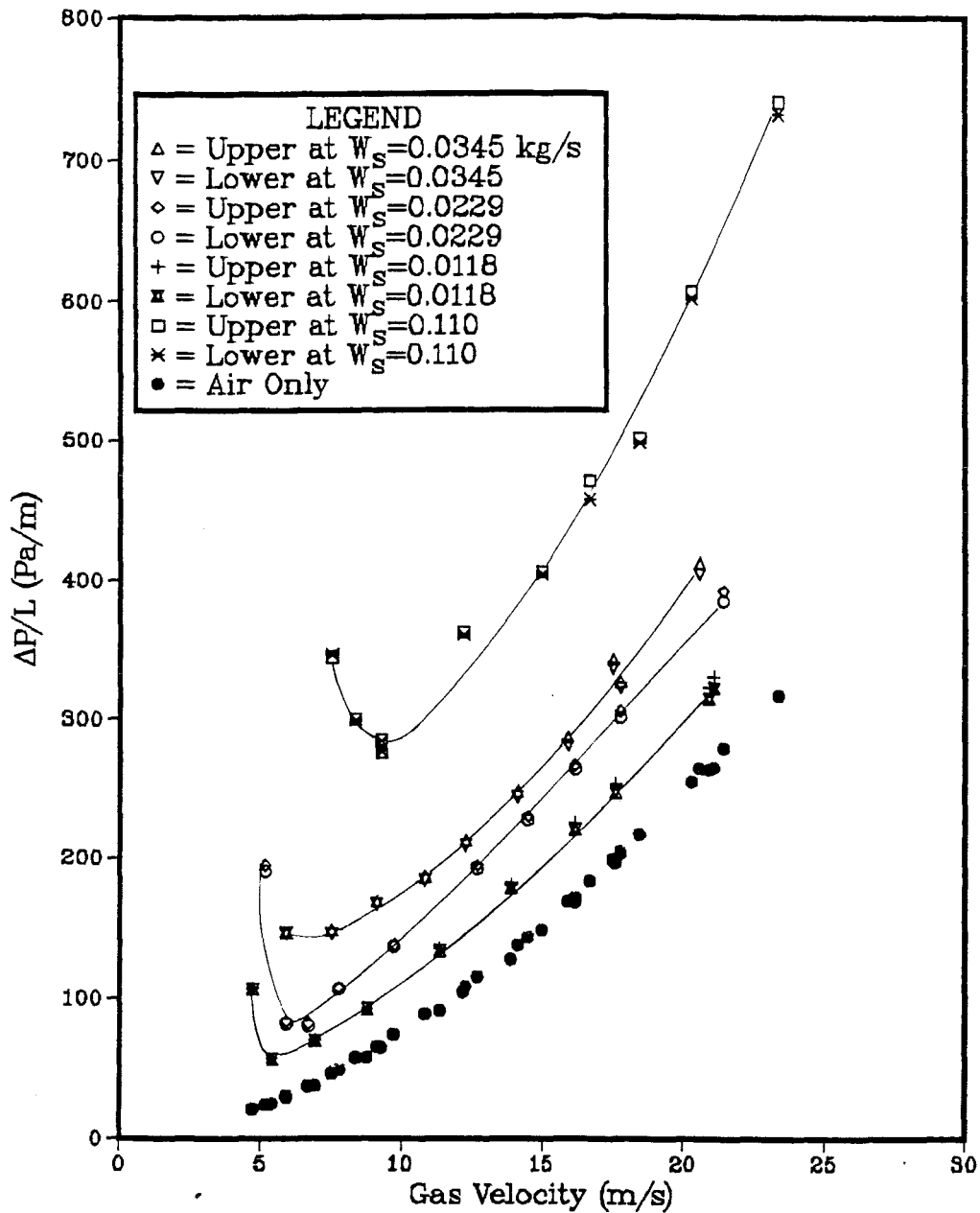


Figure 4-4: Pressure Drop vs. Gas Velocity for the 0.0266 m Diameter Bench Scale System Using 450 μ m Glass Beads

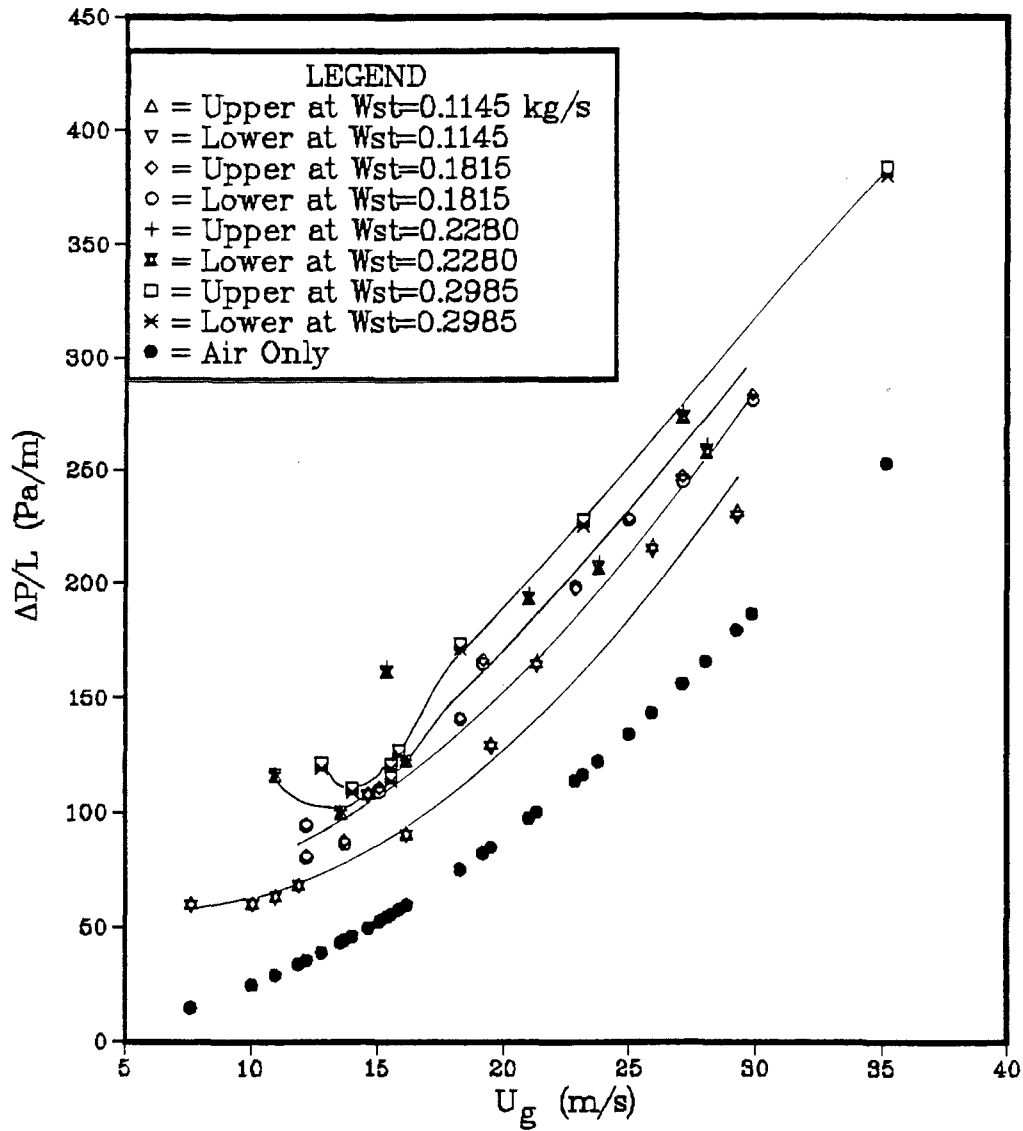


Figure 4-5: Pressure Drop vs. Gas Velocity for the 0.0504 m Diameter Full Scale System Using 450 μ m Glass Beads

occurred for a specific length. This is shown in Figure 4-6. Further decrease in gas velocity caused this deposition to lengthen. For a given deposition at the feed point, the test section, which was well away from the acceleration zone, remained in a steady flow condition. The pressure drop vs. gas velocity curve for the system at the beginning of the acceleration zone for one condition is shown in Figure 4-7⁽⁵⁹⁾. This appears to be the condition that Zenz⁽⁵⁷⁾ described. A comparison of the length of the system from which Zenz acquired his data shows that the data was probably very much influenced by the acceleration region. His pipe diameter was 0.0445 m, while the test section was located 1.22 m from the feed point, and was only 1.12 m long. This entire length would approximately extend to the 6th acceleration pressure tap on the 0.0504 m diameter system. The mass flow rates used by Zenz were approximately the same as used in this study. The characteristic curve of the blower was not given. Zenz⁽⁴¹⁾ also states that the length of time necessary for the system to attain a steady state near the point of saltation can be as long as 4 hours or more. Although the times for each run in the 0.0504 m section were much shorter than this, a lengthening of the salted layer near the feed during a run which did not completely plug the pipe was not observed. As stated before, a system near saltation which employs a

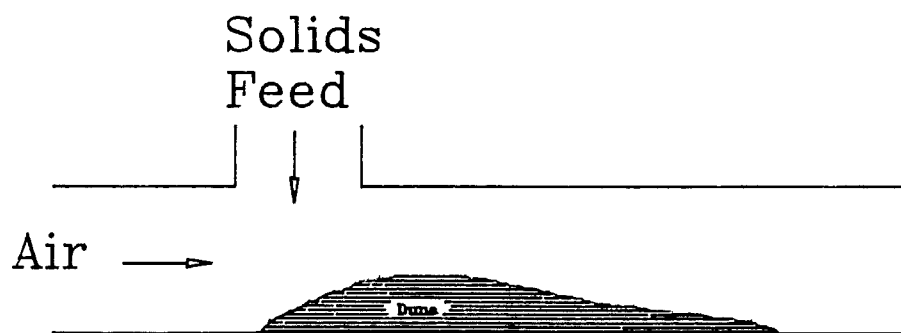


Figure 4-6: Layer of Deposited Solids Formed at the Feed Point

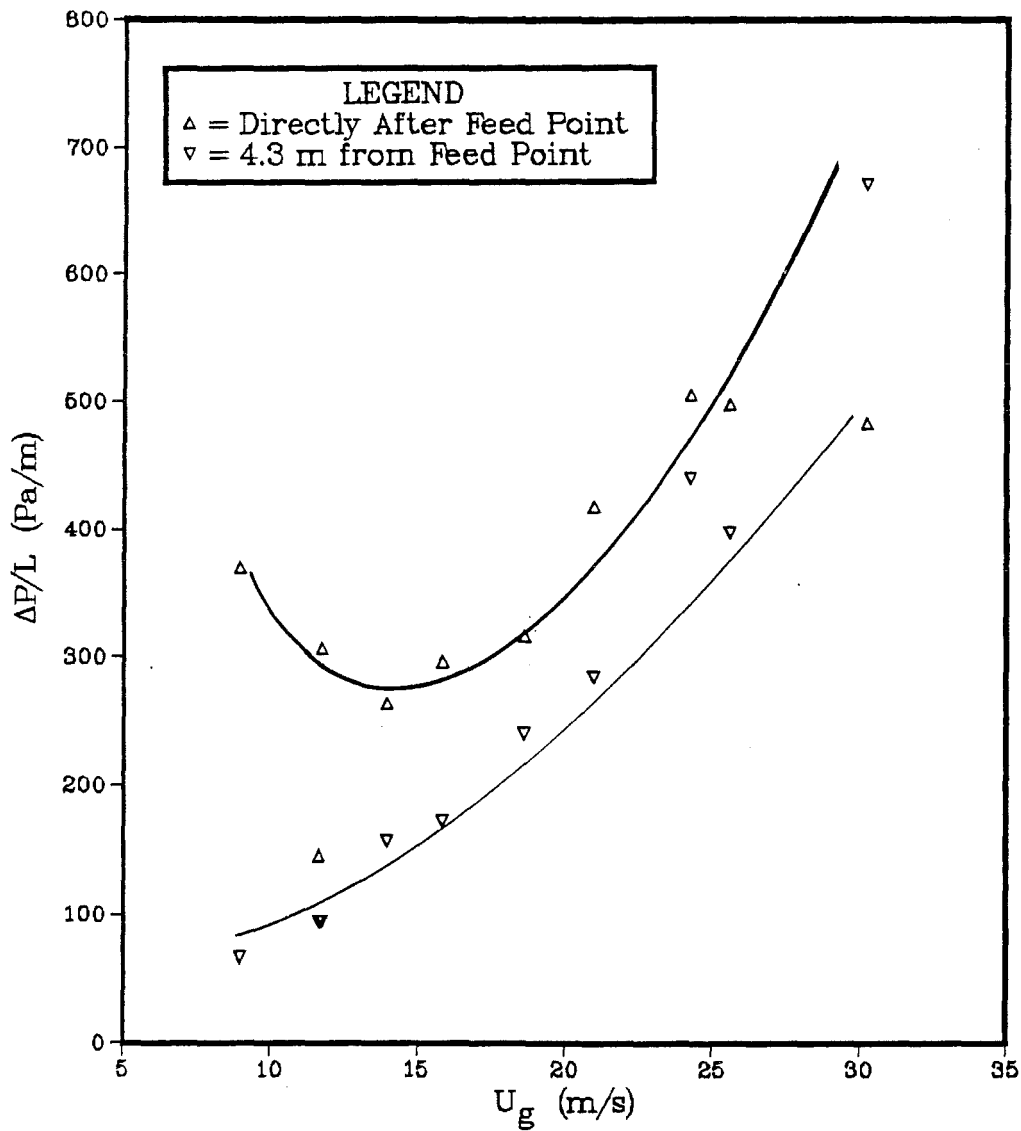


Figure 4-7: Pressure Drop vs. Gas Velocity in the Acceleration Zone from Dhodapkar⁽⁵⁹⁾

blower/fan and/or a throttling valve is inherently unstable near saltation and small fluctuations in the feed of solids or the air supply itself may trigger the complete or partial plugging of the system.

4.1.2.2 Comparison to Correlations. A comparison of the experimental pressure drops was made with three existing methods of prediction. The chosen methods were:

1. The correlation of Konno, Saito, and Maeda ⁽⁶⁰⁾
2. The correlation of Yang ^(61,62)
3. The method of Weber ^(10,63)

The correlation of Konno, Saito and Maeda is basically a Froude number/loading combination which has been used by many investigators. It does not include any lift term specifically. The correlation is given as:

$$\frac{\Delta P_s}{L} = 0.33 \frac{U_g}{(gD_t)^{0.5}} \rho_f \mu \quad (4-1)$$

The simplicity of this correlation is obvious. A comparison between the experimental and calculated pressure drops is given in Figure 4-8. As can be seen, the data is fairly well correlated but underpredicting for most conditions.

The second correlation is that proposed by Yang ^(61,62) and it is based on a balance of drag and frictional forces. Three equations must be solved simultaneously to obtain a

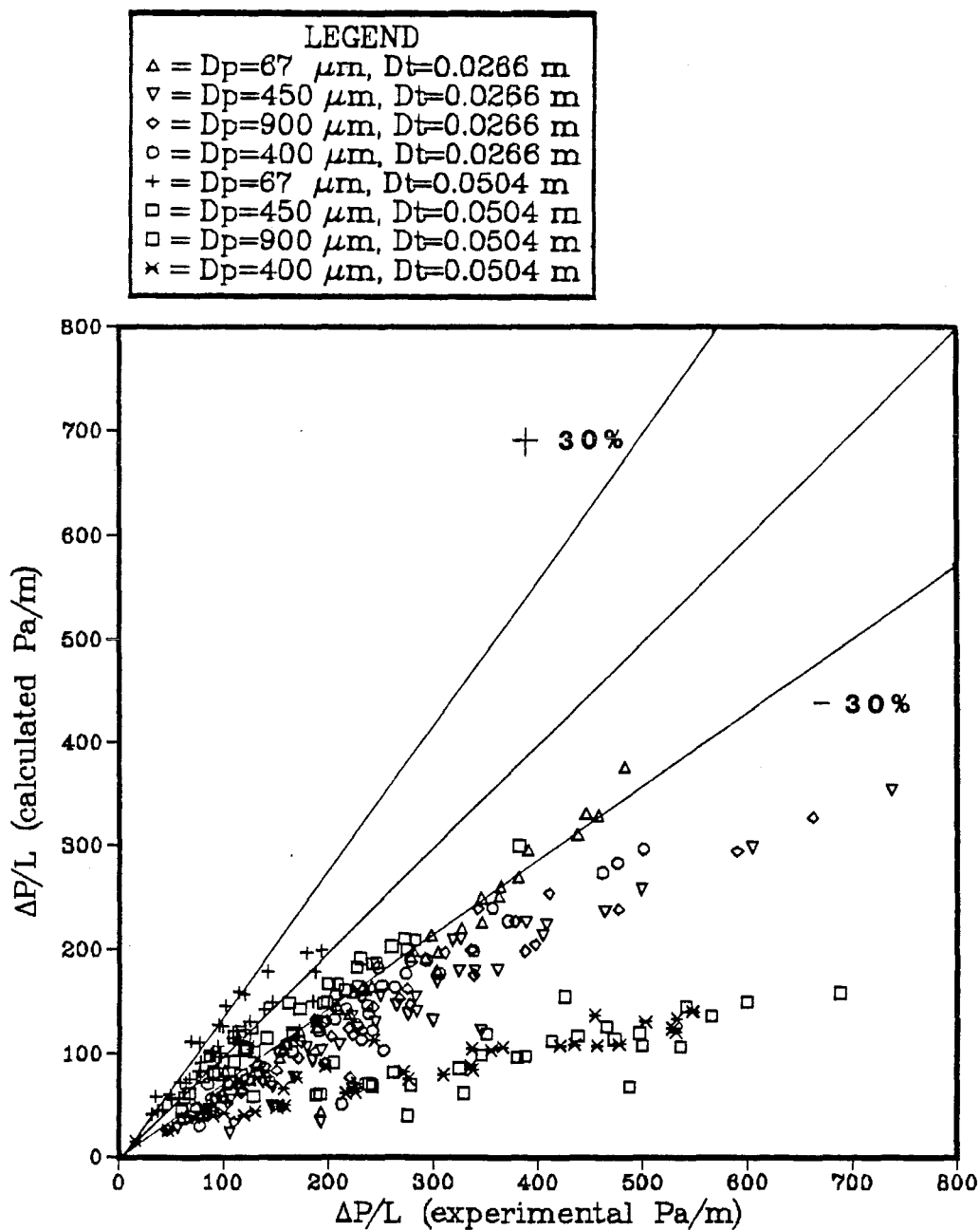


Figure 4-8: Comparison of Pressure Drop Calculated Using the Correlation of Konno, Saito, and Maeda (60) and the Experimental Pressure Drop

calculated friction factor, particle velocity and void fraction. The three equations are:

$$\epsilon = 1 - \frac{W_s}{A_t \rho_p U_p} \quad (4-2)$$

$$U_p = U_f - U_t \left[\left(1 + \frac{2f_s U_p^2}{gD_t} \right) \epsilon^{4.7} \right]^{0.5} \quad (4-3)$$

$$f_s = 0.0293 \frac{1-\epsilon}{\epsilon^3} \left[\frac{(1-\epsilon)U_f}{(gD_t)^{0.5}} \right]^{-1.15} \quad (4-4)$$

Solution of these equations was done by successive substitution on an IBM PC computer. The results are shown in Figure 4-9. Cases in which calculations failed to converge after 250 iterations were not included.

The final method of pressure drop prediction is that of Weber^(10,63). This method incorporates a lift term which was originally proposed by Barth⁽¹⁰⁾. A seeming flaw to the use of this method is the requirement for experimental data to compute the frictional forces. It is not clear from the German literature whether friction factor correlations are generally used or if experimental studies are the accepted practice when designing pneumatic systems. The additional pressure drop due to the solids is given as:

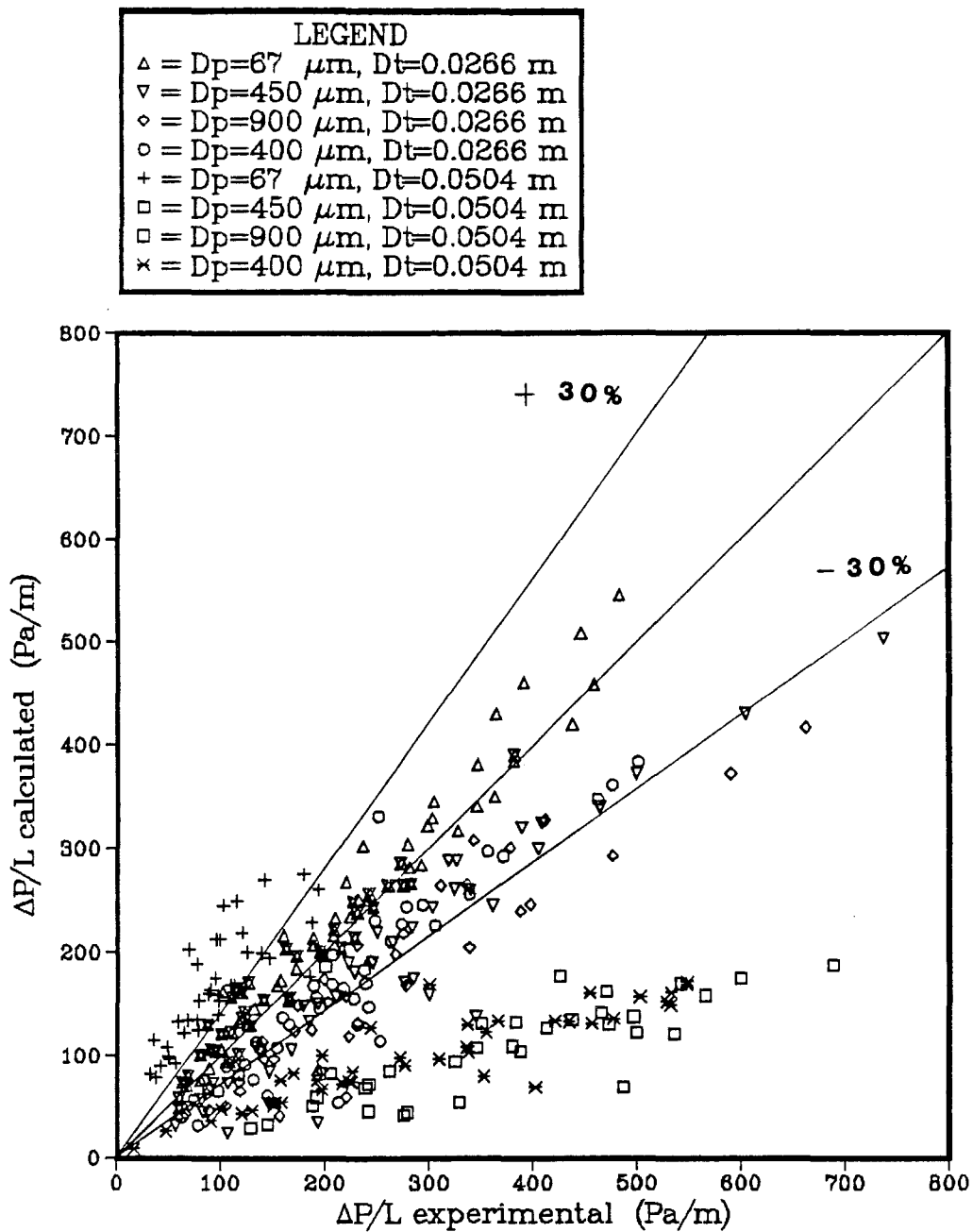


Figure 4-9: Comparison of Pressure Drop Calculated Using the Correlation of Yang (61,62) and the Experimental Pressure Drop

$$\frac{\Delta P}{L} = \frac{\mu \lambda_s \rho_f U_g^2}{2D_t} \quad (4-5)$$

with the following correlation provided for use when no experimental data is available:⁽⁶⁴⁾

$$\lambda_s = 2.1\mu^{-0.3} \frac{gD_t}{U_g^2} \left[\frac{gD_p}{U_t^2} \right]^{0.25} \left(\frac{D_p}{D_t} \right)^{0.1} \quad (4-6)$$

Results from this method are shown in Figure 4-10. This correlation also underpredicts for most conditions. It does not appear that the inclusion of the lift term of Barth provides any improvement in the correlation.

The combined results for the three correlations applied is summarized in Table 4-1. The standard relative deviation was calculated according to the equation 4-7.⁽⁶⁵⁾

$$SRD = \left[\frac{1}{(n-1)} \sum \left(\frac{x_{calc} - x_{exper}}{x_{exper}} \right)^2 \right]^{0.5} \quad (4-7)$$

The correlation of Konno, Saito and Maeda is seen to provide the least overall error. The explanation for this is that the Konno, Saito and Maeda correlation for pressure drop due to solids is simply a constant times the solids flow rate. It cannot predict saltation nor can it be expected to be accurate near saltation conditions.

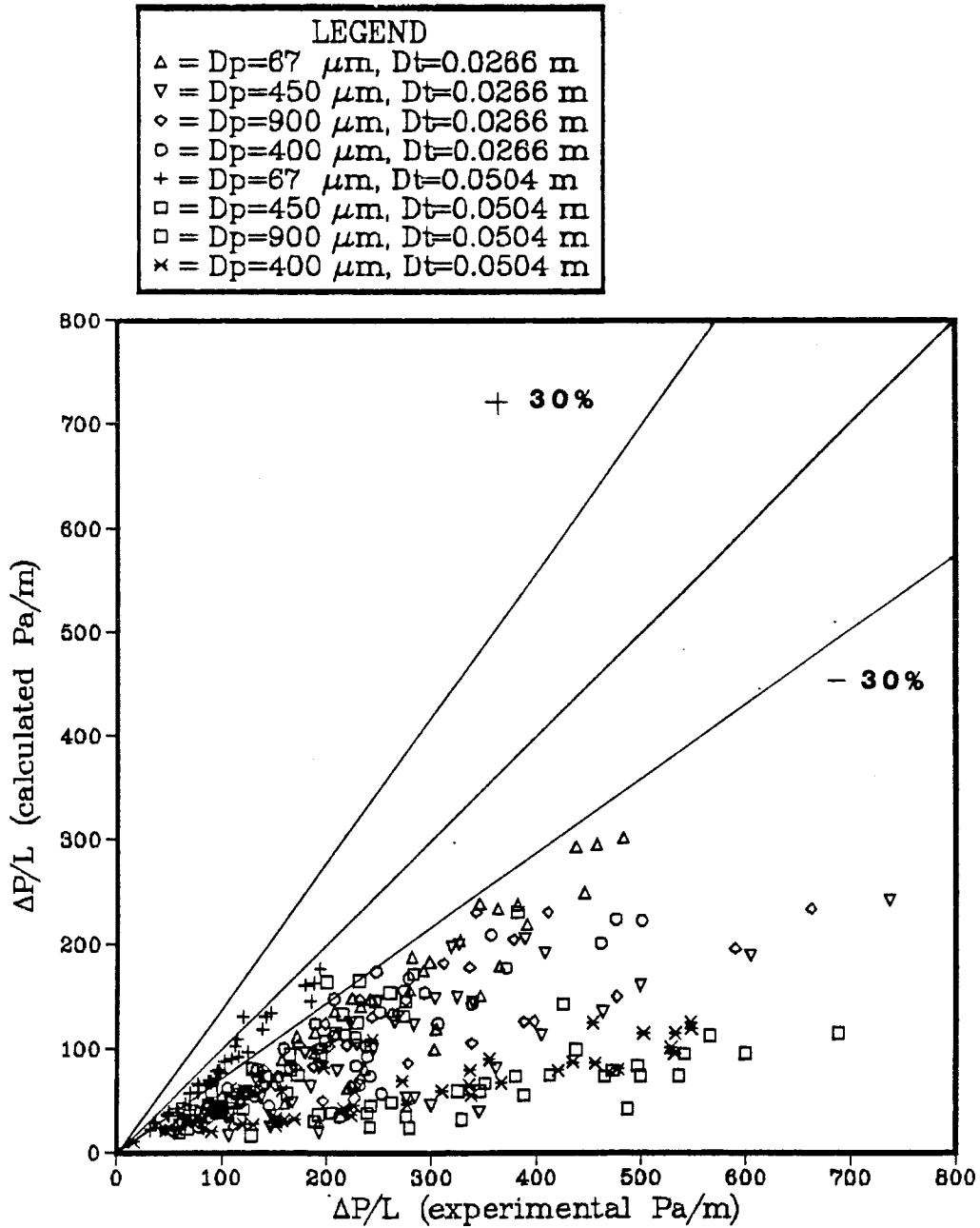


Figure 4-10: Comparison of Pressure Drop Calculated vs. the Correlation of Weber⁽⁶³⁾ and the Experimental Pressure Drop

Table 4-1

Standard Relative Deviation for Pressure Drop
Calculated from Three Methods

D_t (m)	D_p (μm)	Material	SRD (%) Konno, Saito and Maeda	Weber	Yang
0.0266	67	Glass	34.91	49.46	17.72
	450	Glass	50.47	65.47	35.07
	900	Glass	46.79	38.66	36.68
	400	Iron Oxide	40.76	54.32	30.60
0.0504	67	Glass	23.96	21.77	100.42
	450	Glass	19.95	51.98	18.76
	900	Glass	73.18	83.64	72.54
	400	Iron Oxide	68.96	77.14	65.06
Overall SRD			46.61	58.76	52.48

4.1.3 Particle Velocity

The particle velocity in a pneumatic system is probably the most difficult parameter to obtain experimentally. As mentioned previously, many methods have been devised to measure the particle velocity. Results from the use of the split electrostatic probe in the case of 450 micron glass beads in the 0.0266 m diameter bench scale system are shown in Figure 4-11. A slightly different representation of the same data is shown in Figure 4-12 which shows the ratio of

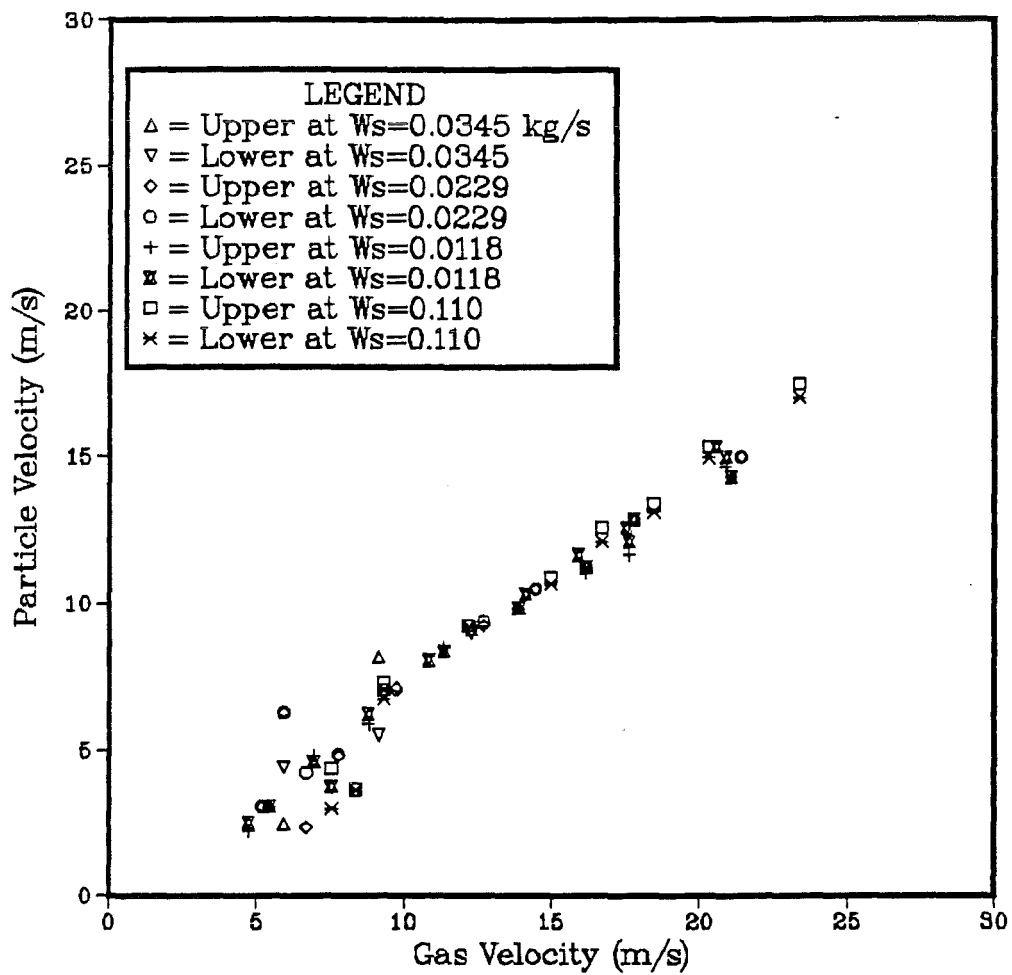


Figure 4-11: U_p vs. U_g for the 450 μm Glass Beads in the 0.0266 m Diameter Bench Scale System

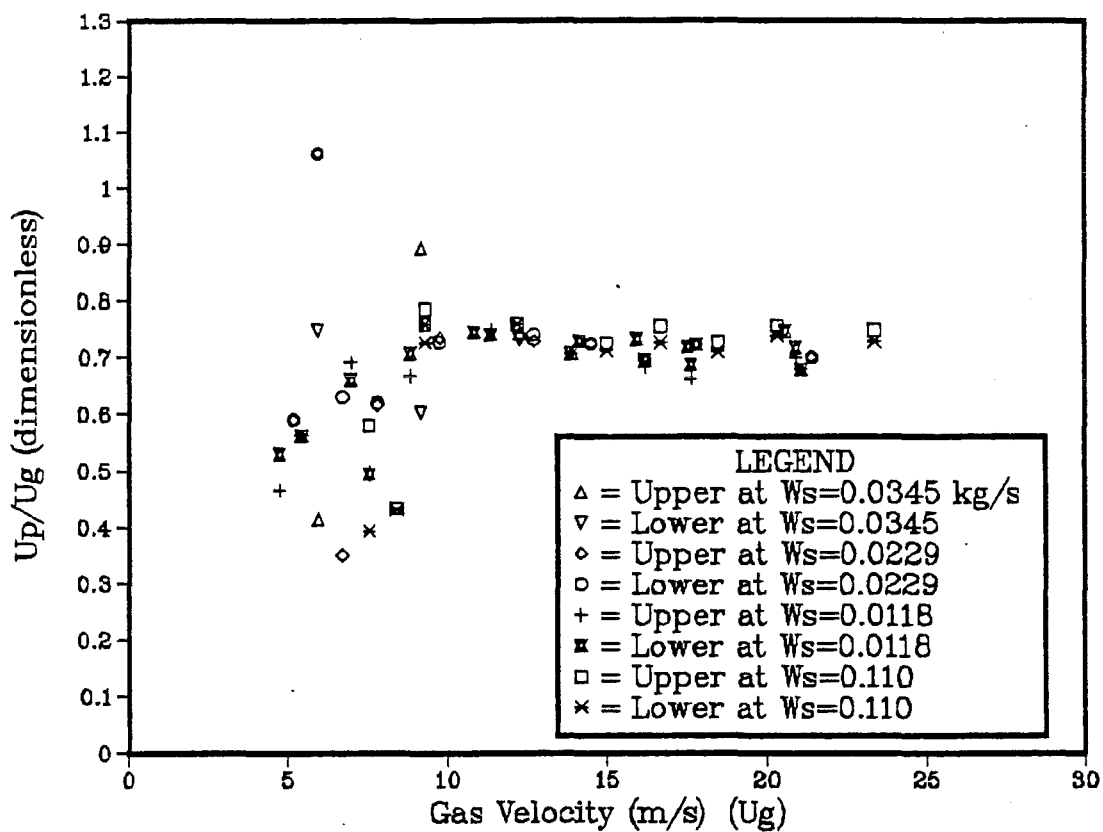


Figure 4-12: U_p/U_g vs. U_g for the 450 μm Glass Beads in the 0.0266 m Diameter Bench Scale System

particle velocity to gas velocity vs. gas velocity. From this figure is seen that the ratio of particle velocity to gas velocity becomes almost constant at high values of the gas velocity. This constant value has significance to the thermodynamic analogy to be discussed later. At lower values of gas velocity the particle velocity is seen to deviate from this constant value considerably. Two values of particle velocity were measured for each run, the upper half of the pipe and the lower half of the pipe. At high gas velocities, the two values are essentially equal, while at lower values of gas velocity, the upper half velocity is normally measured to be higher. This result should be compared to previous results such as those of Rizk⁽⁴⁰⁾ shown previously in Figure 2-3. Previous investigations have shown a decrease only in particle velocity to gas velocity ratio.

The results for the 0.0504 m diameter full scale system are similar except for the range of conditions. Results for the 450 micron glass beads in the full scale system are shown in Figure 4-13. Again, the ratio of particle velocity to gas velocity is seen to approach a constant value with increase in gas velocity. System restrictions prevented operation at higher gas velocities than those shown in Figure 4-13. This will be discussed further in Section 4.3.

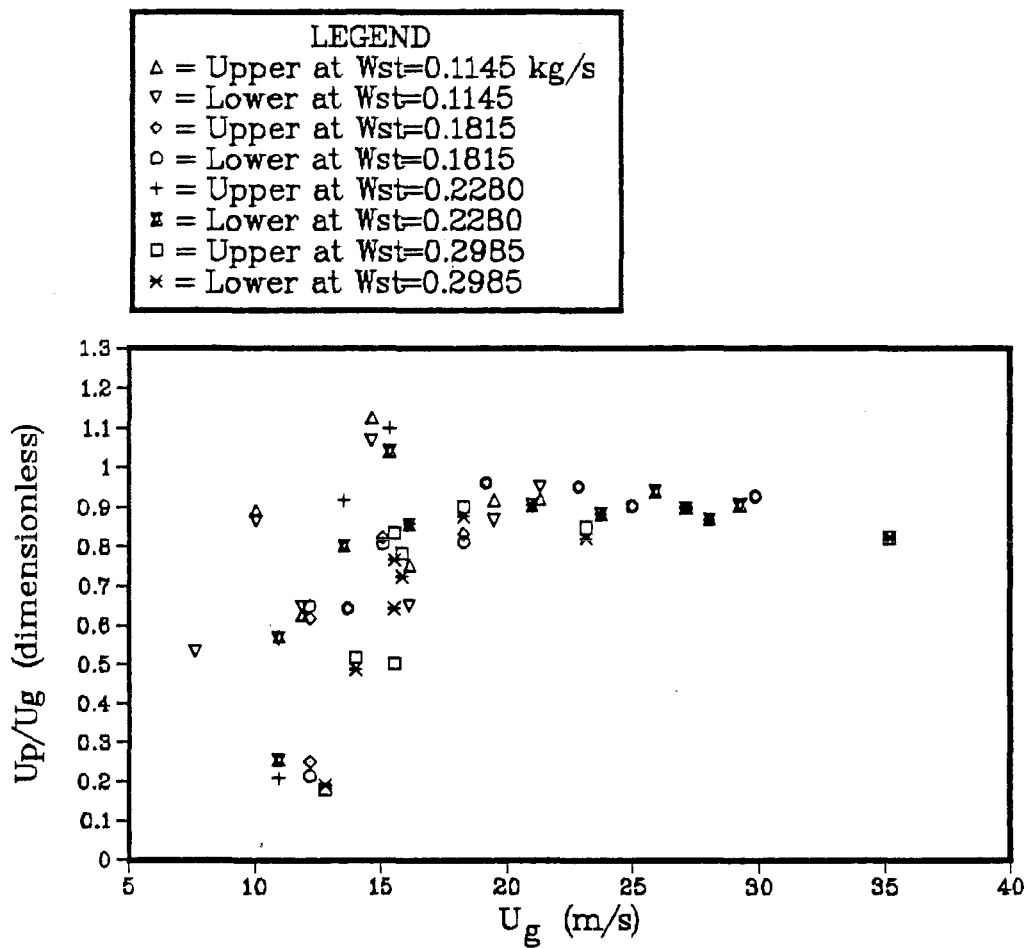


Figure 4-13: U_p/U_g vs. U_g for the 450 μ m Glass Beads in the 0.0504 m Diameter Full Scale System

Prediction of particle velocities was compared with two methods. The first is simply to assume the particle velocity to be equal to the gas velocity minus the terminal velocity of the particle. This has been suggested as a suitable estimate for vertical conveying⁽⁶⁶⁾ and may provide a starting point for horizontal systems as can be seen by the correlation in Figure 4-14. It is interesting to note that the calculated particle velocity is sometimes less than zero, indicating that the experimental velocity at these points was actually less than the single particle terminal velocity. The effect of pipe diameter and the appearance that the experimental particle velocities were less than the single particle terminal velocities suggested a correlation of the experimental data of the following form:

$$U_p = (U_g - U_t^{k1})D_t^{k2} \quad (4-8)$$

The constants were obtained through regression of the experimental data using the BMDP⁽⁶⁷⁾ computer software package. The results of the regression gave the particle velocity as:

$$U_p = (U_g - U_t^{0.71})D_t^{0.019} \quad (4-9)$$

The comparison to the experimental data is shown in Figure 4-15. The improvement over the comparison shown in Figure

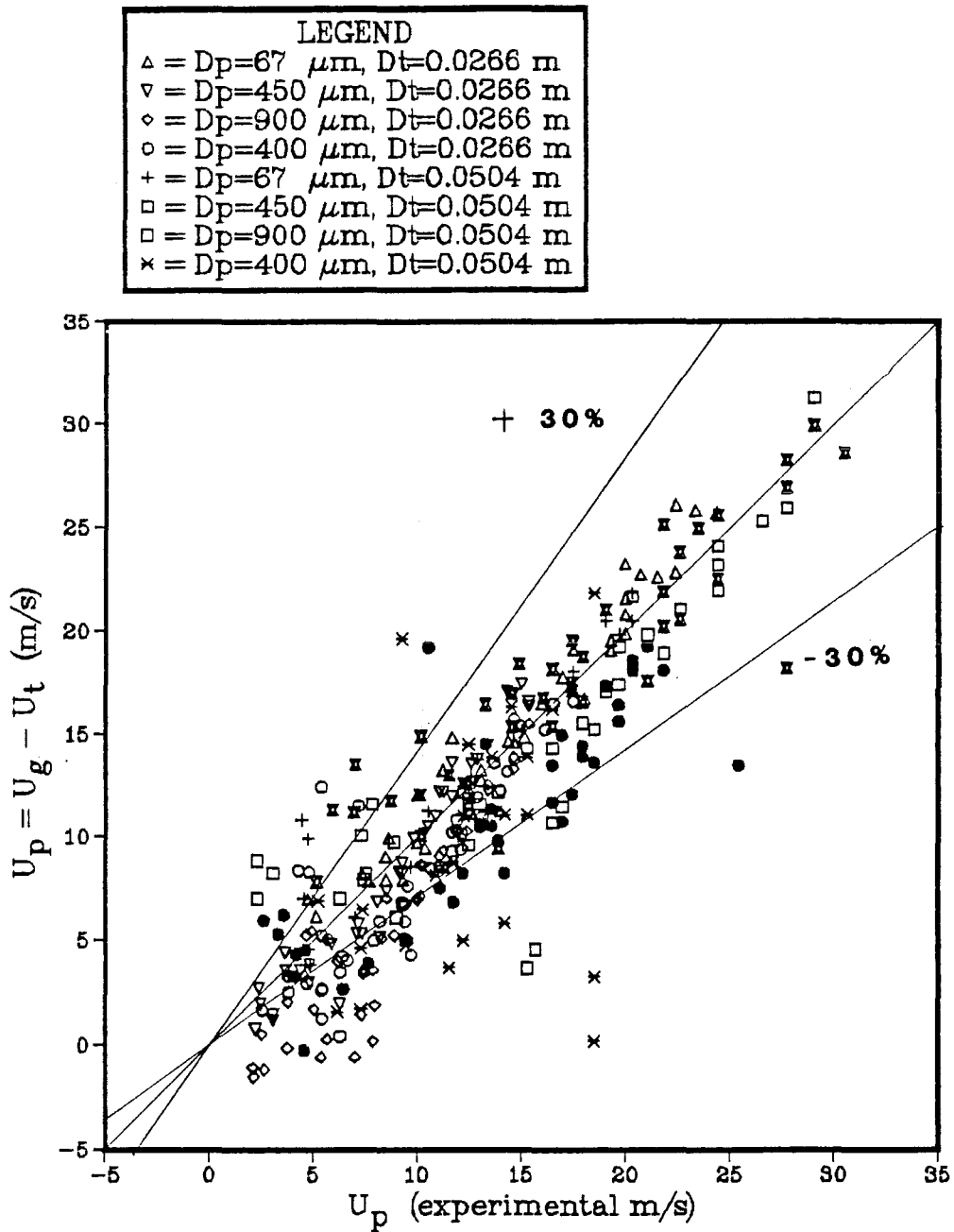


Figure 4-14: $U_g - U_t$ vs. Experimental Particle Velocity

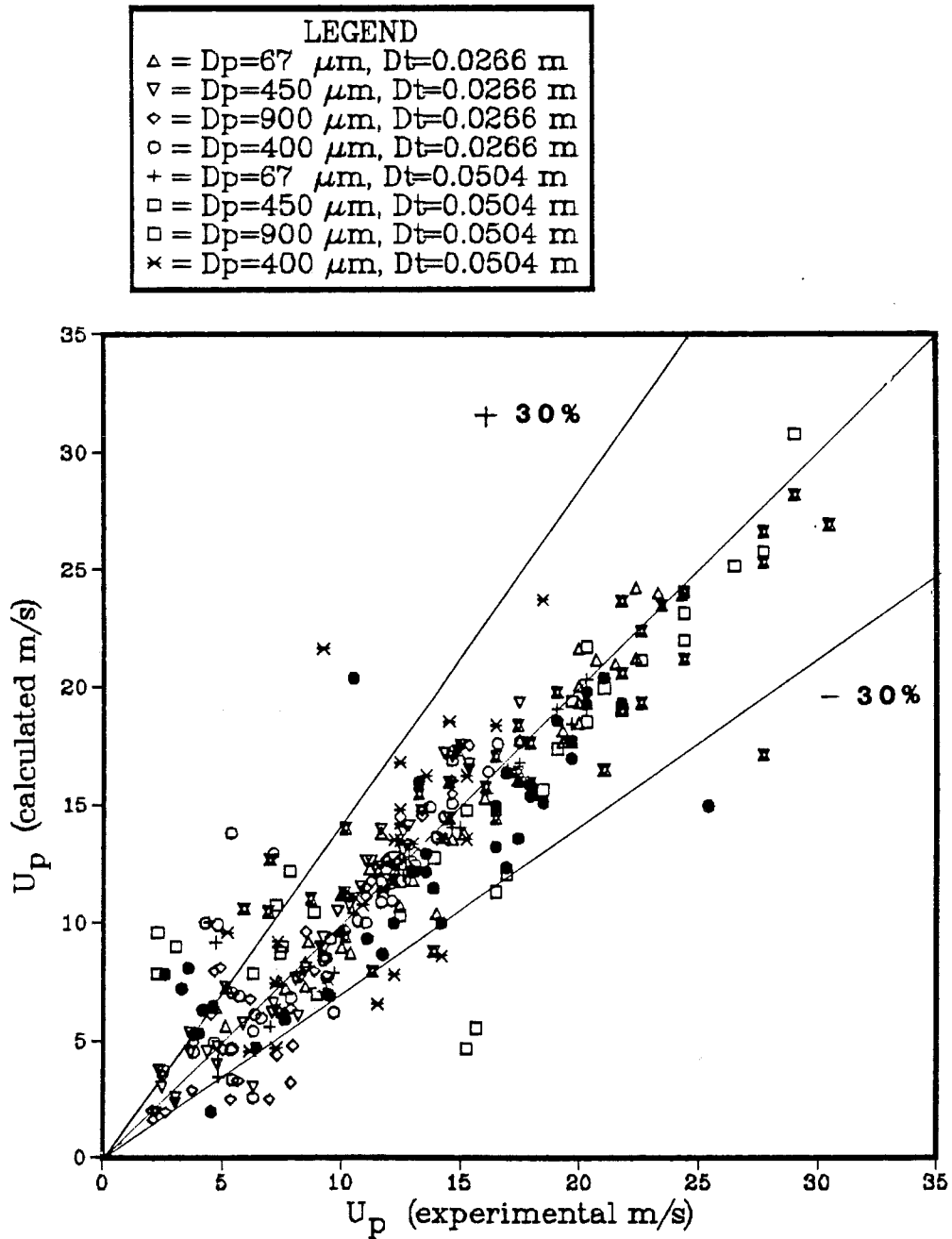


Figure 4-15: Particle Velocity Calculated Using Equation 4-9 vs. Experimental Particle Velocity

4-14 can be seen, especially in the lower range where the calculated velocity is no longer negative.

The correlation of Yang^(61,62) for pressure drop described in Section 4.1.2.1 included the calculation of the particle velocity and the results were compared to the experimental velocities as shown in Figure 4-16. As with the pressure drop prediction, the larger glass and the iron oxide predictions are not very good.

4.1.4 A Method of Pressure Drop Prediction

The method of correlation used by Yang⁽⁶²⁾ is such that a force balance is made between drag and friction assuming these are the only forces at play. Yang chose to correlate using pressure drop data to obtain an expression for friction factor. This method causes the solution to be implicit and requires simultaneous solution of the three equations mentioned earlier. This appears to be the sole drawback in the use of this method according to the Institute of Gas Technology.⁽⁶⁸⁾ This difficulty can be overcome by noting that the force balance can be solved explicitly if the particle velocity is known, as the void fraction does not require the friction factor. The equations to solve become:

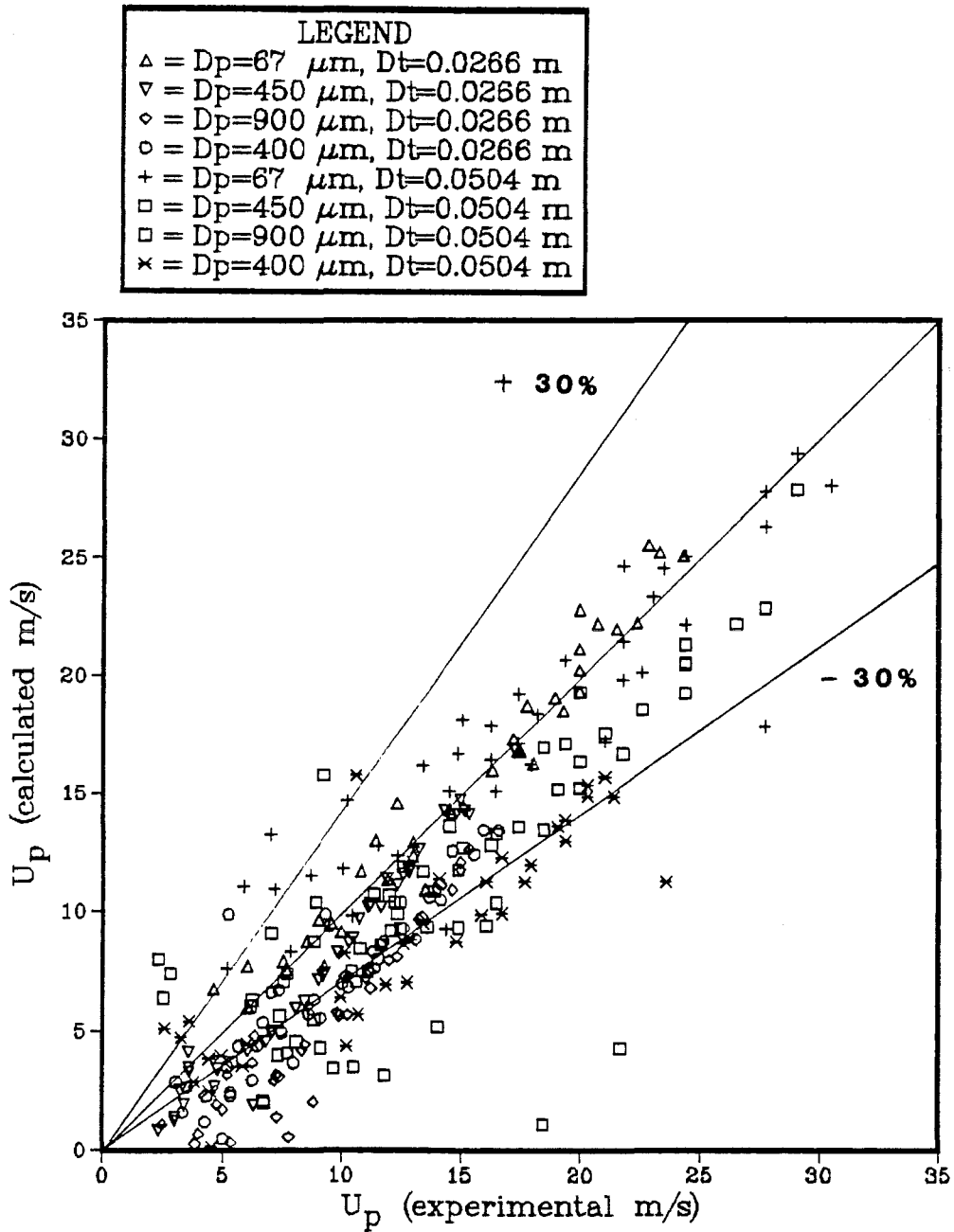


Figure 4-16: Particle Velocity Calculated Using the Correlation of Yang^(61,62) vs. Experimental Particle Velocity

$$U_p = U_p(U_g, D_p, D_t, W_s, \dots) \quad (4-10)$$

but not a function of f_s

$$\varepsilon = 1 - \frac{4W_s}{\rho_p U_p D_t^2 \pi}$$

$$f_s = \frac{3C_{ds} \varepsilon^{-4.7} \rho_f (U_f - U_p)^2 D_t}{4(\rho_p - \rho_f) D_p U_p^2} \quad (4-11)$$

The particle velocity has already been correlated in this form in Equation 4-9. This correlation is, of course, a simplification but it is seen to predict the data reasonably well. A further simplification can be made if the drag coefficient is assumed constant and equal to 0.44. With this assumption, Equation 4-12 yields the following expression for the solids friction factor:

$$f_s = \frac{0.33 \varepsilon^{-4.7} \rho_f (U_f - U_p)^2 D_t}{(\rho_p - \rho_f) D_p U_p^2} \quad (4-12)$$

The comparison of this correlation to the experimental data is shown in Figure 4-17. As with the correlation of Yang, the fit of the 900 μm glass beads and the iron oxide particles in the 0.0504 m diameter system is not very good. There is, however, a slight improvement in the fit of the other data sets. The standard relative deviations for this correlation are given in Table 4-2. The explicit nature of

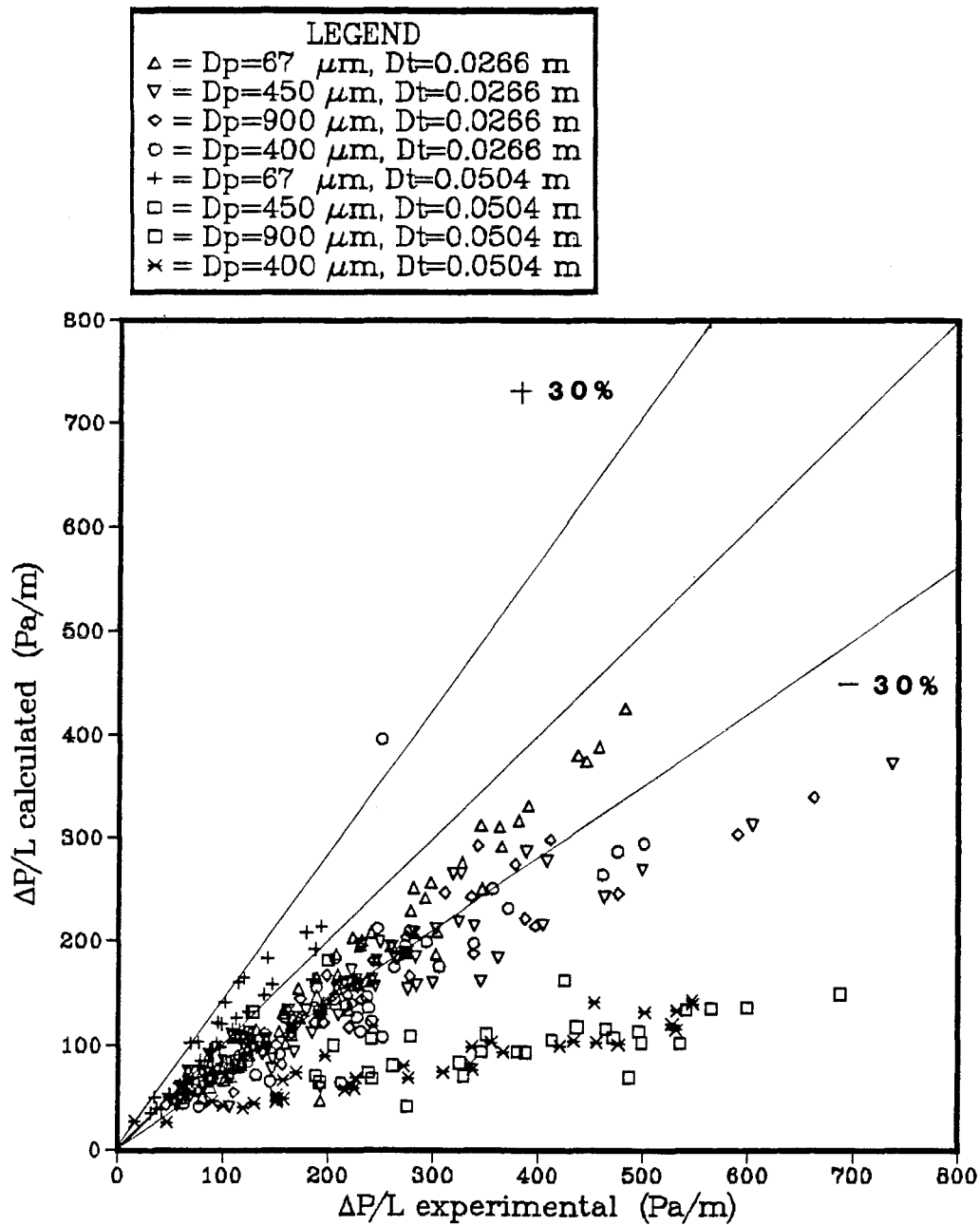


Figure 4-17: Comparison of Pressure Drop Calculated Using Equations 4-9 and 4-12 vs. Experimental Pressure Drop

Table 4-2
Standard Relative Deviation for Pressure Drop Calculated
from Equation 4-7

D_t (m)	D_p (μm)	Material	SRD (%)
0.0266	67	Glass	25.47
	450	Glass	38.77
	900	Glass	32.86
	400	Iron Oxide	37.70
0.0504	67	Glass	18.94
	450	Glass	22.72
	900	Glass	71.62
	400	Iron Oxide	71.62
Overall SRD			42.08

this correlation makes it much simpler to use. A better estimate of the drag coefficient may increase the accuracy of the correlation. The nature of the pressure drop in the case of the 900 μm glass and the 400 μm iron particles is likely to have been influenced by their shape and the generation of fines during transport in the full scale system.

An important additional advantage of the use of this method of correlation is in the range of conditions near

saltation. Using the correlation for particle velocity given by Equation 4-9 and the friction factor from Equation 4-12 a minimum in the pressure drop vs. gas velocity curve is predicted. This minimum may be related to saltation, and therefore, the method of correlation may yield a single correlation for saltation velocities as well as pressure drop, a definite advantage to current practices using multiple correlations. A test of this use was made by generating the calculated pressure vs. gas velocity diagram assuming 450 μm glass beads in an 0.0266 m pipe. This generated diagram then had the saltation prediction from the saltation correlation of Rizk⁽⁴⁰⁾ superimposed on it. This diagram is shown in Figure 4-18. As can be seen, the calculated saltation velocity of Rizk corresponds very closely with the minimum pressure drop calculated using Equations 4-9 and 4-12.

4.2 Application of the Thermodynamic Analogy

4.2.1 The Ideal Gas Analog

The ideal gas analog has already been shown to apply to experimental results in its reduced form of Equation 2-25. It was also pointed out that the ideal gas analog was incapable of describing the flow condition at low gas velocities where separation into a strand type flow

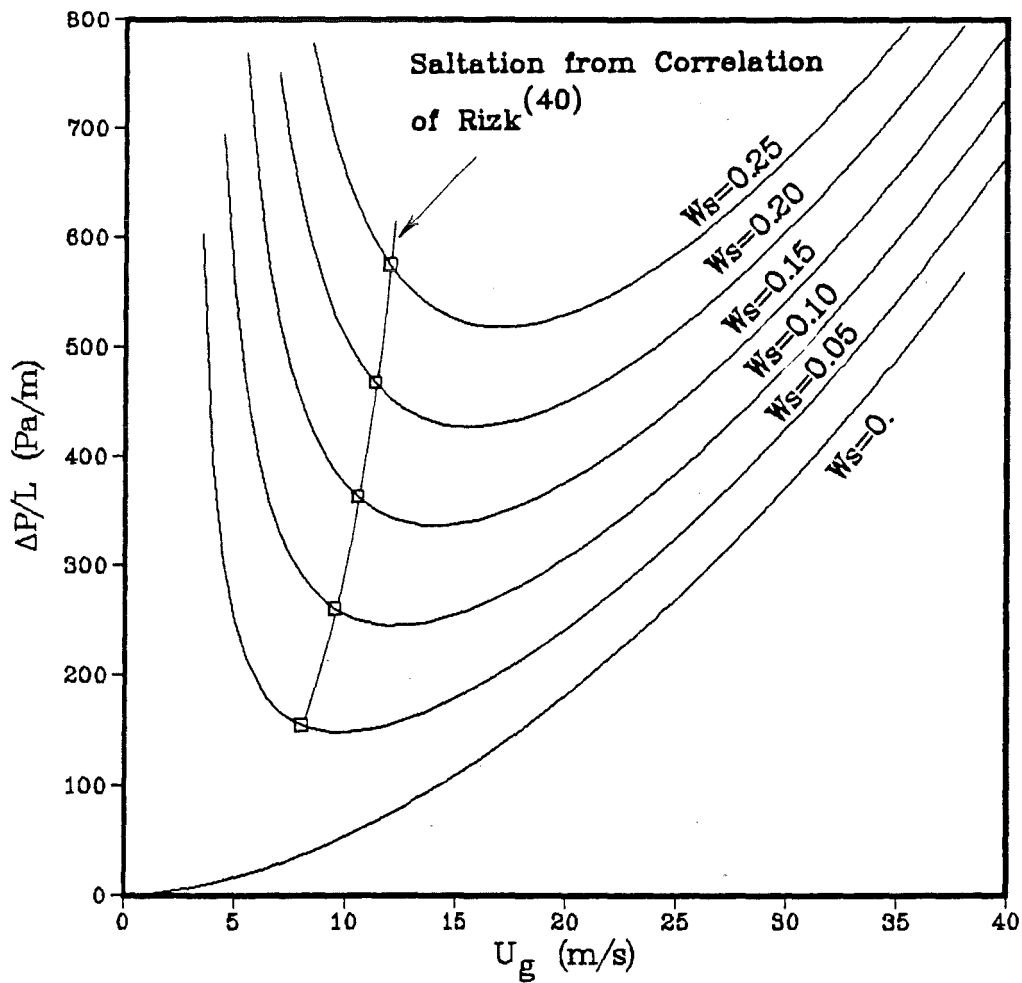


Figure 4-18: Calculated Pressure Drop vs. Gas Velocity Diagram Using Equations 4-9 and 4-12 for 450 μm Glass Beads Showing the Saltation Correlation of Rizk⁽⁴⁰⁾

occurred. The use of the ideal gas analog in the application of the thermodynamic analogy was in obtaining the ideal transport constant, R^* , for each particle size in both the bench scale and the full scale systems. These constants were determined from the mean value of the particle to gas velocity ratio at high gas velocities. They are given in Table 4-3.

Table 4-3

Ideal Transport Constant (R^*) from Experimental Data

	67 μm Glass Bead	450 μm Glass Bead	900 μm Glass Bead	400 μm Iron Oxide
0.0266 m BenchScale System	45.74	33.29	31.97	46.13
0.0504 m FullScale System	43.56	39.76	29.46	55.53

It is apparent that the pipe diameter can have a significant influence on R^* as seen in the case of both the 450 micron glass beads and the 400 micron iron oxide.

4.2.2 The van der Waals Analog

4.2.2.1 Methodology of Data Analysis. Prior to the presentation of the experimental results for the van der Waals analog an explanation of the methodology of data analysis is required. Although the mass flow rate of solids

in the upper and lower halves of the pipe as well as the velocities in these sections were measured, the separation of the flow into two separate solids phases did not occur at the centerline of the pipe. To obtain the solids fluxes in each phase required the additional measurement of the height of the dense phase layer along with an assumption concerning the dilute phase upper flow. The assumption made was that the dilute phase above the dense layer was homogeneous in both particle concentration and velocity. Knowing the height of the layer allowed the calculation of the cross-sectional area of flow for both the dilute and dense phase portions according to Equations 4-13 through 4-17. Figure 4-19 shows the geometry of the separated flow condition.

$$m = r - h \quad (4-13)$$

$$\theta = \cos^{-1} \left(\frac{m}{r} \right) \quad (4-14)$$

$$A_3 = \frac{\pi r^2}{2} (2\theta - \sin 2\theta) \quad (4-15)$$

$$A_1 = \frac{\pi r^2}{2} \quad (4-16)$$

$$A_2 = \frac{\pi r^2}{2} - A_3 \quad (4-17)$$

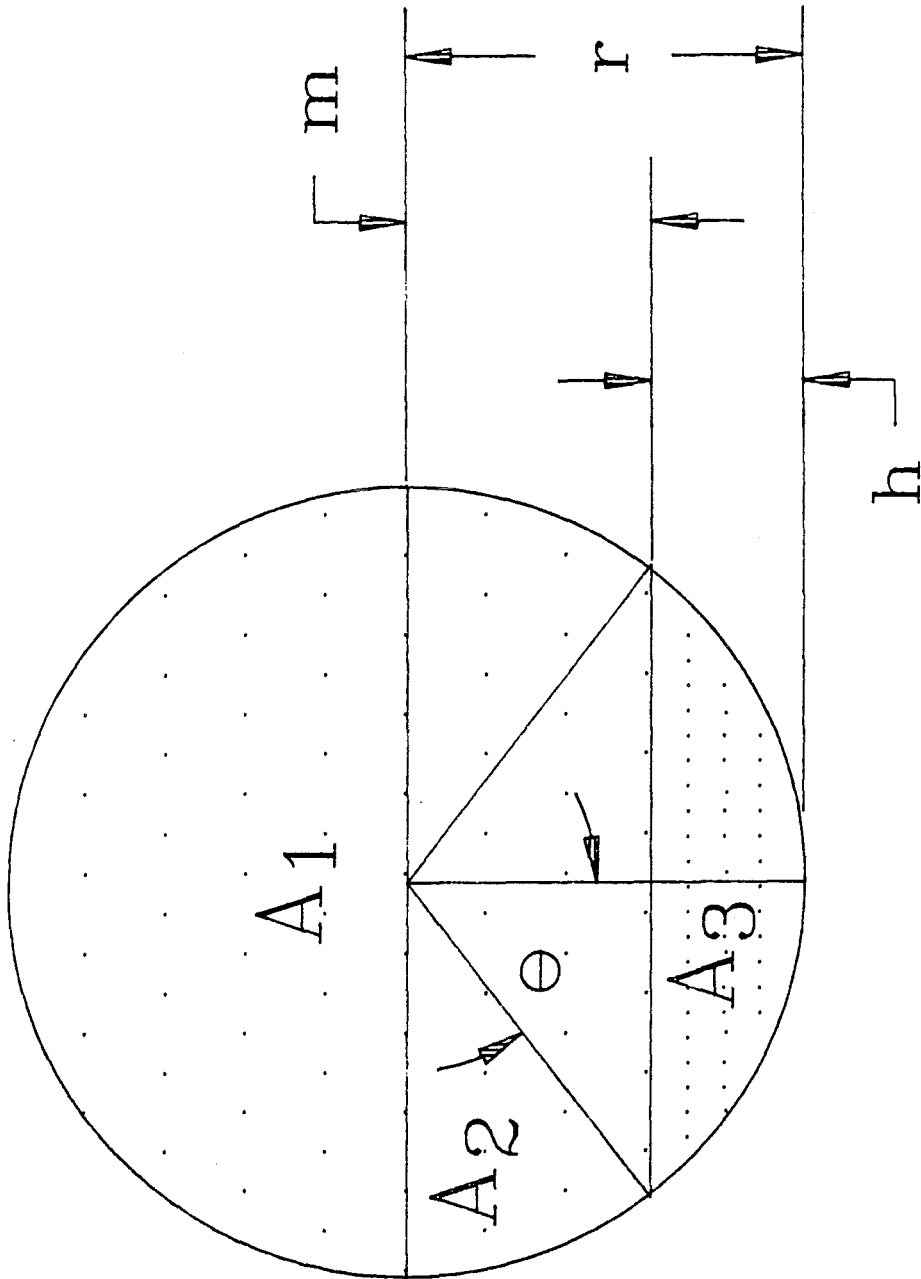


Figure 4-19: Geometry of Separated Flow Condition

With the assumption that the upper dilute phase flow is homogeneous, the mass flow rate of solids in the lower phase flow can be estimated by equation 4-18.

$$W'_{s1} = W_{s1} - W_{su} \left(\frac{A_2}{A_1} \right) \quad (4-18)$$

Knowing the particle velocity, the area and the mass flow rate in the dense layer allows the calculation of the solids fraction using Equation 4-19.

$$\phi_1 = \frac{W'_{s1}}{A_1 \rho_p U_{p1}} \quad (4-19)$$

Two further assumptions are made in the application of the van der Waals analog. First, it is assumed that the gas flux is the same in both the upper and lower sections of the pipe. The second assumption is that the solids flux of the dilute phase is the equilibrium flux corresponding to the equilibrium pressure described in Section 2.2.3.2.

4.2.2.2 Regression of the van der Waals Constants.

Regression of the van der Waals constants a^* and b^* was done using the BMDP⁽⁶⁷⁾ computer software package. A non-linear least squares regression routine named PAR was chosen. An example of the required input code is given in Appendix D. The results of the regression are given in Table 4-4. The effect of particle size, particle density, and pipe diameter

Table 4-4

a^* and b^* From Regression of Experimental Data

<u>Pipe Diameter</u>		<u>67μm Glass Beads</u>	<u>450μm Glass Beads</u>	<u>900μm Glass Beads</u>	<u>400μm Iron Oxide</u>
0.0266m	a^*	1923.78	531.91	937.45	1495.33
	b^*	20.20	8.77	16.46	24.01
	R^*	45.74	33.29	31.97	46.13
0.0504m	a^*	395.51	385.20	240.71	416.47
	b^*	2.72	4.39	2.36	6.20
	R^*	43.56	39.76	29.46	55.53

Note: R^* from Ideal Transport Equation described in Section 4.2.1

cannot be determined exactly from the results shown in Table 4-4. A general observation is the reduction in both constants, (a^* and b^*), with increase in pipe diameter.

Using equations 4-20, 4-21, and 4-22, the critical fluxes and solids fractions were calculated. These are given in Table 4-5. In all cases the solids flux, j_{pc}^* , increases with an increase in pipe diameter along with an increase in solids fraction ϕ_c . The gas flux, j_{gc}^* , does not increase in proportion to the solids flux increase and in the case of the iron oxide particles, j_{gc}^* decreases with increase in pipe diameter. This appears to indicate that a greater loading is possible in a larger pipe diameter.

$$j_{pc}^* = \frac{a^*}{27b^{*2}} \quad (4-20)$$

$$j_{gc}^* = \frac{8a^*}{27b^*R^*} \quad (4-21)$$

$$\phi_c = \frac{1}{3b^*} \quad (4-22)$$

Table 4-5

Critical Point Fluxes and Solids Fraction
from van der Waals Analog Constants

<u>Pipe Diameter</u>		<u>67μm Glass Beads</u>	<u>450μm Glass Beads</u>	<u>900μm Glass Beads</u>	<u>I.O. Glass Beads</u>
0.0266m	J_{gc}^*	0.61693	0.53982	0.52784	0.40003
	J_{pc}^*	0.17462	0.25614	0.12815	0.09607
	ϕ_c	0.0165	0.03801	0.02025	0.01388

0.0504m	J_{gc}^*	0.98907	0.65389	1.02757	0.35842
	J_{pc}^*	1.97996	0.74028	1.60069	0.40127
	ϕ_c	0.12255	0.07593	0.141243	0.05376

4.2.3 The j_p^* vs. Φ Phase Diagram

The use of the thermodynamic analogy to pneumatic transport is based primarily on experimental observation as mentioned earlier. The use of the analogy in horizontal systems is best shown by the j_p^* vs. Φ phase diagram where a two phase envelope can be clearly seen. A diagram of this type is shown in Figure 4-20 for 450 μm glass beads in the 0.0266 m diameter system. In this figure the separation into two phases is clearly seen with the denser phase having a relatively constant solids fraction while the upper phase shows a considerable variation in solids fraction. This is analogous to a vapor-liquid system. The use of the van der Waals analog equation in describing the phase behavior is shown in Figure 4-21. In this figure lines of constant j_g^* are constructed using the van der Waals analog equation and the constants R^* , a^* , and b^* obtained from the experimental data. The ability to predict the phase behavior is fairly good. Results for the other particles studied in both the 0.0266 m and 0.0504 m diameter systems are included in Appendix A. The results for all the systems are similar except for the case of the 400 μm iron oxide in the 0.0504 m system. In this case the range of experimental parameters was severely limited by system constraints, primarily in pressure drop, and the regression of such a small range of

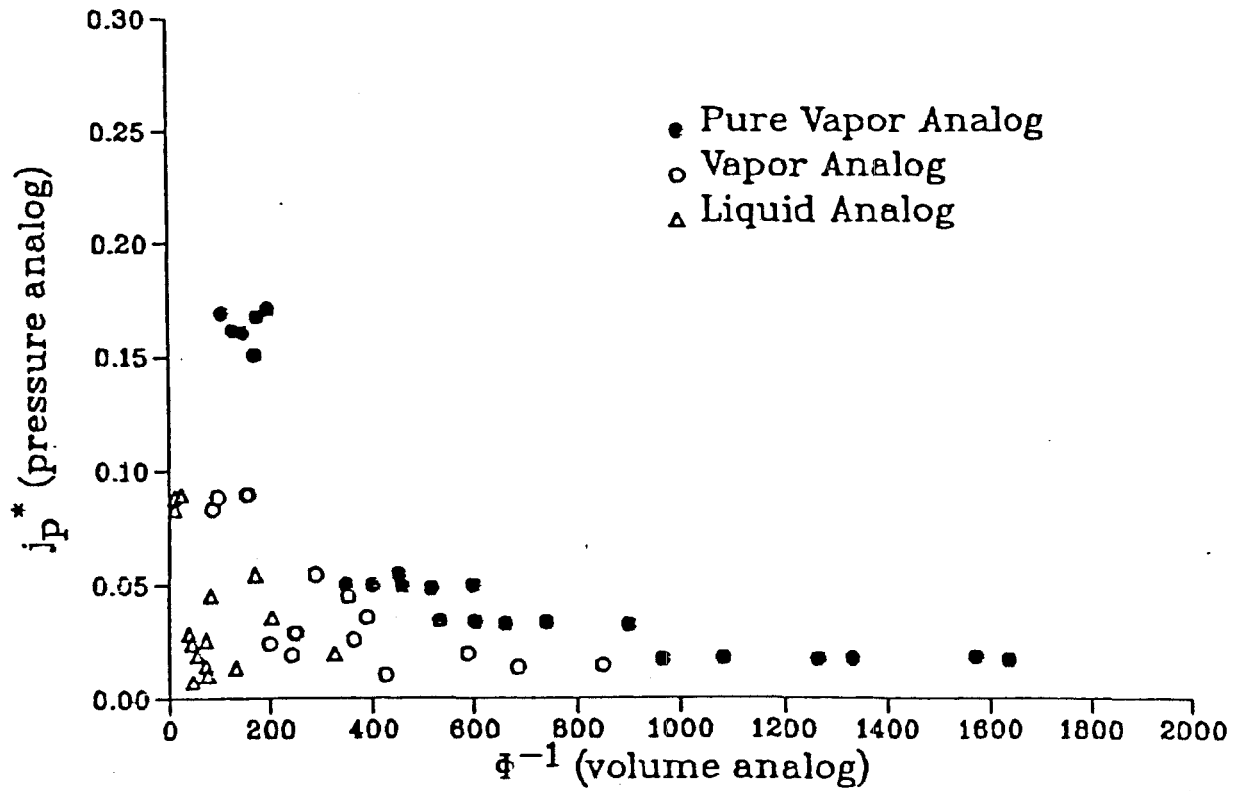


Figure 4-20: j_p^* vs. Φ^{-1} for the 450 μm Glass Beads in the 0.0266 m Diameter System

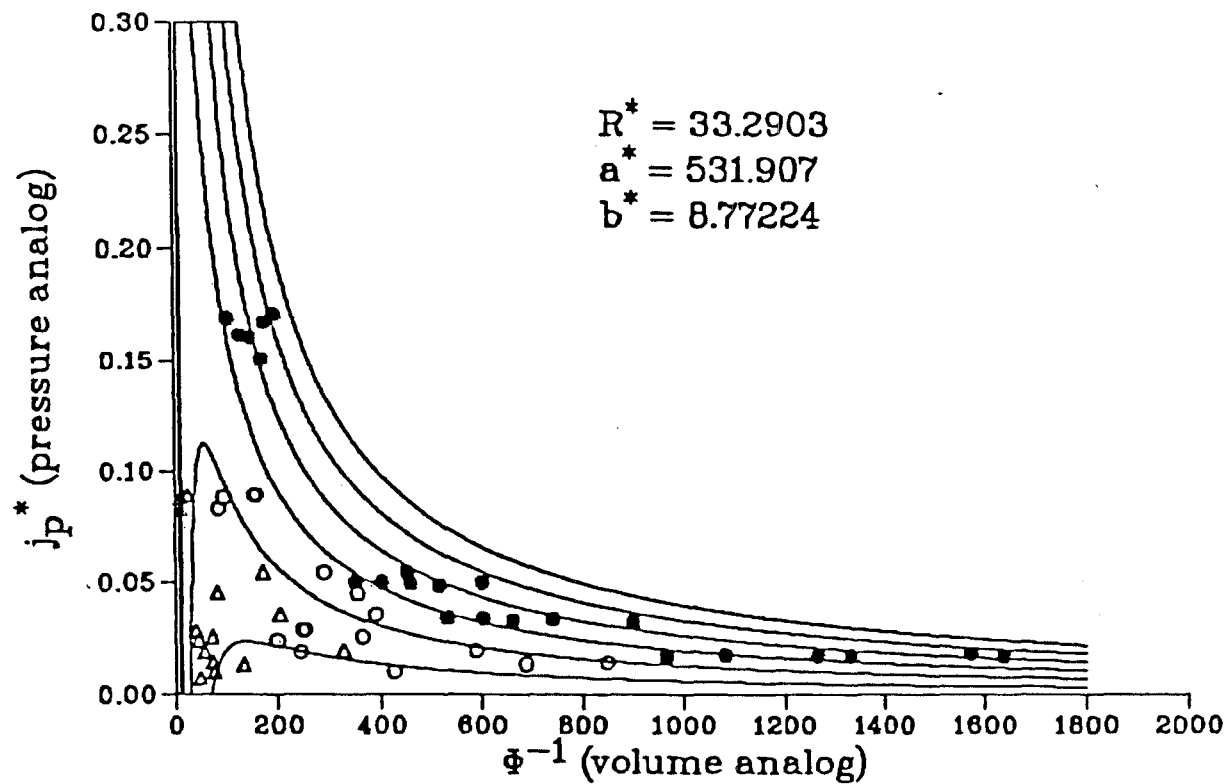


Figure 4-21: j_p^* vs. Φ^{-1} for the 450 μm Glass Beads in the 0.0266 m Diameter System with Lines of Constant j_g^* from the van der Waals Analog Equation Superimposed

parameters did not provide as good a fit of the experimental data.

4.2.4 The Flux-Flux Phase Diagram of Tuba⁽¹⁾

A phase diagram of j_p^* vs. j_g^* was first presented by Tuba⁽¹⁾ for the case of vertical pneumatic conveying. An example is shown in Figure 4-22. In this type of diagram the dilute and dense phase regimes were delineated by a locus of intersections of lines of constant voidage which Tuba called the choking locus. This diagram allowed for three modes of conveying, namely, co-current upflow, co-current down flow, and counter-current flow between the solids and the gas. In horizontal conveying only one mode is normally possible, that of co-current flow. A Flux-Flux phase diagram for horizontal conveying is shown in Figure 4-23 for the case of 450 μm glass beads in the 0.0266 m diameter system. The intersection of the lines of constant voidage cannot be termed a choking in that it delineates suspended flow from strand type conveying. Saltation is not described by this diagram. Phase diagrams for each particle and both pipe diameters are included in Appendix A.

4.2.5 An Estimate of the Critical Point Analog

The range of j_p^* possible in either experimental system was not high enough to operate at the critical point predicted

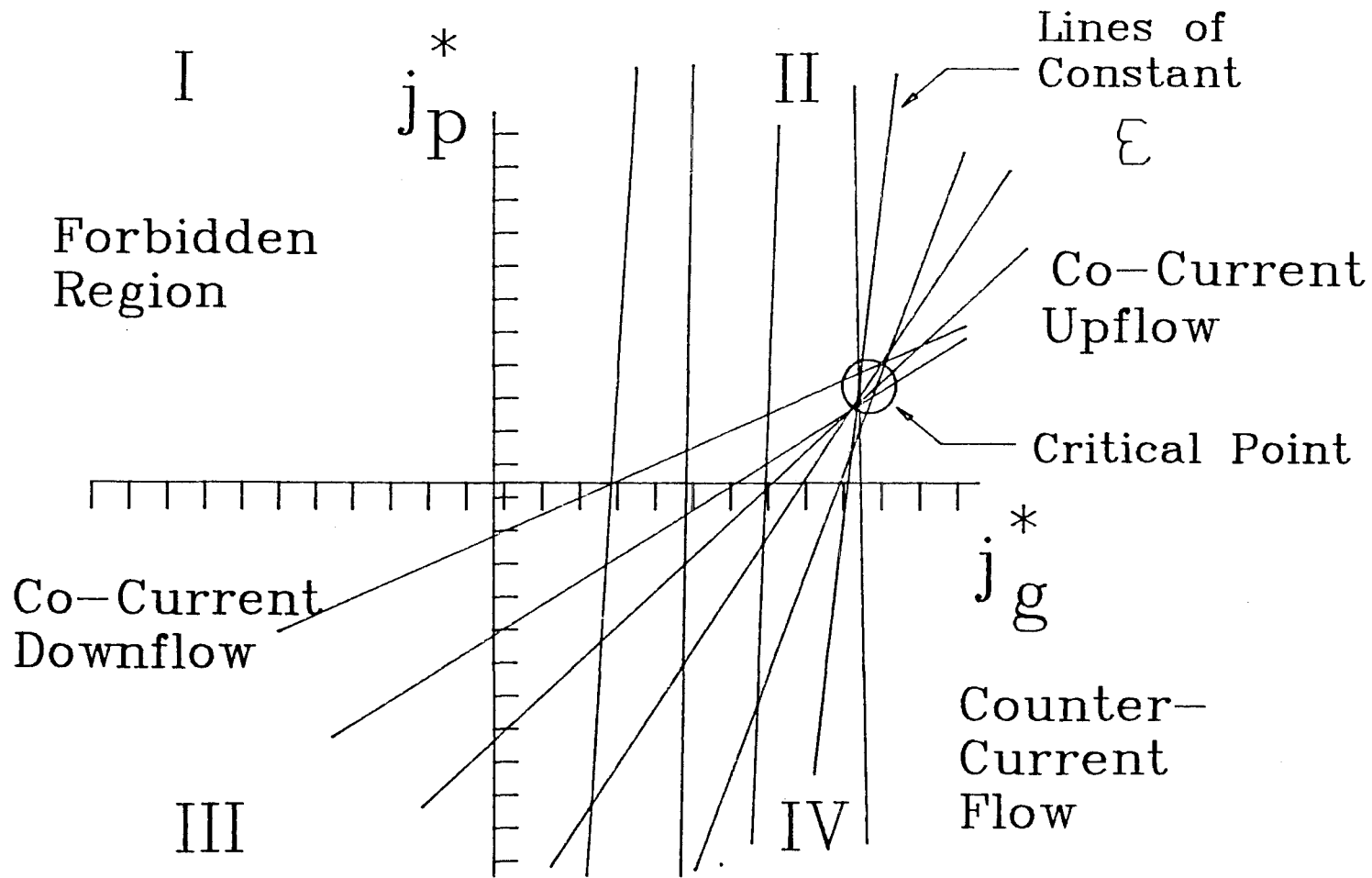


Figure 4-22: j_p^* vs. j_g^* Phase Diagram of Tuba⁽¹⁾

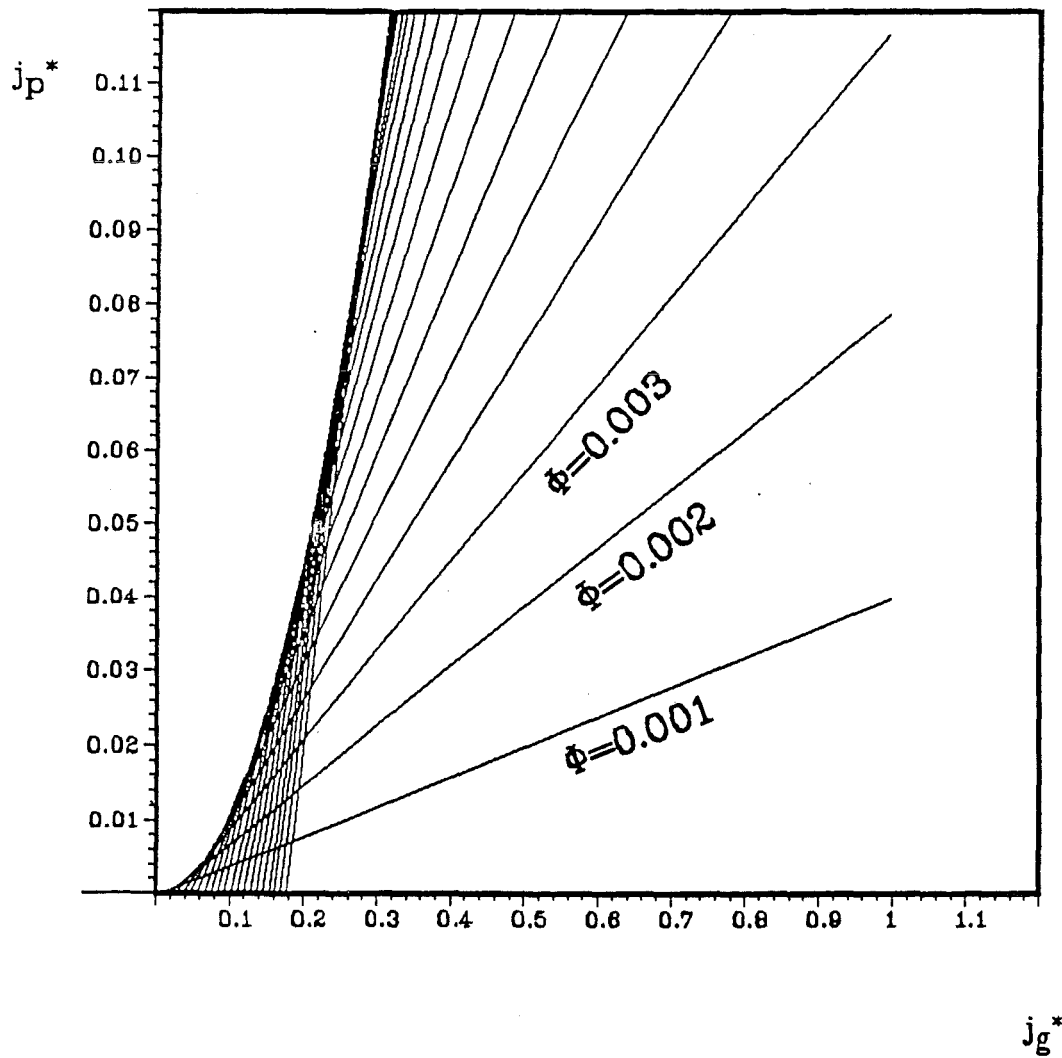


Figure 4-23: j_p^* vs. j_g^* Phase Diagram for the 450 μm Glass Beads in the 0.0266 m Diameter System

by the van der Waals analog. In the 0.0266 m system this limitation was due to the limits of the solids feeder while in the 0.0504 m system the limitation was in both the pressure restrictions of the air delivery system, as well as the capacity of the collection system.

A method of estimating the critical point analog in a pneumatic system was presented by Zaltash, et. al.⁽⁴⁶⁾ in which the pressure drop vs. gas velocity diagram was used. This method was discussed in Section 2.2.3.4. Using the pressure drop vs. gas velocity diagram for the 450 μm glass beads in the 0.0266 m system an estimate was made for j_{gc}^* and Φ_c (see Figure 4-24). Using R^* and these two estimates, a^* and b^* were obtained. The comparison between these estimated constants and those obtained by regression of the experimental data is shown in Figure 4-25. The estimate is seen to be slightly low. It does provide an estimate of the two phase envelope without the regression of experimental data.

4.2.6 Predicting the Pressure Drop Using the van der Waals Analog

Use of the methods for predicting the pressure drop by the thermodynamic analogy discussed in Section 2.2.3.5 were unsuccessful. Although the pressure drop is a state function, the actual form of the function is unknown. The pressure drop vs. j_p^* for the 450 μm glass beads in the

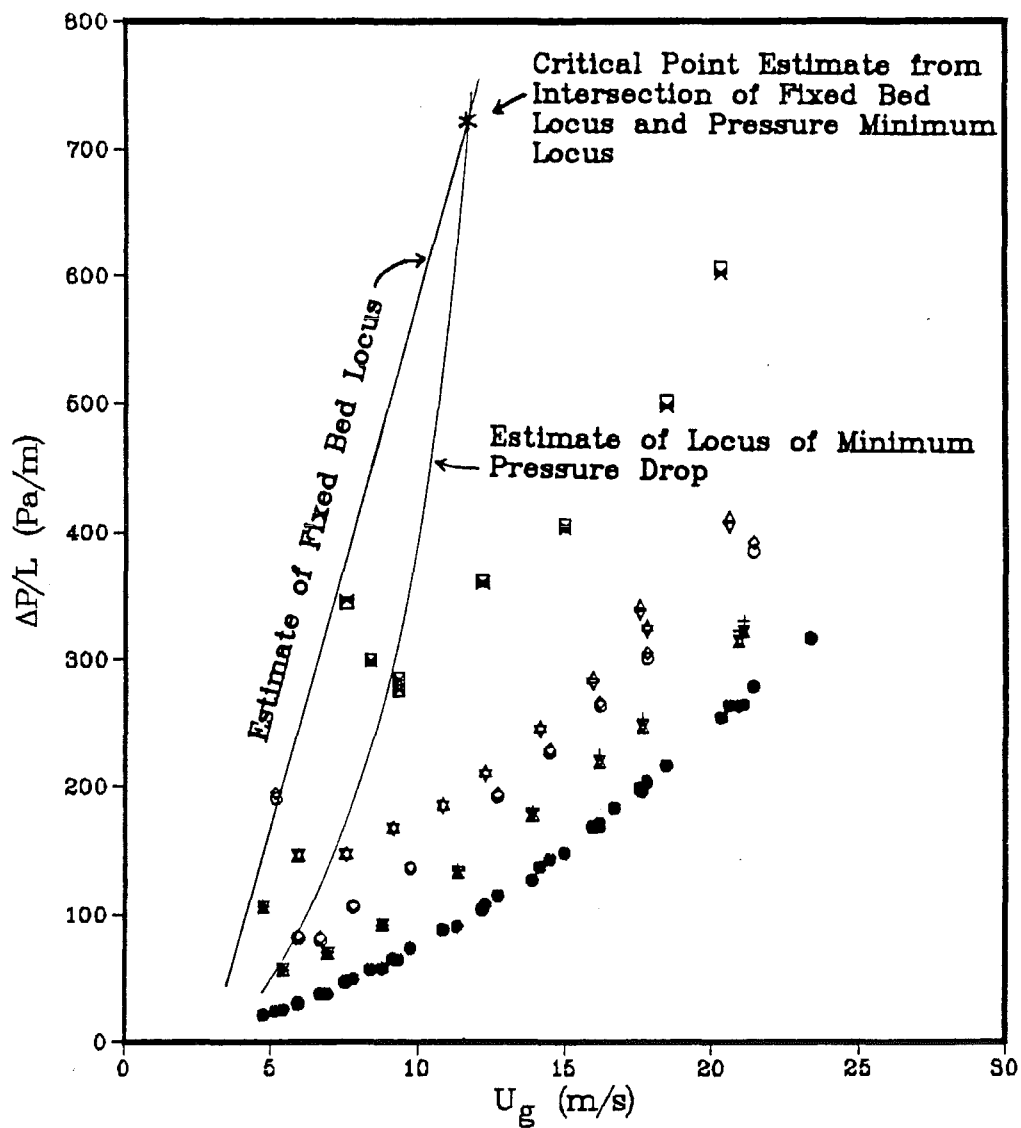


Figure 4-24: Estimation of Critical Point for the 450 μm Glass Beads in the 0.0266 m Diameter System from the Method of Zaltash, et.al. (46)

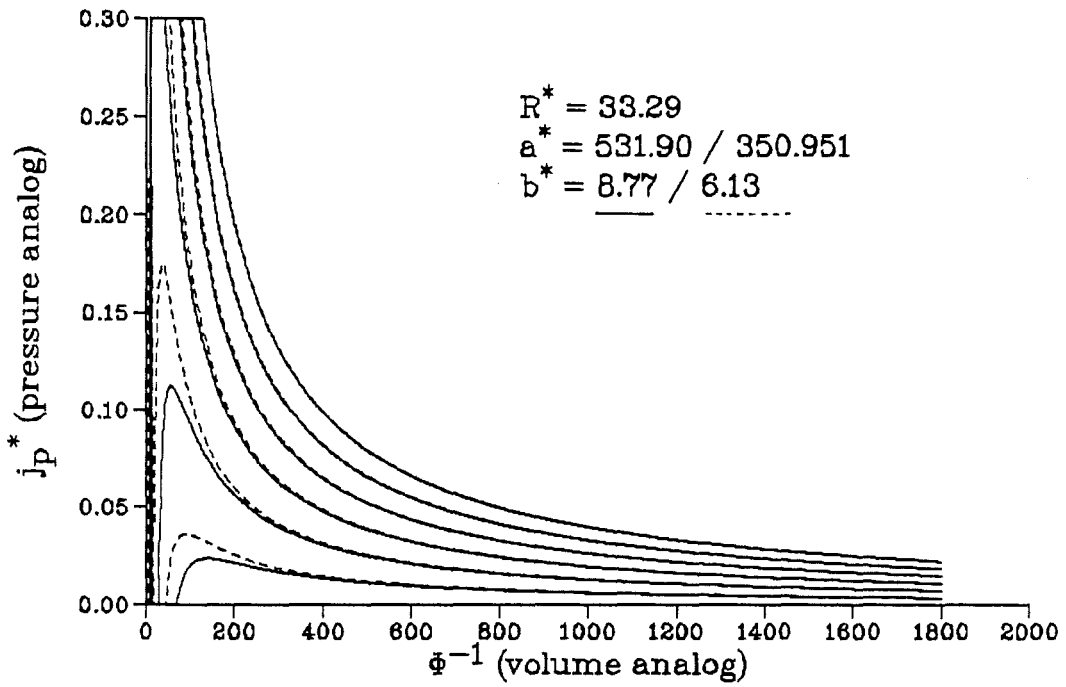


Figure 4-25: Comparison of van der Waals Constants Obtained by Data Regression to Those from Estimation from Pressure Drop Data (450 μm Glass Beads in 0.0266 m Diameter System)

0.0266 m diameter system is shown in Figure 4-26. The models described in Section 2.2.3.5 do not show this behavior. It is felt that an additional system parameter must be identified in order to develop an expression for the pressure drop. This additional parameter should account for irreversibility as an analog to entropy in a thermodynamic system.

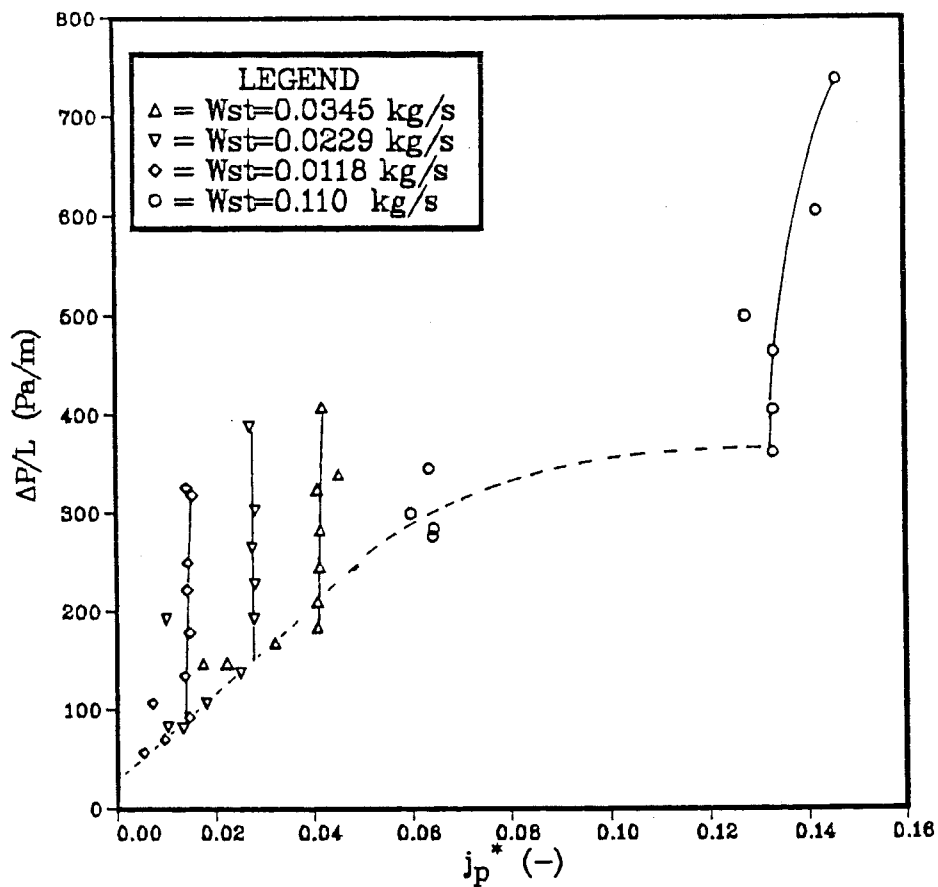


Figure 4-26: $\frac{\Delta P}{L}$ vs. j_p^* for the 450 μ m Glass Beads in the 0.0266 m Diameter System

4.3 Other Results

The methods of experimentation provided some additional results which will now be discussed. These additional results are primarily from the measurements of system properties in the upper and lower halves of the pipe. The particle velocity was already discussed in Section 4.1.3, where a difference between particle velocities in the upper and lower halves were shown to be significant only in the cases of low gas velocities. In addition to the particle velocities, the pressure drop and the mass flow rate were also measured at the top and bottom halves of the pipe. These will be discussed now.

4.3.1. Pressure Drop Between the Upper and Lower Halves of the Pipe

4.3.1.1 Axial Pressure Drop. Pressure drop measurements were made along the top half of the pipe, as well as along the bottom half of the pipe. The original aim of this measurement was to assess the lift forces present in the system. This proved to be an improper method of measurement for lift as it was found that the pressure drop across the top of the pipe was not less than the pressure drop along the bottom half of the pipe. The opposite condition was found to occur in some cases, however. Referring to the pressure drop vs. gas velocity diagram of Figure 4-4,

previously discussed in Section 4.1.2, the pressure drop in the top half of the pipe is greater than that in the lower half of the pipe at high gas velocities. This can be attributed to two possible explanations which need not be mutually exclusive. The first is that the gas velocity in the upper section of the pipe is greater than that in the lower half. A profile of gas velocity showing this behavior was reported by Konno and Saito⁽⁶⁹⁾. The corresponding particle velocity profile was reported as almost constant across the pipe. The corresponding mass flow distribution would be expected to be such that a greater amount of solids were flowing in the bottom half of the pipe. This, however, was not found to be the case and will be treated in greater detail in section 4.3.2. In fact, a greater amount of solids were found to be flowing in the top half of the pipe which leads to the second explanation for the increased pressure drop. With a greater amount of solids flowing in the top of the pipe, more solids wall friction would almost necessarily occur, leading to a greater pressure drop along the top of the pipe. This condition could occur due to increased lift at higher gas velocities especially if the gas velocity profile were skewed toward the upper half of the pipe.

4.3.1.2 Radial Pressure Measurement. A radial pressure measurement was made during experiments with the 0.0508 m

diameter pipe. A precision manometer was connected to pressure taps located at the top and the bottom of the pipe. The results of this pressure measurement were not conclusive in that for most cases a difference between the manometer reading with air only flowing and the reading upon introduction of solids was undetectable. Only in the case of the 900 μm glass beads was there any noticeable difference in the readings and this difference fluctuated considerably. The maximum pressure difference with the addition of solids was approximately 10 Pa and this value was estimated as a mean value about a fluctuation of approximately 5 Pa. In general, it is felt that a radial pressure gradient exists; however, its magnitude is very small. Measurement of this parameter would require a more sensitive measuring device as well as the means to acquire a statistical set of data.

4.3.1.3 Pressure Drop Fluctuation. Fluctuations in the pressure drop in a pneumatic system have been used to characterize phase transitions and choking^(70,71) and may provide new insights into the local effects of the particles on the gas itself.⁽⁵⁹⁾ Pressure drop fluctuations were measured as the standard deviation from the pressure drop measurements taken. The general trend of the fluctuation of pressure drop with change in gas velocity is shown for the 900 μm glass beads in the 0.0266 m diameter pipe in Figure 4-27. The fluctuations go through a minimum with the highest fluctuations occurring at the lower gas velocities.

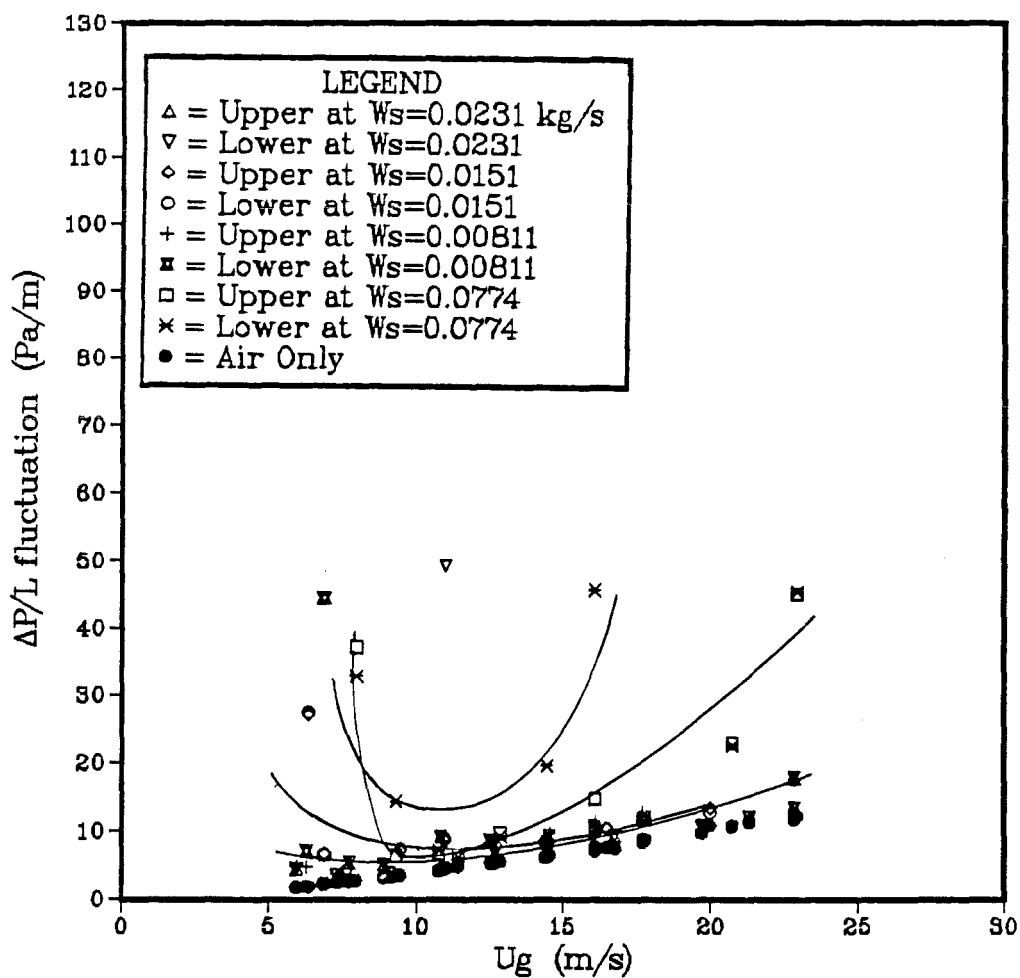


Figure 4-27: Pressure Drop Fluctuation vs. Gas Velocity for the 900 μ m Glass Beads in the 0.0266 m Diameter System

This result is similar to that for vertical systems near choking. At high gas velocities, the fluctuations again increase. As the 67 μm glass beads showed a unique behavior in mean pressure drop; i.e., the pressure drop for these particles in both diameter pipes was considerably lower than expected, especially at the higher mass flow rates; the pressure drop fluctuation should be of some interest. Compare the pressure drop fluctuation for the 67 μm glass beads in the 0.0266 m diameter pipe shown in Figure 4-28 to Figure 4-27. As can be seen, the fluctuations are considerably higher with a marked influence of mass flow rate of solids on the magnitude of the fluctuations.

4.3.1.4 Fluctuations in the Upper and Lower Halves of the Pipe. Again, the measurement of pressure fluctuation in both the upper and lower halves of the pipe allow a comparison to be made. The ratio of the pressure drop fluctuation in the upper half of the pipe to that in the lower half of the pipe with change in gas velocity is shown for the case of 450 μm glass beads in the 0.0266 m diameter pipe in Figure 4-29. This figure shows that the pressure fluctuation along the bottom of the pipe was often much greater than that along the top of the pipe. This figure should be compared to Figure 4-30 which shows the same particles in the 0.0504 m diameter pipe. In the larger pipe, the ratio of fluctuations is almost unity for all cases meaning that the magnitude of fluctuation in the lower

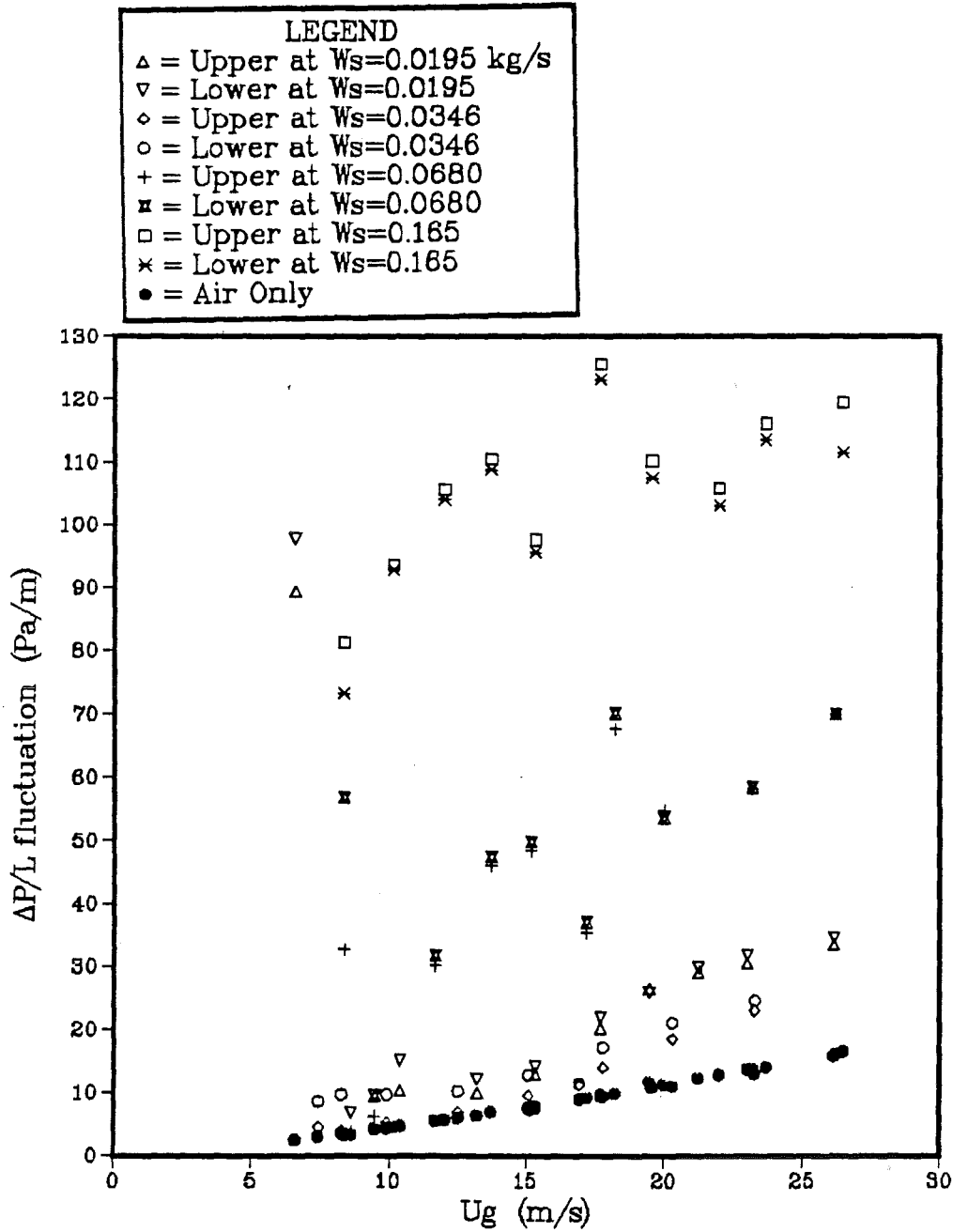


Figure 4-28: Pressure Drop Fluctuation vs. Gas Velocity for the 67 μm Glass Beads in the 0.0266 m Diameter System

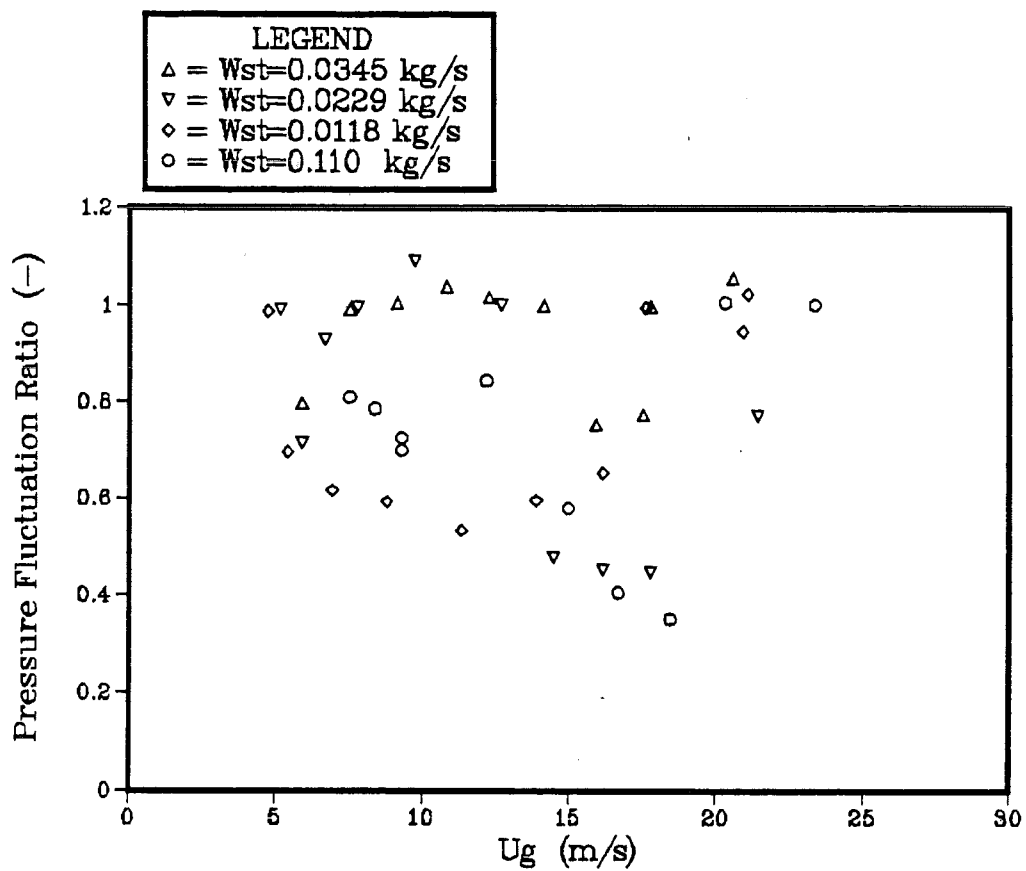


Figure 4-29: Ratio of Pressure Fluctuation in the Upper Half of the Pipe to that in the Lower Half vs. Gas Velocity for the 450 μ m Glass Beads in the 0.0266 m Diameter System

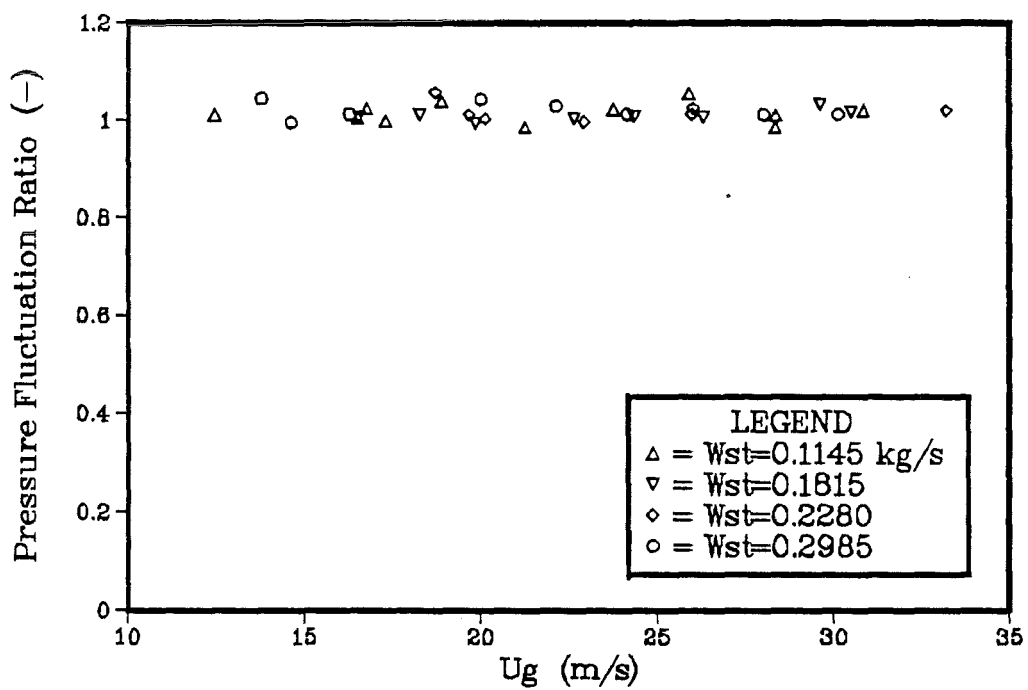


Figure 4-30: Ratio of Pressure Fluctuation in the Upper Half of the Pipe to that in the Lower Half vs. Gas Velocity for the 450 μm Glass Beads in the 0.0504 m Diameter System

half of the pipe was equal to that in the upper half. Compare now the case of the 67 μm glass beads in the 0.0504 m diameter system shown in Figure 4-31.

4.3.2 Mass Flow Distribution between the Upper and Lower Halves of the Pipe

Measurement of the mass flow rate in the upper and lower halves of the pipe showed a unique behavior with changes in gas velocity as well as total mass flow rate. This behavior is shown for the 450 μm glass beads in the 0.0266 m diameter pipe in Figure 4-32. This figure shows the ratio of mass flow rate in the upper half of the pipe to the mass flow rate in the lower half of the pipe with change in gas velocity. It can be seen that at the highest total mass flow rate the ratio exceeds unity. As the gas velocity is decreased, the ratio falls below one with the effect of total mass flow showing a steeper drop in ratio with decrease in gas velocity. At the lowest gas velocities a rise is seen in the ratio which is attributed to the drop in particle velocity in the lower strand type flow with increase in velocity of the dilute flow above. The increase of mass flow ratio above unity was most pronounced in the 900 μm glass beads in the 0.0266 m diameter pipe. Although showing the same general trends, the mass flow ratio of the 67 μm glass beads in the 0.0266 m diameter pipe never

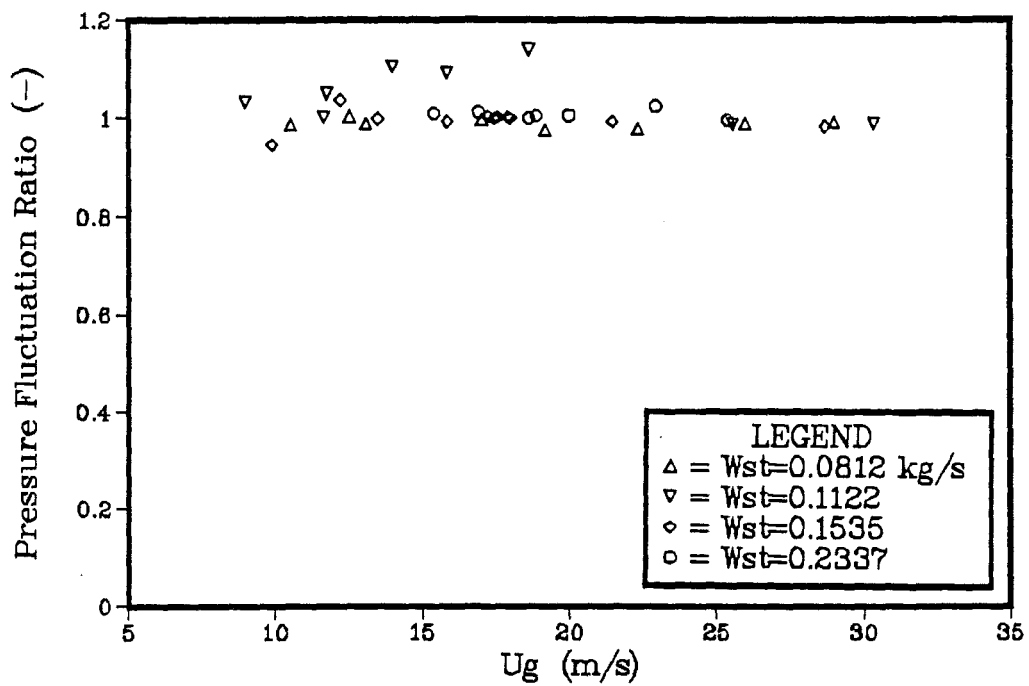


Figure 4-31: Ratio of Pressure Fluctuation in the Upper Half of the Pipe to that in the Lower Half vs. Gas Velocity for the 67 μ m Glass Beads in the 0.0504 m Diameter System

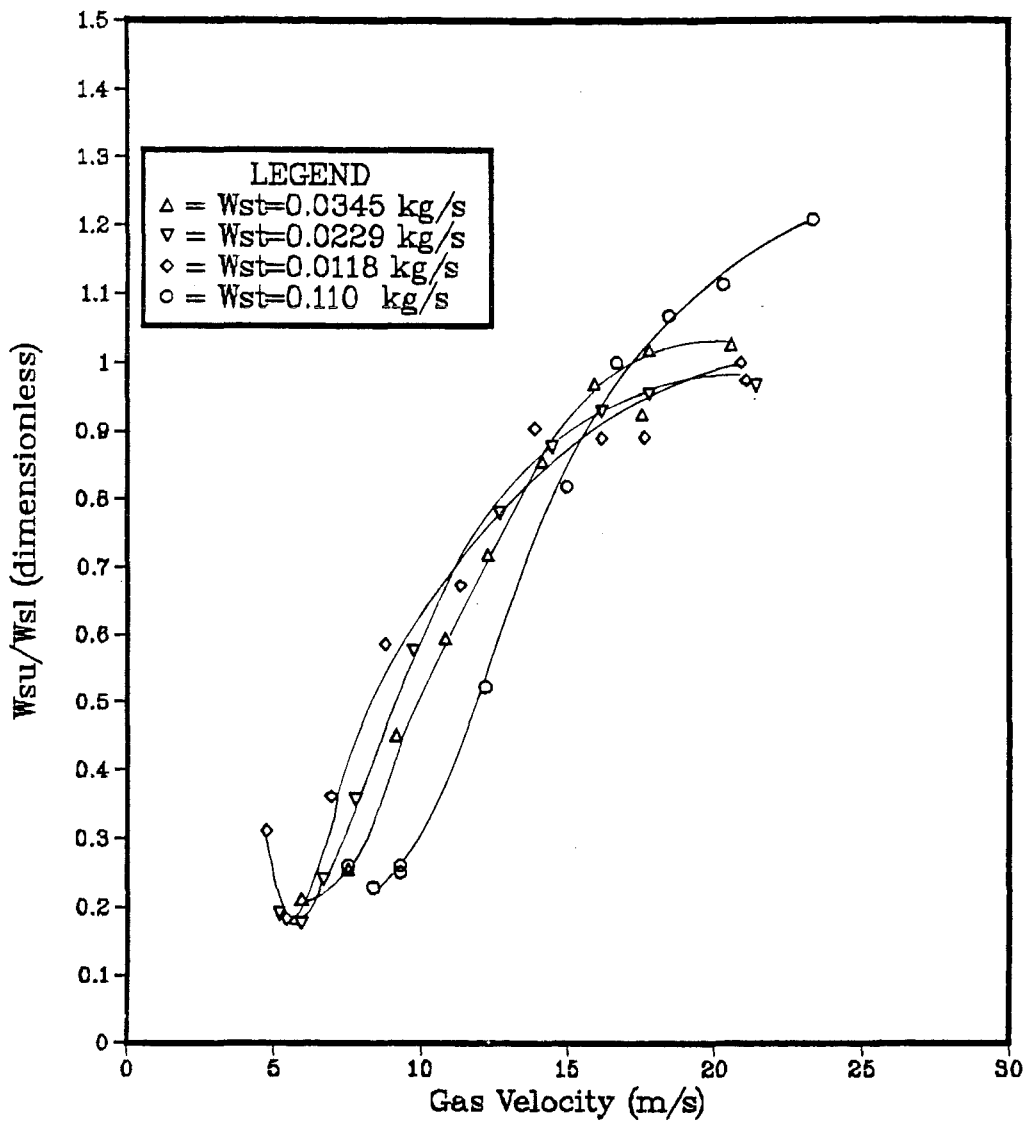


Figure 4-32: $\frac{W_{su}}{W_{sl}}$ vs. U_g for the 450 μ m Glass Beads in the 0.0266 m Diameter System

exceeded unity. This behavior has been reported by Min⁽⁷²⁾ in a study of electrostatic effects, although an explanation for the increase was not given except to state that the presence of an electrostatic potential acting against gravity affected the particle distribution. Another example of this behavior was developed by Tsuji, et. al.⁽⁷³⁾ in a computer simulation which incorporated particle bouncing.

The mass flow distributions in the 0.0504 m diameter pipe were not as large as those in the 0.0266 m diameter pipe. An example is shown in Figure 4-33 for the case of 450 μm glass beads. Again, the mass flow ratio increases with increasing gas velocity but it does not exceed unity. It appears that the mass flow ratio shown in Figure 4-33 levels off at approximately 0.8 for the lower mass flows while the highest mass flow is still increasing at the highest gas velocity studied. Again, system restrictions prevented operation at higher velocities than those shown. Figures showing the mass flow ratio vs. gas velocity for the other systems studied are included in Appendix A.

4.3.3 Electrostatics

It was the intent of this study to eliminate effects due to electrostatics. For the most part, this was accomplished by using sections of copper pipe which were electrically grounded. Also, the relative humidity was

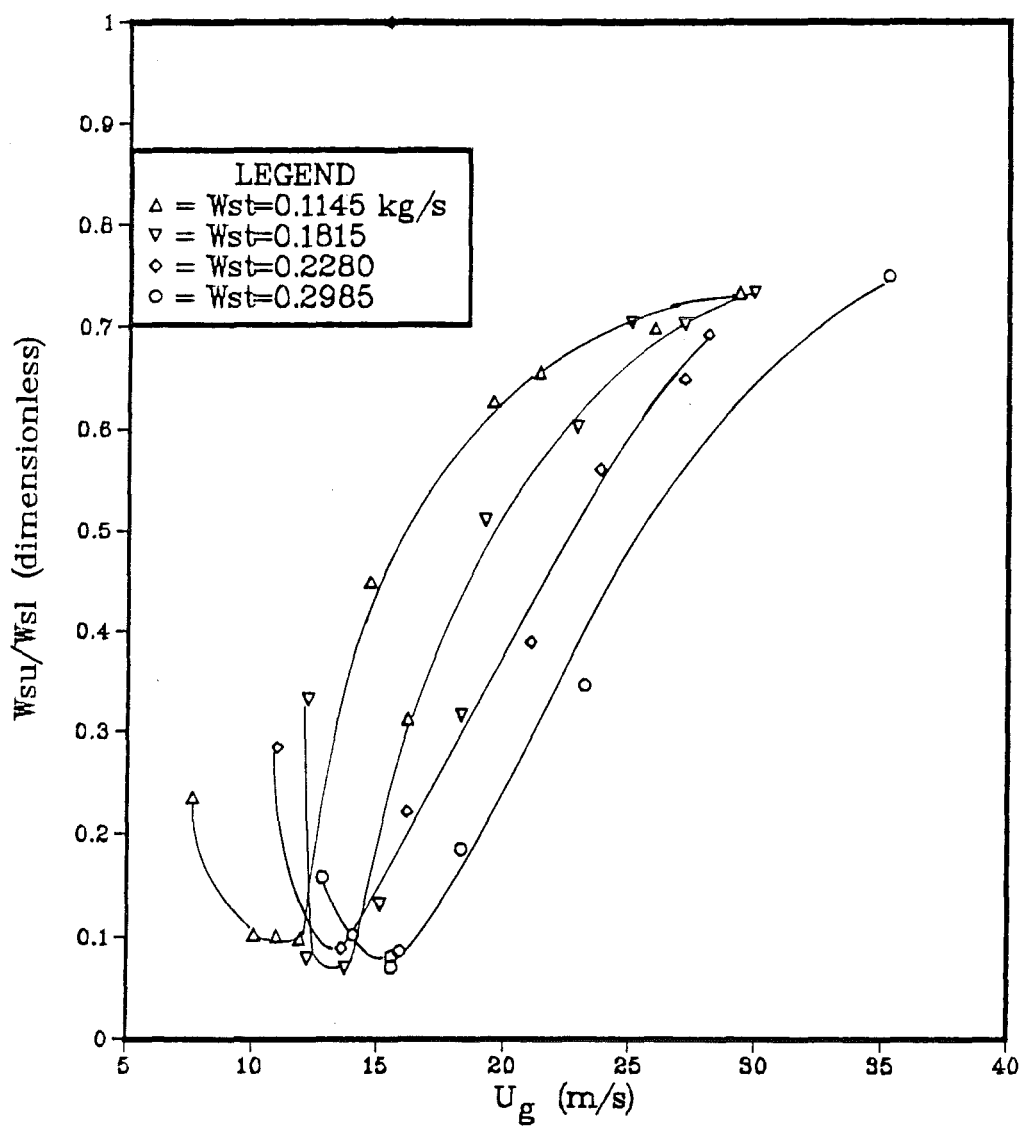


Figure 4-33: $\frac{W_{su}}{W_{sl}}$ vs. U_g for the 450 μ m Glass Beads in the 0.0504 m Diameter System

maintained at suitably high levels to reduce charging. These precautions were sufficient for the glass particles as well as the iron oxide particles but were found to be insufficient in the case of plastic particles. Both PVC and methyl methacrylate particles caused severe electrostatic discharges when transported. This charging was considered severe in that damage to electronic components occurred when discharges from the system happened. For this reason, experiments with the plastic particles were discontinued. The conditions where damaging electrostatics occurred will be reported here. Precautions were continuously taken to avoid these occurrences.

The first case of damaging electrostatic discharging occurred with methyl methacrylate particles in a vertical 0.0506 m diameter system. The pipe material in this system was PVC as the original experimental plan was to use all PVC piping as it is relatively inexpensive and easy to work with. Relative humidity of the transport air was kept above 70 percent. The mass flow rate used was approximately 0.15 kg/s. Small discharges could be heard initially and the presence of electrostatics was obvious. Without prior warning, a loud discharge was heard and the result of this discharge was the destruction of a portion of the DT2818 analog to digital converter. It was felt at this point that the discharge was due to the high mass flow rate of solids

as this flow rate was approximately ten times higher than flow rates investigated previously in this particular equipment.

The second case of damaging electrostatics was in the horizontal 0.0266 m system used for verifying the use of the magnetic coil probes. In this system PVC pipe was again employed but a covering of aluminum foil wrapped with copper braid was applied to the entire pipe. Surface charges from the outside of the pipe were undetectable. As the piping section between the two simultaneous valves had to be opened to determine the mass of solids trapped inside the test section, an assessment of the amount of charging not dissipated through the outer covering of foil was made. It was found that a considerable amount of charge remained on the interior surface of the pipe when opening the union and touching the inside of the pipe wall caused a large electrical shock. Subsequent openings of the pipe were done with a copper braid in direct contact with the interior surface. At this point in the experimentation, the signals from the magnetic probes were measured with an oscilloscope and it was felt that an optical isolation circuit would eliminate damages to the computer system. An isolation circuit was constructed as shown in Figure 4-34. The circuit was tested by operating the system and then bringing a grounded wire in contact with the interior surface of the pipe by touching it to the pressure tap made through the

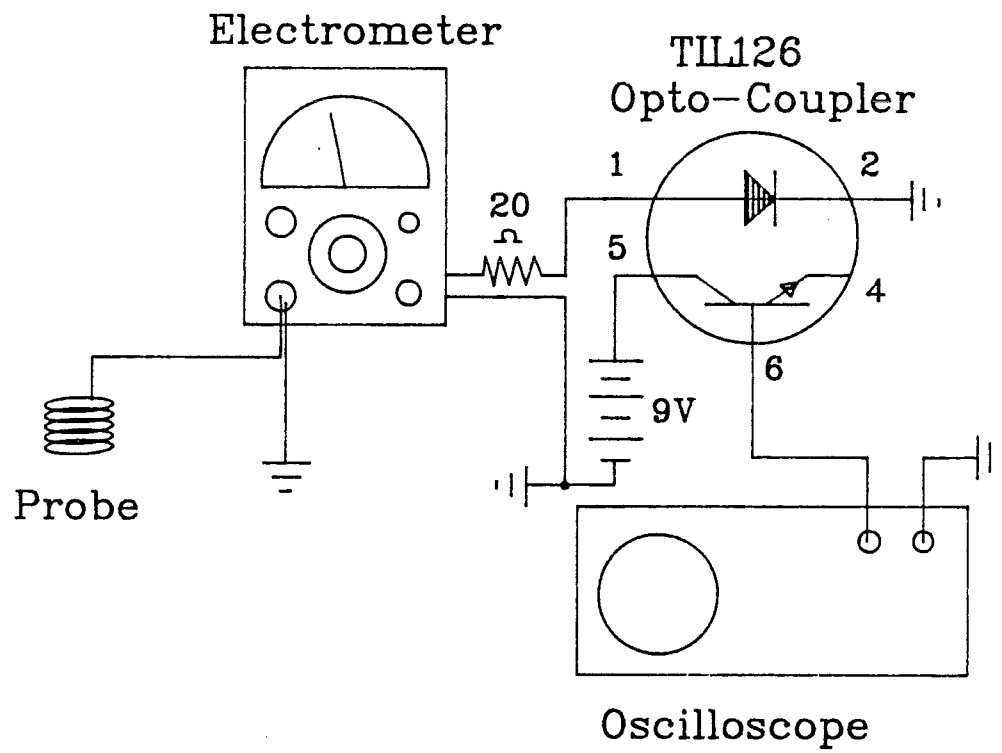


Figure 4-34: Isolation Circuit Designed to Protect from Electrostatic Discharges

pipe wall. Although the isolation circuit as shown worked (the maximum reading on the oscilloscope was 7 volts), the discharge caused the destruction of a portion of the internals of the electrometer. Use of the isolation circuit between the probe and the electrometer caused attenuation of the signal to nearly zero and therefore this circuit was not used.

The third occurrence of damaging electrostatic discharge occurred while conveying PVC particles in the 0.0266 m diameter horizontal system. Copper piping was incorporated into the system however; the test section was of glass and the flow splitter of PVC. It was felt that there would be little electrostatics as the particles were of the same material as the PVC pipe. This was not to be the case. Operating the system with the relative humidity of the air greater than 80 percent and the mass flow rate of the solids at 0.076 kg/s a discharge caused the destruction of the DT2818 analog to digital converter. At this point, experiments with PVC and methyl methacrylate were discontinued.

A fourth case of damaging electrostatic discharging occurred while conveying 450 μm glass beads in an 0.0266 m diameter pipe inclined at 30 degrees. Small discharges could be heard in the system and the computer was disconnected from the electrometers. The pressure transducers were left

connected as it was felt that the electrostatic discharge would have no conductive route to the computer. A large discharge occurred in the vicinity of one of the upstream pressure taps. This discharge caused the destruction of the pressure transducer connected to this tap as well as the destruction of the DT2818 analog to digital converter. It is not clear what condition caused the electrostatic discharge. Also, the only route for the conduction of the discharge was through a 3 m length of plastic tubing used to connect the pressure transducer to the pressure tap.

It is apparent that the nature of electrostatics in pneumatic systems is not fully understood. Taking the normally recommended precaution of high relative humidities was not sufficient to eliminate the buildup and subsequent damaging discharges of electrostatic discharges. This fact should be carefully considered in the conveying of plastics or in the use of non-electrically conductive piping.

5.0 Conclusions

The conclusions based on the experimental results will be divided into the same categories as in Section 4.0, namely:

1. General Conclusions
2. Conclusions on the Thermodynamic Analogy
3. Other Conclusions

5.1 General Conclusions

1. Particle flow in horizontal pipes was observed to occur in three general patterns:

1. Apparent Homogeneous Flow
2. Non-Homogeneous Suspended Flow
3. Separated or Strand Flow

It should be emphasized that these patterns were visually observed. Measurements of the mass flow of solids in the upper and lower halves of the pipe showed that a variation between the upper and lower halves solids flow rates existed at nearly every operating condition.

2. The pressure drop per unit length vs. gas velocity curves for the 0.0266 m diameter system showed an increase in pressure drop with reduction in gas velocity past a minimum point. This increase was not observed in the test

section of the 0.0504 m diameter system. An increase was measured in the acceleration zone. Characteristics of the air delivery system prevented decreases in U_g below the point of saltation near the feed point and; therefore, an increase in pressure drop with reduction in gas velocity could not be obtained.

3. Particle velocities based on cross-correlation of electrostatic signals were measured using two new probes. The technique was verified using void fraction measurements. The magnetic coil probes were inexpensive and easily installed on the pipe, thereby lending their potential for particle velocity measurement high.

4. Comparison of the pressure drop per unit length was made using three correlations. The three correlations used were representative of the types of correlation normally recommended for use in design. The standard relative deviation for all the correlations was approximately 50 percent, with all three correlations generally under predicting.

5. A new correlation for particle velocity was presented based on a modification to the terminal velocity of a single particle. The correlation was presented without justification other than experimental comparison. This correlation was used in a simple force balance to predict

the pressure drop per unit length and was found to predict better than the three standard correlations. In addition to predicting the pressure drop per unit length, the equations used are capable of predicting a minimum point in the pressure drop vs. gas velocity curve. A favorable comparison was made between this minimum point and the minimum point obtained by correlation of Rizk.⁽⁴⁰⁾ Although the correlation has only been tested on the present data set, the above mentioned capability increases its potential utility in design as only one explicit correlation is required. The correlation for particle velocity as well as the expression for friction factor and voidage are given below:

$$U_p = (U_g - U_t^{0.71}) D_t^{0.019} \quad (\text{Note: mks units only})$$

$$f_s = \frac{0.33 \varepsilon^{-4.7} \rho_f (U_f - U_p)^2 D_t}{(\rho_p - \rho_f) D_p U_p^2}$$

$$\varepsilon = 1 - \frac{4W_s}{\pi D_t^2 \rho_p U_p^2}$$

5.2 Application of the Thermodynamic Analogy

6. The thermodynamic analogy to pneumatic transport was applied to horizontal systems. This involved the definition

of two separate solids phases in the flow, a dilute phase which was considered analogous to the gas phase in a thermodynamic system, and a dense phase in the form of a layer or strand, which was considered analogous to a liquid phase. An equilibrium of these phases was observed to occur across a range of conditions.

7. At sufficiently high gas velocities, a single solids phase existed, that being the dilute phase. The ideal gas analog was found to represent the behavior of this type flow with fair accuracy. This was shown to be consistent with measurements of particle velocities from Rizk⁽⁴⁰⁾ as well as the data of this study. A dependency of the ideal transport constant R^* on the pipe diameter was found for two of the four particles used. This dependency may be the result of the limited range of gas velocities obtainable in the larger pipe diameter system.

8. With decrease in gas velocity, the formation of the second phase, that being analogous to a liquid phase, occurred. The cross-sectional area of this phase increased with both increase in solids flow rate as well as with decrease in gas velocity which is analogous to the thermodynamic vapor-liquid system with increase in pressure or decrease in temperature. The van der Waals analog equation was found to be capable of describing the equilibrium between the two phases. The equilibrium solids

flux was assumed to be that of the dilute phase. Using the experimentally determined fluxes and solids fractions the van der Waals analog constants a^* and b^* were determined through regression. A relationship between the system parameters and the constants could not be determined. It was found that the constants a^* and b^* were reduced with increase in pipe diameter suggesting a decrease in particle-particle interactions.

9. A critical point analog was discussed as a point in the flow where the dense phase is indistinguishable from the dilute phase. The experimental range of solids fluxes was far below the critical point predicted with the van der Waals analog equation. A method of estimation of the critical point using the pressure drop vs. gas velocity diagram⁽⁴⁶⁾ was examined for one condition and the results are encouraging but will require data much nearer the critical point to either justify or exclude the use of this method.

10. A method for determining the pressure drop from the van der Waals analog equation was not found. It is felt that a representation of the pressure drop as an energy will require the definition of another property of the flow similar to entropy in a thermodynamic system.

5.3 Other Conclusions

Experimental measurements of particle velocity, pressure drop, and mass flow rate of solids were made in both the upper and lower halves of the pipe. These measurements show that there can be significant differences in the flow between the top and bottom of the pipe. These differences are especially pronounced at lower gas velocities.

11. Pressure drop along the pipe was measured at the top and bottom of the pipe. Under most conditions, these measurements were identical. An increase in pressure drop in the upper half of the pipe was observed in the 0.0266 m diameter system at high gas velocities. This increase might be attributed to the gas velocity profile or to the increased solids friction in the upper half of the pipe.

12. Solids velocities were measured in the upper and lower halves of the pipe and were found to be equal for high gas velocities. With reduction in gas velocity the solids velocities were no longer equal, with the upper velocity normally found to be greater. This was especially true for the condition of strand type flow.

13. Mass flow of solids between the upper and lower halves of the pipe showed a peculiar behavior in the 0.0266 m diameter system. At higher gas velocities, a greater solids

flow rate was found in the upper half of the pipe. This was only true for the two particles which were not spherical and was not seen at all in the 0.0504 m diameter system. An explanation for this behavior may be that an electrostatic force was generated in the flow splitter which caused a lift in opposition to the gravitational force. As the flow splitter was not transparent, the behavior of the solids inside the splitter could not be observed.

In general, the ratio of the solids flow in the top of the pipe to that in the lower half of the pipe decreased with decrease in gas velocity to a point and then increased. This increase at low gas velocity may be due to the increase in particle velocity in the upper half of the pipe.

14. The standard deviation in pressure drop was considered representative of the fluctuation in pressure drop. For particles other than the 67 μm glass beads the fluctuations went through a minimum with decrease in gas velocity. The 67 μm glass beads showed a generally random magnitude of pressure drop fluctuation with change in gas velocity.

As the pressure drop was obtained in both the upper and lower halves of the pipe, pressure drop fluctuation between the upper and lower halves was also obtained. The difference between these two measurements was found to be negligible in the 0.0504 m diameter system. In the 0.0266 m diameter system there was a noticeable difference between

these two measurements which was more pronounced at lower gas velocities.

15. Damaging effects of electrostatics were experienced during experiments with plastic particles and PVC pipes. Precautions to avoid the generation of electrostatics such as grounding conductive portions of the system piping and high relative humidities did not completely eliminate charging or prevent discharges severe enough to destroy electronic equipment. For this reason, it is recommended that electrostatic effects be carefully considered in applications of PVC piping or plastic particles in non-metallic pneumatic systems.

APPENDIX A

APPENDIX A

Figures of Experimental Data Not Included in Text

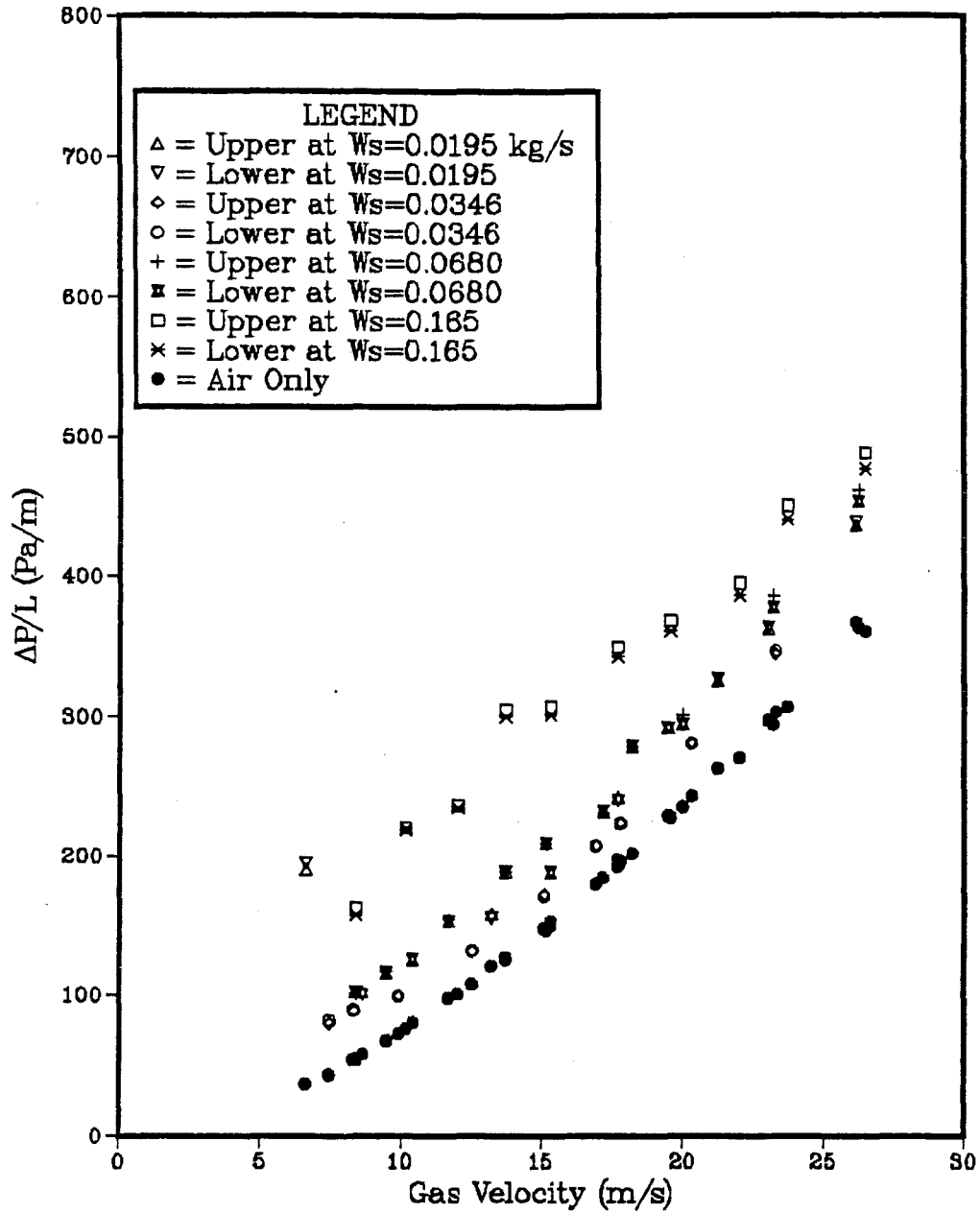


Figure A-1: Pressure Drop vs Gas Velocity for the 0.0266 m Diameter System Using 67 μm Glass Beads.

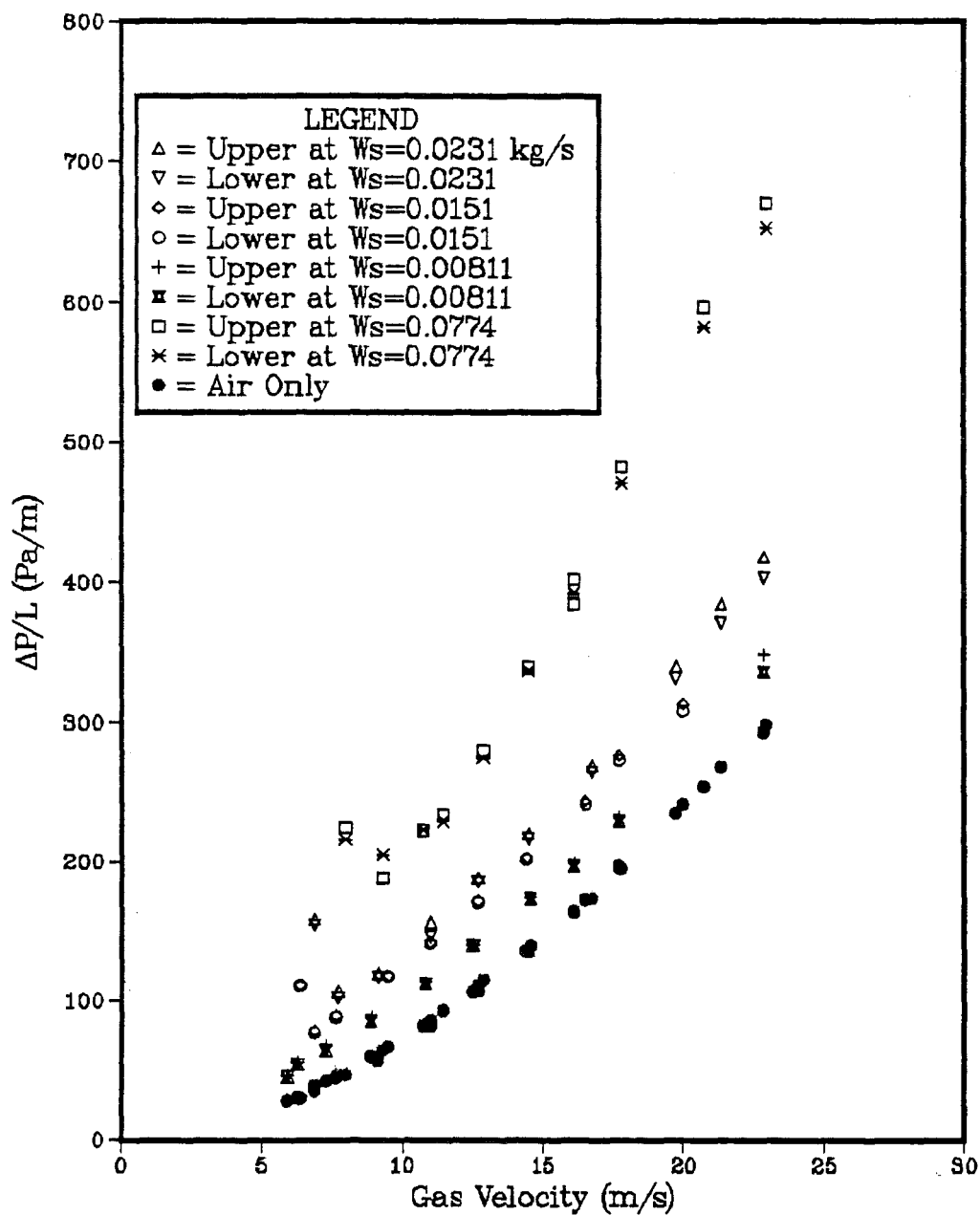


Figure A-2: Pressure Drop vs Gas Velocity for the 0.0266 m Diameter System Using 900 μ m Glass Beads.

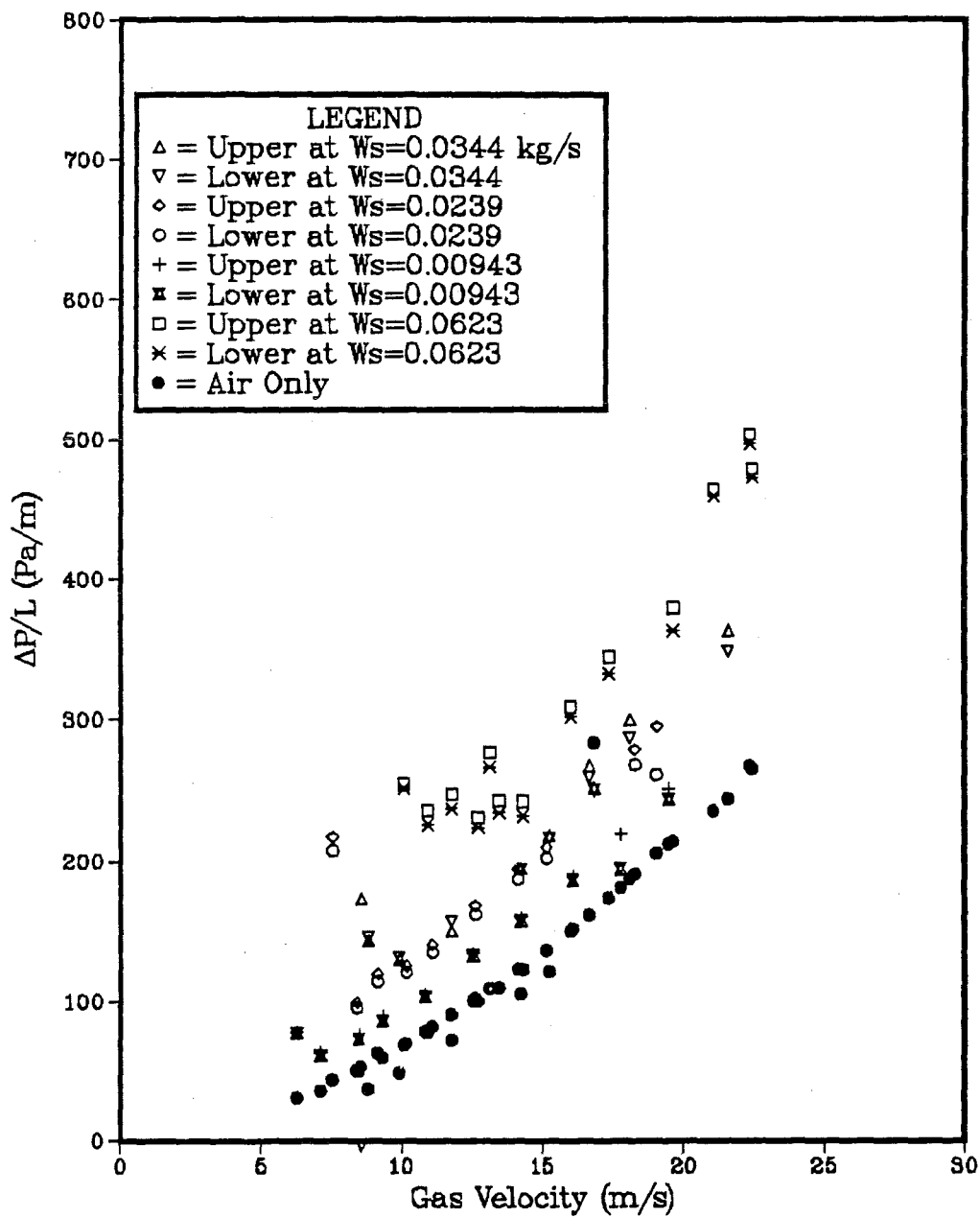


Figure A-3: Pressure Drop vs Gas Velocity for the 0.0266 m Diameter System Using 400 μ m Iron Oxide.

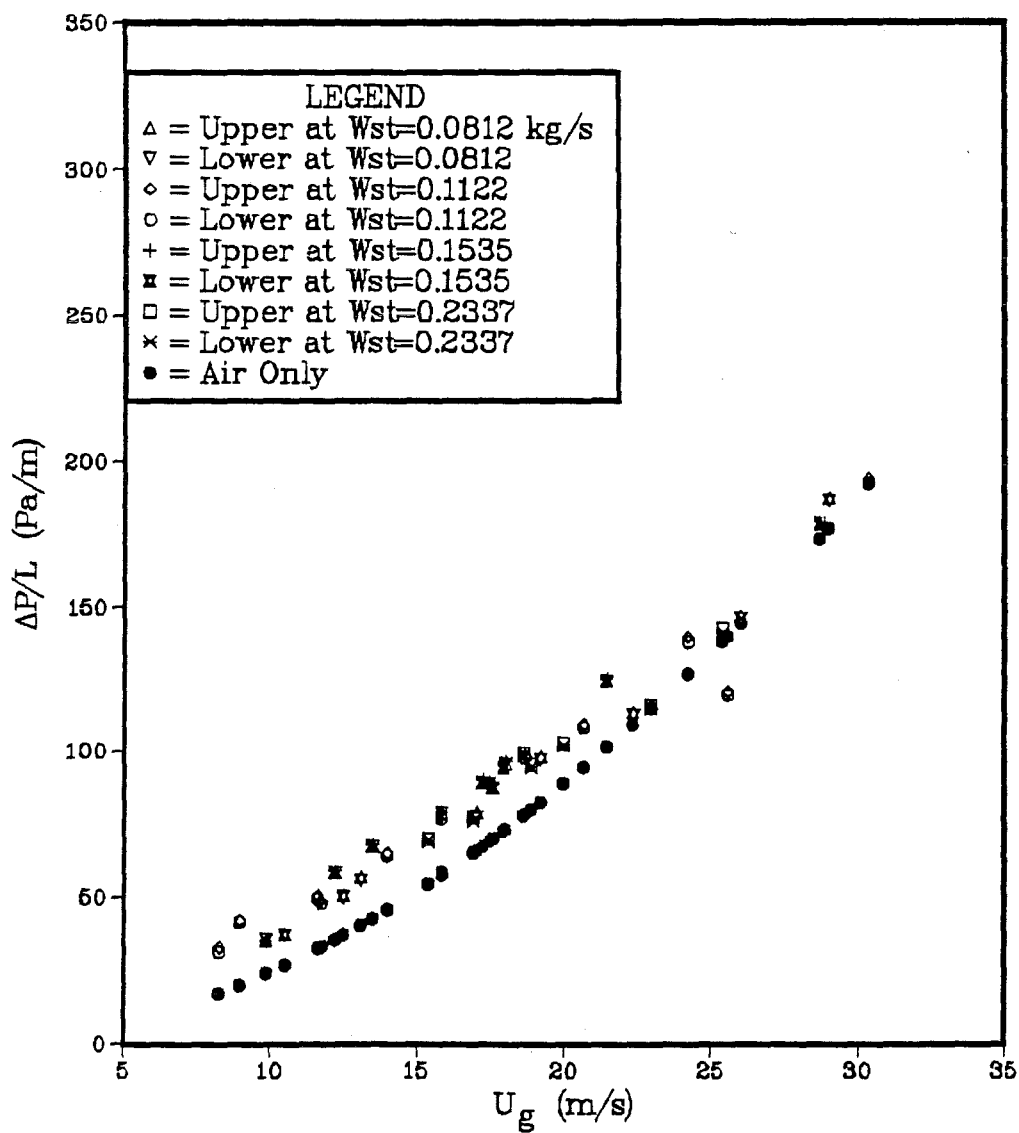


Figure A-4: Pressure Drop vs Gas Velocity for the 0.0504 m Diameter System Using 67 μm Glass Beads.

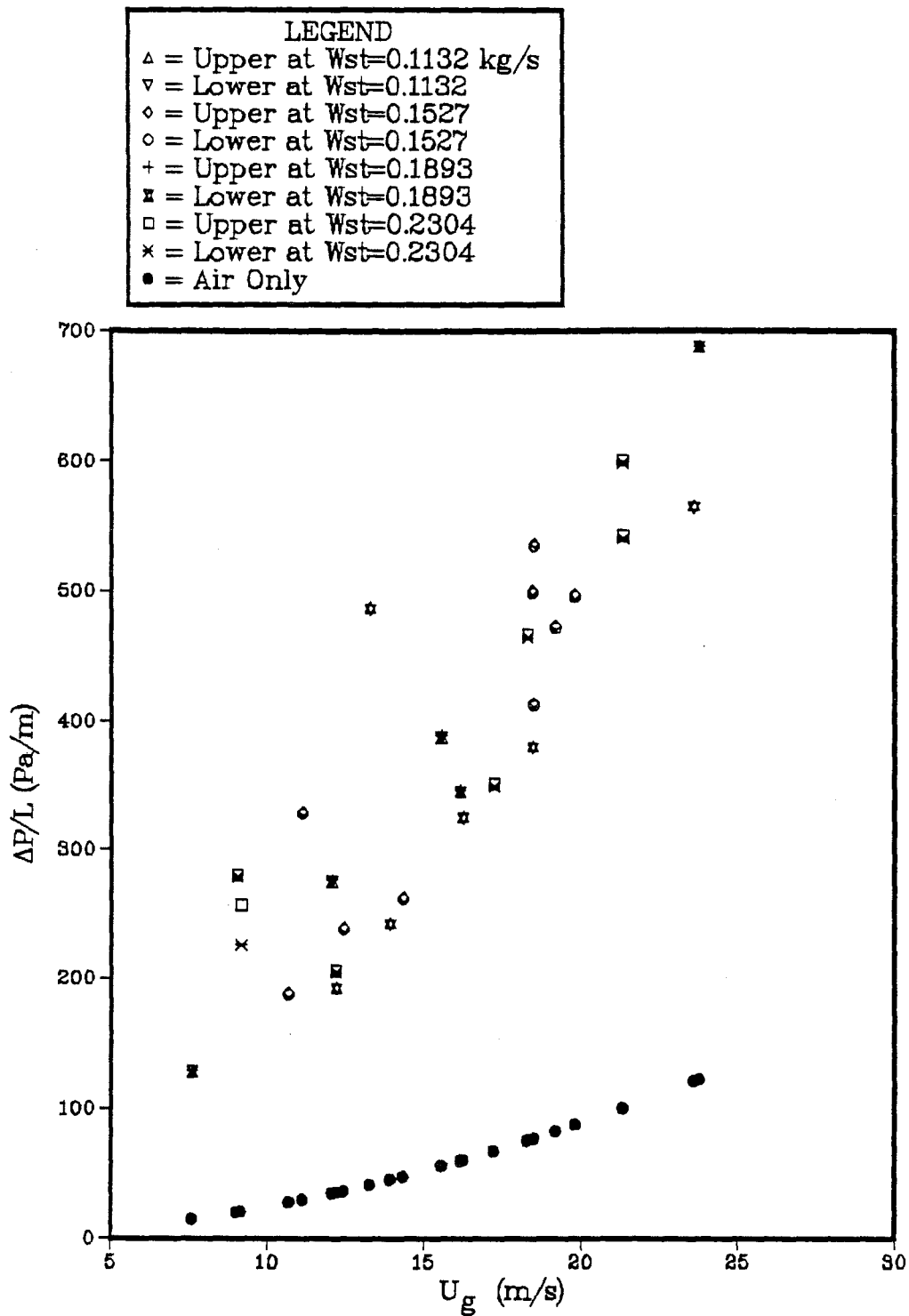


Figure A-5: Pressure Drop vs Gas Velocity for the 0.0504 m Diameter System Using 900 μ m Glass Beads.

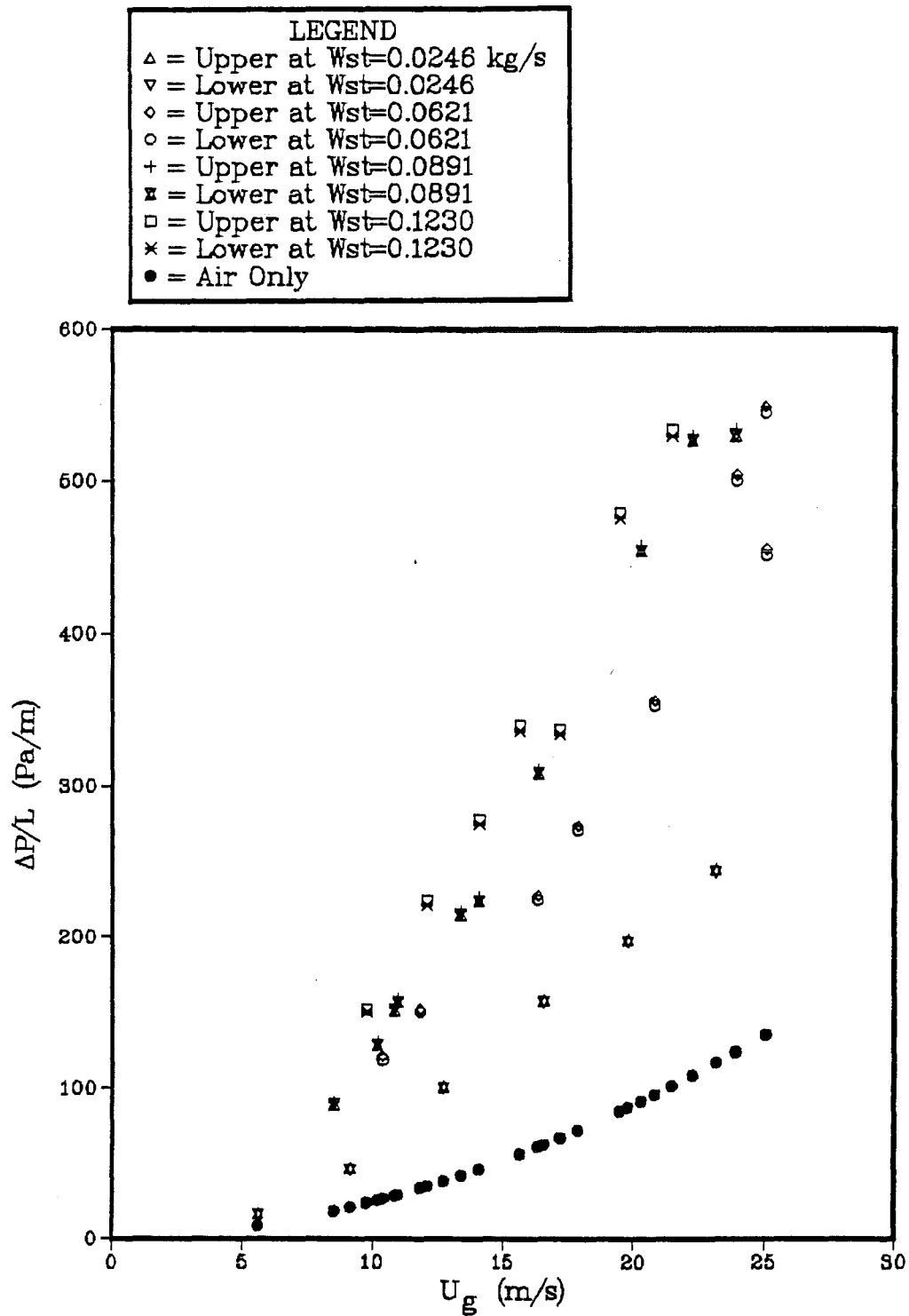


Figure A-6: Pressure Drop vs Gas Velocity for the 0.0504 m Diameter System Using 400 μ m Iron Oxide.

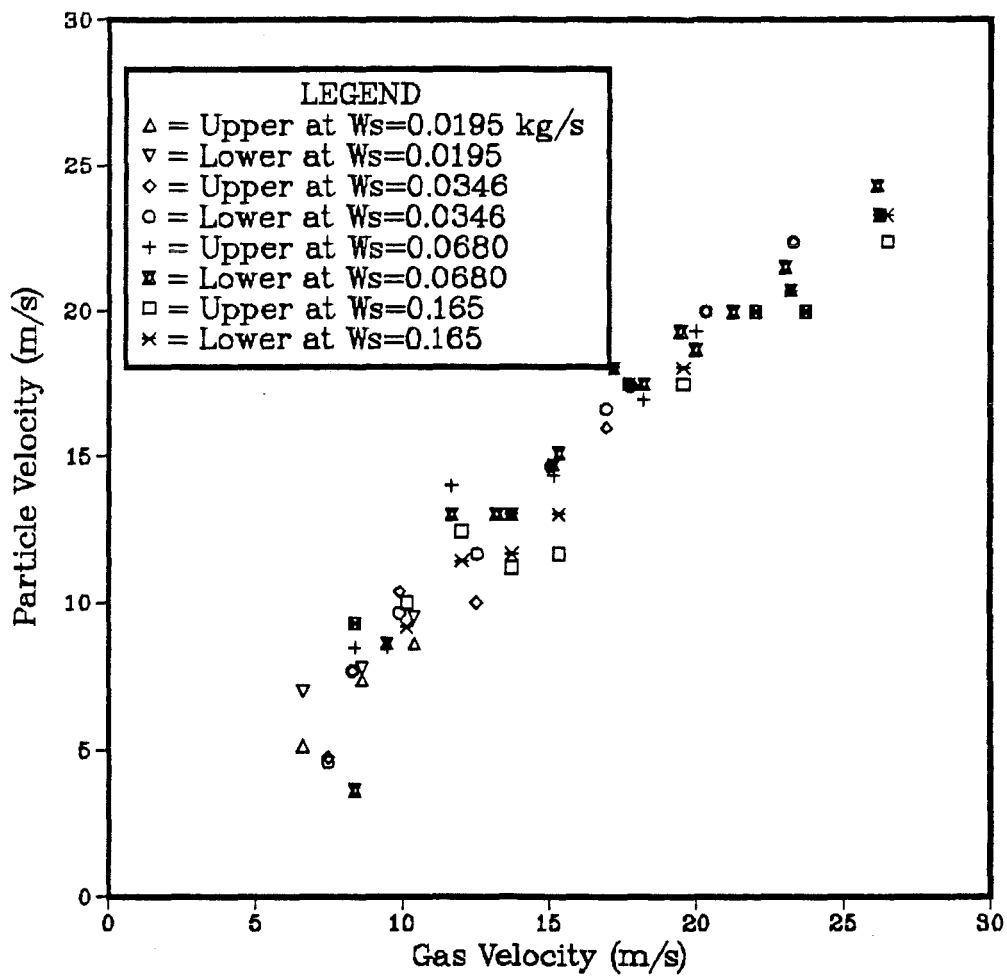


Figure A-7: U_p vs. U_g for the 67 μ m Glass Beads in the 0.0266 m Diameter Bench Scale System.

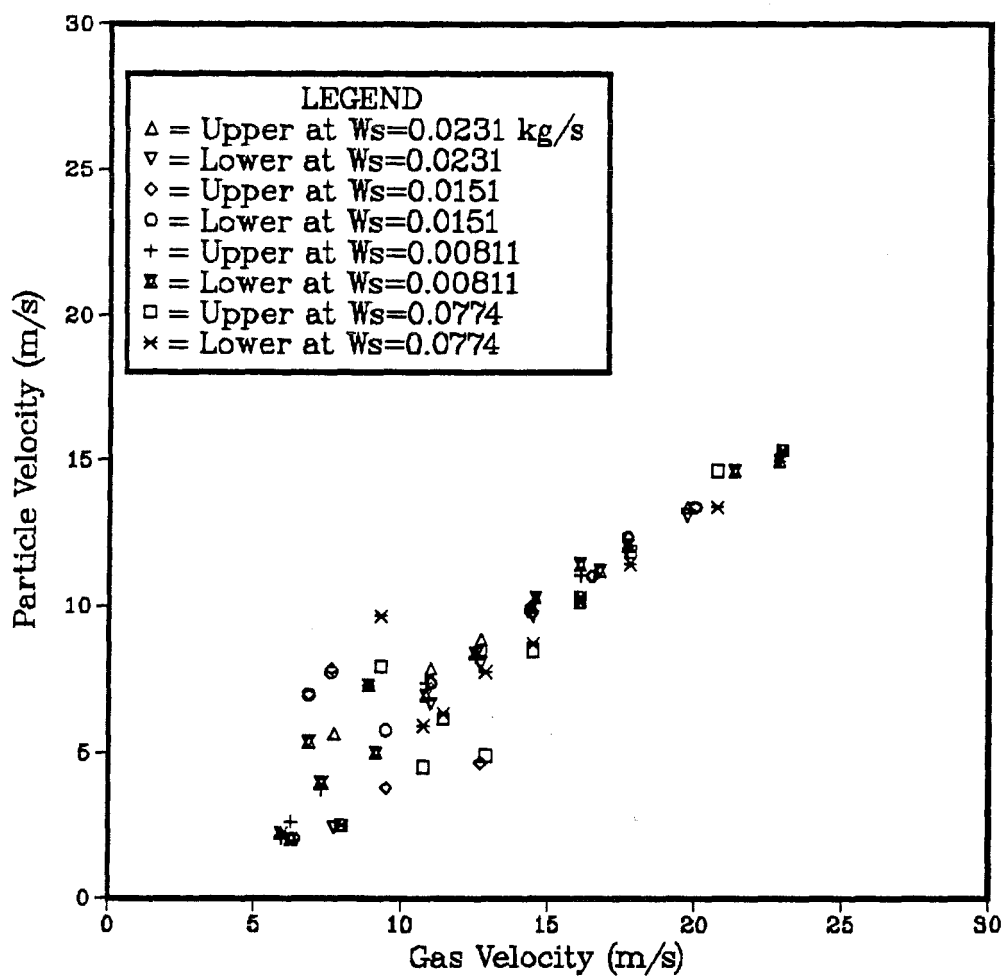


Figure A-8: U_p vs. U_g for the 900 μm Glass Beads in the 0.0266 m Diameter Bench Scale System.

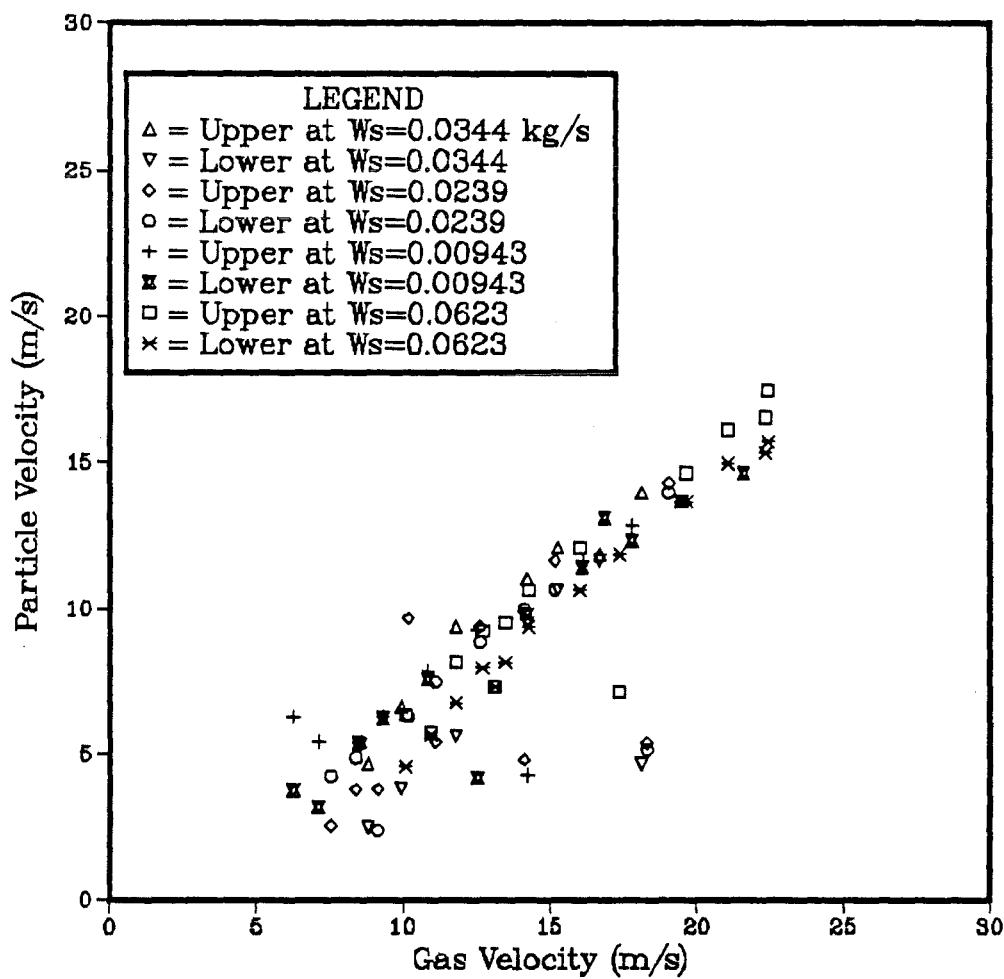


Figure A-9: U_p vs. U_g for the 400 μ m Iron Oxide in the 0.0266 m Diameter Bench Scale System.

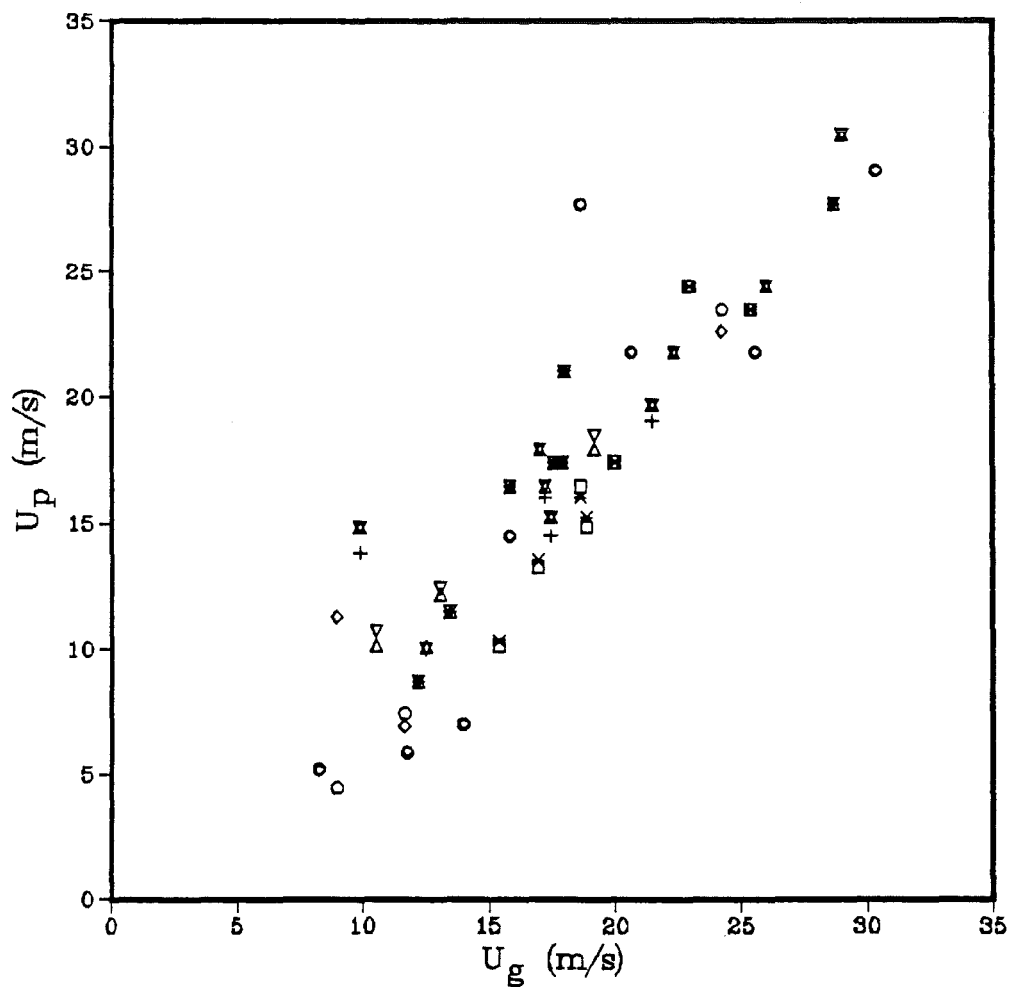
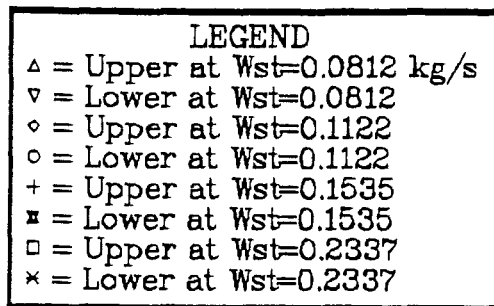


Figure A-10: U_p vs. U_g for the 67 μ m Glass Beads in the 0.0504 m Diameter Full Scale System.

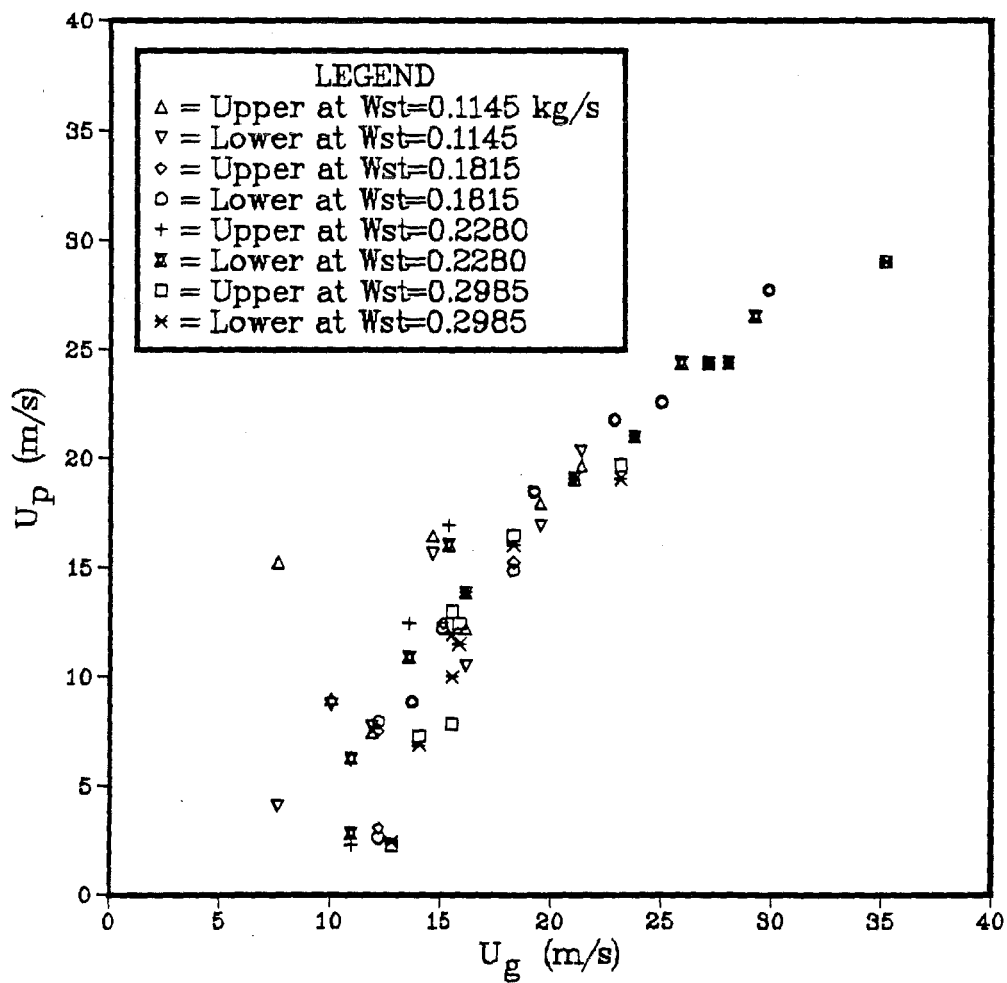


Figure A-11: U_p vs. U_g for the 450 μ m Glass Beads in the 0.0504 m Diameter Full Scale System.

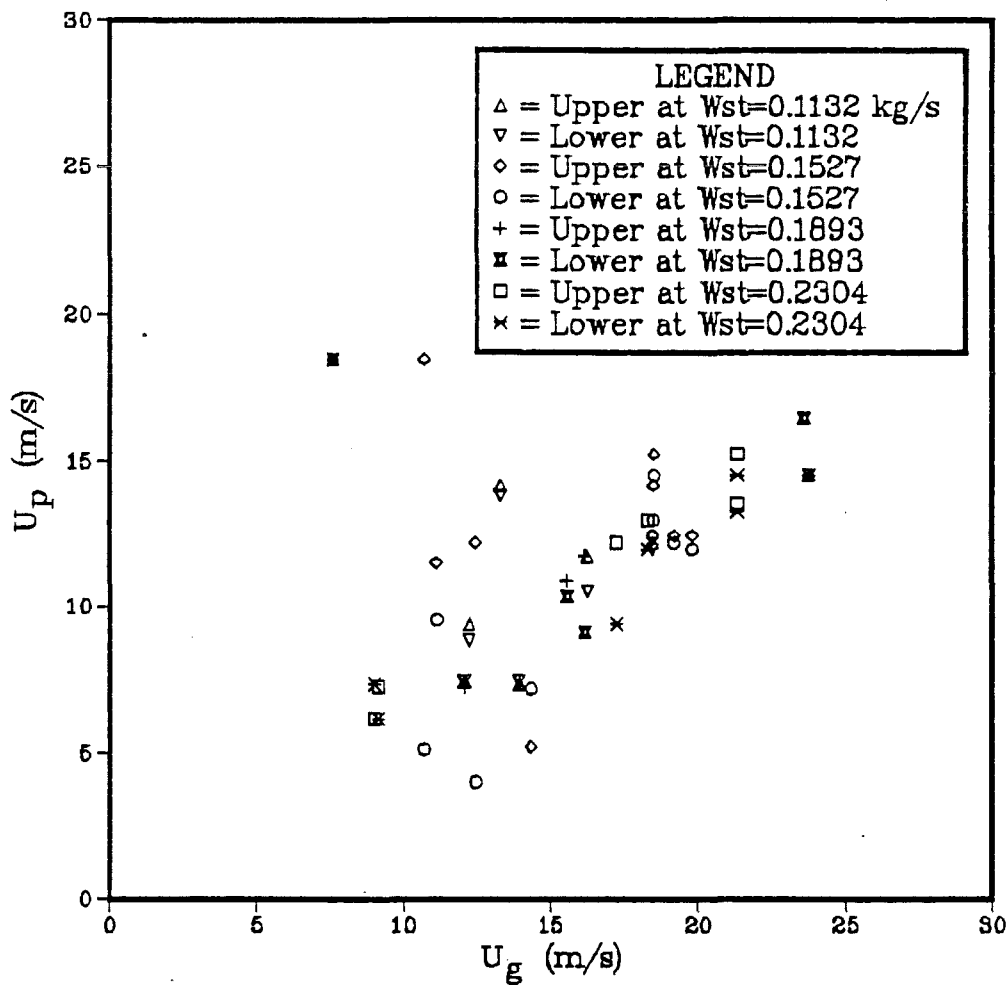


Figure A-12: U_p vs. U_g for the 900 μ m Glass Beads in the 0.0504 m Diameter Full Scale System.

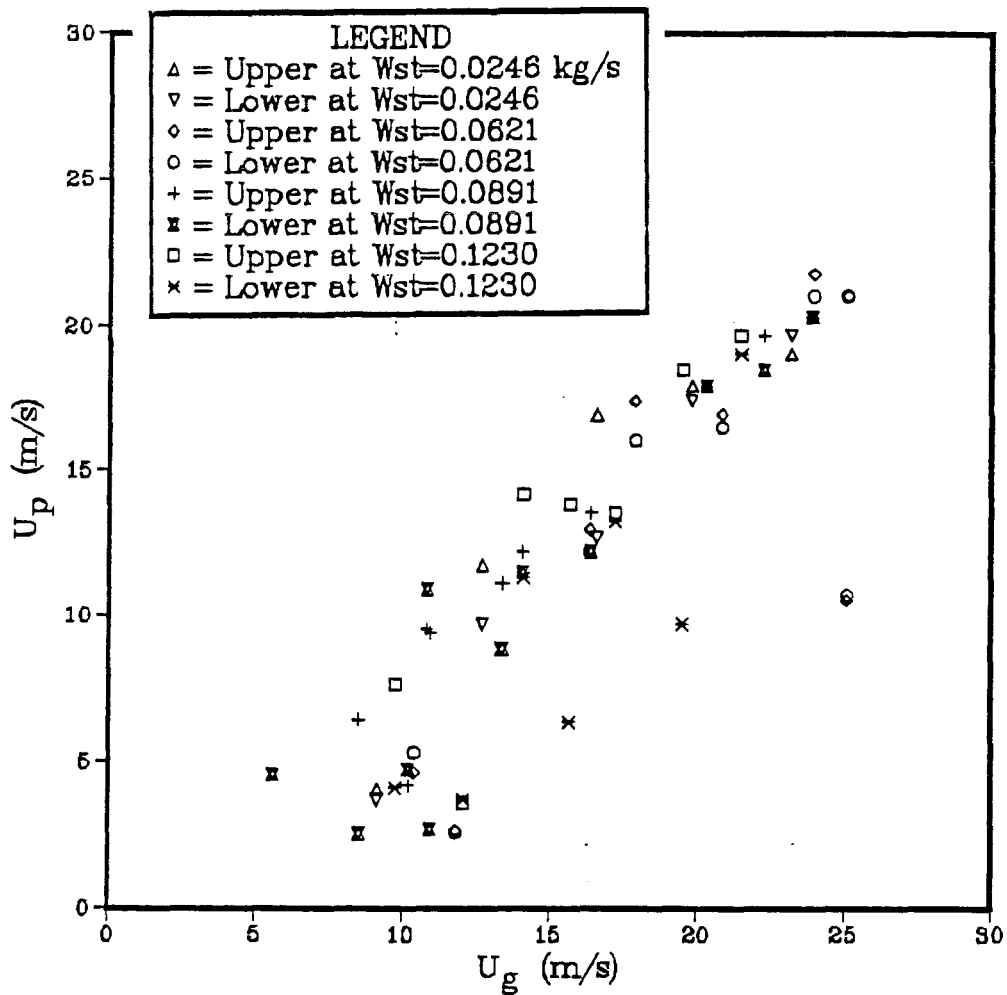


Figure A-13: U_p vs. U_g for the 400 μ m Iron Oxide in the 0.0504 m Diameter Full Scale System.

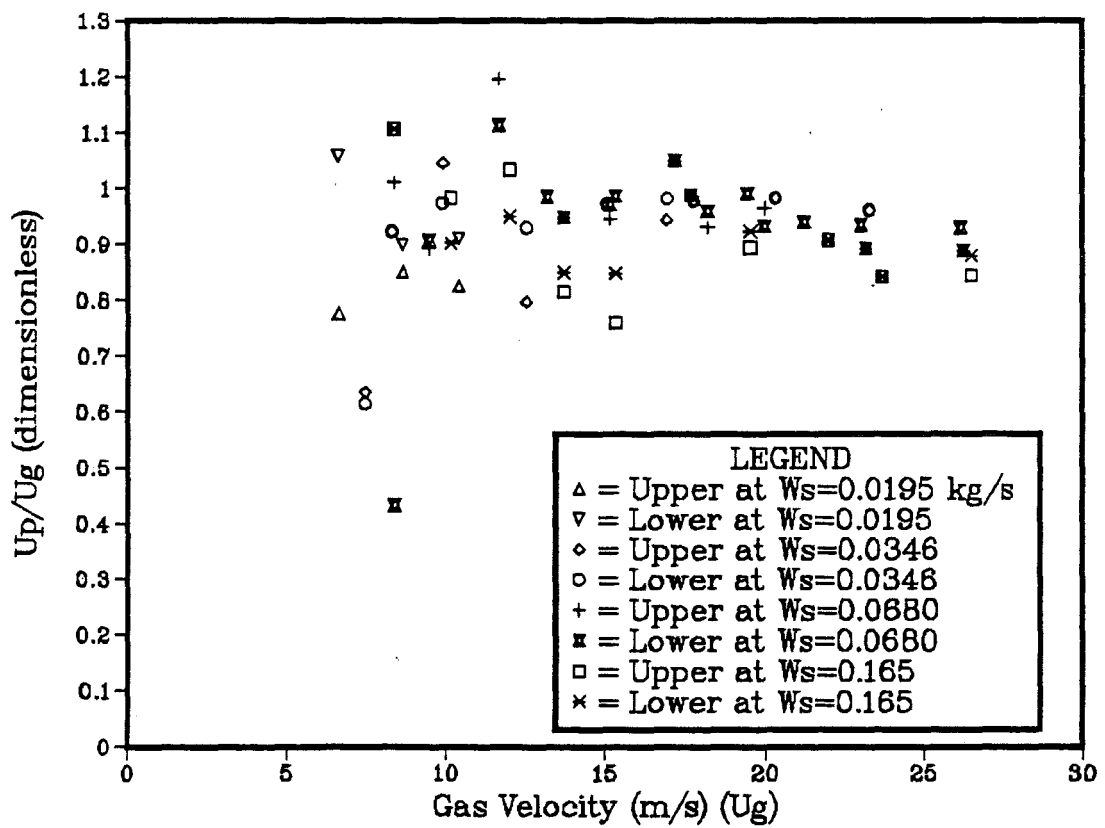


Figure A-14: U_p/U_g vs. U_g for the 67 μ m Glass Beads in the 0.0266 m Diameter Bench Scale System.

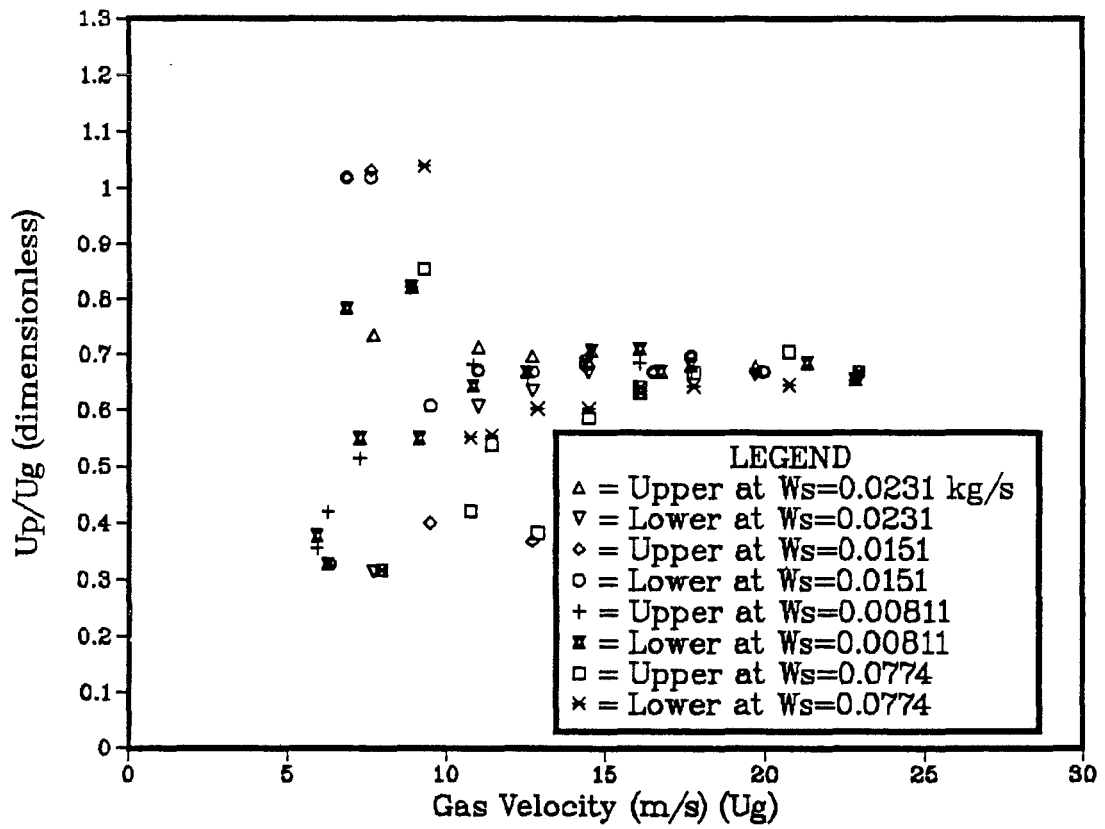


Figure A-15: U_p/U_g vs. U_g for the 900 μ m Glass Beads in the 0.0266 m Diameter Bench Scale System.

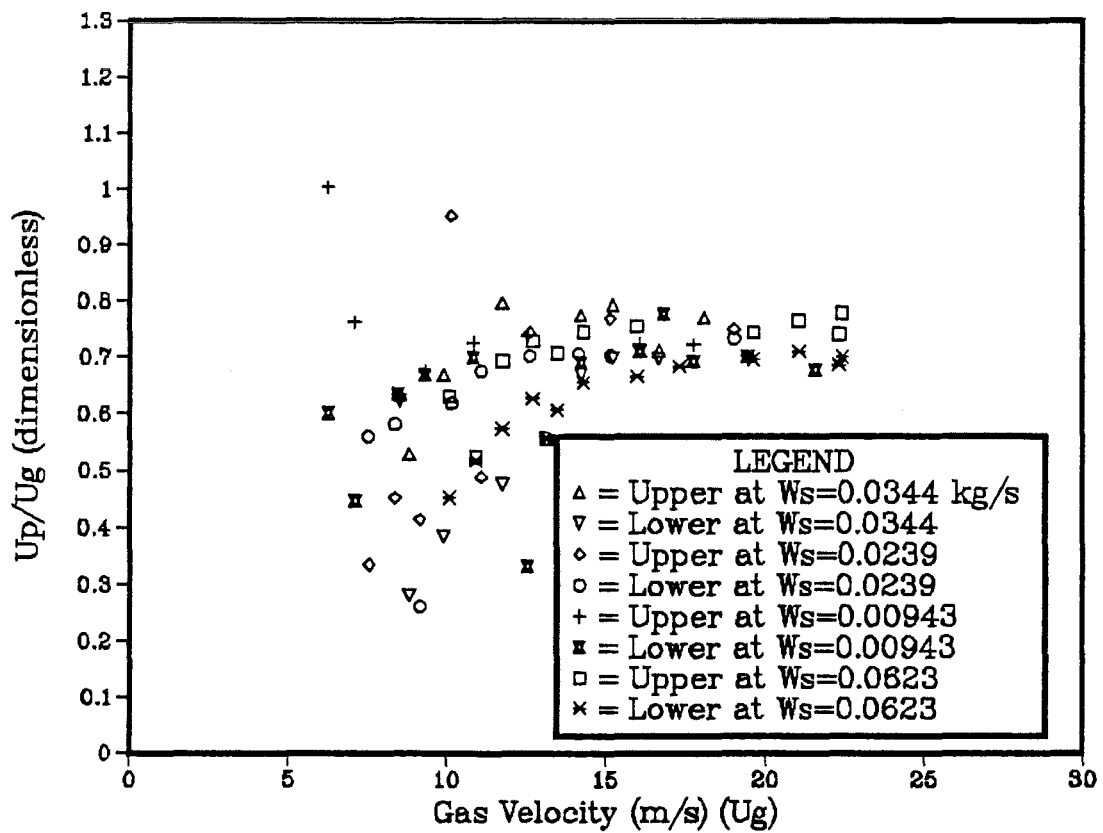


Figure A-16: U_p/U_g vs. U_g for the 400 μ m Iron Oxide in the 0.0266 m Diameter Bench Scale System.

LEGEND
△ = Upper at Wst=0.0812 kg/s
▽ = Lower at Wst=0.0812
◇ = Upper at Wst=0.1122
○ = Lower at Wst=0.1122
+ = Upper at Wst=0.1535
■ = Lower at Wst=0.1535
□ = Upper at Wst=0.2337
× = Lower at Wst=0.2337

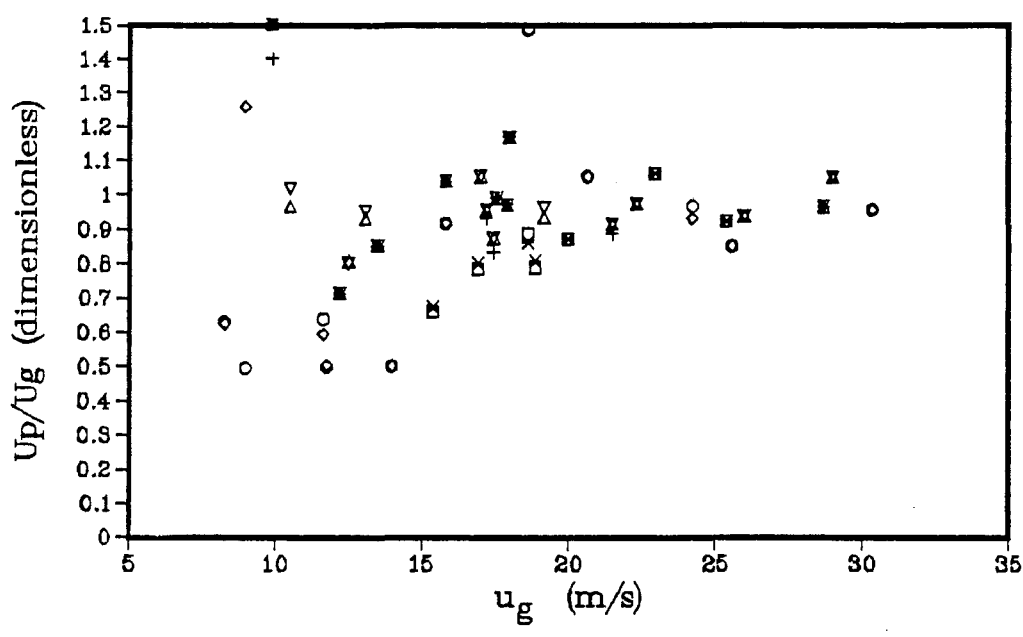


Figure A-17: U_p/U_g vs. U_g for the 67µm Glass Beads in the 0.0504 m Diameter Full Scale System.

LEGEND	
Δ	= Upper at Wst=0.1132 kg/s
∇	= Lower at Wst=0.1132
\diamond	= Upper at Wst=0.1527
\circ	= Lower at Wst=0.1527
$+$	= Upper at Wst=0.1893
\boxtimes	= Lower at Wst=0.1893
\square	= Upper at Wst=0.2304
\times	= Lower at Wst=0.2304

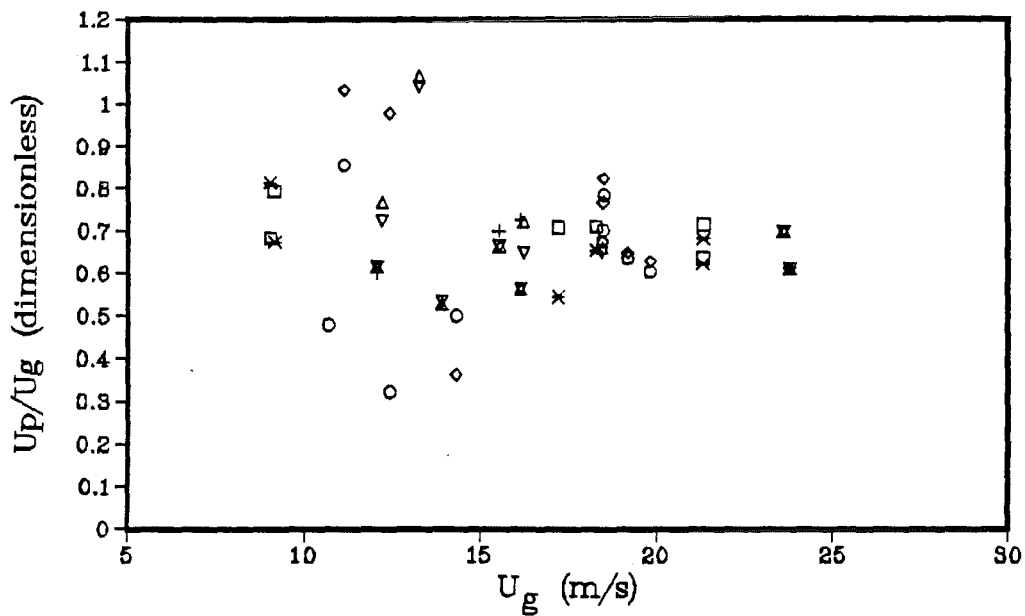
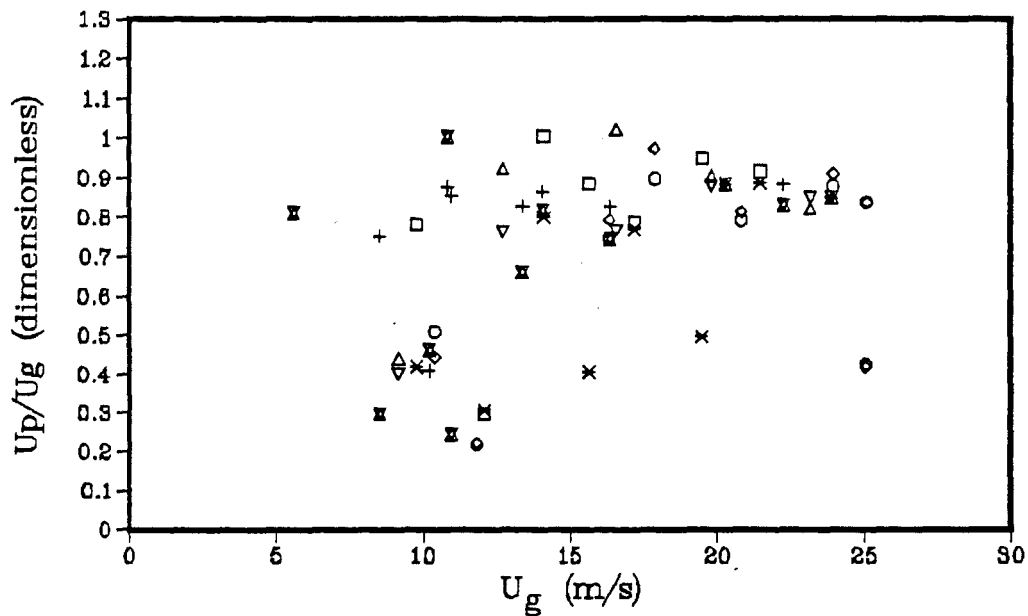
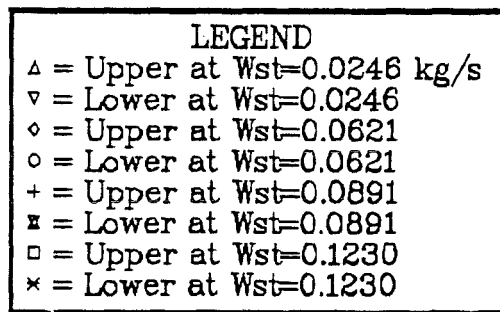


Figure A-18: U_p/U_g vs. U_g for the 900 μ m Glass Beads in the 0.0504 m Diameter Full Scale System.



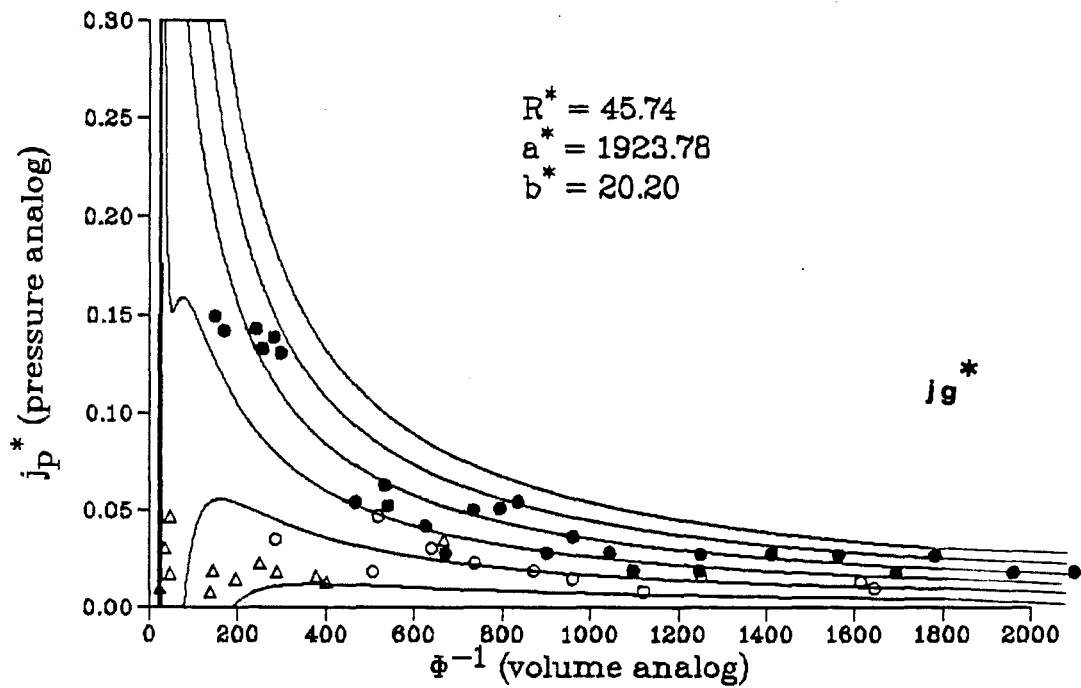


Figure A-20: j_p^* vs. ϕ^{-1} for the 67 μm Glass Beads in the 0.0266 m Diameter Bench Scale System with Lines of Constant j_g^* from the van der Waals Analog Equation Superimposed.

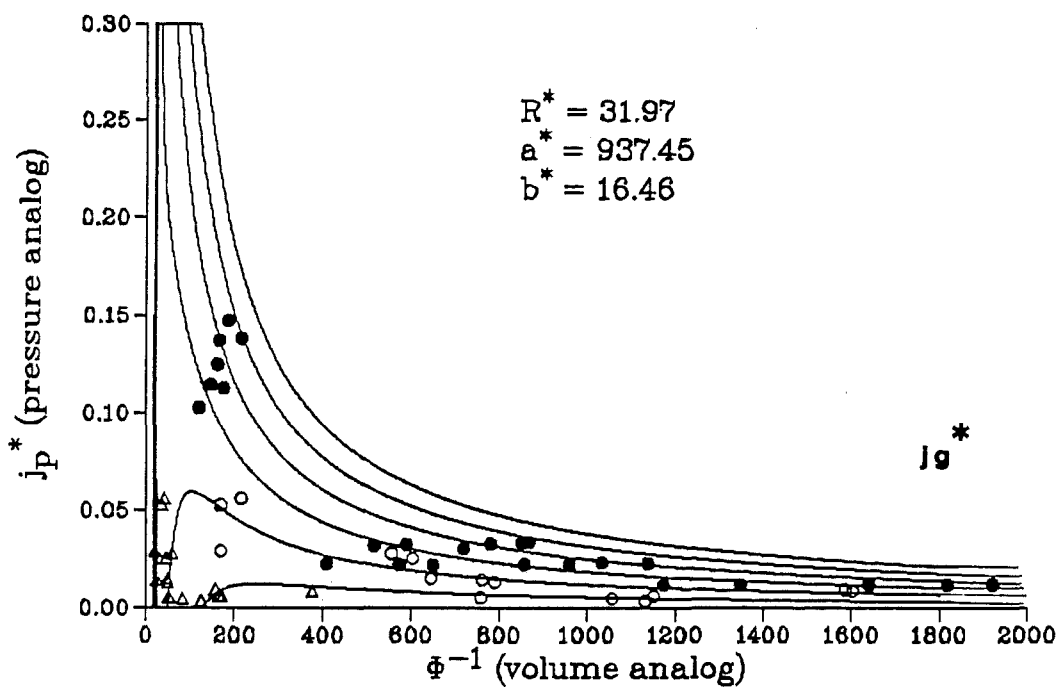


Figure A-21: j_p^* vs. Φ^{-1} for the 900 μm Glass Beads in the 0.0266 m Diameter Bench Scale System with Lines of Constant j_g^* from the van der Waals Analog Equation Superimposed.

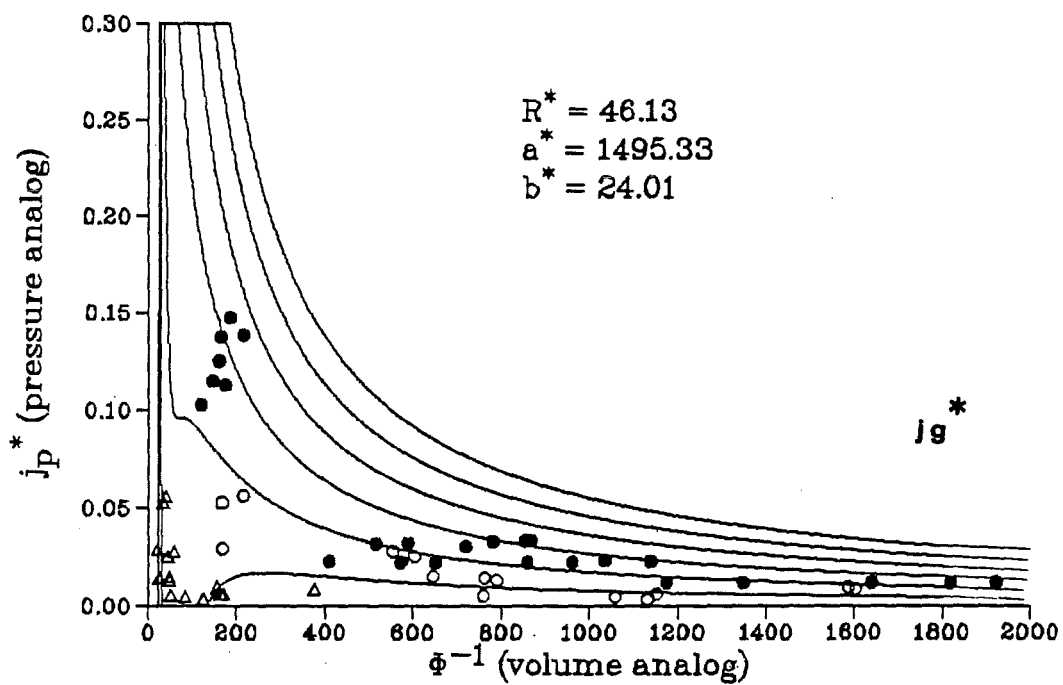


Figure A-22: j_p^* vs. ϕ^{-1} for the 400 μm Iron Oxide in the 0.0266 m Diameter Bench Scale System with Lines of Constant j_g^* from the van der Waals Analog Equation Superimposed.

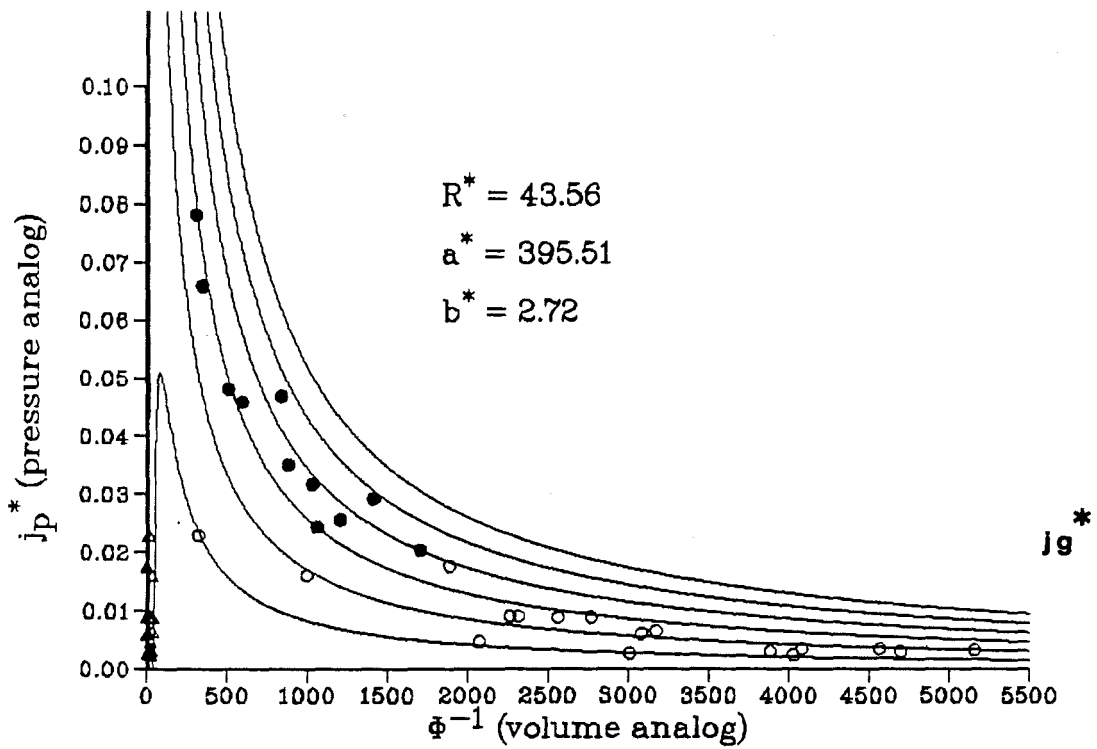


Figure A-23: j_p^* vs. Φ^{-1} for the 67 μm Glass Beads in the 0.0504 m Diameter Full Scale System with Lines of Constant j_g^* from the van der Waals Analog Equation Superimposed.

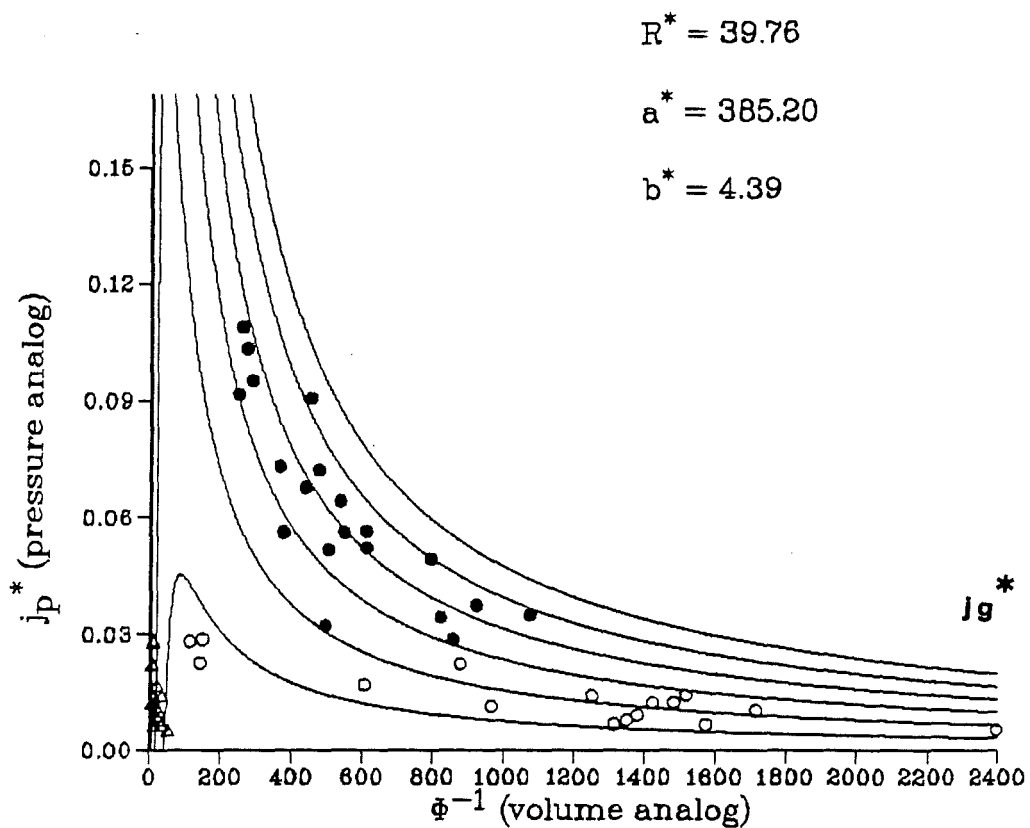


Figure A-24: j_p^* vs. Φ^{-1} for the 450 μm Glass Beads in the 0.0504 m Diameter Full Scale System with Lines of Constant j_g^* from the van der Waals Analog Equation Superimposed.

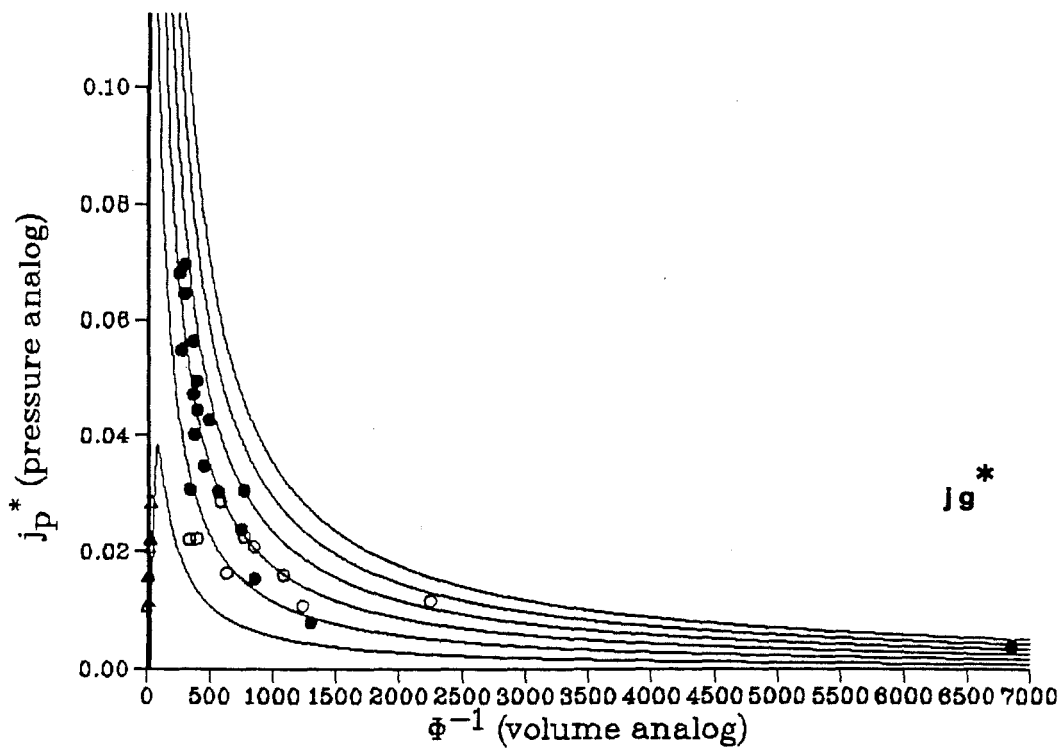


Figure A-25: j_p^* vs. Φ^{-1} for the 900 μm Glass Beads in the 0.0504 m Diameter Full Scale System with Lines of Constant j_g^* from the van der Waals Analog Equation Superimposed.

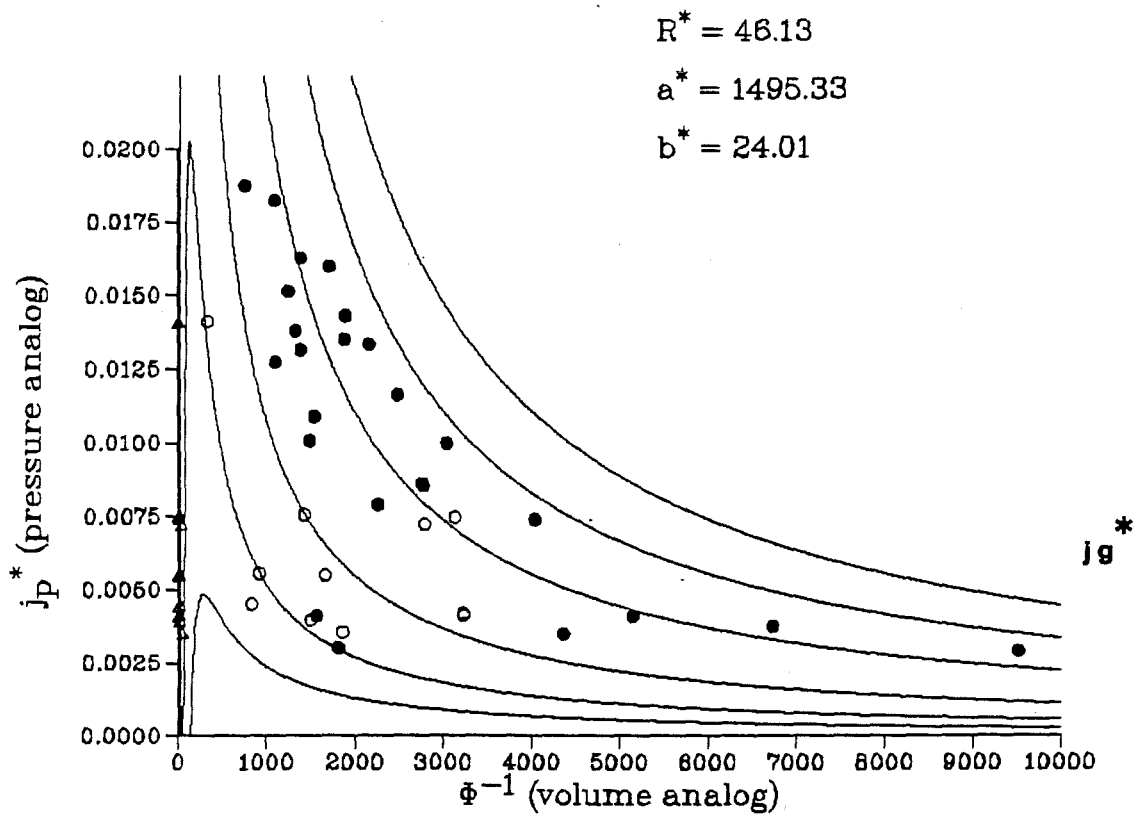


Figure A-26: j_p^* vs. Φ^{-1} for the 400 μm Iron Oxide in the 0.0266 m Diameter Bench Scale System with Lines of Constant j_g^* from the van der Waals Analog Equation Superimposed.

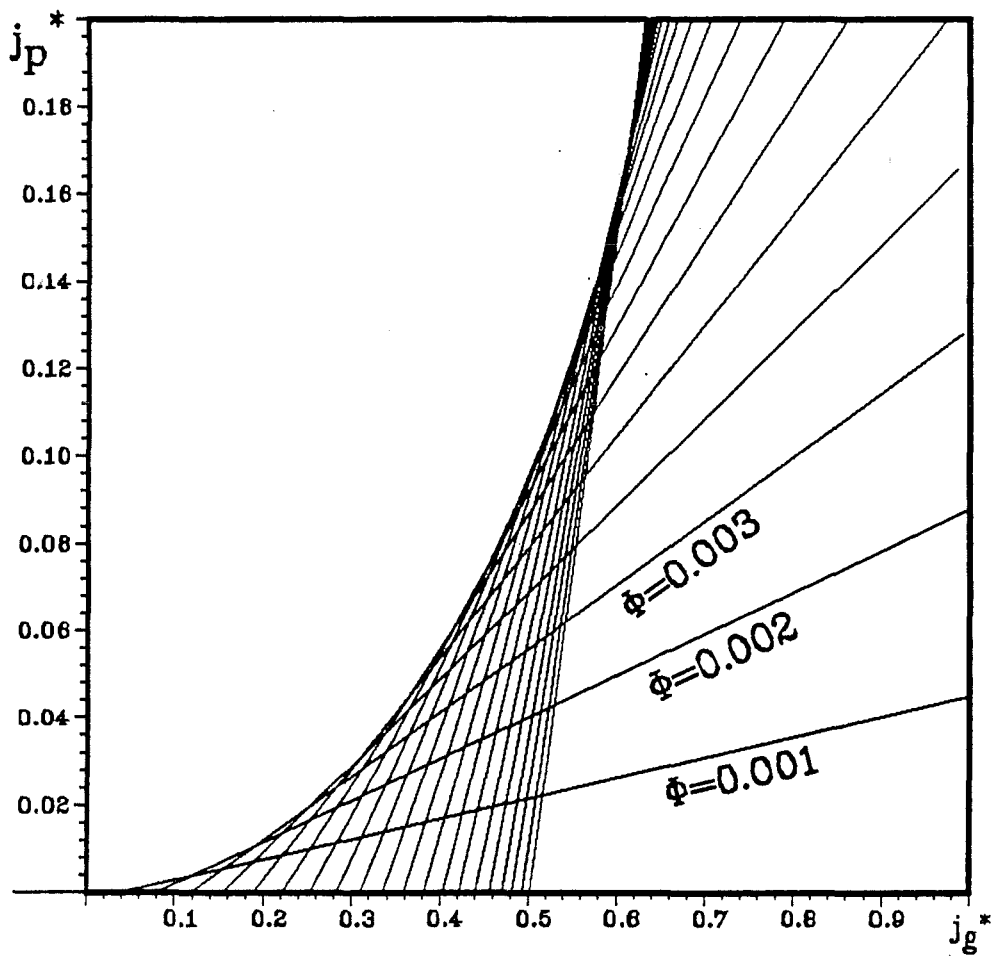


Figure A-27: j_p^* vs. j_g^* for the 67 μm Glass Beads in the 0.0266 m Diameter Bench Scale System with Lines of Constant Φ .

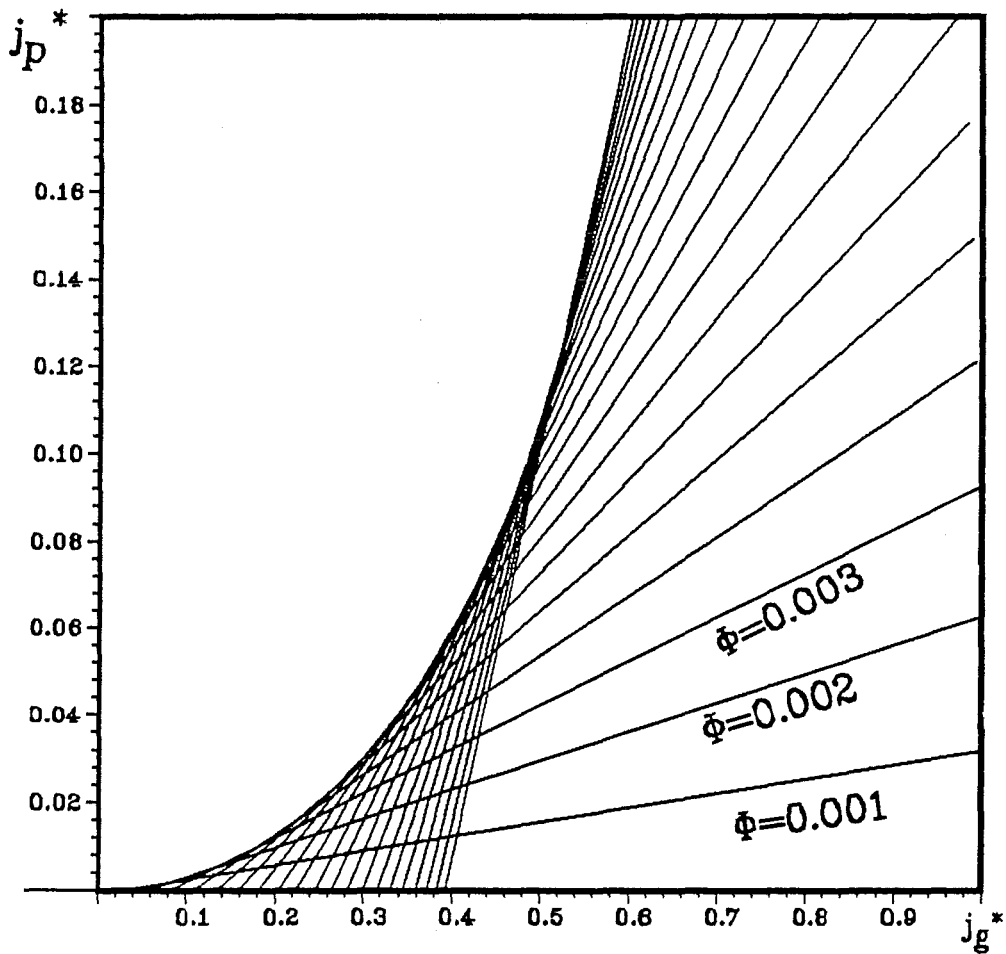


Figure A-28: j_p^* vs. j_g^* for the 900 μm Glass Beads in the 0.0266 m Diameter Bench Scale System with Lines of Constant Φ .

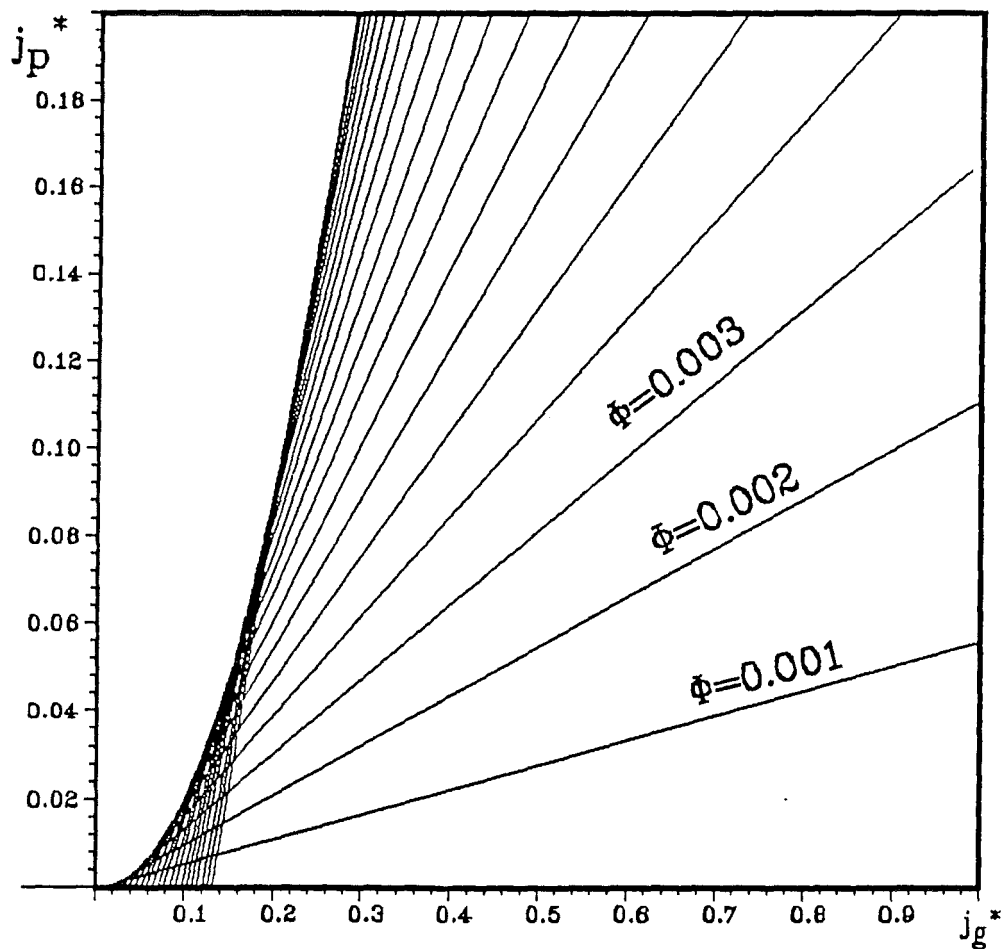


Figure A-29: j_p^* vs. j_g^* for the 400 μm Iron Oxide in the 0.0266 m Diameter Bench Scale System with Lines of Constant Φ .

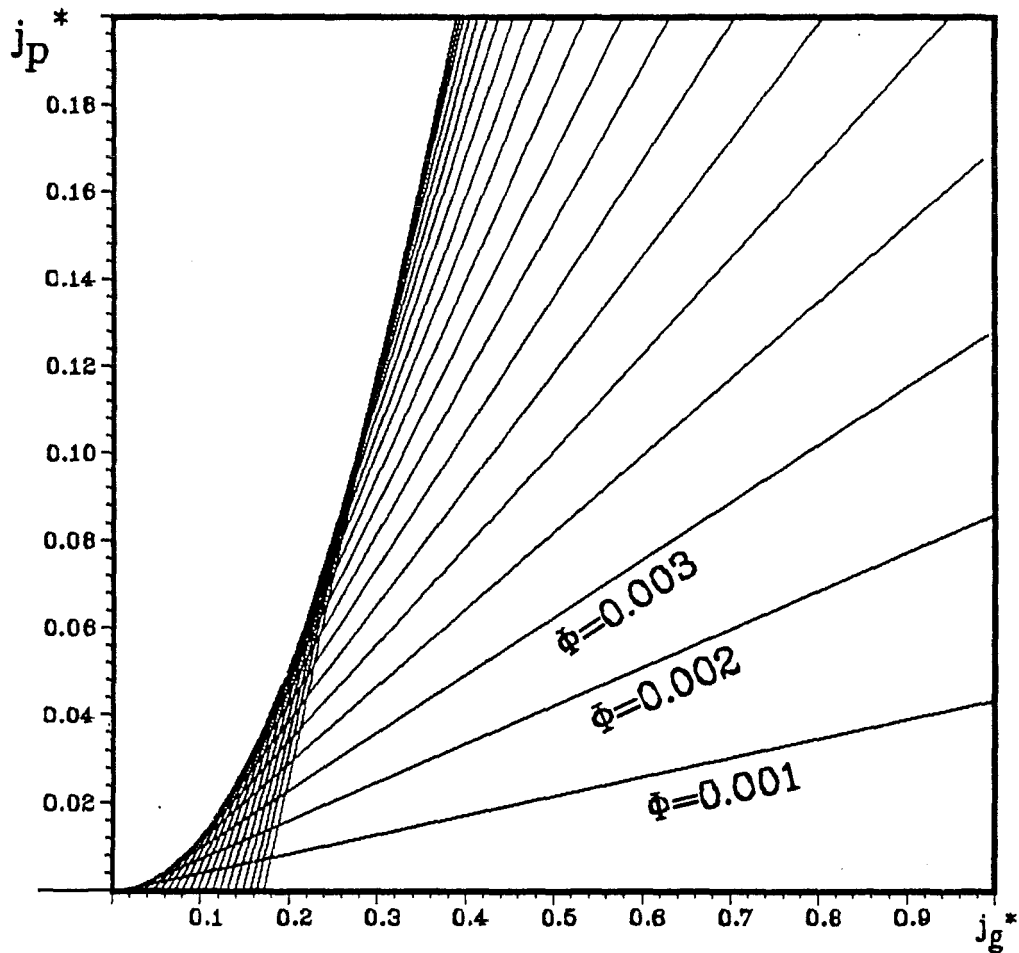


Figure A-30: j_p^* vs. j_g^* for the 67 μm Glass Beads in the 0.0504 m Diameter Full Scale System with Lines of Constant Φ .

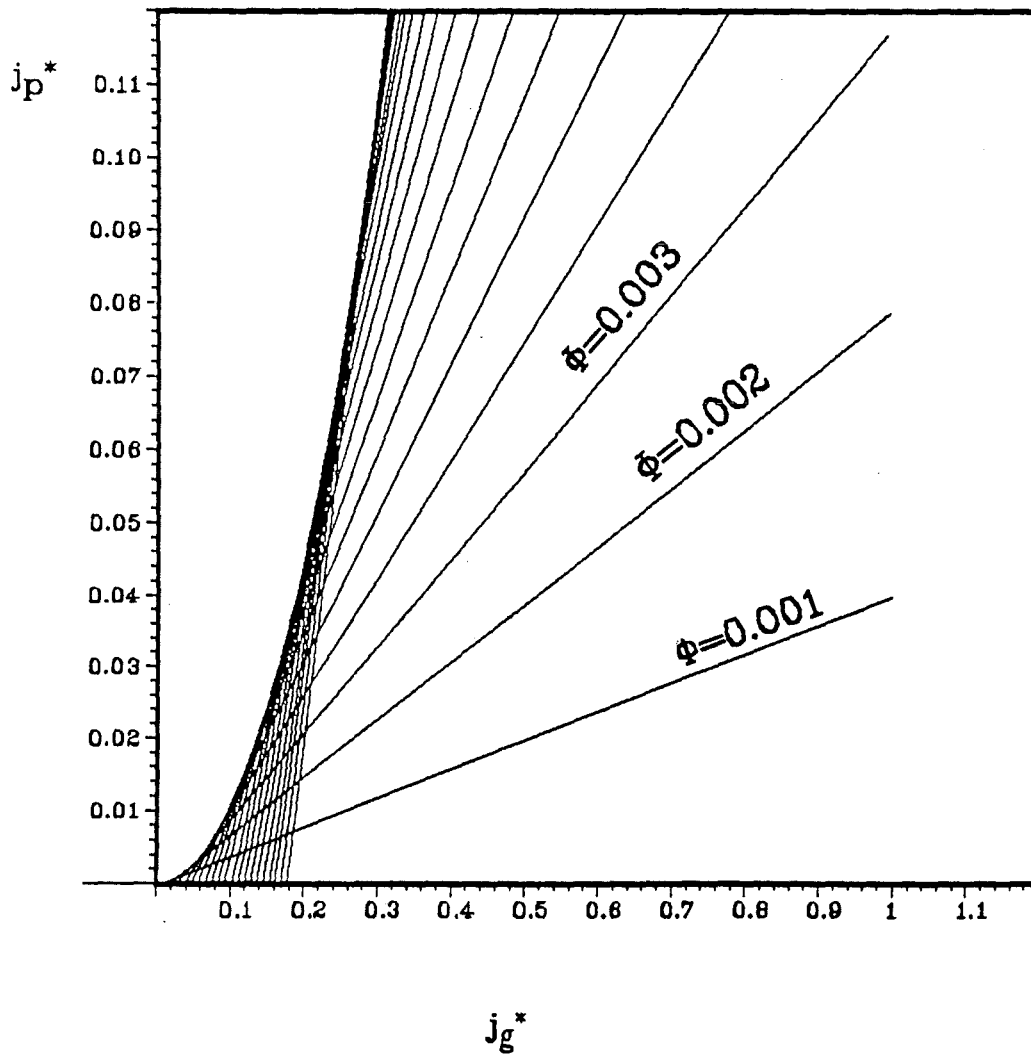


Figure A-31: j_p^* vs. j_g^* for the 450 μm Glass Beads in the 0.0504 m Diameter Full Scale System with Lines of Constant Φ .

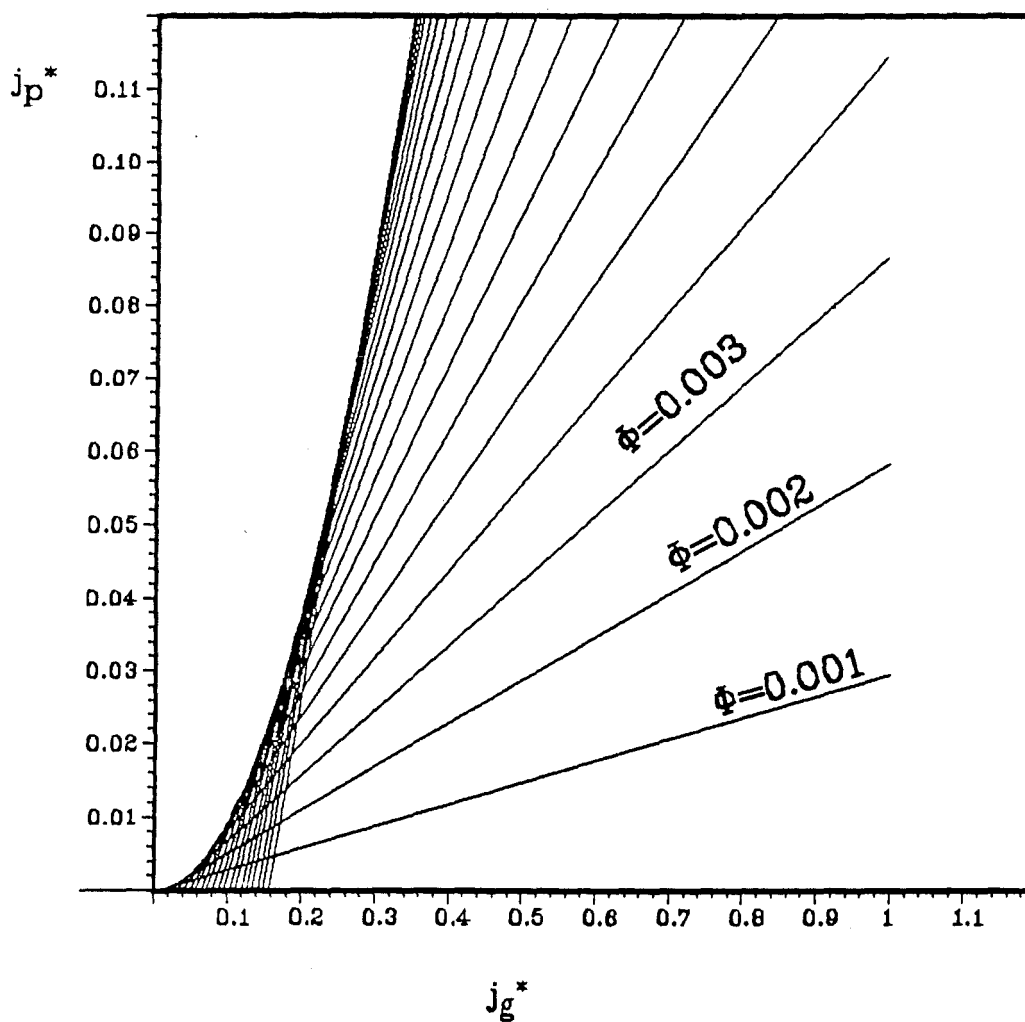


Figure A-32: j_p^* vs. j_g^* for the 900 μm Glass Beads in the 0.0504 m Diameter Full Scale System with Lines of Constant Φ .

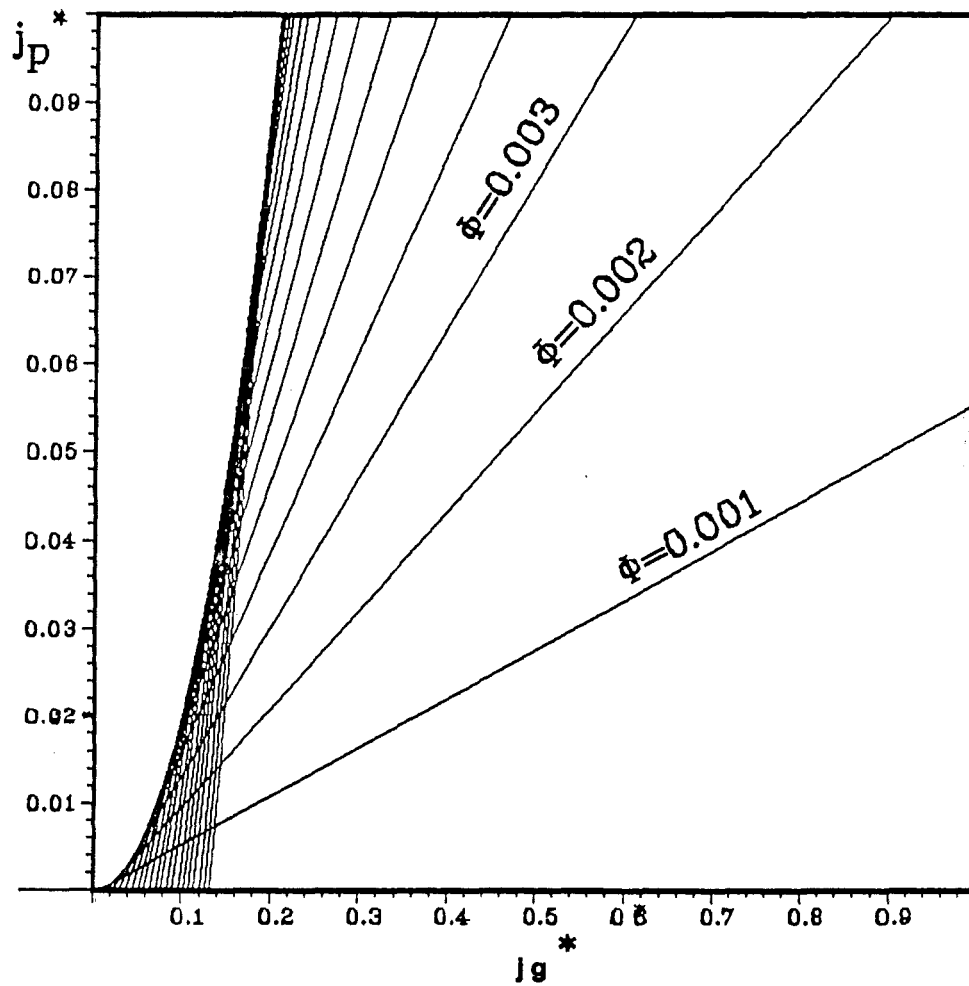


Figure A-33: j_p^* vs. j_g^* for the 400 μm Iron Oxide in the 0.0504 m Diameter Bench Scale System with Lines of Constant Φ .

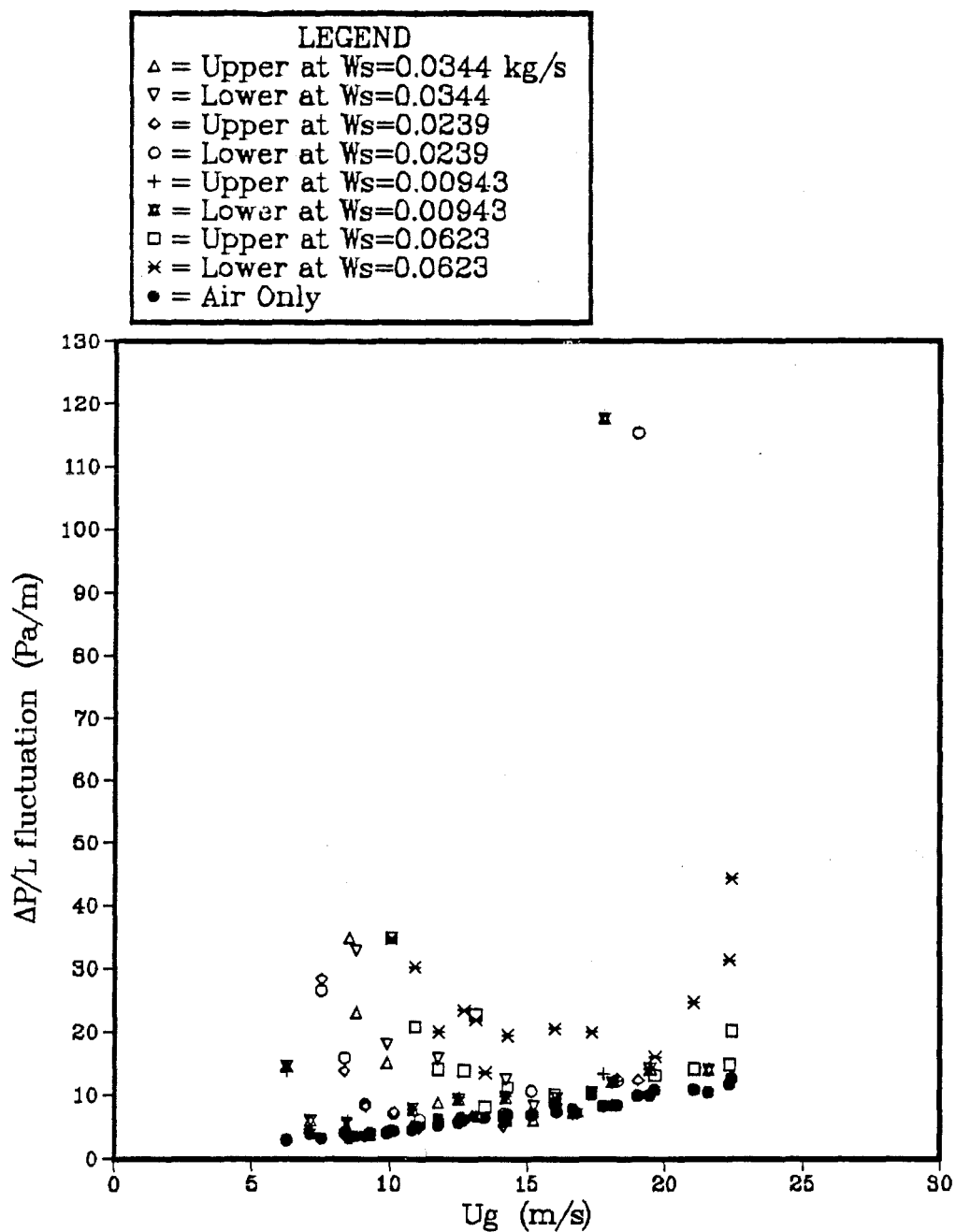


Figure A-35: Pressure Drop Fluctuation vs. Gas Velocity for the 400 μ m Iron Oxide in the 0.0266 m Diameter Bench Scale System.

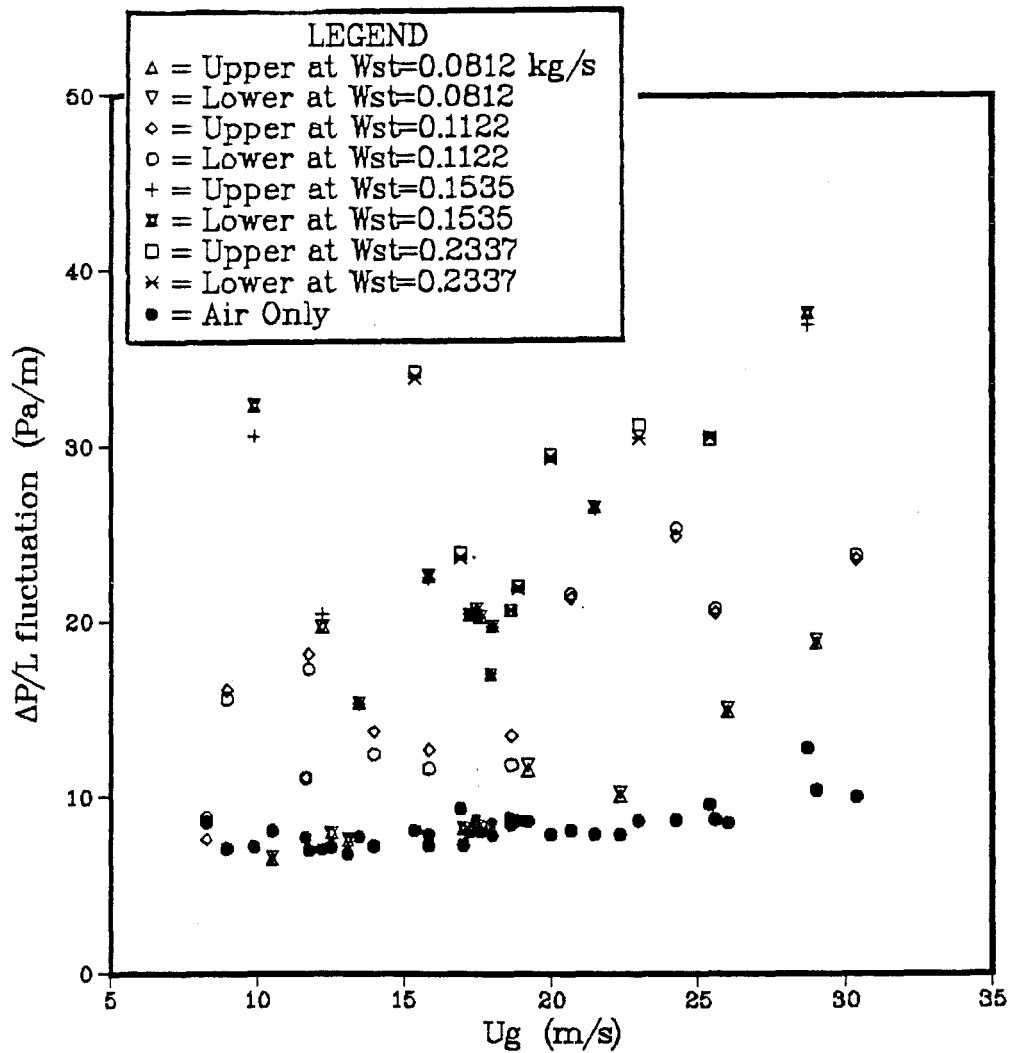


Figure A-36: Pressure Drop Fluctuation vs. Gas Velocity for the 67 μm Glass Beads in the 0.0504 m Diameter Full Scale System.

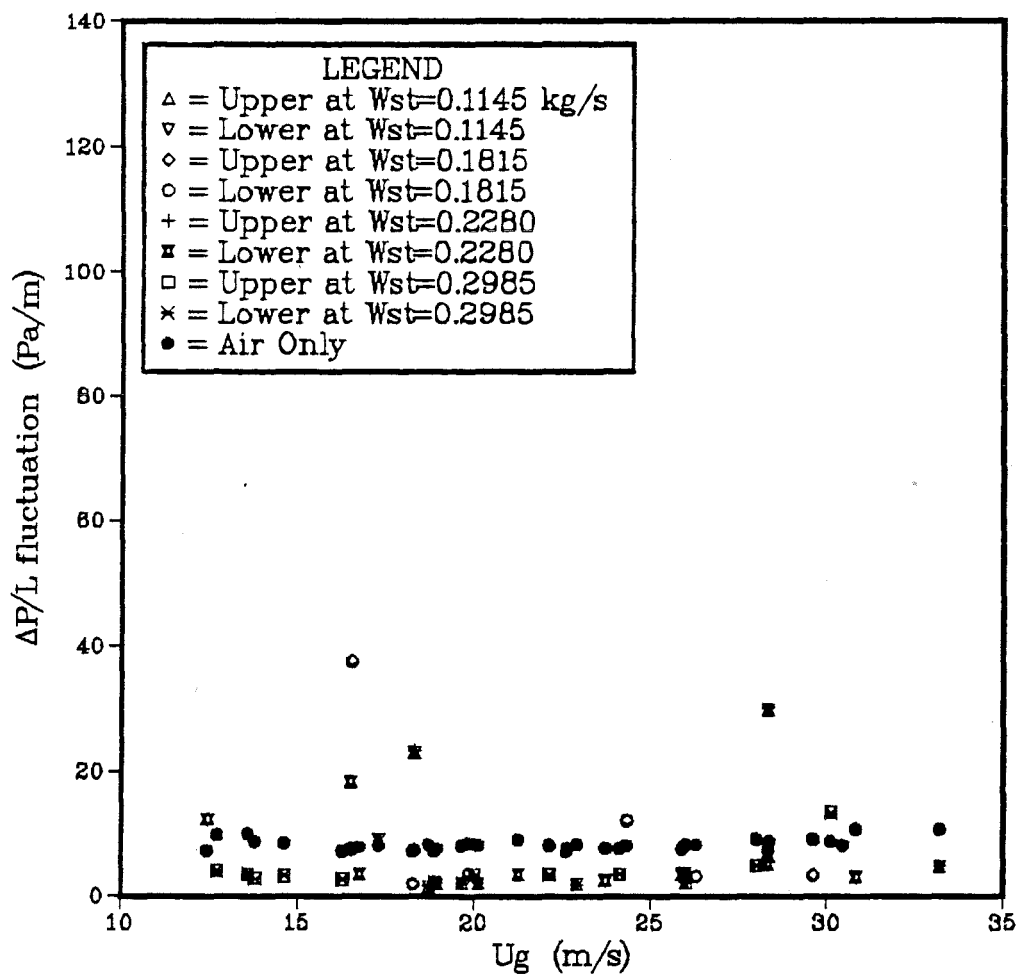


Figure A-37: Pressure Drop Fluctuation vs. Gas Velocity for the 450 μm Glass Beads in the 0.0504 m Diameter Full Scale System.

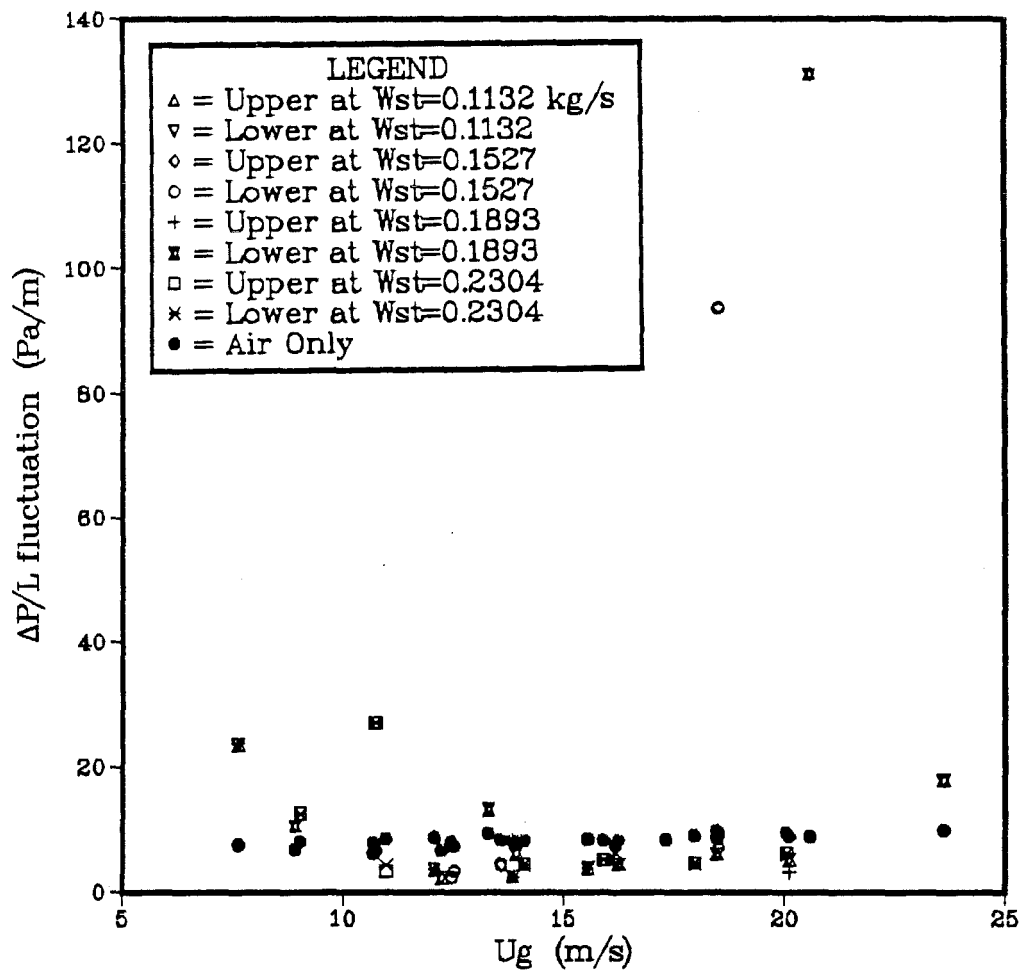


Figure A-38: Pressure Drop Fluctuation vs. Gas Velocity for the 900 μm Glass Beads in the 0.0504 m Diameter Full Scale System.

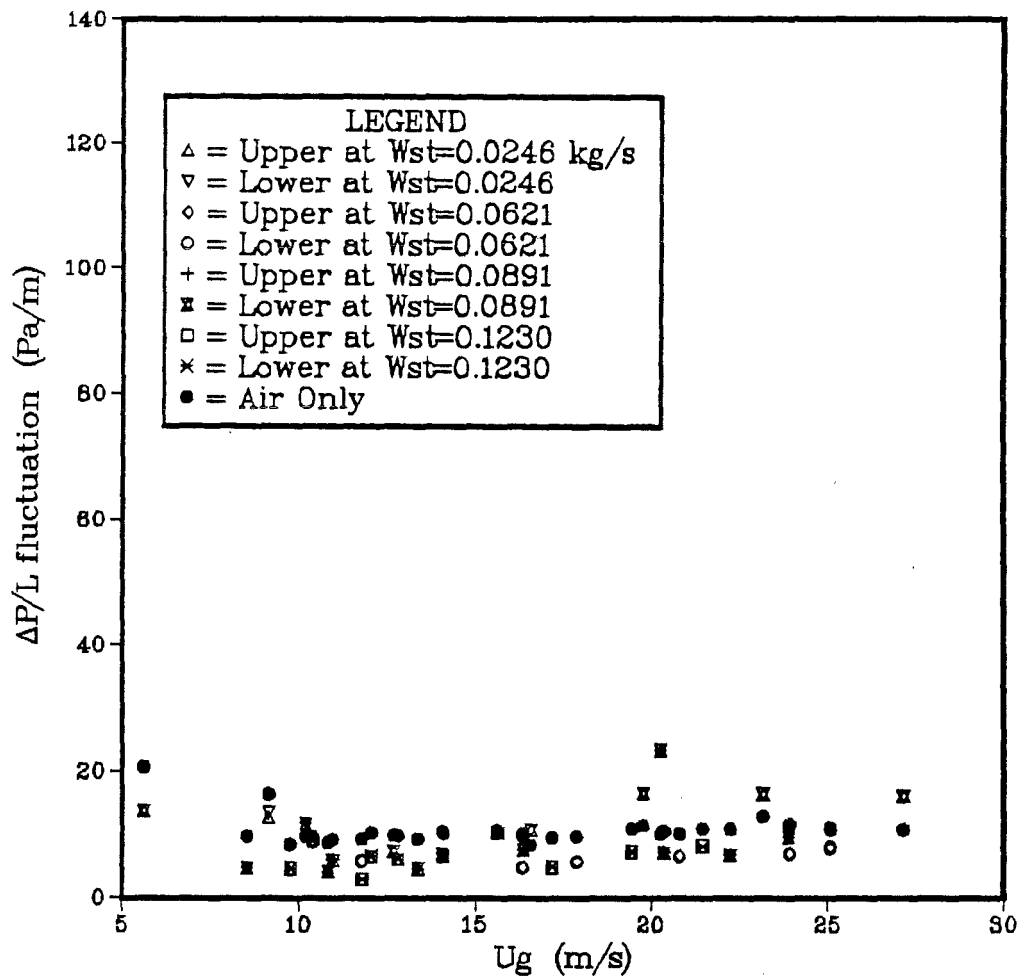


Figure A-39: Pressure Drop Fluctuation vs. Gas Velocity for the 400 μ m Iron Oxide in the 0.0504 m Diameter Full Scale System.

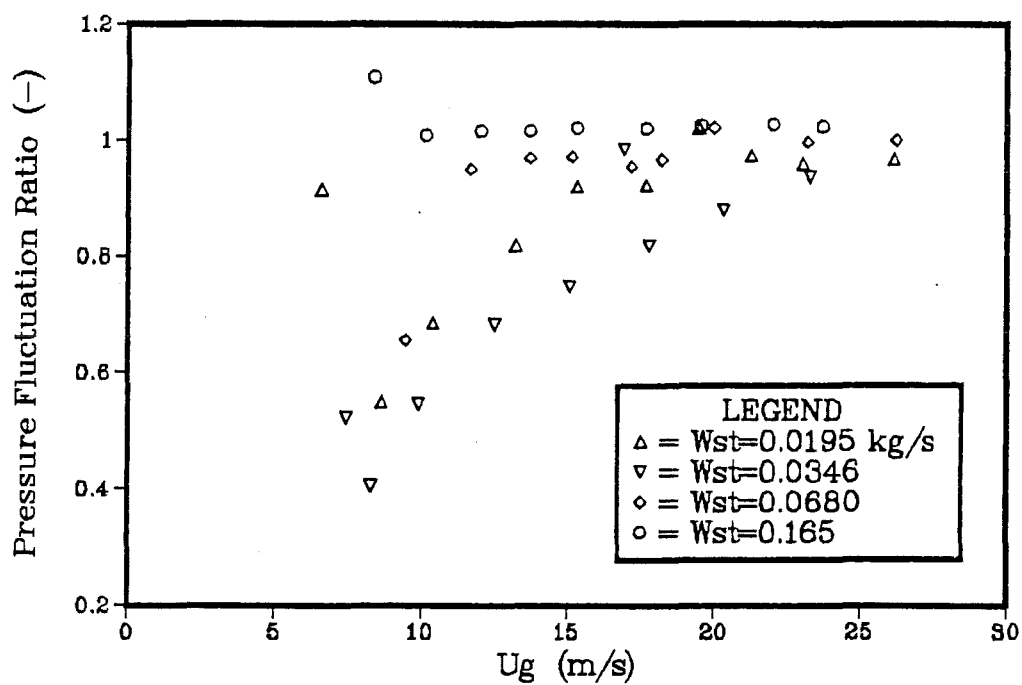


Figure A-40: Ratio of Pressure Fluctuation in the Upper Half of the Pipe to that in the lower Half vs. Gas Velocity for the 67 μ m Glass Beads in the 0.0266 m Diameter Bench Scale System.

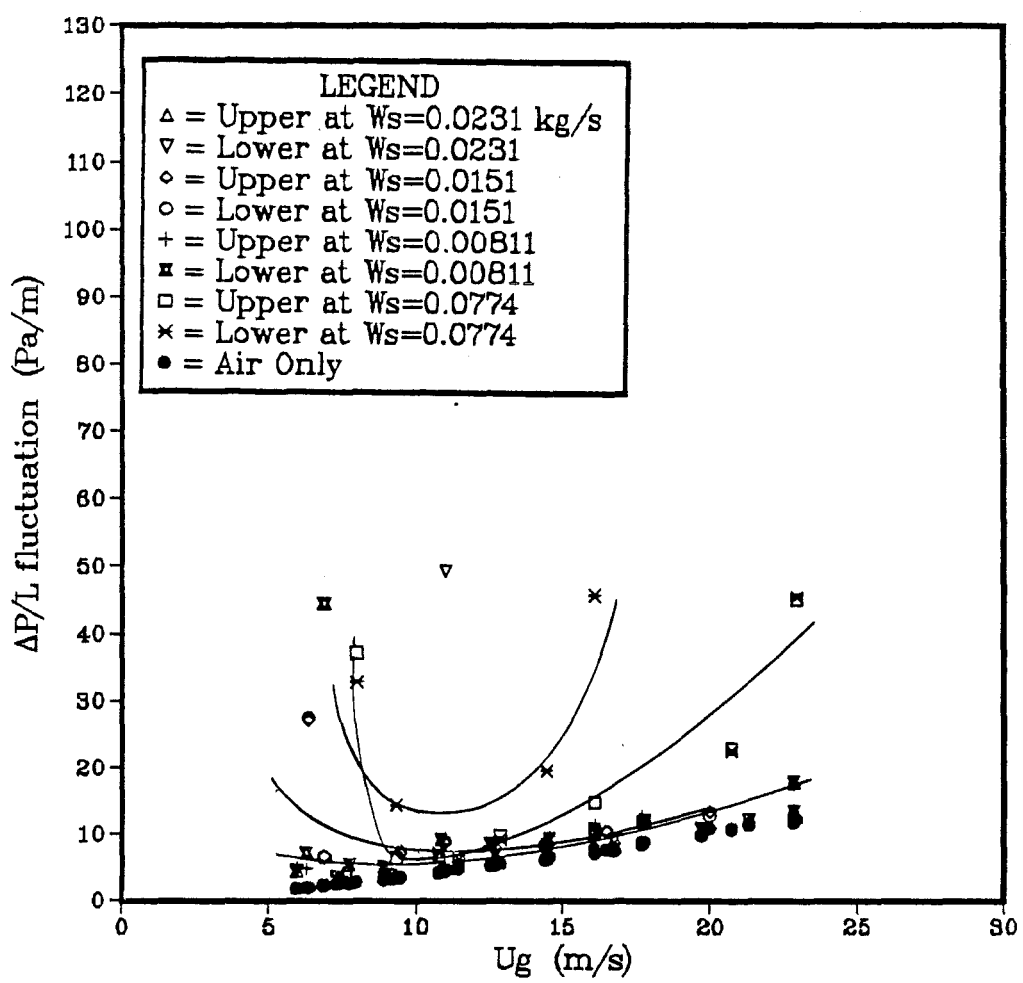


Figure A-41: Ratio of Pressure Fluctuation in the Upper Half of the Pipe to that in the lower Half vs. Gas Velocity for the 900 μm Glass Beads in the 0.0266 m Diameter Bench Scale System.

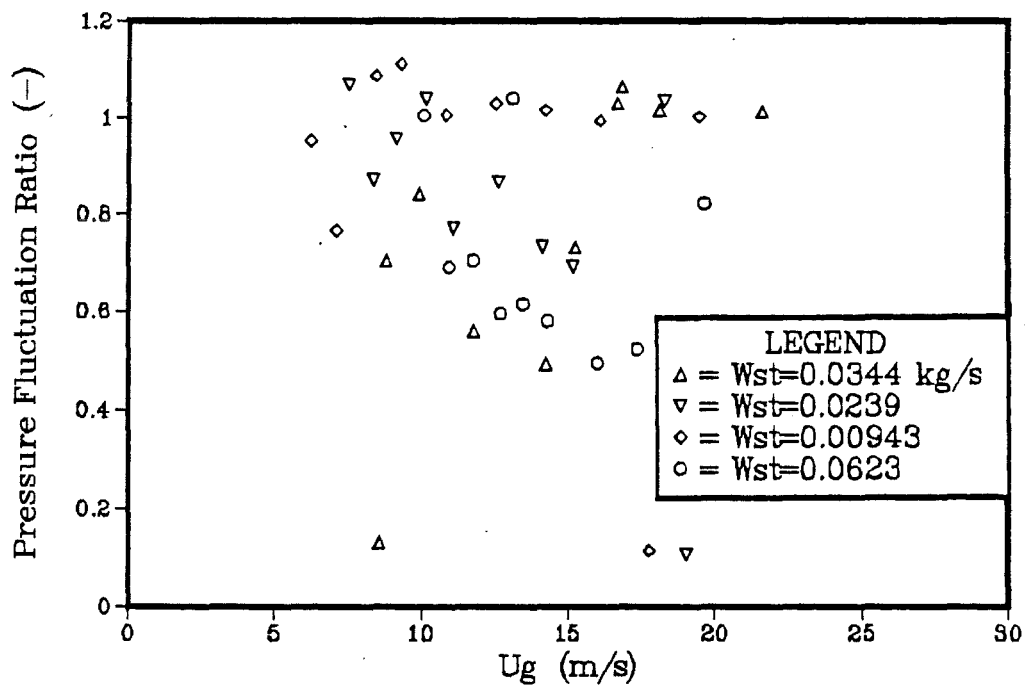


Figure A-42: Ratio of Pressure Fluctuation in the Upper Half of the Pipe to that in the lower Half vs. Gas Velocity for the 400 μ m Iron Oxide in the 0.0266 m Diameter Bench Scale System.

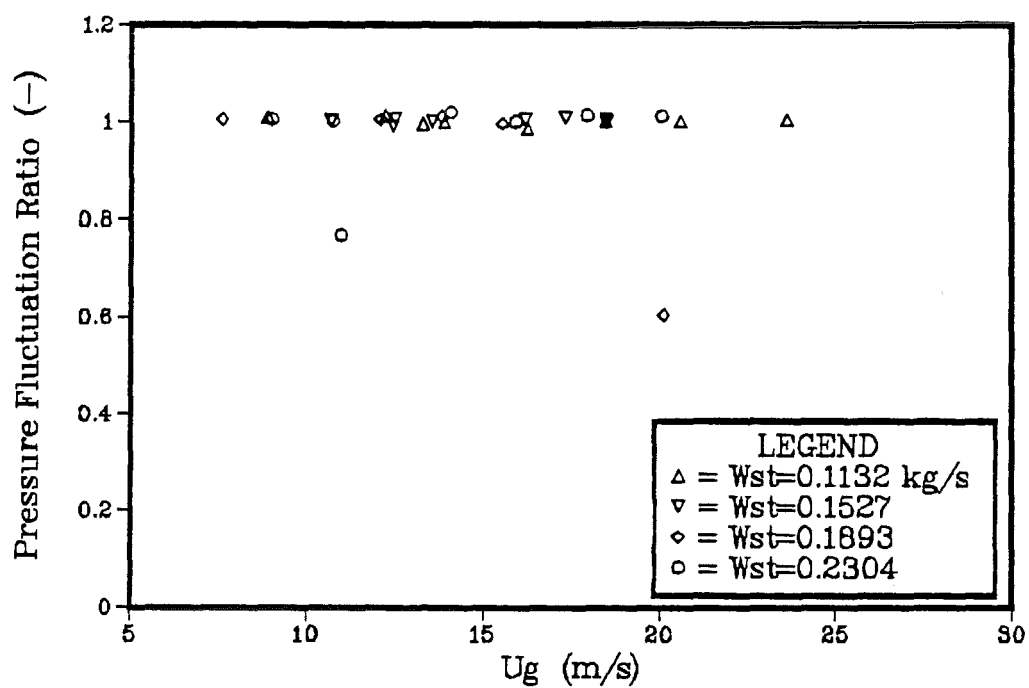


Figure A-43: Ratio of Pressure Fluctuation in the Upper Half of the Pipe to that in the lower Half vs. Gas Velocity for the 900 μ m Glass Beads in the 0.0504 m Diameter Full Scale System.

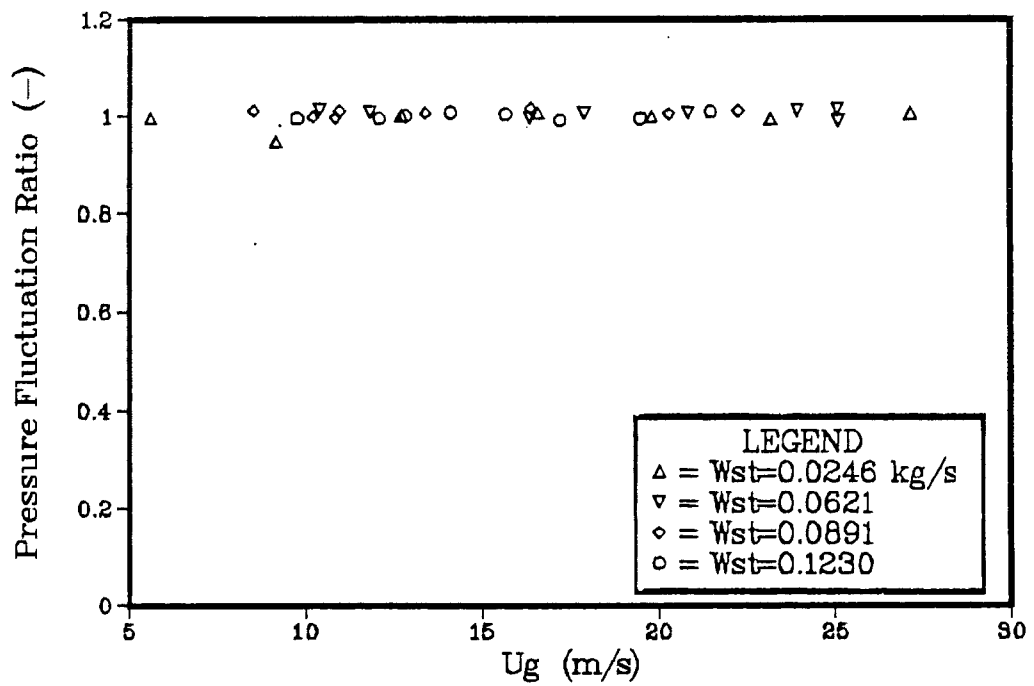


Figure A-44: Ratio of Pressure Fluctuation in the Upper Half of the Pipe to that in the lower Half vs. Gas Velocity for the $400 \mu\text{m}$ Iron Oxide in the 0.0504 m Diameter Full Scale System.

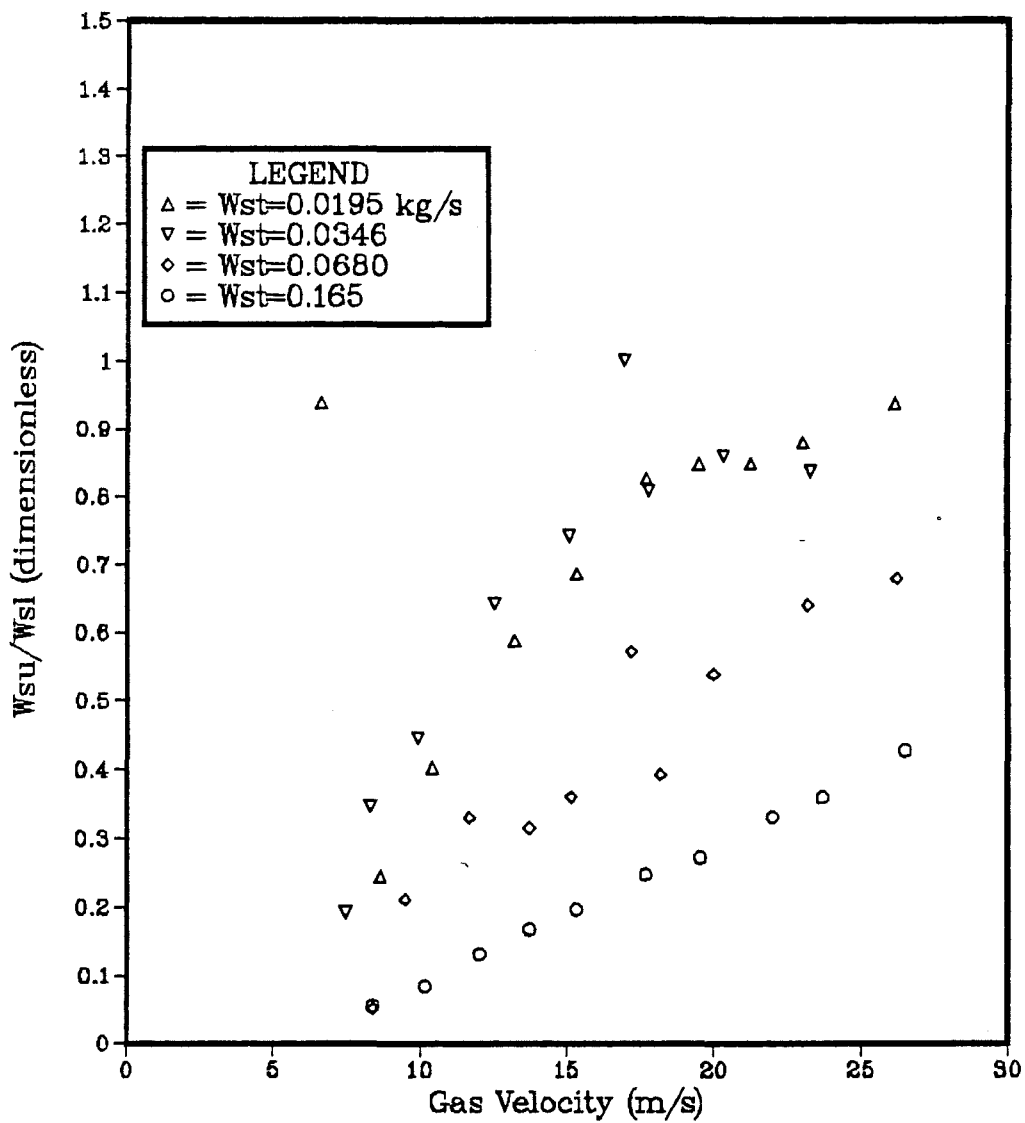


Figure A-45: W_{su}/W_{sl} vs. U_g for the 67 μ m Glass Beads in the 0.0266 m Diameter Bench Scale System.

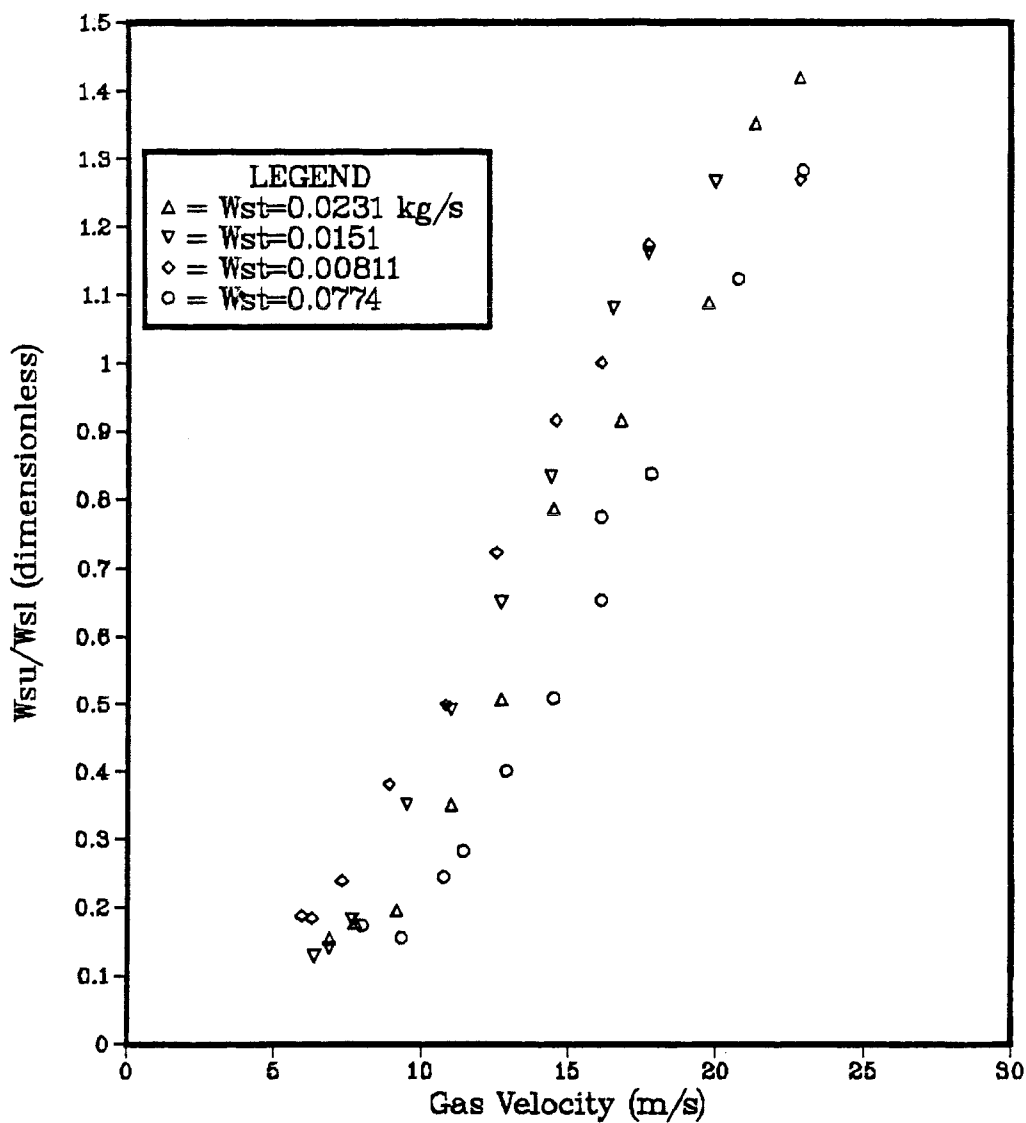


Figure A-46: W_{su}/W_{sl} vs. U_g for the 900 μ m Glass Beads in the 0.0266 m Diameter Bench Scale System.

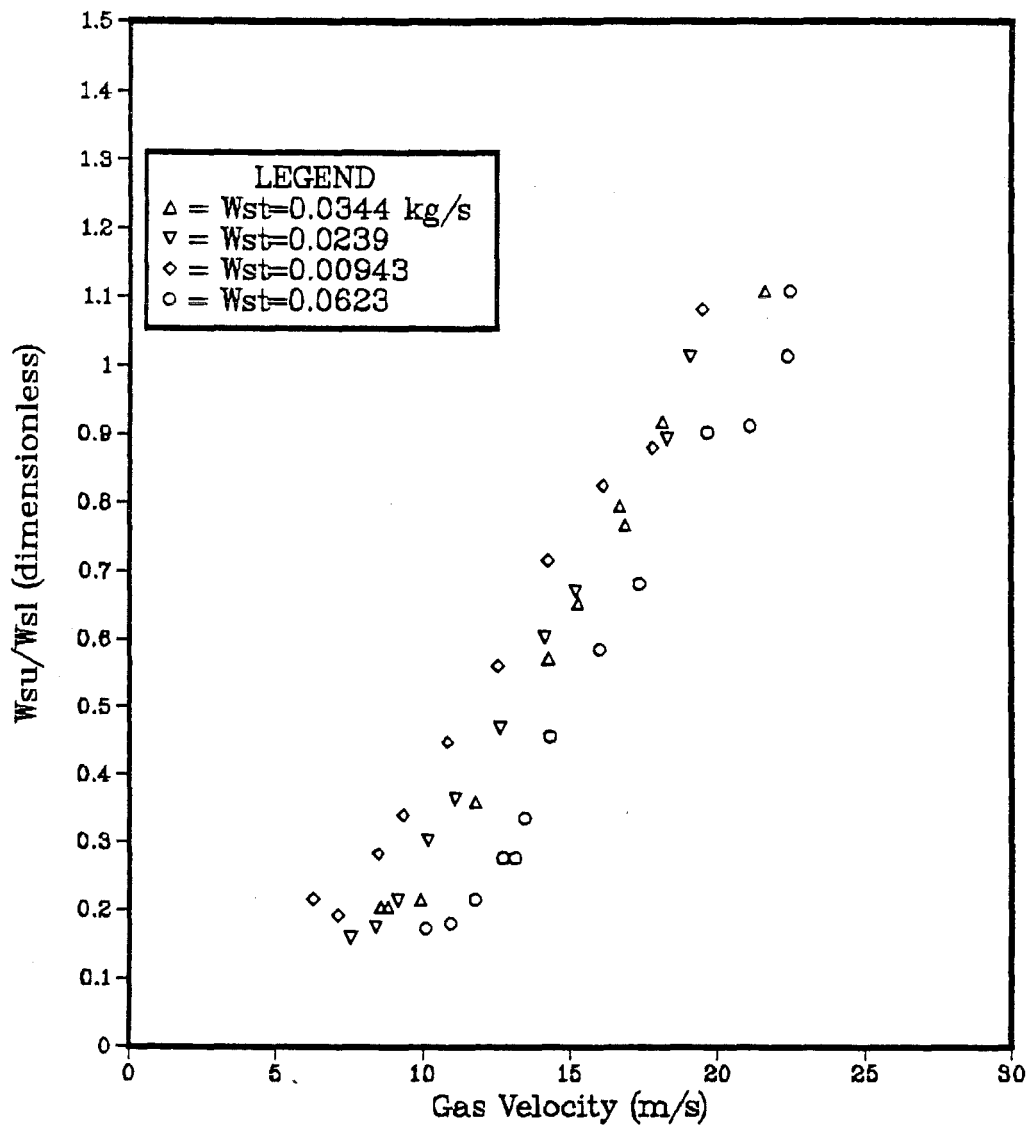


Figure A-47: W_{su}/W_{sl} vs. U_g for the 400 μ m Iron Oxide in the 0.0266 m Diameter Bench Scale System.

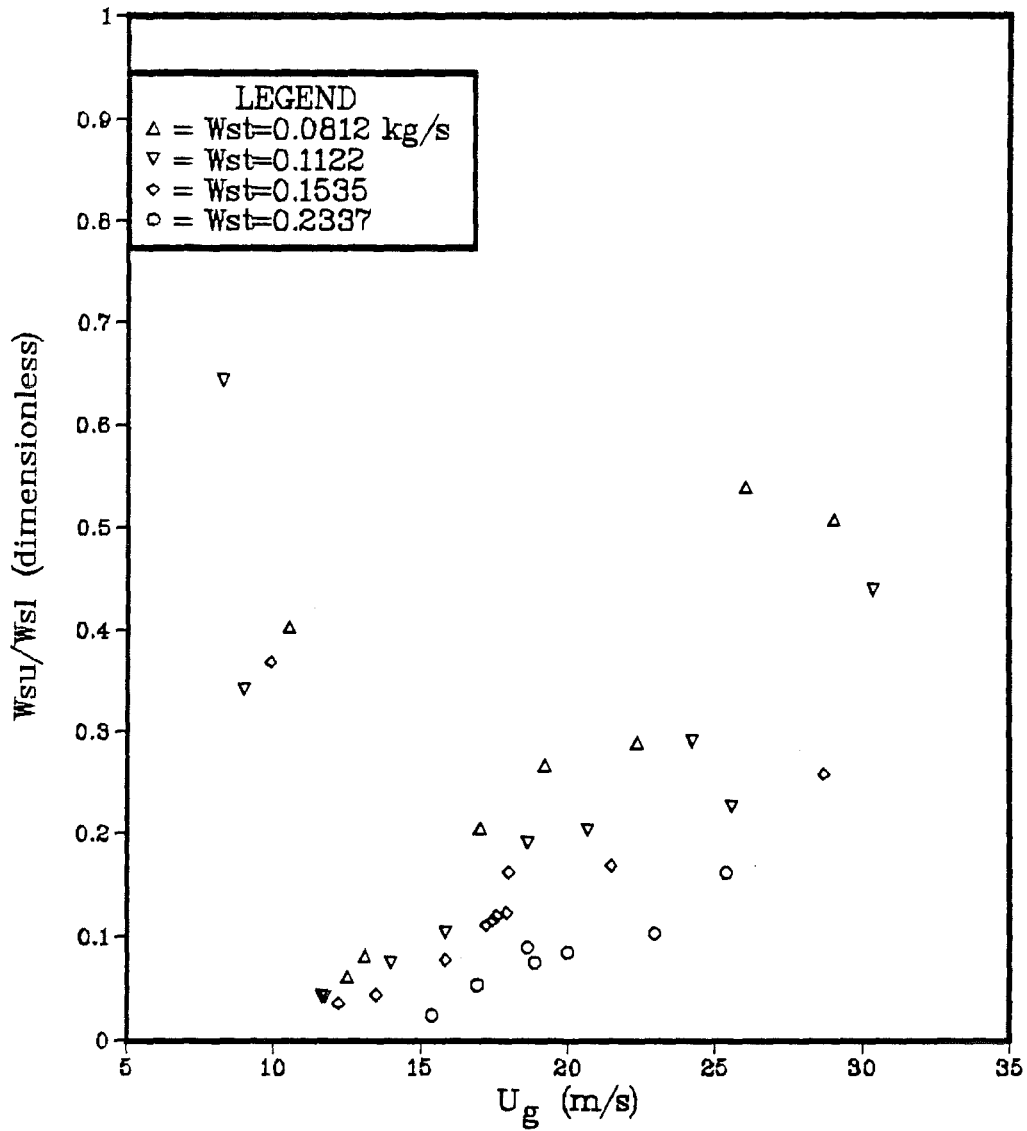


Figure A-48: W_{su}/W_{sl} vs. U_g for the 67 μ m Glass Beads in the 0.0504 m Diameter Full Scale System.

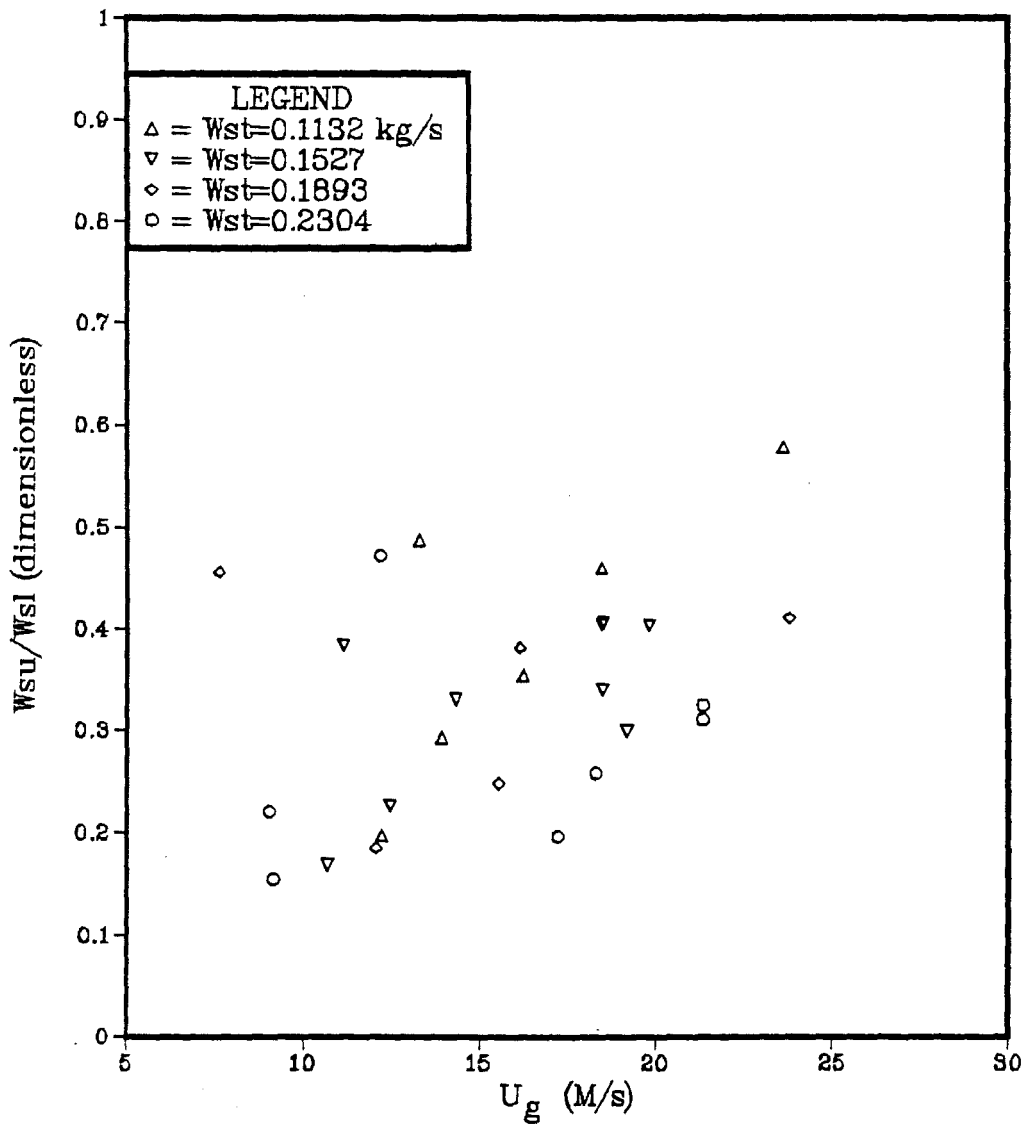


Figure A-49: W_{su}/W_{sl} vs. U_g for the 900 μ m Glass Beads in the 0.0504 m Diameter Full Scale System.

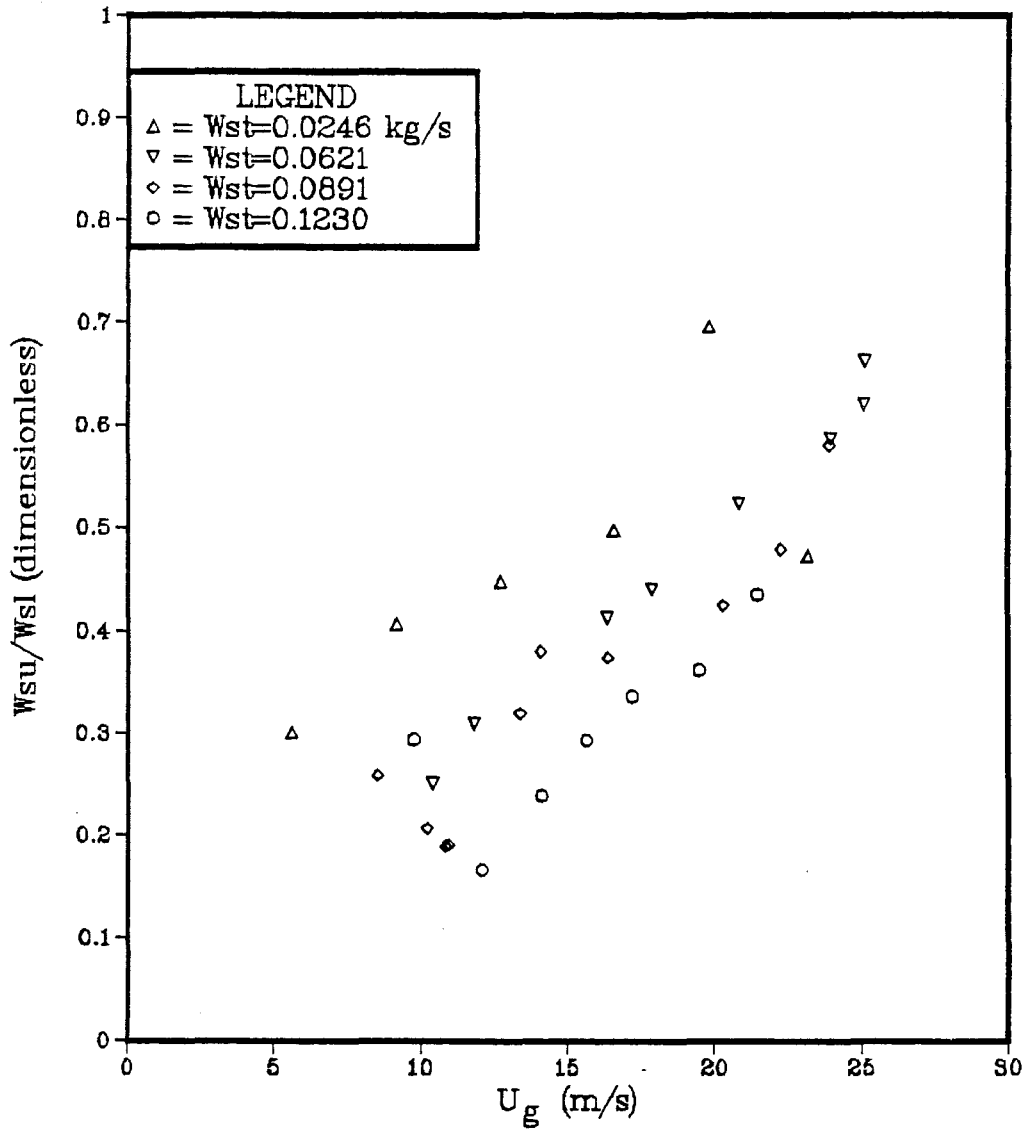


Figure A-50: W_{su}/W_{sl} vs. U_g for the 400 μ m Iron Oxide in the 0.0504 m Diameter Full Scale System.

APPENDIX B

APPENDIX B

Tables of Results from the Regression of Experimental Data
to the van der Waals Analog Equation

Table B-1: BMDP Results for the 67 μ m Glass Beads in the
0.0266 m Diameter System.

RESIDUAL SUM OF SQUARES = 0.348826

PARAMETER	ESTIMATE
a*	1923.78
b*	20.20

THE ESTIMATED MEAN SQUARE ERROR IS 7.1189E-03

CASE NO. NAME	OBSERVED j_g^*	PREDICTED j_g^*	j_p^*	1/ ϕ
1	0.8405	0.9153	0.0231	1631.3360
2	0.7637	0.8340	0.0224	1521.0489
3	0.6614	0.7301	0.0228	1294.2960
4	0.5700	0.6381	0.0224	1134.9090
5	0.9172	0.9460	0.0228	1713.6639
6	0.9939	1.0148	0.0222	1890.4659
7	1.1292	1.1420	0.0222	2140.7519
8	1.0049	1.0494	0.0149	2922.8181
9	0.8770	0.9405	0.0153	2542.3950
10	0.7674	0.8231	0.0150	2266.2338
11	0.6504	0.6999	0.0148	1936.8540
12	0.5408	0.4974	0.0154	1264.6109
13	0.7308	0.7588	0.0142	2194.0690
14	0.5920	0.6638	0.0409	621.3999
15	0.6541	0.7170	0.0399	702.6414
16	0.7418	0.8649	0.0291	1212.8389
17	0.7856	0.8345	0.0483	686.3981
18	0.8624	0.9279	0.0398	948.1441
19	1.0013	0.9912	0.0409	990.8153
20	1.1328	1.1073	0.0440	1036.1350
21	0.5920	0.6871	0.1078	202.9420
22	0.6614	0.6957	0.1035	220.1526
23	0.7637	0.8961	0.0983	347.8228
24	0.8441	0.9019	0.1066	320.8461
25	0.9501	0.9954	0.0988	395.5002
26	1.0232	0.9993	0.1056	369.9755
27	1.1438	1.0923	0.0956	457.8804
28	0.4494	0.4423	0.0164	1026.2829
29	0.4494	0.2815	0.0164	263.7041
30	0.3727	0.3774	0.0112	1282.8530
31	0.3727	0.2616	0.0112	241.7241
32	0.2850	0.3571	0.0263	381.2479
33	0.2850	0.3498	0.0263	354.7766

Table B-1 (continued)

CASE NO. NAME	OBSERVED	PREDICTED		1/0
	j_g^*	j_g^*	j_p^*	
34	0.4275	0.5051	0.0114	1771.4310
35	0.4275	0.2417	0.0114	305.4747
36	0.3581	0.3853	0.0097	1543.0760
37	0.3581	0.2263	0.0097	322.2200
38	0.3215	0.2521	0.0060	1534.4539
39	0.3215	0.2934	0.0060	171.7026
40	0.5043	0.6783	0.0209	1306.6590
41	0.5043	0.3225	0.0209	207.8728
42	0.4092	0.4315	0.0142	1163.8740
43	0.4092	0.3129	0.0142	181.3553
44	0.3617	0.4142	0.0075	2194.7338
45	0.3617	0.3286	0.0075	34.5229
46	0.3617	0.4620	0.0129	1402.0419
47	0.3617	0.5151	0.0129	56.1153
48	0.4385	0.5126	0.0228	854.0828
49	0.4385	0.4153	0.0228	38.2890
50	0.5189	0.6324	0.0351	691.1840
51	0.5189	0.4813	0.0351	43.1813

Table B-2: BMDP Results for the 450 μm Glass Beads in the 0.0266 m Diameter System.

RESIDUAL SUM OF SQUARES = 0.204295

PARAMETER	ESTIMATE
a*	531.91
b*	8.77

THE ESTIMATED MEAN SQUARE ERROR IS 3.8546E-03

CASE NO. NAME	OBSERVED j_g^*	PREDICTED j_g^*	j_p^*	1/0
1	0.9019	0.9143	0.0419	715.2993
2	0.7683	0.7585	0.0453	543.1087
3	0.6978	0.7045	0.0414	549.8690
4	0.6198	0.6299	0.0413	488.4194
5	0.5382	0.5640	0.0409	436.3781
6	0.4751	0.5071	0.0407	387.3091
7	0.7794	0.7713	0.0408	615.4202
8	0.9390	0.8890	0.0271	1078.8570
9	0.7794	0.7663	0.0282	889.3845
10	0.7089	0.6745	0.0276	796.0032
11	0.6347	0.6323	0.0281	730.0725
12	0.5567	0.5629	0.0279	647.4808
13	0.9168	0.8653	0.0154	1853.7220
14	0.7720	0.6920	0.0144	1578.5229
15	0.7089	0.6565	0.0142	1514.9610
16	0.6087	0.5872	0.0147	1305.0040
17	0.4973	0.5105	0.0137	1207.3430
18	0.3860	0.3638	0.0145	789.9470
19	0.9242	0.8455	0.0142	1957.7540
20	0.5344	0.6258	0.1330	136.1495
21	0.6569	0.7029	0.1331	159.4810
22	0.7312	0.7912	0.1332	184.8025
23	0.8091	0.8314	0.1275	205.5184
24	0.8908	0.9399	0.1421	211.3583
25	1.0244	1.0565	0.1461	234.0041
26	0.4008	0.5060	0.0320	498.6312
27	0.4008	0.3018	0.0320	58.2437
28	0.3303	0.2626	0.0222	321.4432
29	0.3303	0.3973	0.0222	32.1916
30	0.2598	0.2019	0.0173	276.8840
31	0.2598	0.2948	0.0173	53.7309
32	0.4268	0.4444	0.0250	558.4669

Table B-2 (continued)

CASE NO. NAME	OBSERVED j_g^*	PREDICTED j_g^*	j_p^*	$1/\Phi$
33	0.4268	0.2234	0.0250	111.2260
34	0.3414	0.3108	0.0180	521.0465
35	0.3414	0.2628	0.0180	65.4127
36	0.2932	0.1848	0.0133	343.8322
37	0.2932	0.2640	0.0133	61.9731
38	0.2598	0.3817	0.0102	1201.9179
39	0.2598	0.2051	0.0102	88.0944
40	0.2264	0.2060	0.0100	595.6979
41	0.2264	0.3106	0.0100	47.2370
42	0.3043	0.2976	0.0095	981.5062
43	0.3043	0.1704	0.0095	118.4031
44	0.2375	0.1937	0.0053	1116.9339
45	0.2375	0.2264	0.0053	71.4440
46	0.2078	0.1572	0.0071	608.3651
47	0.2078	0.2218	0.0071	74.9642
48	0.4082	0.4880	0.0646	221.6849
49	0.4082	0.4477	0.0646	27.0319
50	0.4082	0.4759	0.0643	214.9537
51	0.4082	0.4372	0.0643	29.4695
52	0.3674	0.3343	0.0599	118.8050
53	0.3674	0.3781	0.0599	14.6084
54	0.3303	0.3616	0.0637	134.2469
55	0.3303	0.2905	0.0637	12.8401

Table B-3: BMDP Results for the 900 μm Glass Beads in the
0.0266 m Diameter System.

RESIDUAL SUM OF SQUARES = 0.436294

PARAMETER	ESTIMATE
a*	937.45
b*	16.46

THE ESTIMATED MEAN SQUARE ERROR IS 8.5548E-03

CASE NO. NAME	OBSERVED j_g^*	PREDICTED j_g^*	j_p^*	1/0
1	0.7245	0.7838	0.0253	868.0501
2	0.6257	0.7035	0.0266	732.6715
3	0.5489	0.6298	0.0251	689.8693
4	0.8526	0.9269	0.0280	935.6619
5	0.9221	1.0098	0.0289	989.8079
6	0.9880	1.0331	0.0292	1003.8629
7	0.7648	0.8532	0.0198	1218.0150
8	0.7135	0.7666	0.0189	1139.5839
9	0.6220	0.6970	0.0185	1052.6949
10	0.5489	0.3609	0.0180	505.8360
11	0.4757	0.5280	0.0173	833.1101
12	0.4098	0.3110	0.0172	429.0372
13	0.8636	0.9231	0.0197	1329.1379
14	0.7648	0.8166	0.0103	2237.9660
15	0.6952	0.7605	0.0101	2132.3750
16	0.6294	0.7009	0.0101	1960.1140
17	0.5415	0.5761	0.0098	1651.4689
18	0.4684	0.5176	0.0093	1544.0269
19	0.3842	0.5110	0.0086	1653.0279
20	0.9880	1.0265	0.0109	2684.1699
21	0.9916	1.0831	0.1189	252.6329
22	0.8965	1.0407	0.1250	228.9877
23	0.7684	0.8708	0.1131	205.3520
24	0.6952	0.7742	0.1005	200.8291
25	0.6257	0.6664	0.0901	184.7053
26	0.5562	0.4882	0.0789	121.8275
27	0.4940	0.5245	0.0679	177.6663
28	0.6952	0.7597	0.0923	215.0816
29	0.4647	0.4622	0.0709	124.8186
30	0.4757	0.5576	0.0173	888.7667
31	0.4757	0.4379	0.0173	35.0251
32	0.3952	0.3668	0.0106	928.6704
33	0.3952	0.3637	0.0106	56.9240

Table B-3 (continued)

CASE NO. NAME	OBSERVED j_g^*	PREDICTED j_g^*	j_p^*	1/0
34	0.3330	0.4061	0.0101	1090.3020
35	0.3330	0.4068	0.0101	25.9215
36	0.2964	0.3859	0.0093	1130.6120
37	0.2964	0.3497	0.0093	60.6208
38	0.3293	0.5452	0.0069	2221.9179
39	0.3293	0.1950	0.0069	152.8558
40	0.2964	0.4834	0.0043	3160.0610
41	0.2964	0.1502	0.0043	211.9756
42	0.2744	0.1656	0.0038	1064.1130
43	0.2744	0.3260	0.0038	65.2443
44	0.3147	0.2700	0.0045	1612.2760
45	0.3147	0.1800	0.0045	157.7238
46	0.2707	0.1954	0.0034	1481.2779
47	0.2707	0.2387	0.0034	102.1426
48	0.2561	0.1594	0.0025	1585.3139
49	0.2561	0.1754	0.0025	151.6974
50	0.4025	0.5672	0.0201	774.2084
51	0.4025	0.3959	0.0201	50.9215
52	0.3439	0.2726	0.0216	227.5243
53	0.3439	0.2748	0.0216	20.0993

Table B-4: BMDP Results for the 400 μ m Iron Oxide in the
0.0266 m Diameter System.

RESIDUAL SUM OF SQUARES = 0.358788

PARAMETER	ESTIMATE
a*	1495.33
b*	33.49

THE ESTIMATED MEAN SQUARE ERROR IS 7.0351E-03

CASE NO. NAME	OBSERVED j_g^*	PREDICTED j_g^*	j_p^*	1/ Φ
1	0.5109	0.6019	0.0188	1359.0999
2	0.4621	0.5588	0.0185	1274.6240
3	0.4313	0.5141	0.0184	1172.6710
4	0.3568	0.4461	0.0185	993.0180
5	0.6547	0.6673	0.0192	1487.1459
6	0.5058	0.5501	0.0195	1188.2840
7	0.5494	0.6418	0.0228	1196.0040
8	0.4287	0.2640	0.0145	646.7886
9	0.5545	0.2803	0.0133	788.5371
10	0.3363	0.2815	0.0131	804.8552
11	0.4595	0.5350	0.0134	1698.5770
12	0.5776	0.6494	0.0136	2050.6950
13	0.3825	0.4387	0.0129	1419.0310
14	0.5905	0.6167	0.0057	4695.9409
15	0.5391	0.5796	0.0055	4534.4248
16	0.4878	0.5273	0.0055	4140.7470
17	0.4313	0.2136	0.0054	1530.6169
18	0.3799	0.4222	0.0053	3362.1770
19	0.3286	0.3618	0.0051	2964.7370
20	0.2824	0.2952	0.0053	2284.3688
21	0.2567	0.2562	0.0050	2090.3378
22	0.5956	0.6741	0.0309	925.1856
23	0.5263	0.3869	0.0347	402.2962
24	0.4852	0.5709	0.0330	716.6234
25	0.4339	0.5086	0.0280	744.6557
26	0.4082	0.4653	0.0292	637.7371
27	0.3851	0.4531	0.0281	643.5349
28	0.3568	0.4167	0.0312	512.2178
29	0.6393	0.7435	0.0450	700.6342
30	0.6778	0.7614	0.0458	707.4523
31	0.6803	0.7969	0.0368	927.1812
32	0.3004	0.3161	0.0084	1539.1960
33	0.3004	0.3019	0.0084	85.2376

Table B-4 (continued)

CASE NO. NAME	OBSERVED j_g^*	PREDICTED j_g^*	j_p^*	1/0
34	0.2670	0.2392	0.0085	1069.5980
35	0.2670	0.2835	0.0085	51.8485
36	0.2593	0.2680	0.0084	1260.5479
37	0.2593	0.2797	0.0084	104.9269
38	0.3081	0.4440	0.0077	2434.4909
39	0.3081	0.2488	0.0077	132.5092
40	0.2772	0.1977	0.0060	1220.8480
41	0.2772	0.2392	0.0060	45.4755
42	0.2541	0.1929	0.0050	1480.6030
43	0.2541	0.2896	0.0050	92.3716
44	0.2285	0.1449	0.0043	1131.5179
45	0.2285	0.2487	0.0043	125.4531
46	0.2156	0.2490	0.0020	5241.2241
47	0.2156	0.2059	0.0020	162.9156
48	0.1899	0.2868	0.0020	6079.8208
49	0.1899	0.1261	0.0020	326.8900
50	0.3312	0.2922	0.0131	853.7811
51	0.3312	0.3141	0.0131	63.5522
52	0.3055	0.3140	0.0121	1023.5390
53	0.3055	0.3027	0.0121	56.8250

Table B-5: BMDP Results for the 67 μ m Glass Beads in the 0.0504 m Diameter System.

RESIDUAL SUM OF SQUARES = 0.226410

PARAMETER	ESTIMATE
a*	395.51
b*	2.72

THE ESTIMATED MEAN SQUARE ERROR IS 5.3907E-03

CASE NO.	CASE NAME	OBSERVED j_g^*	PREDICTED j_g^*	j_p^*	1/ ϕ
1		0.6018	0.6289	0.0243	1062.4260
2		0.8158	0.8417	0.0203	1706.1660
3		0.7006	0.7518	0.0256	1208.0500
4		0.8020	0.7521	0.0350	883.0949
5		0.9523	1.0019	0.0292	1413.3039
6		0.7601	0.7947	0.0317	1030.9919
7		0.6735	0.6694	0.0459	599.6124
8		0.9004	0.9566	0.0469	840.3380
9		0.5621	0.6029	0.0481	514.5581
10		0.5835	0.5640	0.0658	351.1766
11		0.6268	0.6041	0.0782	316.9276
12		0.4100	0.4209	0.0033	5157.2749
13		0.3918	0.3488	0.0030	4699.5839
14		0.4964	0.5011	0.0065	3172.8220
15		0.4383	0.2425	0.0048	2074.7661
16		0.3684	0.2047	0.0027	3012.0620
17		0.3649	0.2394	0.0024	4029.1201
18		0.2812	0.3908	0.0161	993.7691
19		0.2589	0.1833	0.0229	319.8992
20		0.4225	0.3971	0.0035	4568.6870
21		0.3825	0.3008	0.0031	3885.6179
22		0.5471	0.5013	0.0091	2261.9641
23		0.5511	0.6013	0.0089	2767.3190
24		0.5398	0.5539	0.0089	2561.3410
25		0.5917	0.5135	0.0091	2317.1320
26		0.5304	0.4576	0.0061	3083.1530
27		0.7963	0.8093	0.0176	1885.6140
28		0.4819	0.3509	0.0035	4085.4951
29		0.4100	0.4633	0.5132	34.4966
30		0.3918	0.4250	0.9566	14.8779
31		0.4964	0.5292	0.5492	37.6133
32		0.4383	0.2936	0.3587	27.7964
33		0.3684	0.2690	0.3772	22.1113

Table B-5 (continued)

CASE NO. NAME	OBSERVED	PREDICTED		1/0
	j_g^*	j_g^*	j_p^*	
34	0.3649	0.3006	0.3252	32.5333
35	0.2812	0.2041	0.2012	31.4748
36	0.2589	0.2779	0.5044	14.7012
37	0.4225	0.4398	0.5840	28.0288
38	0.3825	0.3557	0.5125	24.1812
39	0.5471	0.5691	0.9581	22.6379
40	0.5511	0.6249	0.6468	38.3227
41	0.5398	0.6068	0.9762	24.0202
42	0.5917	0.6294	4.2314	5.1258
43	0.5304	0.5884	4.0767	4.7292
44	0.7963	0.7512	9.7698	3.4155
45	0.4819	0.4147	0.6949	21.1606

Table B-6: BMDP Results for the 450 μm Glass Beads in the 0.0504 m Diameter System.

RESIDUAL SUM OF SQUARES = 0.506742

PARAMETER	ESTIMATE
a*	385.20
b*	4.39

THE ESTIMATED MEAN SQUARE ERROR IS 1.0342E-2

CASE NO.	NAME	OBSERVED j_g^*	PREDICTED j_g^*	j_p^*	1/ ϕ
1		0.9321	0.9564	0.0350	1077.6979
2		0.8253	0.8804	0.0374	925.9003
3		0.6797	0.7231	0.0345	824.5902
4		0.6214	0.6311	0.0288	859.9495
5		0.5146	0.4156	0.0324	498.1171
6		0.7282	0.7880	0.0563	550.1387
7		0.7962	0.8165	0.0523	614.0031
8		0.5826	0.5497	0.0563	380.2485
9		0.8642	0.8812	0.0565	613.4550
10		0.9516	1.0000	0.0495	796.4230
11		0.6117	0.6703	0.0519	506.0714
12		0.8933	0.8816	0.0643	539.3248
13		0.8642	0.8819	0.0723	479.5303
14		0.7574	0.7620	0.0678	440.9935
15		0.6700	0.6925	0.0732	370.0235
16		1.1215	1.0481	0.0906	455.7587
17		0.7379	0.7050	0.0951	289.5877
18		0.5826	0.5960	0.0916	252.4459
19		0.7088	0.7283	0.1088	261.4305
20		0.8156	0.7279	0.1032	275.4631
21		0.3787	0.2703	0.0067	1575.3110
22		0.3495	0.2295	0.0068	1314.0679
23		0.3204	0.3246	0.0053	2398.6979
24		0.2427	0.5510	0.0142	1517.9139
25		0.3884	0.2740	0.0079	1350.1099
26		0.3884	0.1385	0.0288	151.3605
27		0.4806	0.4505	0.0124	1423.1850
28		0.4369	0.3210	0.0091	1380.9119
29		0.5146	0.5026	0.0224	878.3843
30		0.4321	0.4502	0.0103	1715.2800
31		0.3495	0.1200	0.0282	115.4030
32		0.5049	0.4508	0.0141	1250.9530
33		0.4952	0.4695	0.0124	1483.7459

Table B-6 (continued)

CASE NO. NAME	OBSERVED	PREDICTED		1/0
	j_g^*	j_g^*	j_p^*	
34	0.4952	0.2855	0.0114	967.6801
35	0.4466	0.2677	0.0169	607.7792
36	0.4078	0.1128	0.0226	143.8522
37	0.3787	0.4602	0.8329	13.1857
38	0.3495	0.3237	0.2567	34.4862
39	0.3204	0.3757	0.2339	52.9814
40	0.2427	0.2494	0.1588	36.4082
41	0.3884	0.4072	0.4581	24.5962
42	0.3884	0.3412	0.3130	11.8932
43	0.4806	0.4348	3.1028	5.5923
44	0.4369	0.4587	0.6632	18.9588
45	0.5146	0.5324	3.0091	6.5528
46	0.4321	0.4990	0.6374	24.3064
47	0.3495	0.3589	0.3781	10.5730
48	0.5049	0.5538	1.1342	14.4327
49	0.4952	0.5720	1.3850	12.2821
50	0.4952	0.4785	0.6352	22.3900
51	0.4466	0.3940	0.4799	20.3113
52	0.4078	0.3650	0.3968	8.7451

Table B-7: BMDP Results for the 900 μ m Glass Beads in the 0.0504 m Diameter System.

RESIDUAL SUM OF SQUARES = 0.616304

PARAMETER	ESTIMATE
a*	240.71
b*	2.36

THE ESTIMATED MEAN SQUARE ERROR IS 1.8676e-2

CASE NO.	NAME	OBSERVED j_g^*	PREDICTED j_g^*	j_p^*	1/0
1		0.4372	0.3351	0.0306	342.8984
2		0.5101	0.4989	0.0347	455.6527
3		0.5800	0.5406	0.0303	566.6915
4		0.7415	0.7354	0.0304	768.9365
5		0.6222	0.5476	0.0471	368.0371
6		0.3494	0.4730	0.0402	371.8114
7		0.5808	0.6084	0.0494	390.8757
8		0.5799	0.5581	0.0444	398.1434
9		0.5813	0.6654	0.0427	495.3922
10		0.7467	0.6503	0.0563	366.7586
11		0.3789	0.3287	0.0080	1303.8740
12		0.4882	0.4789	0.0548	275.4686
13		0.5744	0.5612	0.0680	260.4826
14		0.6701	0.6019	0.0645	295.4880
15		0.6701	0.6672	0.0696	303.9339
16		0.6892	0.5620	0.0237	751.9799
17		0.9190	0.8229	0.0038	6857.7192
18		0.8501	0.4136	0.0153	855.9920
19		0.3836	0.4192	0.0107	1238.3780
20		0.6031	0.5560	0.0208	848.9824
21		0.4499	0.2387	0.0220	336.4713
22		0.3907	0.5445	0.0160	1082.0579
23		0.3355	0.8232	0.0116	2247.3798
24		0.5073	0.5250	0.0286	583.1566
25		0.2872	0.3265	0.0163	631.9948
26		0.5408	0.5451	0.0224	771.9946
27		0.2832	0.2797	0.0222	394.5104
28		0.3836	0.3841	4.6816	2.6857
29		0.6031	0.6000	0.6830	25.4036
30		0.4499	0.4025	0.4566	22.3502
31		0.3907	0.3574	0.5486	10.4027
32		0.3355	0.3465	0.4423	16.4819
33		0.5073	0.4695	0.4811	26.9128

Table B-7 (continued)

CASE NO. NAME	OBSERVED	PREDICTED		1/0
	j_g^*	j_g^*	j_p^*	
34	0.2872	0.3901	0.5487	15.9709
35	0.5408	0.4787	0.4750	28.0965
36	0.2832	0.3903	0.3473	30.0927

Table B-8: BMDP Results for the 400 μm Iron Oxide in the 0.0504 m Diameter System.

RESIDUAL SUM OF SQUARES = 0.251884

PARAMETER	ESTIMATE
a*	416.47
b*	6.20

THE ESTIMATED MEAN SQUARE ERROR IS 5.7246E-3

CASE NO.	NAME	OBSERVED j_g^*	PREDICTED j_g^*	j_p^*	1/0
1		0.5106	0.5184	0.002891	9529.5517
2		0.4361	0.4734	0.003732	6739.1381
3		0.3653	0.3971	0.004088	5158.1557
4		0.2799	0.2869	0.003484	4370.3901
5		0.2018	0.1047	0.003020	1816.3280
6		0.1235	0.1234	0.004109	1575.3549
7		0.5530	0.5631	0.007388	4048.7380
8		0.5275	0.5732	0.009977	3051.7958
9		0.5525	0.2852	0.010063	1499.3110
10		0.3602	0.3376	0.007895	2267.6240
11		0.3941	0.4484	0.008607	2765.9660
12		0.4588	0.4478	0.008543	2782.7338
13		0.4471	0.4807	0.013493	1890.8590
14		0.3609	0.3458	0.013137	1394.0300
15		0.2949	0.2685	0.012717	1114.4849
16		0.4904	0.5111	0.014291	1898.7459
17		0.5269	0.5445	0.011606	2491.5791
18		0.3102	0.3184	0.010883	1549.0970
19		0.3791	0.3601	0.015122	1260.9599
20		0.4292	0.3783	0.018218	1099.4250
21		0.4732	0.5189	0.015974	1724.4560
22		0.3449	0.2731	0.018735	767.3311
23		0.4263	0.4308	0.016265	1404.5080
24		0.5386	0.5445	0.013331	2169.0449
25		0.4492	0.3487	0.013774	1340.6519
26		0.2603	0.0734	0.004487	829.7722
27		0.2291	0.1250	0.003538	1857.6359
28		0.2388	0.2557	0.004185	3238.8930
29		0.2247	0.1135	0.003948	1505.1309
30		0.2415	0.2518	0.004120	3239.1540
31		0.1879	0.1732	0.005479	1666.3520
32		0.2151	0.2056	0.007550	1436.2180
33		0.3107	0.3802	0.007227	2791.6770

Table B-8 (continued)

CASE NO. NAME	OBSERVED j_g^*	PREDICTED j_g^*	j_p^*	1/0
34	0.2662	0.0989	0.005544	920.4420
35	0.2460	0.0968	0.014087	334.6936
36	0.3858	0.4416	0.007464	3141.2338
37	0.2603	0.2226	0.382157	9.5780
38	0.2291	0.1862	0.146013	51.6592
39	0.2388	0.3502	0.680572	22.7618
40	0.2247	0.2202	0.316891	21.2211
41	0.2415	0.2226	0.366101	10.3928
42	0.1879	0.1922	0.217589	16.5430
43	0.2151	0.2287	0.382459	15.2229
44	0.3107	0.3466	0.482884	33.2684
45	0.2662	0.2364	0.461895	11.3825
46	0.2460	0.2240	0.616793	7.6025
47	0.3858	0.4459	1.318728	16.4457

APPENDIX C

APPENDIX C

Equipment Specifications

Pressure Transducers

Solids Feeder in the Full Scale System

Platform Scale Calibration

Correlation of Air Only Pressure Drop in the Full Scale System

DT2818 Computer Interface

Pressure Transducers

Model: PX-164

Company: Omega Engineering, Inc.

Type: Differential

Range: 0 - 10 Inches of Water
(0 - 2480 Pa)

Linearity: ± 0.50 %F.S.O.

Sensitivity: 0.50 V per inch H₂O

Repeatability and
Hysteresis: ± 0.25 %F.S.O.

Excitation Voltage: 8.0 V

Output: 1.00 to 6.00 V

Response Time: Maximum 1 msec

Solids Feeder in the Full Scale System

The solids feeder in the full scale system was constructed from the feed mechanism and motor drive assemblies from an MSA Model Bantam 400 Rockdusting machine. The modifications to the feed mechanism and motor drive assemblies will be discussed below.

The original motor drive assembly consisted of a 5 hp, 128 V DC motor and a mechanical relay starting device. The maximum load of the motor was 40 A. To obtain variable speed with this motor, a variable voltage source was constructed. This consisted of a variable AC voltage source (variac), a full wave rectifier for the field coils, and a full wave rectifier for the armature. The circuit is shown in Figure C-1. Two different variacs were used depending on the load required by the different solids particles used.

The screw used to feed the solids through the compression chamber of the feed hopper originally did not include a sealed bushing. As both gas and solids could leak past the original bushing, a modification was made. This modification included the reduction of the shaft diameter at the entrance to the feed hopper and the installation of a teflon retaining ring from the inside of the feed hopper. This retaining ring was used to hold a rope packing which was placed around the screw shaft from entering the feed hopper. This design worked well with a complete sealing effect. The packing lasted through the entire series of experiments in

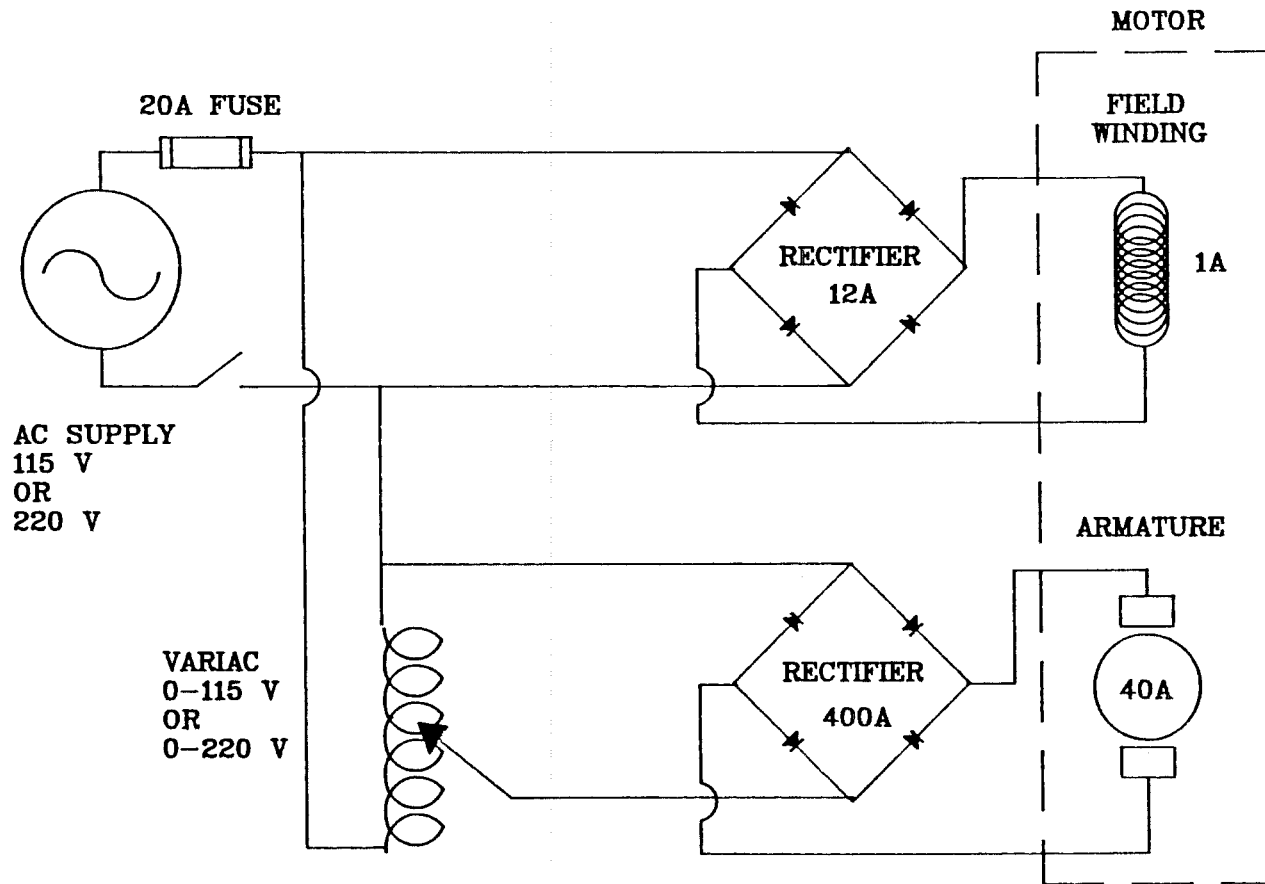


Figure C-1: Circuit Used for the Motor Drive of the Solids Feeder in the Full Scale System

the horizontal orientation. Changing of the packing involved removing the feed hopper, cleaning off the old packing, replacement with new, greased rope packing, and reassembly. Details of the teflon retaining ring assembly are shown in Figure C-2

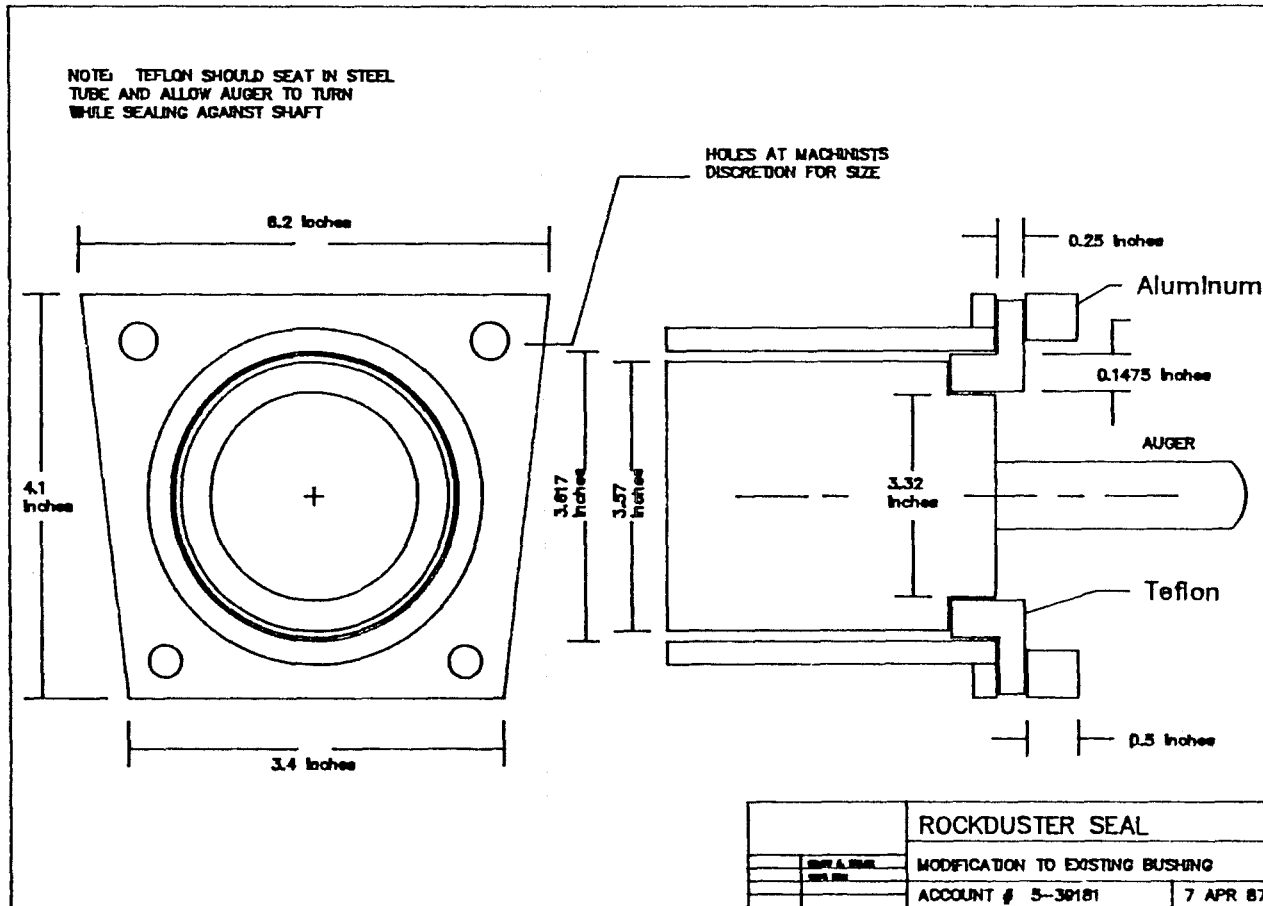


Figure C-2: Teflon Retaining Ring Assembly for the Solids Feeder in the Full Scale System

Scale Calibration

The platform scale used in the full scale system was calibrated with known weights. The calibration data is shown in Figure C-3.

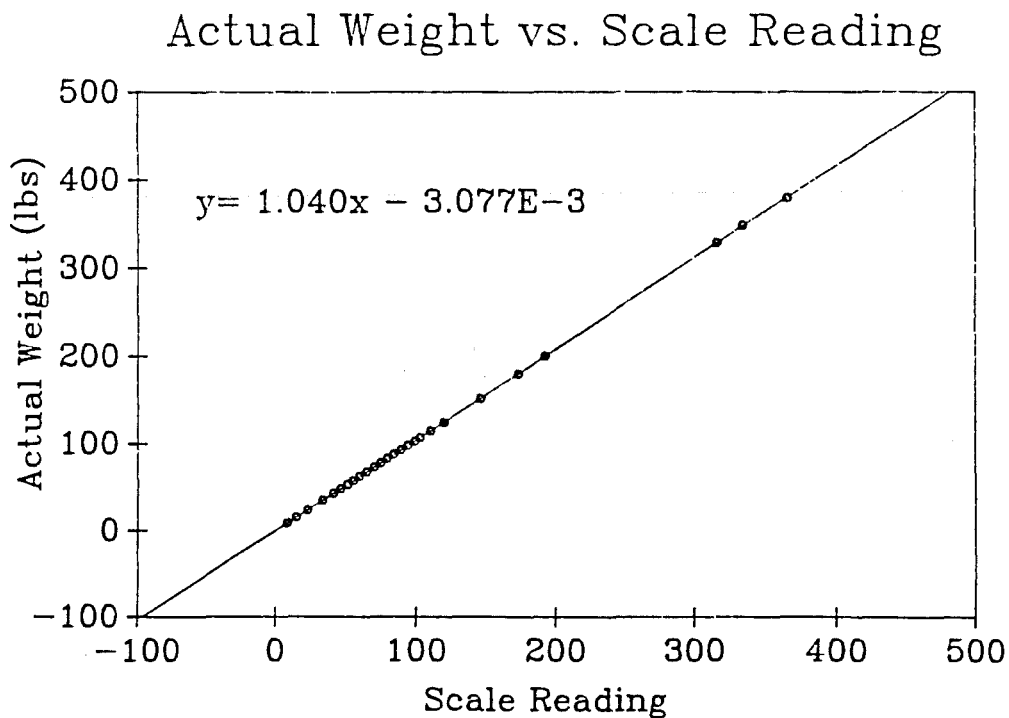


Figure C-3: Calibration Curve for the Platform Scale Used in the Full Scale System

Air Pressure Drop in the Full Scale System

The air only pressure drop in the full scale system was correlated to the following expression:

$$\frac{\Delta P}{L} = 1.2571U_g^2$$

This correlation was necessary as the volumetric flow rate of air changed upon addition of solids in the full scale system due to the characteristics of the blower and the use of a bypass valve to control flow rate.

Computer Interface

Model: DT2818

Company: Data Translations, Inc.

of A/D Channels: 4 (single ended)

Input Range: ± 10 V

Programming: BASIC language
PC-LAB Subroutine Library

Special Functions: Four A/D channels acquired
Simultaneously

Resolution: 12 bits

Channel Acquisition
Time: 6 micro seconds

A/D Conversion
Time: 4 micro seconds

Sample and Hold
Aperture
Uncertainty: ± 5 nano seconds

Connections: DT707 Screw Terminal Panel

All connections to DT2818 made through
DT707.

APPENDIX D

APPENDIX D
Computer Programs

PRESSURE.BAS

The following program was used to collect pressure data using the IBM-AT computer and the Data Translations interface boards. The program is named PRESSURE.BAS and was compiled using the Microsoft Quickbasic Compiler into the executable formed called PRESSURE.EXE.

The program is set up in three parts, the first part is a subroutine section (actually located at the end of the program) which allows pressure transducers to be calibrated. The procedure for calibration was designed to allow calibration of up to two differential transducers and 12 gauge transducers. The program does not require calibration to be performed. The second part of the program reads data for air pressure drop through the system. No solids should be flowing while this part of the program is running. A total of 1000 pressure measurements are taken from the differential pressure transducers while 150 measurements are taken from the gauge transducers used for acceleration length pressure drop measurement. The time of sampling is approximately 1.2 minutes. The average and standard deviation are calculated and held in memory as well as being displayed on the display. The display during measurement is updated to give a visual display of the pressure measurement.

The third part of the program measures the pressure

drop and acceleration data when the solids are added to the system. It is identical to the portion of the program for taking the air pressure drop data. Upon completion of pressure data collection, the data is written to two files; the file PRESSURE.DAT contains the differential pressure drop data while the file ACCELPR.DAT contains the acceleration pressure drop data. Note that channel 0 and 1 of the DT2818 are used for the differential pressure drop inputs while channels 0 through 11 of the DT2806 are used for the acceleration transducers.

```

10 REM PRESSURE TRANSDUCER DATA COLLECTION AND STATISTICS
20 DIM PRESS1(500),PRESS2(500),AIR1(500),AIR2(500)
22DIM ARATIO(12),AZERO(12),
    READING(12),ACCELAIRAVG(12),ACCELAVG(12)
23DIM AIRACCEL(150,12),
    ACCEL(150,12),ACCELAIRVAR(12),ACCELVAR(12)
24 DIM VOLTAGE (12)
29 INPUT"INPUT THE NUMBER OF ACCELERATION
    TRANSDUCERS";ACHAN
30 INPUT"ONE (1) OR TWO (2) TRANSDUCERS?";NUMB
40 SUM1=0:SUM2=0
50 '
60 DEF SEG=7552      ' This specifies where in memory to
                    ' place PCTHERM.
70 '
80 '
90 ANALOG.VALUE% = 0
100 '
110 ADC.VALUE = 3    ' This is the entry point number.
120 '
130 HIGH.V! = +10!   ' Highest voltage in range.
140 LOW.V! = -10!    ' Lowest voltage in range.
150 RANGE! = HIGH.V! - LOW.V! ' Total voltage range.
160 '
170 NOC! = 4096!
180 CHAN1%=0
190 CHAN2%=1
200 GAIN%=1
210 LSB! = RANGE!/NOC! ' Voltage of Least Significant
    Bit.

```

```

220 SCALED.LSB! = LSB! / GAIN%
230 SCALED.LOW! = LOW.V! / GAIN%
240 CLS:PRINT"DO YOU WANT TO CALIBRATE? (Y,N)"
250 W$=INKEY$:IF (W$<>"Y") AND (W$<>"N") GOTO 250
260 IF W$="N" GOTO 280
270 GOSUB 1000
280 OPEN "C:PCAL.DAT" FOR INPUT AS #1:OPEN "C:APCAL.DAT" FOR
  INPUT AS #2
290 INPUT #1, RATIO1,INTERC1,RATIO2,INTERC2
292 FOR I=1 TO ACHAN:INPUT #2, ARATIO(I),AZERO(I):NEXT I
300 CLOSE
301 LOCATE 2,29:PRINT " COMPUTED AIR PRESSURES ARE "
3 0 2 LOCATE 4,10:PRINT"  TRANSDUCER  1
  TRANSDUCER 2"
303 LOCATE 6,6:PRINT"    Pa          in. H2O    cm H2O":LOCATE
  6,51:PRINT"    Pa          in. H2O"
304 LOCATE 12,30:PRINT"ACCELERATION READINGS IN Pa";
310 AIRSUM1=0:AIRSUM2=0:ACOUNT=0
320 FOR I=1 TO 500
321 IF I<4 GOTO 348
322 N=I/4:IF N<>INT(I/4) GOTO 348
323 ACOUNT=ACOUNT+1
324 CALL DT2806(READING())
325 FOR JKL=1 TO ACHAN
326 AIRACCEL(N,JKL)=READING(JKL)*ARATIO(JKL)+AZERO(JKL)
327 ACCELAIRAVG(JKL)=ACCELAIRAVG(JKL)+AIRACCEL(N,JKL)
328 NEXT JKL
329LOCATE16,10:PRINT AIRACCEL(N,1);TAB(30)
  ;AIRACCEL(N,5);TAB(50);AIRACCEL(N,9);
330LOCATE18,10:PRINT AIRACCEL(N,2);TAB(30)
  ;AIRACCEL(N,6);TAB(50);AIRACCEL(N,10);
331LOCATE20,10:PRINT AIRACCEL(N,3);TAB(30)
  ;AIRACCEL(N,7);TAB(50);AIRACCEL(N,11);
332LOCATE22,10:PRINT AIRACCEL(N,4);TAB(30)
  ;AIRACCEL(N,8);TAB(50);AIRACCEL(N,12);
348 CALL ADC.VALUE (CHAN1%, GAIN%, ANALOG.VALUE%)
349 AIR1(I)=((ANALOG.VALUE% * SCALED.LSB!) +
  SCALED.LOW!)*RATIO1 +INTERC1 +AIR1(I)
350 CALL ADC.VALUE (CHAN2%, GAIN%, ANALOG.VALUE%)
360 AIR2(I)=((ANALOG.VALUE% * SCALED.LSB!) +
  SCALED.LOW!)*RATIO2 +INTERC2+AIR2(I)
370 AIRSUM1=AIRSUM1+AIR1(I):AIRSUM2=AIRSUM2+AIR2(I)
372 LOCATE 8,1:PRINT "          "
376LOCATE 8,10:PRINT AIR1(I);"          ";AIR1(I)/248.84;"
  ";AIR1(I)*2.54/248.84
377 LOCATE 8,50:PRINT AIR2(I);"          ";AIR2(I)/248.84
380 NEXT I
390 AVAIR1=AIRSUM1/500:AVAIR2=AIRSUM2/500:FOR I=1 TO
  ACHAN:ACCELAIRAVG(I)=ACCELAIRAVG(I)/ACOUNT:NEXT I
400 AIRVAR1=0:AIRVAR2=0
410 FOR I=1 TO 500

```

```

420AIRVAR1=AIRVAR1+(AIR1(I)-
    AVAIR1)^2:AIRVAR2=AIRVAR2+(AIR2(I)-AVAIR2)^2
430 NEXT I
440 AIRVAR1=AIRVAR1/499:AIRVAR2=AIRVAR2/499
450 STDAIR1=AIRVAR1^.5:STDAIR2=AIRVAR2^.5
451 FOR I= 1 TO ACHAN
452 FOR J=1 TO ACOUNT
453ACCELAIRVAR(I)=ACCELAIRVAR(I)+(AIRACCEL(J,I)-
    ACCELAIRAVG(I))^2
454 NEXT J
455 ACCELAIRVAR(I)=(ACCELAIRVAR(I)/(ACOUNT-1))^.5:NEXT I
460 CLS:LOCATE 4,30:PRINT "AIR AVERAGE AND STD DEVIATION"
470 LOCATE 6,20:PRINT"TRANSDUCER 1":LOCATE
    6,45:PRINT"TRANSDUCER 2"
480 LOCATE 8,20:PRINT AVAIR1;" ";STDAIR1:LOCATE 8,45:PRINT
    AVAIR2;" ";STDAIR2
481LOCATE16,10:PRINT ACCELAIRAVG(1);TAB(30)
    ;ACCELAIRAVG(5);TAB(50);ACCELAIRAVG(9);
482LOCATE18,10:PRINT ACCELAIRAVG(2);TAB(30)
    ;ACCELAIRAVG(6);TAB(50);ACCELAIRAVG(10);
483LOCATE20,10:PRINT ACCELAIRAVG(3);TAB(30)
    ;ACCELAIRAVG(7);TAB(50);ACCELAIRAVG(11);
484LOCATE22,10:PRINT ACCELAIRAVG(4);TAB(30)
    ;ACCELAIRAVG(8);TAB(50);ACCELAIRAVG(12);
490 LOCATE 24,27:PRINT"TYPE ANY KEY TO CONTINUE";
500 V$=INKEY$:IF V$="" GOTO 500
501CLS:LOCATE 4,30:PRINT "AIR AVERAGE AND STD
    DEVIATION":LOCATE 12,25:
    PRINT"ACCELERATION STD DEVIATIONS";
502 LOCATE 6,20:PRINT"TRANSDUCER 1":LOCATE
    6,45:PRINT"TRANSDUCER 2"
503 LOCATE 8,20:PRINT AVAIR1;" ";STDAIR1:LOCATE 8,45:PRINT
    AVAIR2;" ";STDAIR2
504LOCATE16,10:PRINT ACCELAIRVAR(1);TAB(30)
    ;ACCELAIRVAR(5);TAB(50);ACCELAIRVAR(9);
505LOCATE18,10:PRINT ACCELAIRVAR(2);TAB(30)
    ;ACCELAIRVAR(6);TAB(50);ACCELAIRVAR(10);
506LOCATE20,10:PRINT ACCELAIRVAR(3);TAB(30)
    ;ACCELAIRVAR(7);TAB(50);ACCELAIRVAR(11);
507LOCATE22,10:PRINT ACCELAIRVAR(4);TAB(30)
    ;ACCELAIRVAR(8);TAB(50);ACCELAIRVAR(12);
508 LOCATE 24,27:PRINT"TYPE ANY KEY TO CONTINUE";
509 V$=INKEY$:IF V$="" GOTO 509
520 CLS
521 LOCATE 2,29
522 PRINT " COMPUTED PRESSURES ARE "
523 LOCATE 4,10:PRINT " TRANSDUCER 1
    TRANSDUCER 2"
524 LOCATE 6,11:PRINT" Pa in. H2O":LOCATE
    6,51:PRINT" Pa in. H2O"
530 FOR I=1 TO 500

```

```

531 IF I<4 GOTO 570
532 N=I/4:IF N<>INT(I/4) GOTO 570
533 REM ACOUNT=ACOUNT+1
534 CALL DT2806(READING())
535 FOR JKL=1 TO ACHAN
536 ACCEL(N,JKL)=READING(JKL)*ARATIO(JKL)+AZERO(JKL)
537 ACCELAVG(JKL)=ACCELAVG(JKL)+ACCEL(N,JKL)
538 NEXT JKL
539 LOCATE 16,10:PRINT ACCEL(N,1);TAB(30)
      ;ACCEL(N,5);TAB(50);ACCEL(N,9);
540 LOCATE 18,10:PRINT ACCEL(N,2);TAB(30)
      ;ACCEL(N,6);TAB(50);ACCEL(N,10);
541 LOCATE 20,10:PRINT ACCEL(N,3);TAB(30)
      ;ACCEL(N,7);TAB(50);ACCEL(N,11);
542 LOCATE 22,10:PRINT ACCEL(N,4);TAB(30)
      ;ACCEL(N,8);TAB(50);ACCEL(N,12);
570 CALL ADC.VALUE (CHAN1%, GAIN%, ANALOG.VALUE%)
580 '
590 ' Calculate the effective voltage.
600 '
610 PRESS1(I)=((ANALOG.VALUE% * SCALED.LSB!) +
      SCALED.LOW!)*RATIO1 +INTERC1+PRESS1(I)
620 CALL ADC.VALUE (CHAN2%, GAIN%, ANALOG.VALUE%)
630 PRESS2(I)=((ANALOG.VALUE% * SCALED.LSB!) +
      SCALED.LOW!)*RATIO2 +INTERC2+PRESS2(I)
631 rem NEXT K
632 rem PRESS1(I)=PRESS1(I)/60:rem PRESS2(I)=PRESS2(I)/60
640 SUM2=SUM2+PRESS2(I)
650 SUM1=SUM1+PRESS1(I)
700 LOCATE 8,1:PRINT"
710 LOCATE 8,10:PRINT PRESS1(I);"      ";PRESS1(I)/248.84
720 LOCATE 8,50:PRINT PRESS2(I);"      ";PRESS2(I)/248.84
730 NEXT I
740 CLS
741 FOR M=1 TO ACHAN
742 ACCELAVG(M)=ACCELAVG(M)/ACOUNT
743 NEXT M
770 AVG1=SUM1/500:AVG2=SUM2/500
780 VAR1=0:VAR2=0
790 IF NUMB=1 THEN GOTO 930
800 FOR I=1 TO 500
810 VAR1=VAR1+(PRESS1(I)-AVG1)^2
820 VAR2=VAR2+(PRESS2(I)-AVG2)^2
830 NEXT I
840 VAR1=VAR1/499:VAR2=VAR2/499
850 STD1=(VAR1)^.5:STD2=(VAR2)^.5
851 FOR I= 1 TO ACHAN
852 FOR J=1 TO ACOUNT
853 ACCELVAR(I)=ACCELVAR(I)+(ACCEL(J,I)-ACCELAVG(I))^2
854 NEXT J
855 ACCELVAR(I)=(ACCELVAR(I)/(ACOUNT-1))^.5

```

```
856 NEXT I
860 CLS:LOCATE 2,30:PRINT "STANDARD DEVIATIONS ARE"
870 LOCATE 4,20:PRINT STD1:LOCATE 4,40:PRINT STD2
880 LOCATE 6,30:PRINT"AVERAGES ARE"
```

```
856 NEXT I
860 CLS:LOCATE 2,30:PRINT "STANDARD DEVIATIONS ARE"
870 LOCATE 4,20:PRINT STD1:LOCATE 4,40:PRINT STD2
880 LOCATE 6,30:PRINT"AVERAGES ARE"
890 LOCATE 8,20:PRINT AVG1:LOCATE 8,40:PRINT AVG2
891LOCATE16,10:PRINT ACCELAVG(1);TAB(30)
      ;ACCELAVG(5);TAB(50);ACCELAVG(9);
892LOCATE18,10:PRINT ACCELAVG(2);TAB(30)
      ;ACCELAVG(6);TAB(50);ACCELAVG(10);
893LOCATE20,10:PRINT ACCELAVG(3);TAB(30)
      ;ACCELAVG(7);TAB(50);ACCELAVG(11);
894LOCATE22,10:PRINT ACCELAVG(4);TAB(30)
      ;ACCELAVG(8);TAB(50);ACCELAVG(12);
900 LOCATE 24,30:PRINT "TYPE ANY KEY TO CONTINUE";
910 ALS=INKEY$:IF ALS<>"" GOTO 912
911 GOTO 910
912 CLS:LOCATE 2,30:PRINT "STANDARD DEVIATIONS ARE"
913 LOCATE 4,20:PRINT STD1:LOCATE 14,40:PRINT STD2
914 LOCATE 6,30:PRINT"AVERAGES ARE":LOCATE 10,25:PRINT
      "ACCELERATION STD DEVIATIONS";
915 LOCATE 8,20:PRINT AVG1:LOCATE 8,40:PRINT AVG2
916LOCATE16,10:PRINT ACCELVAR(1);TAB(30)
      ;ACCELVAR(5);TAB(50);ACCELVAR(9);
917LOCATE18,10:PRINT ACCELVAR(2);TAB(30)
      ;ACCELVAR(6);TAB(50);ACCELVAR(10);
918LOCATE20,10:PRINT ACCELVAR(3);TAB(30)
      ;ACCELVAR(7);TAB(50);ACCELVAR(11);
919 locate 22,10:PRINT ACCELVAR(4);TAB(30);
      ACCELVAR(8);TAB(50);ACCELVAR(12);
920 LOCATE 24,30:PRINT "TYPE ANY KEY TO CONTINUE";
921 ALS=INKEY$:IF ALS<>"" GOTO 1700
922 GOTO 921
930 FOR I= 1 TO 500
940 VAR1=VAR1+(PRESS1(I)-AVG1)^2
950 NEXT I
960 VAR1=VAR1/499:STD1=(VAR1)^.5:CLS
970 LOCATE 6,20:PRINT "AVERAGE AND STANDARD DEVIATION ARE"
980 LOCATE 8,20:PRINT AVG1:LOCATE 8,40:PRINT STD1
990 GOTO 851
1000 CLS:PRINT"CALIBRATE OP-AMP?(Y,N)"
1010 Q$=INKEY$:IF (Q$<>"Y") AND (Q$<>"N") GOTO 1010
1020 IF Q$="N" GOTO 1280
1030PRINT"APPLY 0 VOLT TO OP-AMP AND TYPE ANY KEY WHEN
      READY"
1040 PRINT"TYPE ANY KEY TO STOP AND CONTINUE"
1050 E$=INKEY$:IF E$="" GOTO 1050
1060 OPAMP=0
1070 FOR U=1 TO 500:NEXT U
1080 FOR N=1 TO 10
1090 CALL ADC.VALUE (CHAN1%, GAIN%, ANALOG.VALUE%)
1100 OPAMP=OPAMP+((ANALOG.VALUE% * SCALED.LSB!) +
```

```
        SCALED.LOW!)
1110 NEXT N
1120 OPAMP=OPAMP/10
1130 LOCATE 10,37:PRINT OPAMP
1140 R$=INKEY$:IF R$="" GOTO 1060
1150 CLS
1160 PRINT"APPLY X VOLT TO OP-AMP AND TYPE ANY KEY WHEN
      READY"
1170 PRINT"TYPE ANY KEY TO STOP AND CONTINUE"
1180 E$=INKEY$:IF E$="" GOTO 1180
1190 OPAMP=0
1200 FOR U=1 TO 1000:NEXT U
1210 FOR N=1 TO 10
1220 CALL ADC.VALUE (CHAN1%, GAIN%, ANALOG.VALUE%)
1230 OPAMP=OPAMP+((ANALOG.VALUE% * SCALED.LSB!) +
      SCALED.LOW!)
1240 NEXT N
1250 OPAMP=OPAMP/10
1260 LOCATE 10,37:PRINT OPAMP
1270 R$=INKEY$:IF R$="" GOTO 1190
1280 IF NUMB=1 GOTO 1470
1290CLS:PRINT"TURN ON PRESSURE TRANSDUCER 2 AND TYPE ANY
      KEY WHEN READY"
1300 E$=INKEY$:IF E$="" GOTO 1300
1310 OPAMP=0
1320 FOR N=1 TO 4000
1330 CALL ADC.VALUE (CHAN2%, GAIN%, ANALOG.VALUE%)
1340 OPAMP=OPAMP+((ANALOG.VALUE% * SCALED.LSB!) +
      SCALED.LOW!)
1350 NEXT N
1360 ZERO2=OPAMP/4000
1370 PRINT"SWITCH TO CALIBRATE FOR TRANSDUCER 2 AND TYPE ANY
      KEY WHEN READY"
1380 E$=INKEY$:IF E$="" GOTO 1380
1390 OPAMP=0
1400 FOR N=1 TO 4000
1410 CALL ADC.VALUE (CHAN2%, GAIN%, ANALOG.VALUE%)
1420 OPAMP=OPAMP+((ANALOG.VALUE% * SCALED.LSB!) +
      SCALED.LOW!)
1430 NEXT N
1440 CAL2=OPAMP/4000
1450INPUT "INPUT THE CALIBRATION PRESSURE FOR TRANSDUCER
      2";PCAL2
1451 PRINT "PRESS C FOR CENTIMETERS OF WATER OR I FOR
      INCHES"
1452 CC$=INKEY$
1453 IF CC$="C" THEN PCAL2=PCAL2/2.54:GOTO 1459
1454 IF CC$="I" GOTO 1459
1455 GOTO 1452
1459 CLS
1460RATIO2=PCAL2/(CAL2-ZERO2)*248.84:INTERC2=-
```

```

      (ZERO2*RATIO2)
1470 PRINT"TURN ON PRESSURE TRANSDUCER 1 WITH 0 PRESSURE
      DIFFERENTIAL":PRINT"AND TYPE ANY KEY WHEN READY"
1480 E$=INKEY$:IF E$="" GOTO 1480
1490 OPAMP=0
1500 FOR N=1 TO 4000
1510 CALL ADC.VALUE (CHAN1%, GAIN%, ANALOG.VALUE%)
1520 OPAMP=OPAMP+((ANALOG.VALUE% * SCALED.LSB!) +
      SCALED.LOW!)
1530 NEXT N
1540 ZERO1=OPAMP/4000
1550 PRINT"APPLY CALIBRATION PRESSURE TO TRANSDUCER 1
      AND":PRINT"TYPE ANY KEY WHEN READY"
1560 E$=INKEY$:IF E$="" GOTO 1560
1570 OPAMP=0
1580 FOR N=1 TO 4000
1590 CALL ADC.VALUE (CHAN1%, GAIN%, ANALOG.VALUE%)
1600 OPAMP=OPAMP+((ANALOG.VALUE% * SCALED.LSB!) +
      SCALED.LOW!)
1610 NEXT N
1620 CAL1=OPAMP/4000
1625 PRINT"THE CALIBRATION VOLTAGE WAS ";CAL1
1630 INPUT "INPUT THE CALIBRATION PRESSURE FOR TRANSDUCER
      1";PCAL1
1631 PRINT"PRESS C FOR CENTIMETERS OF WATER, I FOR INCHES"
1632 CC$=INKEY$
1633 IF CC$="C" THEN PCAL1=PCAL1/2.54:GOTO 1640
1634 IF CC$="I" GOTO 1640
1635 GOTO 1632
1640 CLS
1650 RATIO1=PCAL1/(CAL1-ZERO1)*248.84:INTERC1=-
      (ZERO1*RATIO1)
1660 OPEN "C:PCAL.DAT" FOR OUTPUT AS #1
1670 WRITE #1, RATIO1,INTERC1,RATIO2,INTERC2
1680 CLOSE
1682 CALL CALIBRATE (ARATIO(),AZERO(),ACHAN)
1690 RETURN
1700 CLOSE:OPEN "PRESSURE.DAT" FOR OUTPUT AS #1:OPEN
      "C:ACCELPR.DAT" FOR OUTPUT AS #2
1710 WRITE#1,AVG1,AVG2,STD1,STD2,VAR1,VAR2,AVAIR1,AVAIR2,
      STDAIR1,STDAIR2,AIRVAR1,AIRVAR2
1711 WRITE #2,ACHAN
1712 FOR I= 1 TO ACHAN
1713 WRITE #2,I,ACCELAIRAVG(I),
      ACCELAIRVAR(I),ACCELAVG(I),ACCELVAR(I)
1714 NEXT I
1720 CLOSE
1730 END
1800 SUB CALIBRATE (ARATIO(1),AZERO(1),ACHAN) STATIC
1810 DIM ACALVOLT (17)
1820 CLS:LOCATE 10,10:PRINT "INSURE COMMON ZERO PRESSURE ON

```

```
ACCELERATION TRANSDUCERS"
1830 LOCATE 12,20:PRINT "AND PRESS ANY KEY WHEN READY"
1840 GO$=INKEY$:IF GO$="" GOTO 1840
1850 FOR I=1 TO 100
1860 CALL DT2806 (ACALVOLT())
1870 FOR J=1 TO ACHAN
1880 AZERO(J)=ACALVOLT(J)+AZERO(J)
1890 NEXT J
1900 NEXT I
1910 FOR J= 1 TO ACHAN
1920 AZERO(J)=AZERO(J)/100:PRINT AZERO(J)
1930 NEXT J
1940 LOCATE 12,20:PRINT "APPLY COMMON PRESSURE TO
ACCELERATION TRANSDUCERS";
1950 LOCATE 14,20:PRINT "TYPE ANY KEY WHEN READY"
1960 GO$=INKEY$:IF GO$="" GOTO 1960
1970 FOR I= 1 TO 100
1980 CALL DT2806(ACALVOLT())
1990 FOR J= 1 TO ACHAN
2000 ARATIO(J)=ARATIO(J)+ACALVOLT(J)
2010 NEXT J
2020 NEXT I
2030 FOR J= 1 TO ACHAN
2040 ARATIO(J)=ARATIO(J)/100:PRINT ARATIO(J):NEXT J
2050 LOCATE 10,20:PRINT "WHAT IS THE COMMON PRESSURE IN cm
H2O";
2060 INPUT COMPRESS
2070 COMPRESS=COMPRESS*248.84/2.54
2075 OPEN "C:APCAL.DAT" FOR OUTPUT AS #1
2080 FOR J=1 TO ACHAN
2085 RAT=ARATIO(J):ZER=AZERO(J):PRINT RAT,ZER
2089 IF J=6 GOTO 2095
2090 ARATIO(J)=COMPRESS/(RAT-ZER)
2095 RAT=ARATIO(J):ZER=AZERO(J)
2100 AZERO(J)=- (RAT*ZER)
2110 WRITE #1,ARATIO(J),AZERO(J)
2120 NEXT J
2130 CLOSE
2135 CLS
2140 END SUB
2150 SUB DT2806 (VOLTAGE(1)) STATIC
2170 X=INP(&H4370)
2180 FOR CHAN%=0 TO 11
2190 OUT &H4370,CHAN%
2200 Y=INP(&H4770)
2210 BUSY=Y AND 2:IF BUSY = 0 GOTO 2200
2220 EOC=Y AND 1:IF EOC<> 0 GOTO 2200
2230 X=INP(&H4370)
2240 X=INT(X*16):Y=INT(Y/16):ALOG=X+Y:
VOLTAGE(CHAN%+1)=ALOG*(10/4096)- 5
2250 NEXT CHAN%
```

2260 END SUB

PROBE.BAS

The following program was used to collect particle velocity data as well as catalog data into a useable data format. It was called PROBE.BAS and was also compiled into an executable format.

The program accepts four signals from velocity probes on the four channels of the DT2818 interface. These signals are cross-correlated to obtain the time difference between the signals. Dividing the distance between the probes by this time gives the particle velocity for each of two sets of probes.

```

10 REM ***** PROBE.BAS *****
20 REM CROSSCORRELATION OF 4 SIGNALS FROM DT 2818
30 INPUT"INPUT THE RUN # (ANGLE MATERIAL TSIZE PSIZE
   RUN";XUNS$
40 INPUT"INPUT THE SCFM OF AIR";SCFM
50 INPUT"INPUT THE RELATIVE HUMIDITY";AH
60 INPUT"INPUT THE SOLIDS FLOW RATE (lbs/min)";WS
70 INPUT"INPUT THE PIPE DIAMETER (in)";DT
80 INPUT"INPUT THE PARTICLE DIAMETER (microns)";DP
90 INPUT"INPUT THE PARTICLE MATERIAL";M$
100 INPUT"INPUT THE PARTICLE DENSITY";DEN
110 INPUT"INPUT THE PROBE SEPARATION IN ft";DIST
120 DIST = DIST*1000
130 INPUT"IF ONLY ONE PROBE PRESENT ENTER 999 OTHERWISE
   0";TT2
135 INPUT"IS THIS A RETAKE (Y/N)";RETAKE$:IF RETAKE$="Y"
   GOTO 1290
140 PRINT,"*****
   *****"
150 PRINT
160 PRINT,"****      HIT GO TO BEGIN SIGNAL DATA COLLECTION
   ****"
170 PRINT
180 PRINT,"*****
   *****"
190 INPUT AS$
200 IF AS$<>"GO" GOTO 190
210 ' CROSS CORRELATION OF 4 SIGNALS FROM DT 2818
220 '
230 '
240 DEF SEG=32512      ' This specifies where in memory to
                       place PCTHERM.
250 '
260 '   All variables should be given initial values
270 '   before being used in PCTHERM calls.
280 '
290 DIM ANALOG.ARRAY%(9999)
300 NUMBER.OF.VALUES% = 10000
310 '
320 SETUP.ADC = 9      ' This is a PCTHERM entry
   point.
330 ADC.SERIES = 12    ' This is a PCTHERM entry
   point.
340 SET.CLOCK.DIVIDER = 45 ' This is a PCTHERM entry
   point.
350 ',
360 HIGH.V! = +10!    ' Highest voltage in range.
370 LOW.V! = -10!    ' Lowest voltage in range.
380 RANGE! = HIGH.V! - LOW.V! ' Total voltage range.
390 '
400 NOC! = 4096!

```



```

822 X20=J/4+1:X20=X20/4.163333+27
830 IF AVG1 < ABS(ANALOG.ARRAY%(J)) THEN
    AVG1=ABS(ANALOG.ARRAY%(J)):MAX1T=X20:ZM1=J/4
840 IF AVG2 < ABS(ANALOG.ARRAY%(J+1)) THEN
    AVG2=ABS(ANALOG.ARRAY%(J+1)):MAX2T=X20:ZM2=J/4
850 IF AVG3 < ABS(ANALOG.ARRAY%(J+2)) THEN AVG3=
    ABS(ANALOG.ARRAY%(J+2)):MAX3T=X20:ZM3=J/4
860 IF AVG4 < ABS(ANALOG.ARRAY%(J+3)) THEN AVG4 =
    ABS(ANALOG.ARRAY%(J+3)):MAX4T=X20:ZM4=J/4
870 NEXT J
880 KEY OFF:CLS:SCREEN 2
890 BORD1$="BL293D96 R50":FOR Z= 1 TO 11:BORD1$=BORD1$ + "
    U5 D5 R50":NEXT Z
900 BORD1$=BORD1$+ " U125 L50":FOR Z= 1 TO 11:BORD1$=BORD1$
    + " D5 U5 L50":NEXT Z
910 BORD1$=BORD1$+ " D30"
920 DRAW BORD1$
930 BORD2$="BL310 BD25":BORD3$=" NR18 U2 E2R5F2D1BU7R10L3H3
    U1BU7D1F2R2E2U1H2L1G2BU7NL11"
940 BORD3$=BORD3$+"H2U1E1R4F1D2G1L2BU14BD5U3L2G2D1
    F1R5E2U2BU12":BORD4$="D6U3L18F3"
950 DRAW BORD2$+BORD3$+BORD4$
960 BORD5$="BL340 BD110":BORD6$="BD6BL12H2U2E2R2F6R3U6"
970 DRAW BORD5$+BORD3$+BORD6$
980 FOR J = 0 TO 9988 STEP 4
990 Y1=ANALOG.ARRAY%(J)/AVG1:Y1=Y1+.6:Y1=-46.67*Y1+150
1000 X1=J/4+1:X1=X1/4.163333+27
1010 PSET (X1,Y1)
1020 Y2=ANALOG.ARRAY%(J+1)/AVG2:Y2=-46.67*Y2+150
1030 PSET (X1,Y2)
1040 Y3=ANALOG.ARRAY%(J+2)/AVG3:Y3=Y3+.6:Y3=-46.67*Y3+210
1050 PSET (X1,Y3)
1060 Y4=ANALOG.ARRAY%(J+3)/AVG4:Y4=-46.67*Y4+210
1070 PSET (X1,Y4)
1080 NEXT J
1081 SCR1=-1.55*46.67+150:SCR2=-1.65*46.67+150
1082 LINE (MAX1T,SCR1)-(MAX1T,SCR2)
1083 SCR1=-.95*46.67+150:SCR2=-1.05*46.67+150
1084 LINE (MAX2T,SCR1)-(MAX2T,SCR2)
1085 SCR1=-1.55*46.67+210:SCR2=-1.65*46.67+210
1086 LINE (MAX3T,SCR1)-(MAX3T,SCR2)
1087 SCR1=-.95*46.67+210:SCR2=-1.05*46.67+210
1088 LINE (MAX4T,SCR1)-(MAX4T,SCR2)
1090 LOCATE 2,5:PRINT DATES;" ";TIMES;" RUN # ";XUNS;"
    MATERIAL- ";MS
1100 LOCATE 4,5:PRINT"AIR - ";SCFM ";" SCFM WS - ";WS;"
    lbs/min PIPE DIAM. - ";DT;"in"
1110 LOCATE 6,5:PRINT"Dp - ";DP;" mic. RhoP - ";DEN;"
    lb/ft3 R.H.- ";AH
1120 LOCATE 8,28:PRINT"TYPE ANY KEY TO CONTINUE";
1130 IF INKEY$="" GOTO 1130

```

```
1140 LOCATE 25,1:PRINT"TYPE CORR TO CORRELATE OR REDO TO
      TAKE A NEW SIGNAL"
1150 INPUT A$
1160 IF A$="CORR" GOTO 1190
1170 IF A$="REDO" GOTO 520
1180 GOTO 1140
1190 CLS:SCREEN 0
1200 OPEN "C:SIGNAL1.DAT" FOR OUTPUT AS #1:OPEN
      "C:SIGNAL3.DAT" FOR OUTPUT AS #3
1210 OPEN "C:SIGNAL2.DAT" FOR OUTPUT AS #2:OPEN
      "C:SIGNAL4.DAT" FOR OUTPUT AS #4
1220 FOR J=0 TO 9996 STEP 4
1230 PRINT #1, ANALOG.ARRAY%(J)/AVG1
1240 PRINT #2, ANALOG.ARRAY%(J+1)/AVG2
1250 PRINT #3, ANALOG.ARRAY%(J+2)/AVG3
1260 PRINT #4, ANALOG.ARRAY%(J+3)/AVG4
1270 NEXT J
1280 CLOSE
1290 DIM FBUF(2500),FBUF1(2500),RMULT(2500),SUMT(350),
      SUMMAX(100),TIMMAX(100)
1330 OPEN "C:SIGNAL1.DAT" FOR INPUT AS #1
1340 OPEN "C:SIGNAL2.DAT" FOR INPUT AS #2
1350 GOTO 1380
1360 OPEN "C:SIGNAL3.DAT" FOR INPUT AS #1
1370 OPEN "C:SIGNAL4.DAT" FOR INPUT AS #2
1371 ZM1=ZM3:ZM2=ZM4
1380 FOR I=1 TO 2500
1390 INPUT #1,FBUF(I)
1400 INPUT #2,FBUF1(I)
1410 NEXT
1415 CLOSE
1420 GV=SCFM*3.05577/(DT^2)
1430 INCR1=INT(ZM2-ZM1)-60
1440 INCR2=INCR1+120
1441 IF INCR1>0 GOTO 1510
1442 BEEP:BEEP:BEEP
1443 PRINT"WARNING - WINDOW UNDEFINED"
1444 PRINT"INPUT NEW INCREMENT LIMITS"
1445 INCR1=DIS/GV
1446 PRINT"THE BEST GUESS FOR START POINT OF INCREMENT
      WINDOW IS",INCR1
1447 INPUT"INPUT START POINT OF INCREMENT WINDOW";INCR1
1448 INPUT"INPUT END POINT OF INCREMENT WINDOW";INCR2
1510 PRINT"INCREMENT CHOSEN FROM ";INCR1;" TO ";INCR2
1511 PRINT"(Y) TO ACCEPT (N) TO INPUT NEW INCREMENT"
1512 A$=INKEY$
1513 IF A$="Y" GOTO 1519
1514 IF A$="N" GOTO 1446
1515 IF A$="" GOTO 1512
1519 FOR J=INCR1 TO INCR2
1520 INCR3=2500-INCR2
```

```

1530 FOR I=1 TO INCR3
1540 K=I+J
1550 RMULT(I)=FBUF(I)*FBUF1(K)
1560 NEXT I
1570 SUM=0!
1580 INCR4=INCR3-1
1590 FOR I=1 TO INCR4
1600 C12=(RMULT(I+1)+RMULT(I))/2!
1610 SUM=SUM+C12
1620 NEXT I
1630 SUMT(J)=SUM
1640 LOCATE 20,25
1650 PRINT "THE OUTER LOOP IS AT ",J
1660 NEXT J
1670 TIME=INCR1-1
1680 K1=0
1690 INCR5=INCR2-2
1700 INCR6 = INCR1 - 1: SUMT(INCR6)=0!
1710 SUMMIN=9999!
1720 FOR I=INCR6 TO INCR5
1730 IF I < INCR1 GOTO 1750
1740 IF SUMMIN > SUMT(I) THEN SUMMIN = SUMT(I)
1750 TIME=TIME+1!
1760 IF SUMT(I)<SUMT(I+1) AND SUMT(I+1)>SUMT(I+2) THEN
K1=K1+1:SUMMAX(K1)=SUMT(I+1):TIMMAX(K1)=TIME:PRINT "MAXIMUM
OCCURED= ",TIME," ",SUMMAX(K1)
1770 NEXT I
1780 PMAX=SUMMAX(1)
1790 TIMAX=TIMMAX(1)
1810 FOR I=2 TO K1
1820 IF SUMMAX(I)<PMAX GOTO 1850
1830 PMAX=SUMMAX(I)
1840 TIMAX=TIMMAX(I)
1850 NEXT
1851 IF TIMAX<=0 GOTO 1442
1860 KEY OFF:CLS:SCREEN 2:XINC=600/(INCR2-INCR1):X1=20-XINC
1870 BORD10$= "BL300D79R600U122"
1880 FOR I= 1 TO 5:BORD10$=BORD10$+"L100D3U3":NEXT
1890 BORD10$= BORD10$+ "L100D43"
1900 DRAW BORD10$
1910 NINCR=INCR2-1
1920 SLOPE= 100/(SUMMIN/PMAX -1)
1930 INTER= 70 - SLOPE
1940 FOR II= INCR1 TO NINCR
1950 Y1=SLOPE*SUMT(II)/PMAX + INTER
1960 Y2=SLOPE*SUMT(II+1)/PMAX + INTER
1970 X1=X1+XINC:X2=X1+XINC
1980 LINE (X1,Y1)-(X2,Y2)
1990 NEXT II
2000 PV=DIST/TIMAX:LOCATE 3,20:INPUT"ENTER WS (lb/min)
";WS:LOCATE 3,19:PRINT"
";

```

```
2010 FOR I= 1 TO 5:BORD10$=BORD10$+"L100D3U3":NEXT
2020 PHI=3.05577*WS/(.5*(DT^2)*PV*DEN)
2030 E=1-PHI
2040 LOCATE 1,5:PRINT DATES$;"    ";TIMES$;"    RUN # ";XUNS$
2050 LOCATE 3,5:PRINT"Ug ";GV;" ft/sec    ";Up ";PV;"
ft/sec eps ";E
2060 SCRINC=(INCR2-INCR1)/6
2070 LOCATE 5,5:PRINT"WINDOW ";INCR1;" TO ";INCR2;" msec
IN INCREMENTS OF ";SCRINC
2080 LOCATE 7,28:PRINT"TYPE ANY KEY TO CONTINUE";
2090 IF INKEY$ = "" GOTO 2090
2091 CLS:SCREEN 0
2100 SV=(GV/E)-PV
2150 PRINT
2160 LOCATE 25,1:PRINT "TYPE ANY KEY TO CONTINUE"
2170 A$=INKEY$:IF A$ = "" GOTO 2170
2171 CLS
2200 ALOAD=379*WS/(SCFM/2*29)
2350 IF TT2 = 999 GOTO 2380
2360 TT2=999
2361 PVL=PV:E1=E:SV1=SV:WS1=WS
2370 GOTO 1360
2380 LOCATE 25,1:PRINT "TYPE ANY KEY TO CONTINUE"
2390 A$=INKEY$:IF A$ = "" THEN 2390
2391 OPEN "A:XRUN.DAT" FOR APPEND AS #1
2392WST=WS1+WS:WRITE#1, XUNS$,DATES$,TIMES$,DT,DP,MS$,GV,PVL,
PV,SV1,SV,E1,E,WST,WS1,WS,SCFM,ALOAD,AH
2393 CLOSE
2394 OPEN "PRESSURE.DAT" FOR INPUT AS #1
2395 OPEN "A:XRUN.DAT" FOR APPEND AS #2
2396 FOR VX= 1 TO 12:INPUT #1, SUMT(VX):NEXT
2397WRITE #2,SUMT(1),SUMT(2),SUMT(3),SUMT(4),SUMT(5),
SUMT(6),SUMT(7),SUMT(8),SUMT(9),SUMT(10),SUMT(11),
SUMT(12)
2399 CLOSE
2400 OPEN "ACCELPR.DAT" FOR INPUT AS #1:OPEN
"B:ACCPRESS.DAT" FOR APPEND AS #2
2410 WRITE #2,XUNS$,DATES$,TIMES$,DT,DP,GV,WST,SCFM,ALOAD,AH
2420 INPUT #1,SUMT(1):WRITE #2,SUMT(1)
2430 FOR I=1 TO SUMT(1): INPUT
#1,SUMT(2),SUMT(3),SUMT(4),SUMT(5),SUMT(6)
2440 WRITE #2,SUMT(2),SUMT(3),SUMT(4),SUMT(5),SUMT(6)
2450 NEXT I
2461 CLS:SCREEN 0
2470 END
```

APPENDIX E

APPENDIX E
Tabulated Experimental Data

Table E-1: Experimental Data for 67 μm Glass Beads in the 0.0266 m Diameter System

Run I. D.	U_g (m/s)	U_{pu} (m/s)	U_{pl} (m/s)	W_{su} (kg/s)	W_{sl} (kg/s)	F.A. (-)
H-1-GB-67-1	19.46	19.26	19.26	0.0090	0.0071	No Layer
H-1-GB-67-2	17.69	17.46	17.46	0.0087	0.0070	No Layer
H-1-GB-67-3	15.32	15.10	15.10	0.0080	0.0079	No Layer
H-1-GB-67-4	13.20	12.99	12.99	0.0073	0.0083	No Layer
H-1-GB-67-5	10.41	8.59	9.47	0.0057	0.0096	0.1940
H-1-GB-67-6	8.63	7.35	7.76	0.0039	0.0107	0.2440
H-1-GB-67-7	6.60	5.12	6.98	0.0092	0.0066	0.2440
H-1-GB-67-8	21.24	19.95	19.95	0.0089	0.0070	No Layer
H-1-GB-67-9	23.02	21.49	21.49	0.0088	0.0067	No Layer
H-1-GB-67-10	26.15	24.29	24.29	0.0090	0.0065	No Layer
H-1-GB-67-11	23.27	22.35	22.35	0.0058	0.0046	No Layer
H-1-GB-67-12	20.31	19.95	19.95	0.0060	0.0047	No Layer
H-1-GB-67-13	17.77	17.37	17.37	0.0057	0.0047	No Layer
H-1-GB-67-14	15.06	14.63	14.63	0.0054	0.0049	No Layer
H-1-GB-67-15	12.52	9.97	11.64	0.0052	0.0055	No Layer
H-1-GB-67-16	9.90	10.34	9.63	0.0040	0.0060	0.1390
H-1-GB-67-17	8.29	7.65	7.65	0.0034	0.0066	0.2020
H-1-GB-67-18	7.44	4.73	4.58	0.0021	0.0074	0.2020
H-1-GB-67-20	16.92	15.96	16.61	0.0059	0.0040	No Layer
H-1-GB-67-21	11.68	13.96	12.99	0.0073	0.0149	0.1740
H-1-GB-67-22	13.71	12.99	12.99	0.0091	0.0195	No Layer
H-1-GB-67-23	15.15	14.32	14.70	0.0097	0.0182	No Layer
H-1-GB-67-24	17.18	18.02	18.02	0.0093	0.0110	No Layer
H-1-GB-67-25	18.19	16.93	17.46	0.0124	0.0213	No Layer
H-1-GB-67-26	19.97	19.26	18.62	0.0124	0.0154	No Layer
H-1-GB-67-27	23.19	20.69	20.69	0.0139	0.0146	No Layer
H-1-GB-67-28	26.23	23.28	23.28	0.0155	0.0153	No Layer
H-1-GB-67-29	9.47	8.46	8.59	0.0049	0.0159	0.2440
H-1-GB-67-30	8.37	8.46	3.62	0.0026	0.0352	0.2440
H-1-GB-67-31	8.37	9.27	9.27	0.0045	0.0554	0.2440
H-1-GB-67-32	10.15	9.97	9.16	0.0080	0.0639	0.1940
H-1-GB-67-33	12.01	12.41	11.40	0.0123	0.0630	0.1740
H-1-GB-67-34	13.71	11.17	11.64	0.0150	0.0605	No Layer
H-1-GB-67-35	15.32	11.64	12.99	0.0164	0.0561	No Layer
H-1-GB-67-36	17.69	17.46	17.46	0.0185	0.0503	No Layer
H-1-GB-67-37	19.55	17.46	18.02	0.0214	0.0532	No Layer
H-1-GB-67-38	22.00	19.95	19.95	0.0228	0.0464	No Layer
H-1-GB-67-39	23.69	19.95	19.95	0.0258	0.0482	No Layer
H-1-GB-67-40	26.49	22.35	23.28	0.0260	0.0409	No Layer

Table E-2: Experimental Data for 67 μm Glass Beads in the 0.0266 m Diameter System

Run #	$\Delta P_s/L$ upper	σ_s upper	$\Delta P_s/L$ lower	σ_s lower	$\Delta P_a/L$ upper	σ upper	$\Delta P_a/L$ lower	σ lower
1	292.1	26.3	292.0	25.8	228.9	11.7	227.0	11.4
2	242.3	20.1	239.9	21.8	197.3	9.5	193.2	8.9
3	188.5	12.9	188.5	14.0	153.3	7.8	150.3	7.2
4	158.5	9.8	155.4	12.0	120.7	6.3	117.3	5.2
5	125.3	10.2	125.5	15.0	80.1	4.6	77.8	3.6
6	101.7	3.6	100.3	6.7	57.5	3.3	55.2	2.5
7	190.4	89.3	194.8	97.7	36.3	2.4	33.5	2.0
8	325.8	29.0	327.2	29.8	263.1	12.3	261.5	12.7
9	362.3	30.4	363.5	31.7	297.0	13.6	296.9	12.9
10	436.2	33.3	438.3	34.4	366.6	15.7	364.8	14.7
11	344.2	22.9	346.4	24.5	302.8	12.9	302.4	12.5
12	281.2	18.4	280.8	21.0	243.2	11.0	241.1	9.7
13	223.8	13.9	223.5	17.0	195.9	9.4	193.5	7.8
14	172.4	9.5	170.9	12.7	147.7	7.5	144.8	5.5
15	131.5	6.9	131.7	10.1	107.7	5.9	107.6	4.4
16	99.4	5.2	99.3	9.6	72.1	4.3	70.8	3.0
17	88.1	3.8	89.0	9.6	53.3	3.5	52.0	2.6
18	79.2	4.4	81.7	8.5	42.8	2.9	43.3	2.3
20	207.3	11.2	207.2	11.4	179.8	8.8	177.9	7.8
21	154.2	30.1	153.4	31.7	97.7	5.5	95.9	4.7
22	188.4	45.9	188.6	47.4	125.3	6.8	123.7	5.3
23	208.8	48.3	209.7	49.8	146.6	7.2	145.1	6.2
24	231.6	35.2	231.9	36.9	184.4	9.1	183.0	7.6
25	278.4	67.5	278.8	69.9	201.6	9.9	199.7	8.2
26	301.1	54.7	294.5	53.5	235.2	11.2	229.5	11.2
27	385.3	58.1	377.6	58.4	294.4	13.9	287.1	13.1
28	461.7	69.9	453.3	69.9	363.1	16.0	354.2	14.9
29	116.6	6.2	116.0	9.4	67.1	4.2	66.0	3.9
30	100.5	32.6	101.8	56.8	53.3	3.3	52.2	2.3
31	162.1	81.2	157.2	73.2	54.1	3.4	53.0	3.3
32	220.6	93.5	219.3	92.8	75.5	4.5	74.3	4.4
33	236.7	105.6	234.9	104.0	100.9	5.6	98.6	5.8
34	304.9	110.4	299.8	108.7	126.9	6.9	121.6	6.7
35	306.9	97.5	301.3	95.5	149.5	7.5	145.4	7.4
36	349.2	125.5	342.9	123.1	192.7	9.6	187.4	8.4
37	367.7	110.0	360.4	107.4	227.6	10.8	220.8	9.7
38	394.7	105.7	386.3	102.9	270.6	12.8	263.5	11.8
39	450.0	116.0	440.3	113.4	306.7	14.0	299.8	12.5
40	488.0	119.5	476.5	111.4	360.3	16.4	355.8	15.3

Table E-3: Experimental Data for 450 μm Glass Beads in the 0.0266 m Diameter System

Run I.D.	U_g (m/s)	U_{pu} (m/s)	U_{pl} (m/s)	W_{su} (kg/s)	W_{sl} (kg/s)	F.A. (-)
H-1-GB-450-1	20.56	15.33	15.33	0.0172	0.0112	No Layer
H-1-GB-450-2	17.52	12.57	12.57	0.0178	0.0129	No Layer
H-1-GB-450-3	15.91	11.64	11.64	0.0166	0.0115	No Layer
H-1-GB-450-4	14.13	10.30	10.30	0.0157	0.0123	No Layer
H-1-GB-450-5	12.27	9.11	8.98	0.0143	0.0134	No Layer
H-1-GB-450-6	10.83	8.05	8.05	0.0130	0.0146	No Layer
H-1-GB-450-7	9.14	8.16	5.51	0.0108	0.0162	0.1280
H-1-GB-450-8	7.53	3.65	3.67	0.0075	0.0228	0.1500
H-1-GB-450-9	5.92	2.45	4.42	0.0059	0.0187	0.1710
H-1-GB-450-10	17.77	12.82	12.82	0.0167	0.0110	No Layer
H-1-GB-450-11	21.41	14.96	14.96	0.0108	0.0075	No Layer
H-1-GB-450-12	17.77	12.82	12.82	0.0112	0.0079	No Layer
H-1-GB-450-13	16.16	11.22	11.22	0.0108	0.0078	No Layer
H-1-GB-450-14	14.47	10.47	10.47	0.0108	0.0082	No Layer
H-1-GB-450-15	12.69	9.24	9.38	0.0102	0.0087	No Layer
H-1-GB-450-16	9.73	7.14	7.06	0.0085	0.0099	0.1170
H-1-GB-450-17	7.78	4.79	4.83	0.0061	0.0115	0.1170
H-1-GB-450-18	6.68	2.34	4.21	0.0045	0.0126	0.1390
H-1-GB-450-19	5.92	6.28	6.28	0.0034	0.0132	0.1390
H-1-GB-450-20	5.16	3.04	3.04	0.0034	0.0119	0.1390
H-1-GB-450-21	20.90	14.61	14.96	0.0062	0.0042	No Layer
H-1-GB-450-22	17.60	11.64	12.08	0.0055	0.0042	No Layer
H-1-GB-450-23	16.16	11.02	11.22	0.0055	0.0041	No Layer
H-1-GB-450-24	13.88	9.82	9.82	0.0057	0.0042	No Layer
H-1-GB-450-25	11.34	8.49	8.38	0.0046	0.0046	No Layer
H-1-GB-450-26	8.80	5.87	6.22	0.0046	0.0052	No Layer
H-1-GB-450-27	6.94	4.79	4.58	0.0032	0.0060	0.1170
H-1-GB-450-28	5.41	3.04	3.04	0.0018	0.0066	0.1170
H-1-GB-450-29	4.73	2.21	2.51	0.0024	0.0052	0.1170
H-1-GB-450-30	21.07	14.28	14.28	0.0057	0.0039	No Layer
H-1-GB-450-31	9.31	7.30	6.75	0.0219	0.0587	0.1760
H-1-GB-450-32	9.31	7.06	7.06	0.0218	0.0563	0.1760
H-1-GB-450-33	12.18	9.24	9.24	0.0395	0.0508	No Layer
H-1-GB-450-34	14.98	10.83	10.65	0.0497	0.0407	No Layer
H-1-GB-450-35	16.67	12.57	12.08	0.0541	0.0363	No Layer
H-1-GB-450-36	18.45	13.37	13.09	0.0531	0.0334	No Layer
H-1-GB-450-37	20.31	15.33	14.96	0.0602	0.0363	No Layer
H-1-GB-450-38	23.36	17.46	16.99	0.0638	0.0354	No Layer
H-1-GB-450-39	8.37	3.63	3.61	0.0203	0.0598	0.1810
H-1-GB-450-40	7.53	4.36	2.96	0.0216	0.0558	0.1810

Table E-4: Experimental Data for 450 μm Glass Beads in the 0.0266 m Diameter System

Run #	$\Delta P_s/L$ upper	σ_s upper	$\Delta P_s/L$ lower	σ_s lower	$\Delta P_a/L$ upper	σ upper	$\Delta P_a/L$ lower	σ lower
1	411.8	13.0	403.9	12.3	264.0	11.0	256.3	11.2
2	342.6	18.3	336.0	23.7	197.9	8.6	190.8	6.8
3	286.0	10.9	280.2	14.5	168.3	7.3	161.3	5.0
4	247.2	10.3	242.9	10.3	137.2	6.3	132.9	6.3
5	211.8	6.0	208.0	5.9	107.8	5.5	103.9	5.1
6	186.0	5.4	183.2	5.2	88.2	4.7	85.4	4.5
7	168.5	8.4	166.4	8.4	65.5	3.3	63.2	3.4
8	147.9	6.9	145.6	6.9	46.4	2.6	45.0	2.3
9	146.2	13.2	145.9	16.6	30.6	1.9	30.2	1.2
10	326.7	13.1	321.7	13.1	203.8	8.9	198.5	8.9
11	391.9	15.5	384.7	20.1	278.6	11.5	272.3	10.7
12	305.2	11.5	300.7	25.7	202.3	8.6	197.4	5.7
13	266.0	9.9	263.1	22.0	171.1	7.7	168.0	5.2
14	229.1	8.4	226.7	17.7	142.9	6.7	140.0	4.5
15	194.1	7.7	191.6	7.6	114.9	5.6	111.9	5.3
16	137.4	3.7	136.4	3.4	74.0	3.7	72.5	3.6
17	106.9	3.6	106.2	3.6	49.3	2.6	48.8	2.5
18	82.1	2.9	80.2	3.1	37.4	2.2	35.9	2.0
19	83.4	3.3	81.8	4.6	29.6	1.9	28.0	1.4
20	194.6	54.9	190.2	55.3	24.2	1.7	22.7	1.3
21	322.3	12.7	314.4	13.4	263.3	11.0	254.1	11.3
22	252.4	11.1	246.5	11.2	195.9	8.8	189.8	8.0
23	224.8	10.1	219.4	15.4	168.0	7.7	162.0	5.6
24	180.0	6.7	177.6	11.3	127.3	6.3	124.4	3.9
25	134.8	5.5	133.0	10.3	90.9	4.7	89.1	3.0
26	91.9	4.3	92.3	7.3	57.8	3.3	58.0	2.1
27	69.9	3.9	69.7	6.4	37.8	2.4	37.9	1.6
28	57.0	2.3	56.7	3.4	24.8	1.7	25.3	1.3
29	106.8	31.6	106.1	32.0	20.8	1.5	20.7	1.2
30	330.2	13.7	321.9	13.4	264.4	10.9	255.8	11.2
31	284.6	24.9	283.8	34.3	64.9	3.4	63.4	3.3
32	275.2	30.4	276.1	43.4	64.9	3.6	63.4	2.3
33	361.8	20.0	360.5	23.6	104.2	5.2	101.5	3.5
34	405.3	12.3	403.5	21.2	148.1	6.9	144.6	4.6
35	470.3	24.6	456.9	61.0	182.8	8.1	172.7	5.1
36	500.8	75.9	497.3	216.4	216.2	9.7	205.5	6.3
37	606.7	135.6	601.5	134.9	254.2	10.9	246.7	10.3
38	740.9	219.0	732.4	218.7	316.8	11.7	307.1	11.7
39	299.5	34.2	299.0	43.5	57.4	3.0	55.0	2.5
40	344.5	56.8	346.2	70.1	47.0	2.7	45.1	1.8

Table E-5: Experimental Data for 900 μm Glass Beads in the 0.0266 m Diameter System

Run I.D.	U_g (m/s)	U_{pu} (m/s)	U_{pl} (m/s)	W_{su} (kg/s)	W_{sl} (kg/s)	F.A. (-)
H-1-BG-900-1	16.75	11.22	11.22	0.0102	0.0074	No Layer
H-1-BG-900-2	14.47	9.97	9.67	0.0100	0.0085	No Layer
H-1-BG-900-3	12.69	8.85	8.05	0.0075	0.0100	No Layer
H-1-BG-900-4	11.00	7.85	6.68	0.0060	0.0115	0.0440
H-1-BG-900-5	9.14	5.02	5.02	0.0037	0.0127	0.1050
H-1-BG-900-6	7.70	5.66	2.41	0.0035	0.0134	0.1050
H-1-BG-900-7	6.85	5.37	5.37	0.0032	0.0142	0.1170
H-1-BG-900-8	19.72	13.37	13.09	0.0121	0.0074	No Layer
H-1-BG-900-9	21.32	14.61	14.61	0.0135	0.0067	No Layer
H-1-BG-900-10	22.85	14.96	14.96	0.0138	0.0065	No Layer
H-1-BG-900-11	17.69	12.32	12.32	0.0087	0.0050	No Layer
H-1-BG-900-12	16.50	11.02	11.02	0.0081	0.0050	No Layer
H-1-BG-900-13	14.38	9.97	9.82	0.0071	0.0057	No Layer
H-1-BG-900-14	12.69	4.65	8.49	0.0062	0.0064	No Layer
H-1-BG-900-15	11.00	7.39	7.39	0.0051	0.0070	No Layer
H-1-BG-900-16	9.47	3.78	5.76	0.0041	0.0079	No Layer
H-1-BG-900-17	7.61	7.85	7.76	0.0024	0.0089	0.1280
H-1-BG-900-18	6.85	6.98	6.98	0.0015	0.0072	0.1610
H-1-BG-900-19	6.34	2.08	2.07	0.0013	0.0070	0.1610
H-1-BG-900-20	19.97	13.37	13.37	0.0090	0.0047	No Layer
H-1-BG-900-21	17.69	11.86	12.08	0.0046	0.0026	No Layer
H-1-BG-900-22	16.08	11.02	11.43	0.0042	0.0028	No Layer
H-1-BG-900-23	14.55	10.13	10.30	0.0040	0.0029	No Layer
H-1-BG-900-24	12.52	8.27	8.38	0.0035	0.0033	No Layer
H-1-BG-900-25	10.83	7.39	6.98	0.0027	0.0037	No Layer
H-1-BG-900-26	8.88	7.30	7.30	0.0021	0.0038	No Layer
H-1-BG-900-27	7.27	3.74	4.00	0.0015	0.0044	0.1280
H-1-BG-900-28	6.26	2.61	2.04	0.0012	0.0044	0.1610
H-1-BG-900-29	22.85	14.96	14.96	0.0049	0.0026	No Layer
H-1-BG-900-30	5.92	2.10	2.23	0.0009	0.0032	0.1610
H-1-BG-900-31	22.93	15.33	15.33	0.0545	0.0285	No Layer
H-1-BG-900-32	20.73	14.61	13.37	0.0547	0.0327	No Layer
H-1-BG-900-33	17.77	11.86	11.43	0.0438	0.0352	No Layer
H-1-BG-900-34	16.08	10.30	10.30	0.0346	0.0356	No Layer
H-1-BG-900-35	14.47	8.49	8.73	0.0271	0.0358	No Layer
H-1-BG-900-36	12.86	4.91	7.76	0.0206	0.0345	No Layer
H-1-BG-900-37	11.42	6.16	6.34	0.0140	0.0334	No Layer
H-1-BG-900-38	9.31	7.95	9.67	0.0070	0.0304	0.1170
H-1-BG-900-39	7.95	2.51	2.51	0.0075	0.0293	0.1710
H-1-BG-900-40	16.08	10.13	10.13	0.0345	0.0299	No Layer
H-1-BG-900-41	10.74	4.52	5.93	0.0132	0.0363	No Layer

Table E-6: Experimental Data for 900 μm Glass Beads in the 0.0266 m Diameter System

Run #	$\Delta P_s/L$ upper	σ_s upper	$\Delta P_s/L$ lower	σ_s lower	$\Delta P_a/L$ upper	σ upper	$\Delta P_a/L$ lower	σ lower
1	269.6	9.3	265.0	9.3	173.4	7.5	169.3	7.3
2	220.5	7.0	216.8	7.1	135.1	6.2	131.4	6.2
3	188.0	6.8	185.6	6.7	106.9	5.4	104.5	4.9
4	156.2	9.3	145.8	49.2	81.5	4.4	80.4	4.2
5	119.4	4.1	116.7	4.0	56.9	3.2	55.7	3.1
6	106.9	5.3	102.3	5.5	47.1	2.6	45.4	2.1
7	158.1	44.4	154.0	44.4	38.9	2.3	37.8	1.5
8	340.5	10.8	331.8	10.7	235.0	9.8	226.3	9.4
9	384.6	11.9	371.0	12.0	268.4	11.4	256.5	11.3
10	418.5	13.5	403.4	13.3	294.1	12.6	279.9	11.9
11	276.7	11.9	273.4	12.0	197.0	8.4	192.1	8.6
12	244.2	10.3	241.6	10.4	172.4	7.6	169.5	7.3
13	202.8	8.3	201.6	8.3	135.6	6.2	133.2	5.9
14	171.3	7.9	170.5	7.6	110.7	5.4	109.4	5.2
15	141.8	8.5	141.4	8.8	85.7	4.5	84.8	3.4
16	117.3	7.1	117.3	7.3	66.7	3.5	66.5	2.4
17	89.3	4.3	88.0	4.3	44.5	2.6	44.4	2.5
18	78.1	6.6	76.8	6.5	35.1	2.2	35.2	2.1
19	110.5	27.1	110.4	27.4	30.1	1.8	30.8	1.7
20	313.3	13.3	308.3	12.7	241.5	10.8	235.7	8.3
21	232.0	12.5	229.3	11.7	195.7	8.7	191.7	6.4
22	199.3	11.3	197.2	10.8	163.7	7.4	160.3	5.2
23	174.1	9.7	173.0	9.2	139.2	6.6	138.1	4.7
24	140.1	8.1	139.3	8.6	106.3	5.3	105.6	3.5
25	113.2	8.4	112.4	9.2	82.9	4.4	82.3	3.0
26	88.0	5.3	85.4	5.1	60.0	3.2	58.6	2.2
27	67.8	3.6	64.1	3.5	42.0	2.4	41.0	1.6
28	55.6	4.8	54.4	7.1	30.8	1.9	30.5	1.3
29	348.3	17.5	336.3	17.7	293.3	11.7	282.9	11.6
30	46.4	4.9	45.3	4.4	28.2	1.7	28.9	1.6
31	670.6	44.9	653.2	45.3	298.8	12.1	286.2	7.7
32	596.8	22.8	582.7	22.4	254.7	10.7	244.3	10.3
33	482.1	12.1	470.5	11.7	195.0	8.8	186.7	8.5
34	401.9	10.4	392.5	9.1	164.0	7.2	158.1	6.4
35	339.5	8.3	337.5	19.5	136.5	6.4	133.3	4.4
36	280.4	9.6	274.8	9.2	115.0	5.6	112.4	5.5
37	234.3	6.0	229.2	6.1	93.1	4.8	91.4	4.6
38	187.8	6.4	205.1	14.3	64.5	3.5	70.7	2.5
39	224.7	37.1	215.9	32.8	47.1	2.8	47.5	2.7
40	384.1	14.6	391.5	45.6	163.5	7.7	182.6	11.2
41	222.6	6.7	223.1	7.1	82.0	4.2	81.3	4.2

Table E-7: Experimental Data for 400 μm Iron Oxide in the 0.0266 m Diameter System

Run I.D.	U_g (m/s)	U_{pu} (m/s)	U_{pl} (m/s)	W_{su} (kg/s)	W_{sl} (kg/s)	F.A. (-)
H-1-IO-400-1	16.84	13.09	13.09	0.0143	0.0124	No Layer
H-1-IO-400-2	15.23	12.08	10.65	0.0130	0.0133	No Layer
H-1-IO-400-3	14.21	11.02	9.52	0.0120	0.0141	No Layer
H-1-IO-400-4	11.76	9.38	5.61	0.0091	0.0171	No Layer
H-1-IO-400-5	9.90	6.61	3.81	0.0059	0.0186	0.1500
H-1-IO-400-6	8.80	4.65	2.47	0.0060	0.0199	0.1500
H-1-IO-400-7	21.58	14.61	14.61	0.0170	0.0103	No Layer
H-1-IO-400-8	16.67	11.86	11.64	0.0150	0.0127	No Layer
H-1-IO-400-9	18.11	13.97	4.65	0.0187	0.0137	No Layer
H-1-IO-400-10	8.54	5.41	5.32	0.0059	0.0197	0.1390
H-1-IO-400-11	14.13	4.79	9.97	0.0097	0.0108	No Layer
H-1-IO-400-12	18.28	5.37	5.15	0.0108	0.0081	No Layer
H-1-IO-400-13	10.15	9.67	6.28	0.0055	0.0122	0.0920
H-1-IO-400-14	9.14	3.78	2.38	0.0043	0.0135	0.0920
H-1-IO-400-15	8.37	3.78	4.87	0.0035	0.0136	0.0920
H-1-IO-400-16	7.53	2.52	4.21	0.0031	0.0130	0.1390
H-1-IO-400-17	11.08	5.41	7.48	0.0065	0.0121	No Layer
H-1-IO-400-18	15.15	11.64	10.65	0.0095	0.0095	No Layer
H-1-IO-400-19	19.04	14.28	13.97	0.0116	0.0077	No Layer
H-1-IO-400-20	12.61	9.38	8.85	0.0075	0.0108	No Layer
H-1-IO-400-21	19.46	13.66	13.66	0.0049	0.0030	No Layer
H-1-IO-400-22	17.77	12.82	12.32	0.0044	0.0034	No Layer
H-1-IO-400-23	16.08	11.64	11.43	0.0043	0.0035	No Layer
H-1-IO-400-24	14.21	4.27	9.82	0.0040	0.0037	No Layer
H-1-IO-400-25	12.52	9.24	4.16	0.0034	0.0041	No Layer
H-1-IO-400-26	10.83	7.85	7.57	0.0029	0.0044	No Layer
H-1-IO-400-27	9.31	6.28	6.22	0.0025	0.0050	No Layer
H-1-IO-400-28	8.46	5.37	5.37	0.0021	0.0050	No Layer
H-1-IO-400-29	7.10	5.41	3.17	0.0014	0.0050	0.0920
H-1-IO-400-30	6.26	6.28	3.76	0.0014	0.0044	0.1390
H-1-IO-400-31	19.63	14.61	13.66	0.0251	0.0187	No Layer
H-1-IO-400-32	17.35	7.14	11.86	0.0248	0.0244	No Layer
H-1-IO-400-33	15.99	12.08	10.65	0.0218	0.0250	No Layer
H-1-IO-400-34	14.30	10.65	9.38	0.0161	0.0236	No Layer
H-1-IO-400-35	13.45	9.52	8.16	0.0138	0.0276	No Layer
H-1-IO-400-36	12.69	9.24	7.95	0.0116	0.0282	No Layer
H-1-IO-400-37	11.76	8.16	6.75	0.0107	0.0335	No Layer
H-1-IO-400-38	10.91	5.71	5.66	0.0093	0.0345	0.1390
H-1-IO-400-39	10.07	6.34	4.55	0.0086	0.0335	0.1500
H-1-IO-400-40	21.07	16.11	14.96	0.0368	0.0271	No Layer
H-1-IO-400-41	22.34	16.54	15.33	0.0391	0.0259	No Layer
H-1-IO-400-42	22.43	17.46	15.71	0.0326	0.0197	No Layer

Table E-8: Experimental Data for 400 μm Iron Oxide in the 0.0266 m Diameter System

Run #	$\Delta P_s/L$ upper	σ_s upper	$\Delta P_s/L$ lower	σ_s lower	$\Delta P_a/L$ upper	σ upper	$\Delta P_a/L$ lower	σ lower
1	251.7	7.5	249.7	7.1	283.6	281.5	478.3	335.2
2	217.8	6.0	216.3	8.2	121.5	6.9	122.9	4.8
3	194.6	6.1	194.3	12.4	105.4	5.8	106.3	10.2
4	150.8	8.7	157.2	15.7	72.2	5.3	70.4	8.0
5	130.5	15.2	131.4	18.0	48.6	4.1	49.3	3.3
6	143.9	23.1	146.0	32.8	37.0	3.6	37.8	4.0
7	363.2	14.0	348.5	13.9	243.4	10.4	230.9	10.1
8	266.9	7.4	258.6	7.1	162.0	7.8	155.5	7.2
9	299.7	12.1	287.0	12.0	187.6	8.4	175.7	8.1
10	173.8	34.8	-3.9	266.6	53.1	3.2	49.6	3.0
11	194.7	5.2	187.1	7.1	123.2	6.5	116.4	5.0
12	278.6	12.6	267.8	12.2	190.6	8.4	180.1	8.6
13	125.4	7.3	120.7	7.1	69.9	4.3	66.7	4.1
	119.6	8.2	114.2	8.5	63.0	3.6	59.4	3.3
15	99.5	13.8	95.7	15.8	50.1	4.0	47.1	5.7
16	217.3	28.4	207.6	26.6	43.5	3.3	41.1	2.9
17	141.0	4.7	135.4	6.1	82.1	5.1	77.2	4.5
18	209.7	7.3	202.1	10.5	136.6	6.8	129.0	4.9
19	294.7	12.2	260.7	115.2	205.9	9.8	192.8	6.5
20	168.6	5.7	162.3	6.5	102.5	6.1	96.3	4.1
21	250.9	14.0	243.6	14.0	212.3	9.9	203.9	9.9
22	219.0	13.3	194.5	117.6	181.2	8.3	178.4	8.1
23	189.6	9.4	187.0	9.4	152.2	7.4	149.7	7.5
24	160.0	9.8	157.9	9.6	123.1	6.6	121.7	6.2
25	134.6	9.6	133.0	9.3	100.5	5.8	98.9	5.6
26	105.7	7.8	103.6	7.8	78.6	4.6	77.4	4.3
27	89.4	4.2	86.0	3.8	59.3	4.1	57.0	3.7
28	76.0	6.0	72.9	5.5	49.9	4.2	48.0	3.0
29	63.6	4.5	61.1	5.9	35.7	4.0	34.2	5.2
30	78.1	13.8	77.3	14.5	30.6	2.9	29.8	3.5
31	379.3	13.1	363.2	15.9	214.1	10.7	204.4	9.8
32	344.4	10.3	332.6	19.9	174.0	10.1	165.9	7.1
33	308.9	10.0	302.1	20.4	150.5	8.6	144.9	8.1
34	242.2	11.2	231.8	19.4	122.8	7.0	117.9	5.4
35	242.6	8.3	234.2	13.5	110.0	6.5	104.4	5.0
36	231.0	13.9	223.7	23.4	100.3	6.0	95.5	6.0
37	246.8	14.0	236.8	19.9	90.5	6.2	85.4	5.9
38	235.8	20.8	226.0	30.2	78.0	5.1	74.0	4.8
39	254.1	34.7	251.3	34.6	68.7	4.5	68.3	4.4
40	463.7	14.0	459.3	24.5	235.3	10.9	229.6	7.5
41	503.5	14.8	497.2	31.3	266.8	11.7	260.5	7.4
42	478.6	20.2	472.6	44.3	264.6	12.6	259.2	8.8

Table E-9: Experimental Data for 67 μm Glass Beads in the 0.0504 m Diameter System

Run I.D.	U_g (m/s)	U_{pu} (m/s)	U_{pl} (m/s)	W_{su} (kg/s)	W_{sl} (kg/s)	F.A. (-)
H-2-GB-67-28	19.18	17.92	18.47	0.0177	0.0666	No Layer
H-2-GB-67-29	17.01	17.92	17.92	0.0149	0.0730	No Layer
H-2-GB-67-30	13.07	12.19	12.44	0.0058	0.0712	0.0370
H-2-GB-67-33	29.02	30.48	30.48	0.0246	0.0486	No Layer
H-2-GB-67-34	26.00	24.38	24.38	0.0246	0.0457	No Layer
H-2-GB-67-35	22.33	21.77	21.77	0.0199	0.0689	No Layer
H-2-GB-67-36	12.49	10.10	10.00	0.0052	0.0852	0.0240
H-2-GB-67-37	10.50	10.16	10.69	0.0221	0.0550	0.0670
H-2-GB-67-1	18.63	27.70	27.70	0.0186	0.0976	0.0240
H-2-GB-67-2	15.82	14.51	14.51	0.0112	0.1079	0.0510
H-2-GB-67-3	13.97	7.00	7.00	0.0083	0.1113	0.0840
H-2-GB-67-4	11.74	5.91	5.86	0.0048	0.1138	0.0840
H-2-GB-67-5	11.63	6.92	7.43	0.0042	0.0982	0.0840
H-2-GB-67-6	8.96	11.28	4.44	0.0279	0.0818	0.0840
H-2-GB-67-7	25.57	21.77	21.77	0.0223	0.0991	No Layer
H-2-GB-67-8	30.36	29.02	29.02	0.0308	0.0703	No Layer
H-2-GB-67-16	20.65	21.77	21.77	0.0192	0.0948	No Layer
H-2-GB-67-17	24.23	22.57	23.44	0.0247	0.0852	No Layer
H-2-GB-67-31	8.25	5.16	5.21	0.0398	0.0618	0.0130
H-2-GB-67-9	17.98	21.02	21.02	0.0189	0.1170	No Layer
H-2-GB-67-10	15.83	16.47	16.47	0.0111	0.1434	0.0840
H-2-GB-67-11	13.47	11.50	11.50	0.0062	0.1411	0.0670
H-2-GB-67-12	12.19	8.70	8.70	0.0055	0.1538	0.0840
H-2-GB-67-13	9.88	13.85	14.86	0.0402	0.1092	No Layer
H-2-GB-67-18	21.47	19.04	19.66	0.0229	0.1362	No Layer
H-2-GB-67-19	28.70	27.70	27.70	0.0332	0.1292	No Layer
H-2-GB-67-22	17.92	17.41	17.41	0.0183	0.1485	No Layer
H-2-GB-67-23	17.44	14.51	15.24	0.0158	0.1374	0.0370
H-2-GB-67-24	17.57	17.41	17.41	0.0155	0.1290	0.0510
H-2-GB-67-26	17.21	16.04	16.47	0.0154	0.1394	0.0370
H-2-GB-67-15	18.60	16.47	16.04	0.0187	0.2094	No Layer
H-2-GB-67-20	18.86	14.86	15.24	0.0158	0.2095	0.0130
H-2-GB-67-21	16.91	13.25	13.54	0.0105	0.1974	0.0130
H-2-GB-67-25	25.38	23.44	23.44	0.0306	0.1898	0.0040
H-2-GB-67-27	15.36	10.16	10.33	0.0061	0.2504	0.1020
H-2-GB-67-38	22.96	24.38	24.38	0.0211	0.2050	No Layer
H-2-GB-67-39	19.98	17.41	17.41	0.0211	0.2497	No Layer
H-2-GB-67-14	20.98	22.57	22.57	0.0175	0.0778	No Layer
H-2-GB-67-32	27.35	27.70	27.70	0.0069	0.0144	No Layer

Table E-10: Experimental Data for 67 μm Glass Beads in the 0.0504 m Diameter System

Run #	$\Delta P_s/L$ upper	σ_s upper	$\Delta P_s/L$ lower	σ_s lower	$\Delta P_a/L$ upper	σ upper	$\Delta P_a/L$ lower	σ lower
28	98.1	11.5	96.8	11.8	82.2	8.6	82.2	8.4
29	78.9	8.2	77.5	8.2	65.8	7.3	65.8	7.4
30	56.9	7.5	55.7	7.6	40.3	6.8	40.3	6.7
33	187.3	18.7	186.5	18.9	176.9	10.3	176.9	10.4
34	146.9	14.8	146.0	15.0	144.4	8.5	144.4	8.5
35	113.1	10.0	112.3	10.2	108.9	7.9	108.9	7.8
36	50.4	8.0	50.0	7.9	37.1	7.1	37.1	7.1
37	37.4	6.5	36.9	6.6	26.9	8.1	26.9	8.2
1	98.2	13.4	97.4	11.8	77.8	8.4	77.8	8.0
2	77.4	12.6	76.7	11.5	58.5	7.2	58.5	7.0
3	64.8	13.6	64.0	12.4	45.7	7.2	45.7	7.0
4	48.8	18.1	47.9	17.2	33.1	6.9	33.1	6.6
5	50.4	11.0	49.4	11.0	32.5	7.7	32.5	7.5
6	42.0	16.0	41.5	15.5	20.0	7.1	20.0	6.9
7	120.3	20.4	119.4	20.7	139.9	8.7	139.9	8.5
8	194.1	23.5	192.3	23.7	192.3	10.0	192.3	10.3
16	109.2	21.3	107.9	21.5	94.2	8.1	94.2	8.6
17	139.5	24.8	137.8	25.3	126.7	8.7	126.7	8.7
31	32.8	7.6	31.2	8.8	17.2	8.5	17.2	8.5
9	96.5	19.7	95.5	19.7	72.9	7.8	72.9	8.1
10	78.8	22.4	78.7	22.6	57.6	7.9	57.6	8.0
11	67.6	15.2	67.2	15.3	42.7	7.7	42.7	8.0
12	58.7	20.3	58.2	19.6	35.5	7.0	35.5	7.0
13	35.0	30.5	35.4	32.3	24.0	7.2	24.0	7.0
18	125.1	26.3	124.3	26.5	101.2	7.9	101.2	8.1
19	179.7	36.8	178.6	37.5	173.4	12.7	173.4	12.4
22	95.2	16.9	93.9	16.9	72.4	8.5	72.4	8.5
23	89.9	20.6	88.8	20.6	68.9	8.7	68.9	8.9
24	88.3	20.2	87.0	20.2	69.8	8.0	69.8	8.2
26	90.1	20.4	89.0	20.3	67.2	8.0	67.2	8.0
15	99.2	20.6	98.5	20.6	77.6	8.8	77.6	8.9
20	95.1	21.9	94.2	21.9	79.6	8.6	79.6	8.8
21	76.9	23.8	76.0	23.6	65.0	9.3	65.0	9.1
25	142.6	30.4	141.2	30.5	138.1	9.5	138.1	9.8
27	69.6	34.2	69.0	33.8	54.4	8.1	54.4	8.2
38	115.5	31.2	114.7	30.5	114.7	8.6	114.7	8.4
39	102.4	29.4	101.8	29.3	88.6	7.9	88.6	7.9
14	115.6	15.4	114.7	15.6	97.0	8.8	97.0	8.8
32	184.6	7.4	184.3	7.4	158.5	10.7	158.5	10.7

Table E-11: Experimental Data for 450 μm Glass Beads in the 0.0504 m Diameter System

Run I.D.	U_g (m/s)	U_{pu} (m/s)	U_{pl} (m/s)	W_{su} (kg/s)	W_{sl} (kg/s)	F.A. (-)
H-2-GB-450-10	29.26	26.50	26.50	0.0497	0.0677	No Layer
H-2-GB-450-31	25.90	24.38	24.38	0.0517	0.0740	No Layer
H-2-GB-450-32	21.33	19.66	20.32	0.0458	0.0699	No Layer
H-2-GB-450-33	19.50	17.92	16.93	0.0373	0.0595	No Layer
H-2-GB-450-34	14.63	16.47	15.63	0.0334	0.0744	No Layer
H-2-GB-450-35	16.15	12.19	10.51	0.0258	0.0830	No Layer
H-2-GB-450-36	11.88	7.43	7.71	0.0112	0.1139	0.0370
H-2-GB-450-37	10.97	6.28	6.22	0.0114	0.1128	0.1200
H-2-GB-450-38	10.05	8.96	8.70	0.0089	0.0872	0.1020
H-2-GB-450-39	7.62	15.24	4.06	0.0239	0.1022	0.1610
H-2-GB-450-1	22.86	21.77	21.77	0.0710	0.1180	No Layer
H-2-GB-450-2	24.99	22.57	22.57	0.0726	0.1030	No Layer
H-2-GB-450-3	18.28	15.24	14.86	0.0454	0.1437	No Layer
H-2-GB-450-6	12.19	7.52	7.91	0.0133	0.1675	0.1020
H-2-GB-450-8	12.19	3.06	2.61	0.0483	0.1457	0.1020
H-2-GB-450-22	15.08	12.44	12.19	0.0208	0.1583	0.0130
H-2-GB-450-23	13.71	8.83	8.83	0.0152	0.2193	0.0920
H-2-GB-450-24	27.12	24.38	24.38	0.0783	0.1115	No Layer
H-2-GB-450-25	29.87	27.70	27.70	0.0703	0.0958	No Layer
H-2-GB-450-26	19.20	18.47	18.47	0.0589	0.1154	No Layer
H-2-GB-450-4	16.15	13.85	13.85	0.0376	0.1705	0.0130
H-2-GB-450-5	13.56	12.44	10.88	0.0173	0.1943	0.0840
H-2-GB-450-9	10.97	2.29	2.80	0.0474	0.1672	0.1020
H-2-GB-450-11	28.04	24.38	24.38	0.0883	0.1276	No Layer
H-2-GB-450-27	27.12	24.38	24.38	0.0955	0.1473	No Layer
H-2-GB-450-28	23.77	21.02	21.02	0.0817	0.1459	No Layer
H-2-GB-450-29	21.03	19.04	19.04	0.0688	0.1771	No Layer
H-2-GB-450-30	15.39	16.93	16.04	0.2051	0.2051	No Layer
H-2-GB-450-13	35.20	29.02	29.02	0.1303	0.1739	No Layer
H-2-GB-450-15	23.16	19.66	19.04	0.0819	0.2374	No Layer
H-2-GB-450-16	18.28	16.47	16.04	0.0480	0.2596	No Layer
H-2-GB-450-17	15.84	12.44	11.50	0.0237	0.2762	0.0670
H-2-GB-450-18	15.54	12.97	11.95	0.0208	0.2577	0.0510
H-2-GB-450-19	15.54	7.81	9.99	0.0192	0.2725	0.1200
H-2-GB-450-20	14.02	7.25	6.84	0.0285	0.2790	0.1610
H-2-GB-450-21	12.80	2.29	2.43	0.0380	0.2405	0.1610
H-2-GB-450-14	22.25	20.32	19.66	0.0867	0.2786	No Layer
H-2-GB-450-12	25.60	20.32	19.66	0.1031	0.2436	No Layer
H-2-GB-450-7	8.53	15.63	27.70	0.0133	0.1675	No Layer

Table E-12: Experimental Data for 450 μm Glass Beads in the 0.0504 m Diameter System

Run #	$\Delta P_s/L$ upper	σ_s upper	$\Delta P_s/L$ lower	σ_s lower	$\Delta P_a/L$ upper	σ upper	$\Delta P_a/L$ lower	σ lower
10	231.8	13.4	229.0	13.3	179.6	8.8	179.6	8.1
31	216.4	4.9	213.8	4.8	143.3	9.1	143.3	8.7
32	166.2	3.5	163.8	3.5	100.0	7.6	100.0	7.6
33	130.1	3.5	128.1	3.4	84.7	8.1	84.7	8.1
34	108.4	3.5	106.8	3.3	49.7	8.4	49.7	8.3
35	90.9	2.6	89.5	2.5	59.7	7.1	59.7	6.9
36	68.9	3.2	67.7	3.2	33.8	8.5	33.8	8.4
37	63.8	2.8	62.6	2.7	29.2	8.7	29.2	8.3
38	60.8	3.4	59.6	3.6	24.8	10.0	24.8	9.9
39	60.5	4.0	59.0	3.9	14.8	9.8	14.8	9.4
1	197.3	3.5	198.4	3.4	113.7	7.5	113.7	7.5
2	228.4	5.1	227.8	5.2	134.1	7.3	134.1	7.4
3	141.0	3.4	140.8	3.5	75.2	9.0	75.2	9.3
6	81.2	9.0	80.3	9.0	35.5	8.1	35.5	8.3
8	94.8	18.3	94.2	18.2	35.5	7.6	35.5	7.5
22	110.8	2.2	109.0	2.2	52.6	7.2	52.6	6.2
23	87.7	3.5	86.2	3.4	44.1	7.8	44.1	6.7
24	247.1	6.4	245.0	6.3	156.1	8.8	156.1	8.4
25	283.7	3.0	280.9	3.0	186.6	10.7	186.6	10.1
26	166.6	2.4	164.9	2.4	82.3	7.6	82.3	7.3
4	122.6	3.7	122.4	3.7	59.7	8.5	59.7	8.9
5	100.6	2.0	99.7	1.9	43.2	7.2	43.2	7.3
9	117.2	37.6	116.3	37.4	29.2	7.4	29.2	7.1
11	261.7	8.2	258.2	8.0	166.0	8.2	166.0	7.7
27	276.1	3.4	273.2	3.3	156.1	9.1	156.1	8.8
28	209.2	3.1	206.7	3.1	122.2	8.2	122.2	8.5
29	195.5	12.2	193.3	12.1	97.4	8.1	97.4	7.9
30	163.4	7.2	161.5	7.2	54.6	7.6	54.6	7.4
13	383.6	4.8	380.0	4.7	253.0	10.7	253.0	10.4
15	227.4	2.2	225.4	2.2	116.5	8.2	116.5	8.1
16	173.4	1.9	171.4	1.9	75.2	8.2	75.2	8.2
17	126.8	2.0	125.1	2.0	57.7	8.1	57.7	7.9
18	120.6	2.1	119.1	2.1	55.6	8.2	55.6	8.1
19	115.3	1.6	113.7	1.5	55.6	8.3	55.6	7.9
20	110.6	2.0	108.9	1.9	45.9	7.6	45.9	7.5
21	121.1	23.2	119.2	23.0	38.8	7.3	38.8	7.2
14	242.8	3.6	240.6	3.5	108.1	8.0	108.1	8.0
12	273.7	29.9	271.1	29.7	140.2	8.6	140.2	8.5
7	67.1	12.4	66.5	12.3	18.3	7.3	18.3	7.2

Table E-13: Experimental Data for 900 μm Glass Beads in the 0.0504 m Diameter System

Run I.D.	U_g (m/s)	U_{pu} (m/s)	U_{pl} (m/s)	W_{su} (kg/s)	W_{sl} (kg/s)	F.A. (-)
H-2-BG-900-20	20.58	60.96	60.96	0.0323	0.0857	No Layer
H-2-BG-900-27	12.21	9.37	8.83	0.0186	0.0946	0.0040
H-2-BG-900-28	13.92	7.34	7.43	0.0239	0.0819	No Layer
H-2-BG-900-29	16.24	11.72	10.51	0.0313	0.0886	No Layer
H-2-BG-900-30	18.46	12.19	11.95	0.0329	0.0717	No Layer
H-2-BG-900-31	13.28	14.17	13.85	0.0389	0.0799	No Layer
H-2-BG-900-33	23.60	16.47	16.47	0.0385	0.0667	No Layer
H-2-BG-900-34	8.90	35.85	38.09	0.0776	0.0420	0.0510
H-2-BG-900-2	19.20	12.44	12.19	0.0360	0.1206	0.0370
H-2-BG-900-6	19.81	12.44	11.95	0.0467	0.1161	No Layer
H-2-BG-900-8	11.12	11.50	9.52	0.0385	0.1004	No Layer
H-2-BG-900-9	14.32	5.21	7.17	0.0380	0.1152	0.0510
H-2-BG-900-21	18.49	14.17	12.97	0.0432	0.1274	No Layer
H-2-BG-900-22	18.46	12.44	12.44	0.0441	0.1094	No Layer
H-2-BG-900-24	12.44	12.19	4.01	0.0276	0.1222	0.0510
H-2-BG-900-25	10.68	18.47	5.12	0.0202	0.1200	0.0670
H-2-BG-900-32	18.51	15.24	14.51	0.0426	0.1050	No Layer
H-2-BG-900-5	23.77	14.51	14.51	0.0565	0.1379	No Layer
H-2-BG-900-7	16.15	11.72	9.09	0.0494	0.1297	0.0510
H-2-BG-900-17	12.06	7.25	7.43	0.0276	0.0000	No Layer
H-2-BG-900-19	15.54	10.88	10.33	0.0375	0.1517	No Layer
H-2-BG-900-23	-----	5.21	4.01	0.0317	0.1436	0.0670
H-2-BG-900-26	7.61	18.47	18.47	0.0636	0.1395	No Layer
H-2-BG-900-10	12.19	33.86	32.08	0.0775	0.1643	0.0840
H-2-BG-900-11	9.14	7.25	6.15	0.0282	0.1828	0.0840
H-2-BG-900-12	17.22	12.19	9.37	0.0388	0.1983	0.1020
H-2-BG-900-14	18.28	12.97	11.95	0.0481	0.1870	No Layer
H-2-BG-900-15	21.33	13.54	13.25	0.0527	0.1701	No Layer
H-2-BG-900-16	21.33	15.24	14.51	0.0588	0.1817	No Layer
H-2-BG-900-18	9.01	6.15	7.34	0.0383	0.1741	0.1200
H-2-BG-900-1	21.94	12.44	12.70	0.0259	0.0562	No Layer
H-2-BG-900-3	29.26	18.47	18.47	0.0055	0.0077	No Layer
H-2-BG-900-4	27.06	9.23	9.23	0.0211	0.0319	No Layer
H-2-BG-900-13	18.44	60.96	11.50	0.0587	0.2492	0.0510

Table E-14: Experimental Data for 900 μm Glass Beads in the 0.0504 m Diameter System

Run #	$\Delta P_s/L$ upper	σ_s upper	$\Delta P_s/L$ lower	σ_s lower	$\Delta P_a/L$ upper	σ upper	$\Delta P_a/L$ lower	σ lower
20	383.8	131.1	382.1	131.0	93.6	8.9	93.6	8.7
27	192.7	2.2	191.3	2.2	35.6	6.6	35.6	6.7
28	242.6	6.2	241.0	6.2	45.3	7.7	45.3	7.6
29	325.7	4.4	323.9	4.5	60.4	8.3	60.4	8.7
30	380.7	6.0	379.0	6.0	76.6	8.6	76.6	8.4
31	487.7	13.1	485.9	13.2	41.5	9.4	41.5	9.4
33	566.0	17.7	563.7	17.7	120.7	9.9	120.7	10.2
34	145.1	10.6	143.8	10.5	19.8	6.9	19.8	6.7
2	473.5	5.3	471.7	5.3	82.3	7.5	82.3	7.3
6	497.2	8.5	495.5	8.4	87.2	8.5	87.2	8.2
8	329.4	4.4	327.7	4.4	29.9	8.4	29.9	8.2
9	262.7	3.3	261.2	3.3	47.8	7.3	47.8	7.3
21	414.0	93.6	412.1	93.5	76.7	8.5	76.7	8.7
22	500.6	9.8	498.3	9.7	76.5	8.8	76.5	8.8
24	239.0	2.2	237.5	2.2	36.8	8.0	36.8	7.8
25	188.4	6.2	187.1	6.2	27.8	7.8	27.8	7.5
32	536.4	7.1	534.3	7.1	76.9	9.3	76.9	9.3
5	688.2	3.1	687.8	5.2	122.2	8.9	122.2	8.7
7	346.5	2.5	344.9	2.4	59.7	8.3	59.7	8.2
17	276.0	3.6	274.5	3.6	34.8	8.7	34.8	8.2
19	388.9	3.8	387.1	3.8	55.6	8.4	55.6	8.9
23	249.6	4.4	247.9	4.4	-----	8.3	-----	8.0
26	128.6	23.6	127.9	23.5	14.8	7.6	14.8	7.2
10	205.6	27.0	204.4	26.9	35.5	6.6	35.5	6.7
11	256.6	3.2	225.7	4.2	20.8	8.5	20.8	6.7
12	351.2	4.4	349.5	4.3	67.3	8.3	67.3	8.1
14	466.5	5.3	464.4	5.3	75.2	8.5	75.2	8.7
15	542.4	4.7	540.2	4.6	100.0	9.0	100.0	8.5
16	600.5	6.2	598.4	6.2	100.0	9.5	100.0	9.0
18	279.6	12.5	278.3	12.5	20.3	8.1	20.3	8.1
1	438.2	111.2	436.4	111.1	105.4	8.4	105.4	8.1
3	200.7	10.0	198.8	9.9	179.6	8.9	179.6	8.7
4	426.4	19.2	424.2	19.2	155.4	9.2	155.4	9.0
13	470.4	5.2	468.5	5.1	76.3	8.6	76.3	8.6

Table E-15: Experimental Data for 400 μm Iron Oxide in the 0.0504 m Diameter System

Run I.D.	U_g (m/s)	U_{pu} (m/s)	U_{pl} (m/s)	W_{su} (kg/s)	W_{sl} (kg/s)	F.A. (-)
H-2-IO-400-9	27.15	-----	-----	0.0090	0.0127	No Layer
H-2-IO-400-10	23.17	19.04	19.66	0.0065	0.0137	No Layer
H-2-IO-400-11	19.79	17.92	17.41	0.0107	0.0154	No Layer
H-2-IO-400-12	16.57	16.93	12.70	0.0095	0.0191	No Layer
H-2-IO-400-13	12.70	11.72	9.67	0.0075	0.0168	No Layer
H-2-IO-400-14	9.15	4.03	3.67	0.0061	0.0150	No Layer
H-2-IO-400-15	5.60	4.54	4.54	0.0066	0.0221	No Layer
H-2-IO-400-16	1.74	-----	-----	0.0055	0.0194	No Layer
H-2-IO-400-21	11.81	2.61	2.57	0.0157	0.0508	0.0130
H-2-IO-400-27	25.09	21.02	21.02	0.0206	0.0311	No Layer
H-2-IO-400-28	23.93	21.77	21.02	0.0258	0.0441	No Layer
H-2-IO-400-29	25.07	10.51	10.69	0.0270	0.0435	No Layer
H-2-IO-400-32	16.34	12.97	12.19	0.0161	0.0391	No Layer
H-2-IO-400-33	17.88	17.41	16.04	0.0184	0.0419	No Layer
H-2-IO-400-34	20.82	16.93	16.47	0.0205	0.0393	No Layer
H-2-IO-400-35	10.39	4.61	5.30	0.0124	0.0494	0.0370
H-2-IO-400-17	20.28	17.92	17.92	0.0282	0.0664	No Layer
H-2-IO-400-18	16.37	13.54	12.19	0.0251	0.0670	No Layer
H-2-IO-400-19	13.38	11.08	8.83	0.0216	0.0675	No Layer
H-2-IO-400-22	10.84	9.52	10.88	0.0146	0.0775	0.0130
H-2-IO-400-23	10.19	4.17	4.72	0.0138	0.0669	0.0240
H-2-IO-400-24	10.95	9.37	2.67	0.0144	0.0758	0.0240
H-2-IO-400-25	8.52	6.41	2.52	0.0192	0.0743	0.0370
H-2-IO-400-26	22.25	19.66	18.47	0.0324	0.0677	No Layer
H-2-IO-400-30	23.91	20.32	20.32	0.0298	0.0515	No Layer
H-2-IO-400-31	14.07	12.19	11.50	0.0210	0.0553	No Layer
H-2-IO-400-8	12.83	-----	-----	0.0279	0.1029	0.0130
H-2-IO-400-20	9.76	7.62	4.09	0.0264	0.0901	0.0240
H-2-IO-400-37	17.20	13.54	13.25	0.0267	0.0793	No Layer
H-2-IO-400-39	19.47	18.47	9.67	0.0339	0.0938	No Layer
H-2-IO-400-40	21.47	19.66	19.04	0.0339	0.0780	No Layer
H-2-IO-400-41	15.65	13.85	6.34	0.0298	0.1016	No Layer
H-2-IO-400-42	14.10	14.17	11.28	0.0253	0.1060	0.0240
H-2-IO-400-43	12.08	3.58	3.69	0.0194	0.1167	0.0300
H-2-IO-400-44	11.81	-----	-----	0.0170	0.0971	0.0440
H-2-IO-400-1	11.16	3.31	3.29	0.0494	0.1517	0.0240
H-2-IO-400-2	17.50	16.47	15.24	0.0261	0.1480	0.0130
H-2-IO-400-3	19.34	16.47	15.63	0.0225	0.0915	No Layer
H-2-IO-400-4	24.44	20.32	20.32	0.0284	0.0650	No Layer
H-2-IO-400-5	19.32	25.40	21.77	0.0264	0.0994	No Layer
H-2-IO-400-6	12.07	-----	-----	0.0186	0.1221	0.0370
H-2-IO-400-7	16.45	-----	-----	0.0075	0.0075	No Layer
H-2-IO-400-38	20.38	13.25	12.70	0.0288	0.0677	No Layer

Table E-16: Experimental Data for 400 μm Iron Oxide in the 0.0504 m Diameter System

Run #	$\Delta P_s/L$ upper	σ_s upper	$\Delta P_s/L$ lower	σ_s lower	$\Delta P_a/L$ upper	σ upper	$\Delta P_a/L$ lower	σ lower
9	300.9	16.0	298.3	15.9	156.3	10.7	156.3	10.7
10	244.9	16.2	242.7	16.3	116.6	12.8	116.6	13.1
11	198.0	16.4	196.2	16.4	87.0	11.4	87.0	11.2
12	157.8	10.7	156.4	10.7	62.7	8.3	62.7	8.1
13	101.0	7.3	99.9	7.3	38.3	9.8	38.3	9.9
14	47.4	12.6	45.9	13.3	20.9	16.3	20.9	16.7
15	16.7	13.6	16.0	13.6	8.4	20.6	8.4	20.5
16	2.8	5.1	1.9	5.1	0.9	15.1	0.9	14.7
21	151.9	5.8	150.1	5.7	33.4	9.2	33.4	8.9
27	455.3	7.9	451.5	8.0	135.1	10.7	135.1	10.7
28	504.2	7.0	500.4	6.9	123.8	11.5	123.8	11.9
29	549.1	7.9	545.0	7.8	134.9	11.0	134.9	11.3
32	227.7	4.7	224.7	4.8	61.1	10.0	61.1	10.2
33	273.9	5.7	270.7	5.7	72.1	9.6	72.1	9.8
34	356.5	6.5	353.1	6.5	95.6	10.1	95.6	9.8
35	121.0	8.8	118.6	8.7	26.4	9.8	26.4	10.1
17	457.4	23.3	454.1	23.2	91.1	10.1	91.1	10.3
18	311.2	7.5	308.5	7.4	61.3	9.6	61.3	9.5
19	217.0	4.6	214.9	4.6	42.2	9.3	42.2	9.5
22	152.9	4.0	151.4	4.1	28.5	8.6	28.5	8.5
23	130.6	11.6	128.5	11.6	25.5	9.6	25.5	9.8
24	158.9	5.9	156.7	5.9	29.1	9.1	29.1	9.2
25	91.0	4.7	89.2	4.6	18.3	9.7	18.3	9.5
26	530.3	6.7	526.3	6.7	108.2	10.8	108.2	10.8
30	534.1	9.5	529.9	9.5	123.5	11.3	123.5	11.6
31	226.7	6.9	223.9	6.9	46.3	10.4	46.3	10.4
8	354.0	6.0	351.9	6.0	39.0	9.7	39.0	9.5
20	151.6	4.6	150.1	4.6	23.5	8.3	23.5	8.4
37	337.2	4.8	334.4	4.8	67.1	9.4	67.1	9.2
39	479.1	7.1	475.4	7.2	84.5	10.8	84.5	11.0
40	533.6	8.2	529.5	8.1	101.2	10.9	101.2	10.8
41	339.8	10.2	336.5	10.2	56.4	10.6	56.4	10.7
42	277.9	6.5	275.0	6.5	46.4	10.2	46.4	9.8
43	224.0	6.5	221.3	6.5	34.9	10.2	34.9	9.9
44	198.3	2.8	195.6	2.8	33.4	9.2	33.4	9.5
1	170.7	17.4	169.2	17.4	30.1	7.7	30.1	7.7
2	367.2	12.4	365.3	12.5	69.4	8.5	69.4	8.3
3	337.7	11.2	336.3	11.2	83.5	8.7	83.5	8.4
4	548.8	44.1	546.6	44.0	128.7	10.2	128.7	10.3
5	421.6	13.9	420.1	13.8	83.3	9.7	83.3	9.6
6	193.0	21.3	191.8	21.2	34.8	9.4	34.8	9.2
7	403.1	35.4	401.4	36.3	61.8	9.7	61.8	9.6
38	436.5	7.1	433.0	7.0	92.0	10.6	92.0	10.4

APPENDIX F

APPENDIX F

Some Correlations for Solids Friction Factor

Following is a short list of expressions for solids friction factor, f_s . This is not a complete list by far, yet it may show the type of variation that friction factor correlations have gone through.

Year	Investigator(s)	Solids Friction Factor or Pressure Representation
1933	Gasterstadt ⁽²³⁾	$\frac{\Delta P_T}{\Delta P_a} = (1 + .35\mu)$
1962	Stemerding ⁽⁷⁴⁾	$f_s = 0.003$
1967	Konno, Saito, and Maeda ⁽⁶⁰⁾	$f_s = 0.165 \frac{(gD_t)^{0.5}}{U_p}$
1978	Institute of Gas Technology ⁽⁶⁸⁾	$f_s = \frac{3C_d \rho_f D_t (U_g - U_p)^2}{8\rho_p D_p U_p^2}$
1976 1977	Yang ^(61,62)	$f_s =$ $0.02925 \frac{(1 - \epsilon) [(1 - \epsilon) U_f]^{-1.15}}{\epsilon^3 [U_p (gD_t)^{0.5}]}$

APPENDIX G

APPENDIX G

Recommendations for Future Study

1. The relationship between system parameters and mass flow ratio between the upper and lower halves of the pipe might yield an approach to scaling pneumatic transport systems. It is evident from the experimental data collected that the mass flow ratios obtained in the 0.0504 m diameter pipe are still increasing at gas velocities as high as 35 m/s, while the mass flow ratios in the 0.0266 m diameter pipe, in general, level off at gas velocities of about 25 m/s. This type of study would require data in the larger diameter pipe at higher gas velocities than those obtainable with the current air supply system. Additionally, operation at higher gas velocities might yield improvement in the estimate of R^* for the larger diameter system.

2. The concept of a critical point in the thermodynamic analogy requires experimental verification. Values of critical gas and solid fluxes have been presented. Apparatus capable of operation at these critical conditions should be constructed with careful attention given to flow visualization and pressure drop measurement.

3. Further study of electrostatics in pneumatic transport is needed. First, on an immediately practical basis, the avoidance of electrostatic discharge and the resulting damage it can cause should be studied. This study might concentrate solely on the development of protective devices for electronic equipment associated with a pneumatic transport facility.

Second, the surface wave phenomena discovered while transporting PVC particles may provide a unique opportunity to study the nature of the electrostatic field present. Most studies on electrostatics in pneumatic transport have been concerned with flow properties, such as particle velocity and pressure drop, or with the charge per particle, while very little is known about the electrostatic field associated with the flow of particles. The presence of a surface wave provides a visual record of electrostatic influence.

BIBLIOGRAPHY

1. Tuba, S.T., "Phenomenology of Vertical Gas-Solid Transport", (unpublished M.S. Thesis, Department of Chemical and Petroleum Engineering, School of Engineering, University of Pittsburgh, 1983).
2. Matsen, J.M., "A Phase Diagram for Gas-Particle Flow", Fluidization, IV.
3. Matsen, J. M., "Mechanisms of Choking and Entrainment", Powder Technology, Vol. 32 (1982), pp. 21-33.
4. Smith, R.A., Klinzing, G.E., "Investigation of Particle Velocities in a Gas-Solid System", AICHE Journal, Vol. 32 (1986), pp. 313-316.
5. Myler, C.A., "Gas-Solid Transport In a 0.0508 m Pipe At Various Inclinations With And Without Electrostatics", (unpublished M.S. Thesis, Department of Chemical and Petroleum Engineering, School of Engineering, University of Pittsburgh, 1985).
6. Zaltash, A., "Stability Analysis of Gas Solid Transport with Electrostatics", (unpublished M.S. Thesis, Department of Chemical and Petroleum Engineering, School of Engineering, University of Pittsburgh, 1985).
7. Beck, M.S., Drane, J., Plaskowski, A., Wainwright, N., "Particle Velocity and Mass Flow Measurement in Pneumatic Conveyors", Powder Technology, Vol. 2 (1969), pp. 269-277.
8. Klinzing, G. E., Gas-Solid Transport, (Mc. Graw Hill Book Co., New York, 1981), pp. 70.
9. Barth, W., "Physikalische und wirtschaftliche Probleme des Transportes von Festteilchen in Flüssigkeiten und Gasen", Chemie-Ing.-Techn, Vol 32, (1960), pp. 164-171.
10. Weber, M., "Principles of Hydraulic and Pneumatic Conveying in Pipes", Bulk Solids Handling, Vol. 1, (1981), pp. 57-63.

11. Bohnet, M., "Experimentelle und Theoretische Untersuchungen über das Absetzen, das Aufwirbeln und den Transport Feiner Staubteilchen in Pneumatischen Förderleitungen", VDI-Forschungsheft 507, Dusseldorf: VDI Verlag, 1965.
12. Siegel, W., "Experimentelle Untersuchungen Zur Pneumatischen Förderung Korniger Stoffe in Waagerechten Röhren und Überprüfung der Ähnlichkeitsgesetze", Dusseldorf: VDI-Forschungsheft 538, Dusseldorf: VDI Verlag, 1970.
13. Ettehadieh, B. and Gidaspo, D., "Fluidization in Two Dimensional Beds with a Jet", Quarterly Report for the Period 10 Oct to 31 Dec 1981, Gas Research Institute, Contract # GRI 5081-360-04765, 1981.
14. Massoudi, M., "Application of Mixture Theory to Fluidized Beds", (unpublished PhD Dissertation, Department of Mechanical Engineering, School of Engineering, University of Pittsburgh, 1986).
15. Molerus, O., "Description of Pneumatic Conveying", International Chemical Engineering, Vol. 20, (1980), pp. 7-18.
16. Nieh, S., Chao, B.T., and Soo, S.L., "Modeling of Pipe Flow of a Gas-Solid Suspension--Electrostatic and Gravity Effects", (Dept. of Mechanical and Industrial Engineering, University of Illinois at Urbana-Champaign, 1984), unpublished.
17. Wallis, G.B., One-Dimensional Two Phase Flow, (McGraw Hill, New York, 1969), pp. 89-103.
18. Prandtl, L., Essentials of Fluid Dynamics, (Blackie and Son, London, 1952), pp. 71-73, 142.
19. Tiejens, O.K., Applied Hydro and Aeromechanics, (McGraw Hill, N.Y., 1934).
20. Barkala, H.M. and Auchterlonie, L.J., "The Magnus or Robins Effect on Rotating Spheres", J. of Fluid Mechanics, Vol. 47, Part 3, (1971), pp. 437-447.
21. Rubinow, S.I., and Keller, J.B., "The Transverse Force on a Spinning Sphere Moving in a Viscous Fluid", J. of Fluid Mechanics, Vol. 11, (1961), pp. 447-459.

22. Tsuji, Y., Morikawa, Y., Mizuno, O., "Experimental Measurement of the Magnus Force on a Rotating Sphere at Low Reynolds Numbers", Transactions of the ASME Vol. 107, 1985, pp. 484-488.
23. Gasterstadt, J., "Die Experimentelle Untersuchung Des Pneumatischen Forder Vorganges", Forshungsarbeiten auf dem Gebeite des Ingenieurwesens, Heft 265, VDI Verlag, Berlin, (1924), pp. 2-76.
24. Matsumoto, S. and Saito, S., "Monte Carlo Simulation of Horizontal Pneumatic Conveying Based on the Rough Wall Model", J. of Chem. Eng. of Japan, Vol. 3, No. 2, (1970), pp. 223-230.
25. Matsumoto, S. and Saito, S., "On the Mechanism of Suspension of Particles in Horizontal Pneumatic Conveying: Monte Carlo Simulation Based on the Irregular Bounce Model", J. of Chem. Eng. of Japan, Vol. 3, No. 1, (1980), pp. 83-92.
26. Tsuji, Y., Oshima, T., Morikawa, Y., "Numerical Simulation of Pneumatic Conveying in a Horizontal Pipe", Kona, No. 3, (1985), pp. 38-51.
27. Ottjes, J.A., "Digital Simulation of Pneumatic Particle Transport", Chem. Eng. Science, Vol. 33, (1978), pp. 783-786.
28. Boothroyd, R. G., Flowing Gas-Solid Suspensions, (Chapman & Hall, New York, 1971), pp. 196-211.
29. Boothroyd, R.G., "Pressure Drop in Duct Flow of Gaseous Suspensions of Fine Particles", Trans. Instn. Chem. Engrs. Vol. 44, (1966), pp. 306-313.
30. Oshima, N., "Motions of Particles in a Stream", Proc. of the 7th Japan National Congress for Applied Mechanics, 1957, pp. 219-223.
31. Oshima, N., "Motion of Particles in Turbulence", Proc. of the 8th Japan National Congress for Applied Mechanics, 1958, pp. 319-325.
32. Torobin, L.B. and Gauvin, W.H., "Fundamental Aspects of Solids-Gas Flows Part IV", Canadian J. of Chem. Eng., Oct., (1960), pp. 142-153.
33. Torobin, L.B. and Gauvin, W.H., "Fundamental Aspects of Solids-Gas Flows Part V", Canadian J. of Chem. Eng., Dec., (1960), pp. 189-200.

34. Owen, P.R., "Pneumatic Transport", J. Fluid Mech., Vol. 39, (1969), pp. 407-432.
35. Stanley, E.H., Phase Transitions and Critical Phenomena, (Oxford University Press, N.Y., 1971), pp. 21.
36. Gelperin, N.I., Einstein, V.G., "The Analogy Between Fluidized Beds and Liquids", Moscow Institute of Fine Chemical Technology, Fluidization, Ed. Davidson, J.F. and Harrison, D, Academic Press, N.Y., (1971), pp. 541-568.
37. Furukawa, J., Ohmae, T., "Liquidlike Properties of Fluidized Systems", Ind. and Eng. Chemistry, Vol. 50, (1958), pp. 821-828.
38. Andrade, E. N. da C., Nature, Vol. 125, (1930), pp. 309-582.
39. Kondukov, N.B., Sosna, M.K., "Phase Rule and the Classification of the Constituent Phases of a System of Solid Particles Plus Gas", Theoretical Foundation of Chem. Eng., Translated from Russian, (1967), pp. 642-644.
40. Rizk, F., "Pneumatische Forderrung von Kunststoffgranulat in Horizontalen Rhorleitungen unter Berücksichtigung des Gewichtseinflusses in Zusammenhang mit Gut und Rhorwerkstoffeigenschaften, insbesondere im Optimalen Forderbereich", PhD dissertation, University of Karlsruhe, 1973.
41. Zenz, F.A., "Two-Phase Fluid-Solid Flow", Ind. and Eng. Chem., Vol. 41, (1949), pp. 2801-2806.
42. Canning D.A. and Thompson, A.I., "Recent Progress with Dense Phase Pneumatic Conveying," Proc. of the Century II Conference, ASME Meeting, San Francisco, CA, Aug (1982).
43. Hinkle, B.L., "Acceleration of Particles and Pressure Drops in Pneumatic Conveying", PhD thesis, Georgia Institute of Tech., (1953).
44. Lee, S.L., "A Study of Particle Motion in Turbulent Shear Flow of a Suspension", Particulate Science and Technology, Vol. 4, (1986), pp. 333-342.

45. Wallas, S.M., Phase Equilibria in Chemical Engineering, (Butterworth Publishers, Boston, 1985), pp. 12-19.
46. Zaltash, A., Myler, C.A., Klinzing, G.E., and Rizk, F., "Determination of a Critical Point for the Thermodynamic Analogy in Gas-Solid Transport", Proc. of Pneumatech III, Channel Islands, March (1987).
47. Klinzing, G.E., Rohatgi, N.D., Zaltash, A., and Myler, C.A., "Pneumatic Transport (A Review)", Power Technology, Vol. 51, No. 2 (1987), pp. 135-149.
48. Mathur, M.P., Wildman, D.J., Tuba, S.T., Klinzing, G.E., "Explorations into Thermodynamic Analogies and Critical Points in Reference to Gas-Solid Transport", AICHE Symposium Series, (1984), pp. 72-78.
49. Analytis, G.Th. and Lubbesmeyer, D., "A Novel Cross-Correlation Technique for the Determination of Radial Velocity Profiles in Two-Phase Flows", EIR-Bericht Nr. 483, Wurenlingen, FRG, Feb (1983).
50. Mathur, M. P., Klinzing, G. E., "Measurement of Particle and Slip Velocities in Coal/Gas System", AICHE Symposium Series Vol. 79, (1983), pp. 60-63.
51. Klinzing, G.E., Zaltash, A., and Myler, C.A., "Particle Velocity Measurements Through Electrostatic Field Fluctuations Using External Probes", Part. Sci. and Tech., Vol. 5, (1987), pp. 95-104.
52. Chi, S.M.B., "Effect of Entrapped Air Bubble on Fine Coal Filtration and Dewatering", (unpublished M.S. Thesis, Department of Chemical and Petroleum Engineering, School of Engineering, University of Pittsburgh, 1984).
53. NUMODES, Dilute Phase Pneumatic Transport Software, University of Pittsburgh, Copyright 1986.
54. Richardson, J.F., McLeman, M., "Pneumatic Conveying- Part II Solids Velocities and Pressure Gradients in a one-inch Horizontal Pipe", Trans. Instn. Chem. Engrs., Vol. 38, (1960), pp. 257-266.
55. Molerus, O., "Prediction of Pressure Drop With Steady State Pneumatic Conveying of Solids in Horizontal Pipes", Chem. Eng. Sci., Vol. 36, No. 12, (1981), pp. 1977-1984.

56. Ally, M. R., "Electrostatic Effects in Dilute and Dense Phase Gas-Solid Pneumatic Transport", (unpublished PhD Dissertation, Department of Chemical and Petroleum Engineering, School of Engineering, University of Pittsburgh, 1981).
57. Zenz, F. A., Othmer, D. F., Fluidization and Fluid-Particle Systems, (Reinhold Publishing Corporation, New York, 1960), pp. 314-318.
58. Matsumoto, S., Sato, H., Suzuki, M., and Maeda, S., "Prediction and Stability Analysis of Choking in Vertical Pneumatic Conveying", J. of Chem. Eng. of Japan, Vol. 15, (1982), pp. 440-445.
59. Dhodapkar, S., Masters Thesis, University of Pittsburgh, (to be completed).
60. Konno, H., Saito, S., and Maeda, S., "Pneumatic Conveying of Solids through Horizontal Straight Pipes", Kagaku Kogaku, Vol. 31 (1967), pp. 243. (in Japanese)
61. Yang, W. C., "Correlations for Solid Friction Factors in Vertical and Horizontal Pneumatic Conveyings", AIChE Journal, Vol. 20, (1974), pp. 605-607.
62. Yang, W. C., "A Unified Theory on Dilute Phase Pneumatic Transport", J. of Powder and Bulk Solids Tech., Vol. 1, No. 1, (1977), pp. 89-95.
63. Weber, M., "Compressible Flow of Gas-Solid Mixtures", Special Seminar, University of Pittsburgh, 1986.
64. Stegmaier, W., "Zur Berechnung der Horizontalen Pneumatischen Forderung Fein Korniger Stoffe", Fordern and Heben, Vol. 28, Nr. 5/6, (1978), pp. 363-366.
65. Coal Conversion Systems Technical Data Book, Sec. IVC.52.4, DOE/FE/05157-2, (1982).
66. Gas Fluidization Technology, Edited by D. Geldart, (John Wiley and Sons, Chichester, 1986), pp. 350-357.
67. BMDP Statistical Software 1981, Edited by W. J. Dixon, (Univ. of Calif. Press, Berkeley, 1981), pp. 305-314.

68. Institute of Gas Technology, "Preparation of a Coal Conversion Systems Technical Data Book", Project 8979, ERDA Contract No. EX-76-C-01-2286, 1978.
69. Konno, H., Saito, S., "Pneumatic Conveying of Solids Through Straight Pipes", Chem. Eng. Japan, Vol. 2, (1969), pp 211-217.
70. Fan, L.S., Wisecarver, K., and Kitano, K., "Pressure Fluctuation in a Multisolid Pneumatic Transport Bed", First Intl. Conf. on Circulating Fluidized Beds, Halifax, Canada, 18-20 November (1985).
71. Satija, S., Young, J.B., Fan, L.S., "Pressure Fluctuations and Choking Criterion for Vertical Pneumatic Conveying of Fine Particles", Powder Technology, Vol. 43, (1985), pp. 257-271.
72. Min, K., "Particle Transport and Heat Transfer in Gas-Solid Suspension Flow Under the Influence of an Electric Field", (PhD dissertation, University of Illinois, 1965).
73. Tsuji, Y., Oshima, T., Morikawa, Y., "Numerical Simulation of Pneumatic Conveying in a Horizontal Pipe", Kona, No. 3, (1985), pp. 38-51.
74. Stemerding, S., "The Pneumatic Transport of Cracking Catalyst in Vertical Risers", Chemical Eng. Sci., Vol. 17, (1962), pp. 599-608.